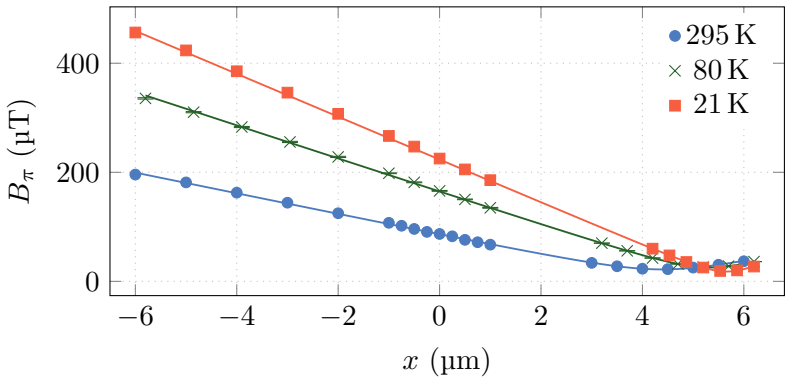
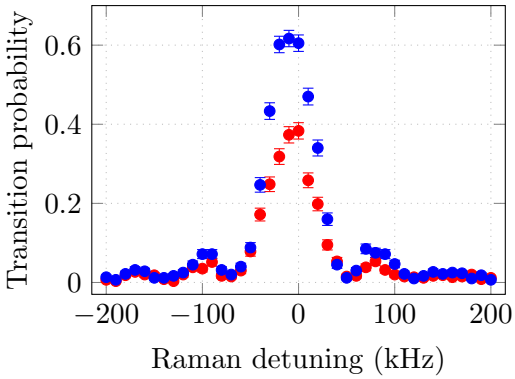
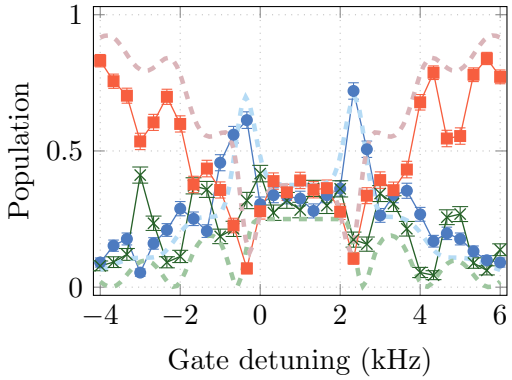
A cryogenic trap for microwave-driven quantum logic using $^{43}Ca^{+}$ ions







Clemens Löschnauer

A thesis submitted for the degree of
Doctor of Philosophy

University of Oxford

Christ Church College

Michaelmas Term 2021

Abstract

A cryogenic trap for microwave-driven quantum logic using $^{43}Ca^{+}$ ions
DPhil thesis
Clemens Löschnauer
Christ Church College
University of Oxford

The encoding and manipulation of information using the quantum states of trapped ions currently represents one of the most promising routes towards the realisation of a universal quantum computer. Although quantum gates in this system were originally driven by lasers, an alternative approach that uses the magnetic field gradients generated by current-carrying structures integrated directly into the trap has gained traction in recent years. This laser-free approach offers a few advantages, but the implementation of fast two-qubit gates with fidelities below the threshold required for quantum error correction remains challenging.

In this thesis I describe progress in an ion trap system aimed at improving the fidelity and speed of two-qubit gates driven by magnetic field gradients oscillating near the transition frequency of the qubit. Work is based on a hyperfine qubit in $^{43}Ca^{+}$ that has not been used for quantum logic before. We operate at a static magnetic field of 28.8 mT, at which point the qubit frequency of approximately 3.1 GHz becomes to first order insensitive to field fluctuations, enabling an internal coherence time that is orders of magnitude larger than the duration of quantum gates. The strong magnetic field results in a complex energy level structure, with adjacent states in the ground level being split by several multiples of the linewidths of the cooling lasers. Nevertheless, we demonstrate cooling to a temperature of 0.5 mK for a single ion, close to the Doppler limit, by exploiting dark resonances that form between fine-structure levels. Furthermore, we implement resolved-sideband cooling using two laser beams driving a Raman transition, achieving an average occupation number $\bar{n} = 0.08$ for the two-ion motional mode of interest.

Experiments are carried out in a surface trap that is suitable for operation at room and cryogenic temperatures. It features a U-shaped microwave electrode, which produces a microwave magnetic field such that the field component coupling the qubit states exhibits a strong gradient, but significantly reduced amplitude around the trap centre. I discuss measurements of parameters that will impact two-qubit gate fidelity, such as heating rates, drifts in motional frequencies, ac Zeeman shifts and the spatial dependence of the microwave magnetic field.

Furthermore, we demonstrate spin-motion entanglement for a single ion using the Mølmer-Sørensen scheme and present the results of initial attempts at a two-qubit gate, for which we measure a fidelity of 0.77(2). I also provide a brief analysis of dominant sources of error that will have to be addressed in future experiments.

Acknowledgements

During my time in Oxford and also before, I met many people without whom the last few years would not have been so memorable and enjoyable. I want to take this opportunity to thank all of them sincerely.

My supervisor, Prof. Andrew Steane, provided guidance throughout my time as a DPhil student. He offered valuable insights during discussions on various topics in ion trapping and gave very useful suggestions while I was writing up my thesis.

Work in the lab was facilitated by the other head of the research group, Prof. David Lucas, who regularly came by Lab 3 to check for any problems. As I realised soon after starting my DPhil, quite often in experimental physics things do not go to plan, which made it just the more important that David was around to offer advice.

I had the opportunity of working with three post-docs in my lab. Dr. Thomas Harty was in charge of the initial stages of the experiment and taught me a lot about the intricacies of operating an ion trap. In Tom's absence, Dr. Joseph Goodwin helped out for a few months, providing his expertise in optical components. Later, Dr. Ryan Hanley took over responsibility for Lab 3 with cheerful enthusiasm. He kept his calm in many situations, not least during the strenuous days we spent together in the cleanroom.

I would also like to thank all the other people whom I had the pleasure of working with in my lab. Jochen Wolf designed large portions of the apparatus, was responsible for the fabrication of the trap chip and assembled the vacuum chamber. Marius Weber did a great job tracking down noise sources and will continue work towards implementing high-fidelity two-qubit gates. Dr. Mario Gely carried out important simulations and will soon be assuming duties as post-doc in Lab 3.

Other people in the research group deserve being mentioned just as much. Dr. Raghu Srinivas was always available for a chat, not just about football or movies, and readily provided support when needed. Kaitlin Gili made sure I did not neglect my sense of adventure. Dr. Gabriel Araneda, Dr. Fabian Pokorny, Dr. Mariella Minder, Dougal Main, Ana Sotirova, Sebastian Saner, Oana Bazavan, Amy Hughes, Peter Drmota and Bethan Nichol were always happy to join for a trip to the pub or other social activity. Dr. Chris Ballance gave many useful suggestions for the experiment, while David Nadlinger could be relied on when it came to fixing software bugs. A big thanks also to Martin Sepiol, Vera Schäfer, Laurent Stephenson, Dr. Tim Ballance, James Tarlton and Keshav Thirumalai.

Outside the research group, David Drahi and Shaobo Gao were great company during our many lunches and dinners.

I gratefully acknowledge funding through a scholarship from Christ Church College.

My family in Austria offered support in many ways. I also highly valued the time spent travelling with friends as a way of replenishing my energy and motivation. Frieda was a constant source of encouragement for many years.

Finally and most importantly, I want to thank my parents, Rosemarie and Rupert, and my brother, Simon. My mum and dad have always supported me in my decisions, be it emotionally or financially, and encouraged me to do what I enjoy most. My brother has been a great companion throughout my life. To all three of you, thank you for keeping me moving forward.

Contents

1 Introduction **2**
- 1.1 Ion traps as a platform for quantum computing . . . 4
- 1.2 Laser-free quantum logic with trapped ions . . . 6
  - 1.2.1 Static magnetic field gradient . . . 7
  - 1.2.2 Near-motional-frequency magnetic field gradient . . . 8
  - 1.2.3 Near-qubit-frequency magnetic field gradient . . . 9
- 1.3 Contents of this thesis . . . 10

2 $^{43}Ca^{+}$ as a trapped-ion qubit **12**
- 2.1 Atomic structure of $^{43}Ca^{+}$ . . . 13
- 2.2 Radiative transitions . . . 19
- 2.3 Photoionisation . . . 20
- 2.4 Laser cooling . . . 21
- 2.5 Qubit initialisation . . . 21
  - 2.5.1 Optical pumping . . . 22
  - 2.5.2 Microwave transfer pulses for state preparation . . . 22
- 2.6 Readout . . . 24
  - 2.6.1 Microwave transfer pulses for readout . . . 25
  - 2.6.2 Shelving to $D_{5/2}$ level . . . 26
  - 2.6.3 State-dependent fluorescence detection . . . 29

3 Apparatus **31**
- 3.1 Vacuum system . . . 31
  - 3.1.1 Trap chip . . . 32
  - 3.1.2 Vacuum equipment . . . 37
- 3.2 Magnetic field coils . . . 39
- 3.3 Laser systems . . . 40
  - 3.3.1 Photoionisation lasers . . . 40
  - 3.3.2 Ca^{+} lasers . . . 41
  - 3.3.3 Trap table optics . . . 46
  - 3.3.4 Imaging system . . . 51
  - 3.3.5 Laser diagnostic system . . . 54
- 3.4 Cryogenic equipment . . . 54
- 3.5 Control software and electronics . . . 56
  - 3.5.1 Sinara hardware . . . 56
  - 3.5.2 Trap rf signal . . . 58
  - 3.5.3 Trap dc signals . . . 59
  - 3.5.4 Stabilisation of laser intensities ("noise-eating" system) . . . 60
  - 3.5.5 Microwave electronics . . . 60

4 Motion of a single ion in a surface trap **62**
4.1 Classical description . . . 63
4.1.1 Homogeneous case . . . 67
4.1.2 Inhomogeneous case . . . 68
4.2 Quantum description . . . 71
4.2.1 Homogeneous case . . . 73
4.2.2 Inhomogeneous case . . . 76
4.3 Pseudopotential approximation . . . 78
4.4 Operation of our surface trap . . . 79
4.4.1 Trap geometry . . . 79
4.4.2 Trapping potentials . . . 81
4.4.3 Trapping under pseudopotential approximation . . . 84
4.4.4 Calculation of voltage sets . . . 85
4.4.5 Trapping parameters . . . 88

5 Interaction of a single ion with external fields **90**
5.1 Making use of the interaction picture . . . 91
5.2 Magnetic-dipole transitions . . . 93
5.2.1 Magnetic-dipole matrix elements . . . 96
5.2.2 Dependence of magnetic field on position operator . . . 98
5.2.3 Coupling internal and external degrees of freedom . . . 99
5.2.4 Ac Zeeman shifts . . . 111
5.3 Raman transitions . . . 113
5.4 Rabi pulses . . . 117
5.5 Ramsey interferometry . . . 119

6 Laser cooling of $^{43}Ca^{+}$ in a static magnetic field of 28.8 mT **121**
6.1 Theoretical considerations . . . 122
6.1.1 Two-state model . . . 123
6.1.2 Cooling scheme for $^{43}Ca^{+}$ . . . 127
6.1.3 Raman sideband cooling . . . 134
6.1.4 Thermometry of the motional state . . . 137
6.2 Experimental implementation . . . 141
6.2.1 Doppler cooling . . . 141
6.2.2 Raman sideband cooling . . . 151
6.3 Laser cooling of two ions . . . 152

7 Trap characterisation and calibration experiments **157**
7.1 Methods to measure transition frequencies . . . 157
7.1.1 Ramsey spectroscopy . . . 159
7.2 Calibration routines . . . 162
7.2.1 Laser beam alignment . . . 162
7.2.2 Setting laser frequencies . . . 163
7.2.3 Microwave transfer pulses . . . 164
7.2.4 Calibration of static magnetic field . . . 165
7.2.5 Measurements of secular frequencies . . . 167
7.2.6 Micromotion compensation . . . 170
7.3 Validation of model for electric field of trap . . . 173
7.4 Coherence times . . . 175
7.5 Transition frequency of clock qubit . . . 176

7.6 Single-ion heating rates . . . 178
7.7 Two-ion heating rates . . . 183
7.8 Microwave magnetic field . . . 184
7.8.1 Field model . . . 185
7.8.2 Measurements of field gradient . . . 188

8 Spin-motion entanglement driven by microwaves 195
8.1 Collective motion of a string of ions . . . 195
8.2 Spin-dependent forces . . . 199
8.3 Mølmer-Sørensen force applied to a single ion . . . 204
8.3.1 Theoretical description . . . 204
8.3.2 Observation of the Mølmer-Sørensen force on a single ion . . . 205
8.4 Mølmer-Sørensen force applied to two ions . . . 209
8.4.1 Theoretical description . . . 209
8.4.2 Implementation of a Mølmer-Sørensen gate with two ions . . . 216
8.5 Simulations of projected gate fidelity . . . 219
8.5.1 Fluctuations in microwave power . . . 220
8.5.2 Variations in motional frequency . . . 225
8.5.3 Off-resonant excitation on the carrier . . . 227
8.5.4 Off-resonant driving of spectator modes . . . 228
8.5.5 Cross-coupling of motional modes . . . 231
8.5.6 Off-resonant excitation of internal spectator states . . . 233
8.5.7 Heating rate . . . 234
8.5.8 Motional dephasing . . . 234
8.5.9 Suppression of gate errors . . . 236

9 Conclusions 238
9.1 Comparison with other experiments . . . 240
9.2 Outlook . . . 241

A Atomic structure of Ca^+ ions 251
A.1 Hyperfine interaction . . . 252
A.2 Interaction with an external static magnetic field . . . 254
A.3 The ground level of $^{43}Ca^+$ . . . 257
A.3.1 Field-insensitive transitions . . . 261
A.3.2 Magnetic-dipole transition matrix elements . . . 262

B Solutions to Mathieu equation 265
B.1 Homogeneous case . . . 266
B.1.1 Lowest-order approximation . . . 268
B.2 Inhomogeneous case . . . 269
B.2.1 Lowest-order approximation . . . 271

C Dynamics of multi-state quantum systems 272
C.1 Rotating frames . . . 273
C.1.1 Heisenberg picture . . . 276
C.1.2 Interaction picture . . . 276
C.2 Magnus expansion . . . 276
C.3 Adiabatic elimination of intermediate states . . . 277
C.3.1 Ac Zeeman shifts . . . 280

C.4 Rabi Hamiltonian 281

List of Figures

2.1 Energy level diagram of $^{43}Ca^{+}$ in an external static magnetic field of 28.778 28 mT . . . 17
2.2 Illustration of scheme used for photoionisation . . . 20
2.3 Illustration of scheme used for state preparation . . . 23
2.4 Microwave transitions in ground level relevant for state preparation and readout . . . 23
2.5 Illustration of scheme used for shelving . . . 27

3.1 Block diagram of apparatus . . . 32
3.2 Photograph of main equipment located on trap table . . . 33
3.3 Rendering of trap chip and illustration of electrodes around trap centre 33
3.4 Photograph of rf PCB and trap chip . . . 34
3.5 Schematic illustration of rf and microwave electrodes . . . 35
3.6 Microwave power reflected from trap chip as function of frequency . 37
3.7 Rendering of interior of vacuum chamber . . . 38
3.8 Arrangement of optical components on laser breadboards . . . 41
3.9 Configuration of optical components on 397/393 nm AOM breadboard 44
3.10 Configuration of optical components on 854 nm and 866 nm AOM breadboards . . . 45
3.11 Configuration of laser beams launched into vacuum chamber . . . 47
3.12 Beam path for Doppler and photoionisation beams . . . 49
3.13 Beam path for blue sigma beams . . . 50
3.14 Beam path for 397 nm Raman beams . . . 51
3.15 Imaging system used for detection of fluorescence at 397 nm . . . 53

4.1 Illustration of trap with relevant coordinate systems . . . 80
4.2 Electric potentials in radial plane . . . 89

5.1 Transitions between internal and motional states . . . 107
5.2 Ac Zeeman shifts on clock qubit . . . 112
5.3 Raman transition. . . . 113

6.1 Illustration of scheme used for Doppler cooling . . . 129
6.2 Dark resonance in a three-state system . . . 132
6.3 Transitions involved in main dark resonances arising in cooling scheme 133
6.4 Raman transition used for sideband cooling and motional thermometry 135
6.5 Arrangement used for Doppler cooling beams . . . 142
6.6 Fluorescence rate and population of $4\,P_{1/2}$ level as a function of frequency of 866 nm beam . . . 144

6.7 Average occupation number of in-plane mode for different intensities of 397 nm and 866 nm beams . . . 146
6.8 Average occupation number of in-plane mode as a function of frequencies of 397 nm and 866 nm beams . . . 146
6.9 Fluorescence profile as a function of frequency of 866 nm beam for optimum cooling parameters . . . 147
6.10 Rabi flopping on motional carrier with Raman beams . . . 149
6.11 Fluorescence rate and population of $4\,P_{1/2}$ level as a function of frequency of 866 nm beam for readout parameters . . . 150
6.12 Occupation probabilities of different number states for a thermal ion 151
6.13 Sideband thermometry on radial in-plane mode of a single ion . . . 152
6.14 Influence of off-resonant spectator mode during sideband thermometry 155
6.15 Sideband thermometry on radial in-plane rocking mode of two ions . 156

7.1 Pulse sequence in basic Ramsey scheme . . . 159
7.2 Transition probability as a function of parameters in the Ramsey scheme 160
7.3 Ramsey sequence with spin-echo and off-resonant probe pulses . . . 162
7.4 Method used for calibration of static magnetic field . . . 166
7.5 Measurements of secular frequency of in-plane mode for a single ion 169
7.6 Drift in secular frequency of radial in-plane mode of a single ion over time . . . 170
7.7 Compensation of micromotion in radial directions . . . 172
7.8 Secular frequencies of radial modes as a function of mode angle . . . 174
7.9 Transition frequency of clock qubit as a function of static magnetic field . . . 177
7.10 Transition frequency of clock qubit as function of output power of rf source . . . 178
7.11 Heating rate of in-plane mode of a single ion at different temperatures 181
7.12 Heating rates of radial in-plane modes of two ions at 85 K . . . 184
7.13 Schematic model of microwave electrode . . . 186
7.14 Model for microwave magnetic field . . . 187
7.15 Parameters of microwave magnetic field for carrier and sideband transitions . . . 187
7.16 Variation of π-component of microwave magnetic field along x-axis at different temperatures . . . 189
7.17 Variation of σ^--component of microwave magnetic field along x-axis at different temperatures . . . 191

8.1 Spin-motion entanglement for a single ion using the Mølmer-Sørensen scheme . . . 209
8.2 Evolution of two-qubit system in phase space under the action of the Mølmer-Sørensen Hamiltonian . . . 212
8.3 Populations of qubit states as a function of detuning of two-qubit gate pulse . . . 217
8.4 Observed parity as a function of phase of analysis pulse for two-qubit gate . . . 219
8.5 Gate error caused by fluctuations in Rabi frequency . . . 222
8.6 Gate error caused by fluctuations in ac Zeeman shift . . . 224
8.7 Gate error caused by fluctuations in motional frequency . . . 227
8.8 Gate error caused by motional heating . . . 235

8.9 Gate error caused by motional dephasing 236

A.1 Energies of states in $4\,S_{1/2}$ ground level as a function of external magnetic field. 257
A.2 Energies of states in $4\,P_{1/2}$ level as a function of external magnetic field. 258
A.3 Energies of states in $4\,P_{3/2}$ level as a function of external magnetic field. 258
A.4 Energies of states in $3\,D_{3/2}$ level as a function of external magnetic field. 259
A.5 Energies of states in $3\,D_{5/2}$ level as a function of external magnetic field. 259
A.6 Structure of the $4\,S_{1/2}$ ground level of $^{43}Ca^{+}$ in a static magnetic field of 287.7828 G 260
A.7 Sensitivity of transition frequency to changes in magnetic field for transitions in ground level of $^{43}Ca+$ 262

Chapter 1

Introduction

Constructing a device that carries out computations based on the laws of quantum rather than classical mechanics has been a goal in physics for several decades. Ever since Feynman introduced the concept of the quantum computer to a broader audience [Fey82], tremendous theoretical and experimental work has gone into developing methods that enable the controlled evolution of a quantum system from an arbitrary initial state. As an important first step, these efforts have already given rise to the field of quantum simulation [GAN14]. In this approach, systems that are difficult to handle experimentally are mapped to a system that can be manipulated much more precisely, in such a way that the interactions which govern the evolution of the former are exactly replicated in the simulator system. While this already allows analysing the behaviour of systems that would require excessive resources from classical computers, a given simulator is only suitable for a restricted number of target systems.

More desirable therefore is a universal quantum computer, a machine that can implement arbitrary unitary operations on a full register of quantum bits [LJL+10]. Realising such a device in practice is a challenging endeavour. While it has been shown that a universal set of quantum gates is provided by arbitrary single-qubit rotations and a two-qubit entangling operation [BBC+95; BDD+02], there remains the difficult task of increasing the fidelity of these two kinds of operation to the level where quantum computers may realise their full potential. Many systems exist that provide a mapping from the abstract concept of a qubit to a concrete pair of physical states, but not all of them are equally suitable as a platform for quantum computa-

tion. It is now generally accepted that for a system to be considered a viable option, it needs to fulfil certain criteria [DiV00]: it has to contain rigorously defined qubits and be scalable, offer a way to initialise qubits in a fiducial state, maintain coherence for much longer than the time required to carry out gate operations, implement a universal set of quantum gates and be capable of qubit-specific measurements.

Apart from these essential requirements, the practical implementation of a quantum computer will also need ways to mitigate the impact of errors that will inevitably occur during gate operations, caused by limited precision of control hardware, imperfections in the mechanisms underlying the gates or unintended interactions of the apparatus with the environment. Early work in the field of quantum information processing showed that useful computation in the presence of decoherence is in principle possible and introduced the concept of quantum error correction [Sho95; Ste96]. The key idea behind proposals for fault-tolerant quantum computation is to encode one logical qubit in several physical qubits and find operations to be carried out on the latter that enable one to check for errors without disturbing the state of the logical qubit. If an error has been detected, the physical qubits are then manipulated appropriately so as to correct the state of the logical qubit. It has by now been proven for several error models that computational sequences of any length may be carried out correctly with this approach if the error probability per gate performed on physical qubits lies below a certain threshold [Pre98]. The exact threshold depends on the error correcting code and noise model assumed, but values close to 10^{-2} have recently been reported for surface codes [FMM+12]. It is important to note, however, that high thresholds are in general bought by increasing the number of physical qubits used to represent a logical qubit, which means that the resources required to tolerate high error probabilities may not be feasible in practice. An error per gate of 10^{-4} is therefore often quoted [Kni05] as a requirement for a fault-tolerant quantum computer that might realistically be built in the not-too-distant future. While the value assumed evidently depends on the relative weights that one assigns to system size and gate quality and is thus somewhat arbitrary, I will take an error per gate of 10^{-4} as a guideline for the remainder of this work.

1.1 Ion traps as a platform for quantum computing

Several potential systems for quantum computation are currently being explored, such as superconducting qubits [Wen17; GCS17], Rydberg atoms [SWM10; Saf16], photonic networks [SP19; PFA+21] and nitrogen vacancy centers [DMD+13; PM21]. The platform which has arguably advanced furthest in this area so far — and which forms the basis for the work described in this thesis — is trapped ions. They offer the advantage that preparation of identical qubits is not limited by manufacturing defects because each atom of a given species is intrinsically the same. Furthermore, ions in a vacuum chamber can be isolated from their environment to an excellent degree, enabling long coherence times and reducing the amount of noise that may negatively affect gate fidelities. One drawback of this platform in the past has been limited scalability. However, with the development of surface traps and proposals to transfer quantum information within and between traps, such as the "quantum CCD" architecture [KMW02] or photonically linked modules [MRR+14], this issue is expected to become less severe in the future.

Single-qubit gates can be implemented with relative ease through the coherent interaction of electromagnetic multipole moments of individual ions with external fields. The challenge lies in realising fast, high-fidelity multi-qubit gates between different ions. The most direct approach would perhaps be to exploit the force that the spins of the valence electrons of neighbouring atoms exert on each other. While this force has been observed experimentally [KAN+14], it is so small that it cannot feasibly be used for entangling gates in ion traps. As Cirac and Zoller suggested in a highly impactful paper [CZ95], different qubits in a string of ions may instead be coupled indirectly through the collective motion of their centres of mass. They noted that the force arising from a spatially varying electromagnetic field excites the motion conditional on the internal states of the ions, which can be used to change the spin state of one qubit dependent on that of another and thus realise a two-qubit gate. A number of variations of this scheme have since been developed [MS99], but they are all based on the idea that a motional mode can act as a quantum bus that generates entanglement through a spin-dependent force. The achievable gate speed

depends on the strength of the coupling between electronic states and centre-of-mass motion, which is determined by the change in strength of the driving field over the extent of the motional wavepackets. The coupling is therefore higher the larger the gradient of the driving field and the weaker the confinement of the ions in the trapping potential.

Historically, the first demonstrations of quantum logic gates in ion traps made use of lasers to drive transitions between qubit states. Single-qubit gates for optical qubits may be implemented with a single laser, whereas Zeeman and hyperfine qubits require at least two laser beams, which couple the qubit states via a two-photon Raman process. Gate errors below 10^{-4} have been achieved for laser-driven single-qubit operations in optical and hyperfine qubits [BXN+17], with typical pulse durations of a few microseconds.

Methods to address individual ions have also been explored with the laser-based approach. Perhaps the most obvious solution is provided by tightly focussing the laser beams, resulting in beam waists that are smaller than the spacing between ions [MBM+16]. Alternatively, addressing may be achieved by separating the ions in frequency space, either via spatially varying ac Stark shifts [SD02], a static magnetic field gradient [WLG+09] or micromotion sidebands [ANK+15].

In addition to single-qubit operations, lasers have been used with great success to implement multi-ion entangling gates. The first demonstration of a two-qubit logic gate [MMK+95] came shortly after the initial proposal of the Cirac-Zoller scheme, but only operated on a single trapped ion, the two qubits being formed by a pair of internal and a pair of harmonic oscillator states of the ion. This was later followed by generation of entanglement between two ions [TWK+98] and an implementation of the Cirac-Zoller CNOT gate with two ions [SHR+03]. Since then, a variety of gate mechanisms have been demonstrated experimentally and fidelities have increased steadily. The lowest two-qubit gate errors that have been achieved with the laser-based approach to date were recently reported as $1.1(7) \times 10^{-3}$ (corrected for errors resulting from state preparation and single-qubit operations) with a gate duration of 100 µs [BHL+16], $8(4) \times 10^{-4}$ (corrected for errors resulting from state preparation) with a duration of 30 µs [GTL+16] and $6(3) \times 10^{-4}$ with a duration of

35 µs [CTS+21]. Fidelities are thus approaching the 10^{-4} threshold for fault-tolerant quantum computing.

Despite the impressive achievements that have been obtained by driving quantum logic operations with lasers, there are some drawbacks to this approach. Qubit gates enabled by Raman beams suffer from a fundamental error caused by spontaneous photon scattering from the auxiliary level [OIB+07]. Increasing the detuning of the beams from the auxiliary level reduces this error, but in order to maintain gate speed the optical power in the beams has to be raised correspondingly, making the gate operation more resource-intensive. For optical qubits, a fundamental limit is set by the finite decay rate from the metastable excited state, although the impact of this error mechanism diminishes as gates become faster. Apart from these fundamental constraints, there are problems connected with the relatively high technical complexity of laser systems. Fluctuations in laser intensity or phase contribute to gate infidelity and it is not straightforward to keep these parameters stable to the degree where they would result in negligible error.

1.2 Laser-free quantum logic with trapped ions

For these reasons, an alternative approach has been explored for Zeeman and hyperfine qubits in the last decade. Rather than relying on indirect coupling via Raman lasers, the qubit transition is driven directly via the magnetic-dipole interaction by applying an oscillating magnetic field. By tailoring the driving magnetic field appropriately, both single- and two-qubit gates may be implemented. Following [SBS+19], I will call this the "laser-free" scheme, in order to include both kinds of qubits mentioned. It offers several advantages compared to laser-driven qubit gates. Firstly, errors caused by spontaneous scattering are absent since no auxiliary internal level is involved. Secondly, amplitude and phase can be controlled more precisely and kept more stable at low frequencies than in the optical domain. Thirdly — and this comes in connection with the previous point — microwave devices are a more mature technology than laser systems, with key components readily available off the shelf and at relatively low cost. Furthermore, wires generating the required magnetic

fields can be integrated into trap structures directly as electrodes.

Single-qubit operations may be implemented in a straightforward manner without lasers as they only require a magnetic field resonant with the transition frequency of the qubit to be applied. Free-space radiation is suitable for this purpose, which may be generated by sources outside the vacuum chamber [WRW+16]. More commonly, the field is produced by electrodes built directly into the trap [OWC+11]. The speed of single-qubit gates is determined by the amplitude of the oscillating magnetic field at the position of the ion, which can easily be made large enough in modern surface traps to enable sub-microsecond gate durations. The quality of laser-free single-qubit gates is highlighted by the fact that an average gate error as low as $1.0(3) \times 10^{-6}$ has been demonstrated [HAB+14], the lowest achieved to date in any quantum computing platform.

Addressing of individual qubits is also possible without lasers. While the driving field cannot be focussed selectively onto one ion at a time because of its long wavelength, other techniques such as a spatially varying ac Zeeman shift [WOC+13a], static field gradient [PSV+14], suppression of microwave fields in different zones [CLS17] or a micromotion sideband [WOC+13a] may be used.

The main challenge for the laser-free approach lies in achieving fast, high-fidelity two-qubit gates, which requires the driving magnetic field to exhibit a strong gradient. Unlike lasers, free-space radiation in the rf and microwave domain does not satisfy this criterion. However, with the advent of surface traps it has become possible to make use of the near-field regime of current-carrying conductors integrated into the trap chip, which allows generating magnetic fields with much larger gradients. In the past decade, different methods have been developed to exploit these gradients and achieve strong spin-motion coupling without lasers.

1.2.1 Static magnetic field gradient

Coupling between internal and external degrees of freedom may be achieved by applying a static inhomogeneous magnetic field to the ions, so that the energies of the qubit states depend on the position of the particle [MW01; JBT+09; WRW+16]. This gives rise to a state-dependent force. If the internal state undergoes a transition,

the ion is displaced by a small amount, which corresponds to the desired interaction between electronic state and centre-of-mass motion. Since this section concerns Zeeman or hyperfine qubits, the internal transitions can be driven by long-wavelength radiation. One then finds that even though the magnetic field of the radiation itself exhibits only negligible variation over the extent of the motional wavepacket, the strength of the interaction between spin and motion is characterised by an effective coupling parameter that depends on the strength of the static field gradient and can be made much larger than what would result from the radiation field alone. This approach offers the advantage that the magnetic field providing the strong gradient needs to be generated only at zero frequency, which can be achieved via permanent magnets [KPS12; WRW+16] or dc currents [WLG+09]. The fields oscillating near the qubit frequency (rf for Zeeman qubits and mw for hyperfine qubits) are allowed to be relatively weak. Furthermore, single-qubit addressing is straightforward if the gradient is chosen to be aligned with the trap axis. One large drawback of this method is that it requires use of a qubit which is first-order sensitive to changes in magnetic field. Such qubits are susceptible to magnetic field noise, which negatively affects coherence time. Some protection can be gained through microwave dressing techniques [TBJ+11], but this increases technical complexity. Another disadvantage is the fact that the gate speed scales unfavourably with larger motional frequencies.

1.2.2 Near-motional-frequency magnetic field gradient

Another method to implement two-qubit gates without lasers has recently been proposed [SSB19; SBS+19] and implemented experimentally [SBS+19; SBK+21]. It represents a generalisation of the static-gradient scheme in that it also employs separate low- and high-frequency magnetic fields, but makes use of a gradient that oscillates with a frequency near that of the motional mode which the gate is driven on. In ref. [SBK+21], fidelities of $1^{+0}_{-0.0017}$ and $0.9977^{+0.0010}_{-0.0013}$ have been reported for the generation of symmetric and anti-symmetric Bell states, respectively. Together with the results of ref. [HSA+16], these values represent the current state of the art for laser-free two-qubit gates. This method shares many of the advantages of the static-gradient case, but through use of an oscillating gradient it scales more

favorably when the motional frequency is increased.

1.2.3 Near-qubit-frequency magnetic field gradient

It is also possible to induce an interaction between spin and motional states by using magnetic field gradients that oscillate with frequencies near the internal transition frequency. More specifically, the gradient needs to contain two tones that are detuned symmetrically from the motional sidebands of the qubit transition. This approach, which was proposed [OLA+08] and first demonstrated [OWC+11] several years ago, may be used with qubits that are to first order insensitive to changes in magnetic field. Its main drawback lies in the fact that the strong gradient fields need to be produced at higher frequencies than in the other two approaches. This is particularly challenging at microwave frequencies since the reduced skin depth leads to an increase in power dissipated for given current, limiting the maximum current that can safely be applied to the trap chip. Additionally, return currents induced in neighbouring electrodes are larger at higher frequencies. These currents generate opposing magnetic fields, thus resulting in smaller gradient for given current flowing through the microwave electrodes. Both effects reduce the gradient that can be produced for given input power to the trap.

This method has been used previously in our group to achieve a two-qubit gate with a low error of $3(1) \times 10^{-3}$ [HSA+16]. It is also chosen for two-qubit gates in the trap described in this work. In experiments based on this scheme, it has been observed that the driving field itself contributes two important sources of error: fluctuating ac Zeeman shifts and off-resonant excitation of the carrier transition. One may therefore conclude that in order to obtain high gate fidelity and speed for fixed power consumption, the field gradient at the positions of the ions should be as large as possible, while the field amplitude should be minimised. Early experiments pursued this objective by using several separate microwave electrodes, such that the amplitude and phase of the current flowing through each could be controlled independently [OWC+11]. However, the careful calibration required for this purpose adds complexity and is furthermore prone to drifts in experimental parameters such as microwave powers. More recently, attempts have therefore been made to use

only a single microwave electrode, but tailor its shape to null the field amplitude in a passive fashion and achieve the desired field characteristics. Depending on the geometry of the electrode, it is possible to suppress field components along more than one direction, as has been demonstrated successfully with a design based on a meander shape [HZB+19; ZHM+19].

1.3 Contents of this thesis

I describe progress made towards high-fidelity quantum gates with a surface ion trap that represents the next generation of devices for microwave-driven quantum logic in our group. Compared to the previous generation [Har13], several improvements have been made that should allow us to achieve higher gate fidelities and speeds. Gates are carried out on a pair of hyperfine states in the ground level of $^{43}Ca^{+}$ that has not been utilised for quantum logic previously. The states form a clock qubit in a static magnetic field of approximately 28.8 mT and transitions between them are driven by the π-component of a magnetic field oscillating at a frequency of 3.123 GHz. We conduct experiments in a newly designed surface trap that features a single U-shaped microwave conductor to achieve passive nulling of the amplitude of the π-component. This should reduce the impact of detrimental carrier transitions while generating a strong field gradient. In comparison with the previous generation, the ion is located closer to the surface of the trap chip in order for it to experience a stronger gradient. Furthermore, the trap is designed for cryogenic operation so as to mitigate the impact of anomalous heating, which is expected to increase with reduced ion height. Since the resistivity of electrodes decreases with lower temperatures, cooling of the trap should have the additional advantage that larger currents and thus stronger gradients may be generated for given power dissipated.

The structure of this thesis is as follows. In chapter 2, I present the hyperfine qubit that is the focus of quantum computing experiments in our trap and elaborate on the methods we employ for state preparation and measurement. The apparatus in which experiments were carried out is described in chapter 3. This is followed in chapter 4 by an account of the motion of a single ion in our surface trap and of

the parameters used for trapping. Chapter 5 contains a thorough description of the theory underlying the interaction of a single ion with the microwave magnetic field and Raman lasers. Results for laser cooling of $^{43}Ca^{+}$ ions at a static magnetic field of 28.8 mT are presented in chapter 6, while chapter 7 provides the results of trap characterisation and calibration experiments. In chapter 8, I describe the theory for spin-dependent forces generated by near-qubit-frequency magnetic field gradients for one and two ions, including the Mølmer-Sørensen two-qubit gate mechanism. I also present an experimental demonstration of a spin-dependent force on a single ion in our trap and the results of an initial attempt at a two-qubit gate there, before I draw conclusions in chapter 9.

Chapter 2

$^{43}Ca^{+}$ as a trapped-ion qubit

Calcium has a long history of use in experiments with trapped ions, for a number of reasons. As an alkaline earth element, neutral calcium possesses two valence electrons so that a particularly simple atomic structure results upon ionisation to singly-charged ions. Additionally, the wavelengths of optical transitions connecting the relevant energy levels fall into a range from 378 nm to 866 nm, which is very convenient from a practical point of view as lasers and optical components are readily available for these wavelengths. Another advantage lies in the existence of a stable isotope with non-zero nuclear spin, leading to the possibility of encoding qubits in states from different hyperfine sublevels. The utility of calcium as a trapped-ion species is highlighted by the fact that gate operations for optical qubits, Zeeman qubits and hyperfine qubits have all been demonstrated.

Our research group has previously used both $^{40}Ca^{+}$ and $^{43}Ca^{+}$ in experiments. The nuclear spin of the former isotope is zero, which means that fine-structure levels are not split further by a hyperfine interaction. The resulting atomic structure makes laser cooling and state preparation especially simple, but the absence of hyperfine splitting means that optical or Zeeman qubits have to be used. For the experiments described in this thesis, we instead work with $^{43}Ca^{+}$, which is characterised by non-zero nuclear spin. While the resulting hyperfine interaction makes its level structure more complicated, particularly in the presence of strong external magnetic fields, it offers the possibility to use hyperfine states to form a qubit. These hyperfine qubits provide the advantage that they can exhibit coherence times of the order of minutes

[WUZ+17; WLQ+21] and quantum gates can be driven directly with magnetic fields oscillating at microwave frequencies. Additionally, they allow schemes for qubit readout with significantly higher fidelities than those that can be achieved with Zeeman qubits. Singly-charged $^{43}Ca^{+}$ ions have been successfully trapped and cooled before in both a weak magnetic field of a few Gauss[1] [Szw09] and an intermediate field of 146 G [Har13]. In the experiments described in this thesis, we have extended the range further and demonstrated that hyperfine states of this ion can be used as a qubit at a field of 288 G.

In this chapter, I present the atomic properties of $^{43}Ca^{+}$ and give a description of the methods we employ to use this ion species for quantum computation. The focus here is on auxiliary processes, which includes everything before and after the actual logic gates, such as laser cooling, state preparation and readout. Results for coherent operations and two-qubit gates are reported in chapters 7 and 8.

2.1 Atomic structure of $^{43}Ca^{+}$

I give a brief description of the atomic structure of $^{43}Ca^{+}$ in this section. More details, including compilations of atomic properties such as transition frequencies, g-factors and hyperfine constants may be found in appendix A.

The isotope ^{43}Ca has nuclear spin of $I = 7/2$. This means that, in addition to the electrostatic and fine-structure contributions, the Hamiltonian for an ion contains a term arising from the hyperfine interaction between the valence electron and the nucleus. In the presence of a static external magnetic field, the Hamiltonian further includes a contribution from the Zeeman interaction of the atomic magnetic dipole moment with the applied magnetic field. At low magnetic fields, the Zeeman interaction with the external field can be considered a small perturbation with respect to the hyperfine interaction internal to the atom. As the strength of the magnetic field increases, the intermediate-field regime is reached in which neither the hyperfine nor the Zeeman interaction can be treated as a small perturbation compared to the other. However, both are still weak in comparison to the fine-structure splitting.

[1] I make frequent use of this non-SI unit (1 G = 0.1 mT) throughout this work.

The energy eigenvalues and eigenstates may therefore be obtained to first order by applying degenerate perturbation theory within each subspace corresponding to a fine-structure level of fixed angular momentum J, taking as the perturbation the sum of hyperfine and Zeeman terms in the form $H_1 = H_{\mathrm{hfs}} + H_{\mathrm{Zeeman}}$, with

$$H_{\mathrm{hfs}} = A_{\mathrm{hfs}}\,\mathbf{I}\cdot\mathbf{J} + B_{\mathrm{hfs}}\,\frac{6(\mathbf{I}\cdot\mathbf{J})^2 + 3(\mathbf{I}\cdot\mathbf{J}) - I(I+1)J(J+1)}{4I(2I-1)J(2J-1),} \tag{2.1}$$

$$H_{\mathrm{Zeeman}} = (g_J\mu_{\mathrm{B}}\mathbf{J} - g_I\mu_{\mathrm{N}}\mathbf{I})\cdot\mathbf{B}\ . \tag{2.2}$$

The g-factors for electronic and nuclear magnetic dipole moments are denoted by g_J and g_I, respectively, while μ_{B} and μ_{N} are the Bohr and nuclear magnetons. The variable $\mathbf{B}$ represents the external magnetic field, which I take to define the atomic quantisation axis through $\mathbf{B} = B\,\hat{\mathbf{z}}$. The first term of H_{hfs} describes the interaction of the nuclear magnetic dipole moment with the magnetic field produced by the electrons at the position of the nucleus, while the second term, which is only present for states with $J \geq 1$, describes the interaction of the nuclear electric quadrupole moment with the gradient of the electric field generated by the electrons. The constants A_{hfs} and B_{hfs} depend on the fine-structure level considered.

The component F_z of the total angular momentum operator $\mathbf{F} = \mathbf{I}+\mathbf{J}$ commutes with H_1, which means that each energy eigenstate can be assigned a definite value of the corresponding magnetic quantum number m_F and subspaces of fixed m_F are not mixed by the perturbation, regardless of the strength of the magnetic field. I will hereafter just use $m = m_F$ to denote the magnetic quantum number specifying the projection of the total angular momentum operator on the z-axis. The operator $\mathbf{F}^2$ does not commute with H_{Zeeman}, which means that eigenstates of the total atomic Hamiltonian are superpositions of the hyperfine eigenstates $|F, m\rangle$ and no unique quantum number F can in general be assigned to the former. The only exception are the states with extremal values of m in each level, as these form a one-dimensional eigenspace of F_z and H_1. It follows that $|F_{\mathrm{max}}, \pm F_{\mathrm{max}}\rangle$ in each level are strict energy eigenstates regardless of the strength of the external magnetic field.

In order to solve for the eigenvalues and eigenstates of H_1, one introduces a set of basis states within each fine-structure level. Either the uncoupled ba-

sis $\{|\gamma LSIm_I Jm_J\rangle\}$ (eigenstates of H_{Zeeman}) or the coupled basis $\{|\gamma LSIJFm\rangle\}$ (eigenstates of H_{hfs}), where γ represents any additional quantum numbers required to fully specify the state, can be used for this purpose. I choose the former since H_1 in eq. (2.1) is already directly expressed in terms of the operators $\mathbf{I}$ and $\mathbf{J}$.

For general J, the perturbation Hamiltonian H_1 may be diagonalised numerically to obtain the atomic energies and eigenstates. When the external magnetic field vanishes, the energy eigenstates are of course given by the hyperfine states $|F, m\rangle$. As the strength B of the external field increases, the eigenstates become superpositions of different $|F, m\rangle$ states. As follows from the discussion above, only $|F, m\rangle$ states with the same m can be mixed. The degree of mixing between hyperfine eigenstates within each fine-structure level depends on the magnitude of the hyperfine splitting in that level relative to the strength of the Zeeman interaction. For the $4\,\mathrm{S}_{1/2}$ and $4\,\mathrm{P}_{1/2}$ levels, the hyperfine constants A_{hfs} are large enough that the energy eigenstates at a field of 288 G are still separated into distinct groups derived from the two hyperfine sublevels. In this case, it is convenient to specify energy eigenstates in the intermediate-field regime by labelling each with F of that hyperfine state that the energy eigenstate would reduce to if the external magnetic field were adiabatically decreased to zero. I will follow this convention in the present thesis and will denote a specific energy eigenstate in the $4\,\mathrm{S}_{1/2}$ and $4\,\mathrm{P}_{1/2}$ levels as $4\,L_J^{F,m}$, suppressing the superscript corresponding to the total spin quantum number $S = 1/2$ as this is the same for all states. When the fine-structure level is clear from context, I will also use the notation $|F, m\rangle$. In the $3\,\mathrm{D}$ and $4\,\mathrm{P}_{3/2}$ levels, hyperfine eigenstates are mixed so strongly that F is not a useful designation anymore. Instead, I label states in the $3\,\mathrm{D}_{3/2}$ and $4\,\mathrm{P}_{3/2}$ levels by means of the magnetic quantum number m and, if relevant, an index $k = 1, 2, \ldots$ in order of increasing energy for states with the same m. As concerns the $3\,\mathrm{D}_{5/2}$ level, the hyperfine splitting is small enough that at 288 G the high-field regime holds and the uncoupled states $|m_I, m_J\rangle$ are approximate energy eigenstates. The relevance of this particular field strength will become obvious momentarily.

For fine-structure levels characterised by $J = 1/2$, the eigenvalues and eigenvectors of H_1 can also be determined analytically. In this case, there are at most

two states with the same value of m and each energy eigenstate can therefore be expanded as

$$|m,\chi\rangle = \alpha_\chi^{(m)}\,|m_I = m+1/2, m_J = -1/2\rangle + \beta_\chi^{(m)}\,|m_I = m-1/2, m_J = +1/2\rangle\ , \tag{2.3}$$

where χ distinguishes between the two states for given m. I have tabulated the expansion coefficients α and β for the energy eigenstates in the $4\,\mathrm{S}_{1/2}$ ground level at an external magnetic field of approximately 288 G in appendix A. The eigenvalues of H_1 within each subspace corresponding to a certain fine-structure level with $J = 1/2$ are given by the Breit-Rabi formula

$$E_1 = -\frac{\Delta E_{\mathrm{hfs}}}{2(2I+1)} - m g_I \mu_{\mathrm{N}} B \pm \frac{\Delta E_{\mathrm{hfs}}}{2}\sqrt{1 + \frac{4m}{2I+1}x + x^2}\ , \tag{2.4}$$

where $\Delta E_{\mathrm{hfs}} = A_{\mathrm{hfs}}(I+1/2)$ and $x = (g_J\mu_{\mathrm{B}} + g_I\mu_{\mathrm{N}})\,B/\Delta E_{\mathrm{hfs}}$. It should be noted that ΔE_{hfs} for the ground level of $^{43}\mathrm{Ca}^+$ is negative. The energy corrections E_1 are measured relative to the centre-of-mass (com) energy of the respective fine-structure level, which is the energy that each degenerate state in the level would have in the absence of the perturbing Hamiltonian H_1. A schematic diagram of the atomic structure of a $^{43}\mathrm{Ca}^+$ ion placed in a static magnetic field of 287.7828 G is shown in figure 2.1.

Any pair of states connected by a suitable transition could in theory be used as a qubit. However, a natural choice is a pair of states in the $4\,\mathrm{S}_{1/2}$ ground level since their negligible rate of spontaneous decay means that gate errors caused by this mechanism can thus be completely eliminated. The selection of qubit is further influenced by the sensitivity of the transition frequency of the qubit to fluctuations in the external magnetic field. This is where one of the big strengths of hyperfine qubits lies. In the intermediate-field regime, the energies of states in the ground level do not depend linearly on the strength B of the applied magnetic field, as is evident from eq. (2.4). This means that the transition frequency $f_{ij} = (E_{1,i} - E_{1,j})/h$ for a transition between two states in the ground level is also non-linear with respect to B, which gives rise to the possibility that for certain transitions $df_{ij}/dB = 0$ at some

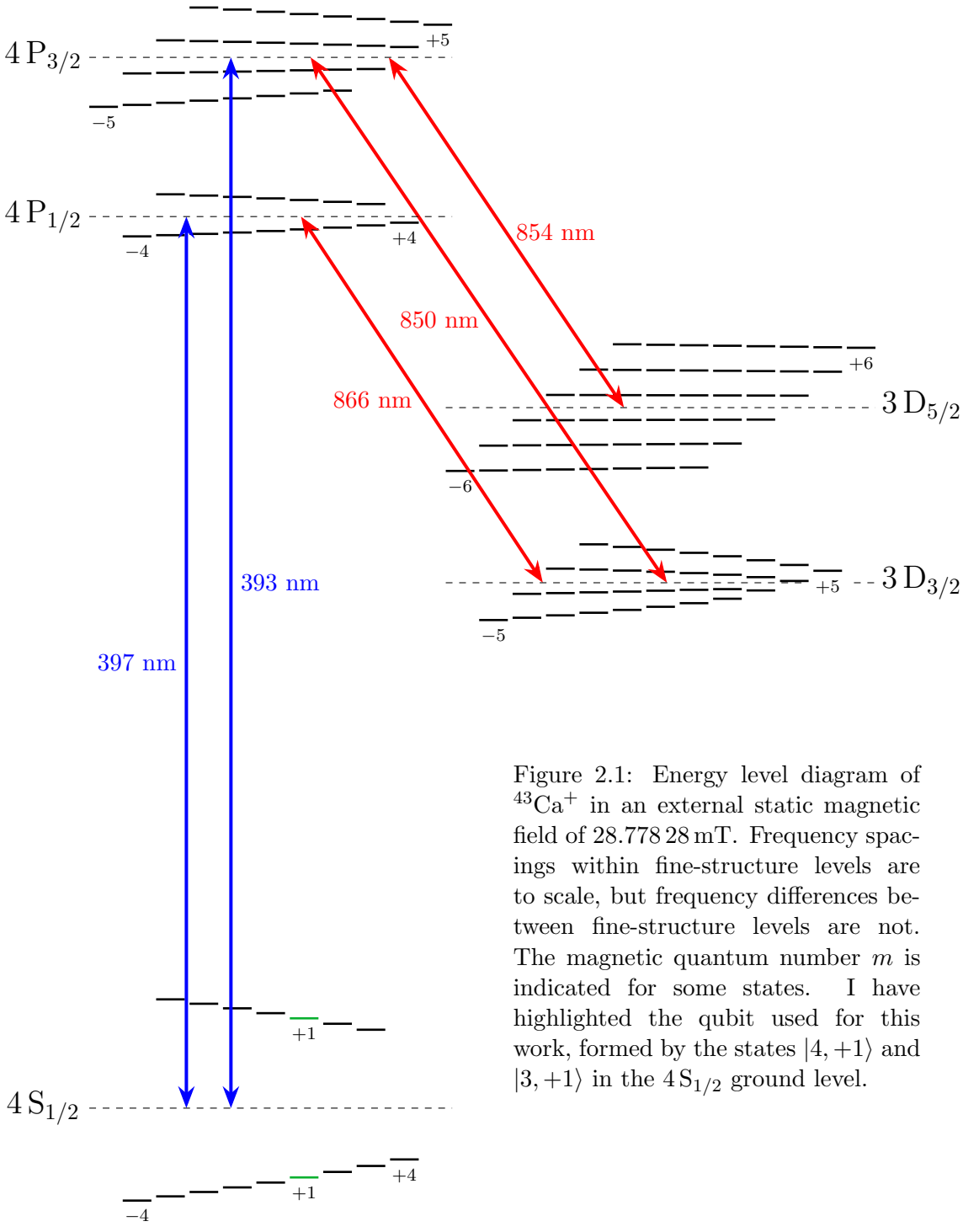


Figure 2.1: Energy level diagram of $^{43}Ca^{+}$ in an external static magnetic field of 28.778 28 mT. Frequency spacings within fine-structure levels are to scale, but frequency differences between fine-structure levels are not. The magnetic quantum number m is indicated for some states. I have highlighted the qubit used for this work, formed by the states $|4, +1\rangle$ and $|3, +1\rangle$ in the $4\,S_{1/2}$ ground level.

critical field strength B_0. The transition frequency is then to first order independent of the external magnetic field. The corresponding qubits, known as *clock qubits* for their use in atomic frequency standards, are therefore much less sensitive to fluctuations of the field and, as a result, may display remarkable coherence times [Har13; WLQ+21].

There are several possible clock transitions in $^{43}Ca^{+}$, each of them requiring a different critical field B_0. The $|4,0\rangle \leftrightarrow |3,0\rangle$ transition, for example, is field-insensitive at 0 T. However, states in the two hyperfine sublevels are degenerate in energy at this field, which causes a lack of frequency discrimination when trying to selectively drive transitions between certain states. Furthermore, it leads to the formation of dark states during Doppler cooling [BB02]. For these reasons, a slight bias field has to be applied to lift the degeneracy. In doing so, however, the transition ceases to be an ideal clock transition and some of the potential benefits are lost. Instead, it is advantageous to use a pair of states that is field-insensitive at non-zero B_0. The next clock transition is found at a field of approximately 146 G, involving the states $|4,0\rangle$ and $|3,+1\rangle$. This qubit has been used previously in our group and high-fidelity single- and two-qubit gates [Har13; Sep16] have been demonstrated.

Going up in field strength, another clock qubit is provided by the states $|4,+1\rangle$ and $|3,+1\rangle$ at a field of 287.7828 G. This particular qubit is the one we use as the unit for quantum computation in the experiments described in this work. Inducing magnetic-dipole transitions between its states requires a dynamic magnetic field with π-component (see chapter 5). Compared to the $|4,0\rangle \leftrightarrow |3,+1\rangle$ qubit used previously, the present choice has a few advantages:

- Given the geometry of the microwave electrode in our trap, the dynamic magnetic field produced at the trap centre is predominantly orthogonal to the static field of the main coils that defines the quantisation axis. For two-qubit gates based on the Mølmer-Sørensen scheme, the amplitude of the component of the magnetic field which couples the qubit states should be suppressed, but the spatial gradient of this component should be large. This can be achieved in our trap by choosing a π-qubit.

- The stronger the magnetic field, the larger the separation in frequency between the qubit transition and unwanted spectator transitions to other internal states. Making use of a higher magnetic field should therefore reduce the error from off-resonantly driving the latter.

- The magnetic-dipole transition matrix element for the $|4, +1\rangle \leftrightarrow |3, +1\rangle$ transition is larger by a factor of approximately $\sqrt{2}$. This results in a higher Rabi frequency for given magnetic field for transitions within the clock qubit. Additionally, the Rabi frequency for spectator transitions – which are σ-polarised – is correspondingly lower, again reducing the error from off-resonant excitation.

In addition to the clock qubit, the other qubit in the ground level worth noting is the field-sensitive "stretch qubit" formed by the states $|4, +4\rangle$ and $|3, +3\rangle$. The known variation of its transition frequency as a function of external magnetic field allows us to calibrate the magnitude of the static field to the critical value B_0 required by the clock qubit.

2.2 Radiative transitions

We drive electric-dipole transitions at optical frequencies between states from different fine-structure levels by means of laser beams with wavelengths of 393 nm and 397 nm ("blue lasers") and 850 nm, 854 nm and 866 nm ("red lasers"). These are used for laser cooling, qubit initialisation and readout. We find it convenient to parameterise the intensities used for these lasers as multiples of the respective saturation intensity I_0. The latter is defined as that intensity at which the rates of spontaneous and stimulated emission for the transition in question are equal and is given by

$$I_0 = \frac{\hbar\omega_0^3\Gamma}{6\pi c^2} \,, \tag{2.5}$$

where ω_0 is the (angular) transition frequency and Γ the total decay rate from the fine-structure level involved.

States within the ground level, however, are all characterised by the same total orbital angular momentum quantum number $L = 0$. It follows that both electric-

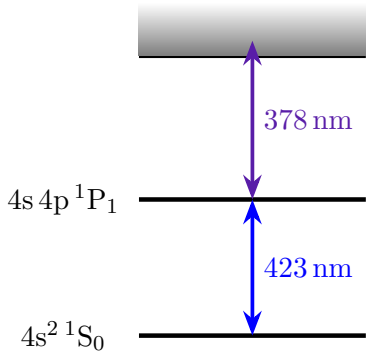


Figure 2.2: Photoionisation scheme. Isotope-selective excitation of a valence electron to $4s\,4p\,{}^1P_1$ is followed by ionisation through a laser with energy above the first ionisation potential.

dipole and electric-quadrupole transitions between them are forbidden since $L = 0 \leftrightarrow 0$ is not allowed for either. Instead, transitions are driven by the magnetic-dipole interaction with a dynamic magnetic field generated by a microwave electrode integrated in our trap chip.

2.3 Photoionisation

We use a two-step photoionisation process to create singly charged calcium ions [LRH+04]. The first step consists in promoting one of the two valence electrons of a neutral calcium atom to the 4p configuration through resonant excitation on the $4s^2\,{}^1S_0 \leftrightarrow 4s\,4p\,{}^1P_1$ transition with a laser of wavelength 423 nm. The exact frequency of this transition is isotope-dependent. In particular, in ^{43}Ca (measured from the centre of mass of the hyperfine-split ground level) it is 612 MHz lower than in ^{40}Ca [Kra20], which is a large shift compared to the natural linewidth of 35 MHz. This allows selection of a specific isotope during the loading process. The second step is ionisation proper by ejecting the excited electron to the continuum of unbound states. This can be achieved through any laser with a frequency above the ionisation threshold for the $4s4p\,{}^1P_1$ level; we use a wavelength of 378 nm. The ionisation method is summarised in fig 2.2.

2.4 Laser cooling

As is evident from fig. 2.1, $^{43}Ca^{+}$ ions contain a multitude of states, leading to a large number of transitions that can be driven between them, many of which have resonance frequencies that are separated by hundreds of megahertz. Devising schemes to efficiently cool such a system using lasers is not straightforward. I do not go into details in this section, but instead present a thorough account of the theoretical considerations underlying our approach and the experimental implementation in chapter 6.

As far as cooling is concerned, both the $4\,S_{1/2} \leftrightarrow 4\,P_{1/2} \leftrightarrow 3\,D_{3/2}$ or the $4\,S_{1/2} \leftrightarrow 4\,P_{3/2} \leftrightarrow 3\,D_{3/2,5/2}$ system could be used. However, since fluorescence from the cooling transition is also to be used for state-dependent fluorescence detection via the $3\,D_{5/2}$ shelf level as part of our readout process (see section 2.6), the cooling cycle must not involve this level. This only leaves $4\,S_{1/2} \leftrightarrow 4\,P_{1/2}$ as a viable option. Cooling thus proceeds using a 397 nm laser containing two frequency components to address states in both hyperfine sublevels of the ground level, in combination with an 866 nm laser to repump population from the $3\,D_{3/2}$ level. Through suitable choice of laser frequencies and polarisations, this allows us to reach the Lamb-Dicke regime for ions in our trap, such that the extent of the motional wavepacket is much smaller than the wavelength of the 397 nm radiation. We follow up the initial stage of Doppler cooling just described with resolved-sideband cooling on a Raman transition using two additional 397 nm beams. For the harmonic oscillator corresponding to the in-plane radial mode of motion, as introduced in chapter 4, we achieve an average occupation number of $\bar{n} \approx 0.1$, close to the motional ground state and suitable for two-qubit entangling gates using this mode.

2.5 Qubit initialisation

Before the start of quantum computation operations, the qubit needs to be prepared in a known state. In our case, direct optical pumping into one of the clock qubit states is not possible since they are located in the centre of the ground level and do not form a dark state that could be used to coherently trap population there.

Instead, we initialise the system by a combination of optical pumping to the $|4, +4\rangle$ state and microwave transfer pulses.

2.5.1 Optical pumping

After laser cooling has finished, we apply a σ^+-polarised 397 nm beam containing two frequency components to address the $F = 3$ and $F = 4$ levels, alongside the standard 866 nm repumper also used for Doppler cooling. This predominantly transfers population into the $|4, +4\rangle$ state of the ground level. However, polarisation impurities in the 397 σ^+ laser may cause some population to be left in states with $m < 4$ in both hyperfine sublevels. We try to recover this population in the next step: we apply another pulse of 397 σ^+ and 866 light, but this time only with the 397 frequency component that addresses the $F = 3$ level. This transfers most population to states with higher m in the $F = 4$ level. We then apply microwaves to drive Rabi π-pulses on the transitions $|4, +2\rangle \leftrightarrow |3, +2\rangle$ and $|4, +3\rangle \leftrightarrow |3, +3\rangle$, followed by another optical pumping pulse with a single-frequency 397 σ^+ beam addressing the $F = 3$ sublevel. The combined effect of this sequence is to move any population that is not in the desired $|4, +4\rangle$ state into the $F = 3$ level, from where it is selectively pumped towards the target state. The choice of microwave transitions is based on the fact that most population typically resides in states with $m \geq 2$. The sequence can be repeated several times to further reduce the error in state preparation. The scheme is illustrated in fig. 2.3.

2.5.2 Microwave transfer pulses for state preparation

After completion of the microwave-enhanced optical pumping scheme, the ion occupies the state $|4, +4\rangle$ with high probability. Experiments using the stretch qubit, which we employ for calibration purposes as described in later chapters, start from this point. For work with the clock qubit, however, microwave transfer pulses are required, which are shown in fig. 2.4. We use resonant Rabi π-pulses in the sequence $\{A(\pi), B(\pi), C(\pi)\}$ to initialise the qubit in the energy eigenstate $|3, +1\rangle$.

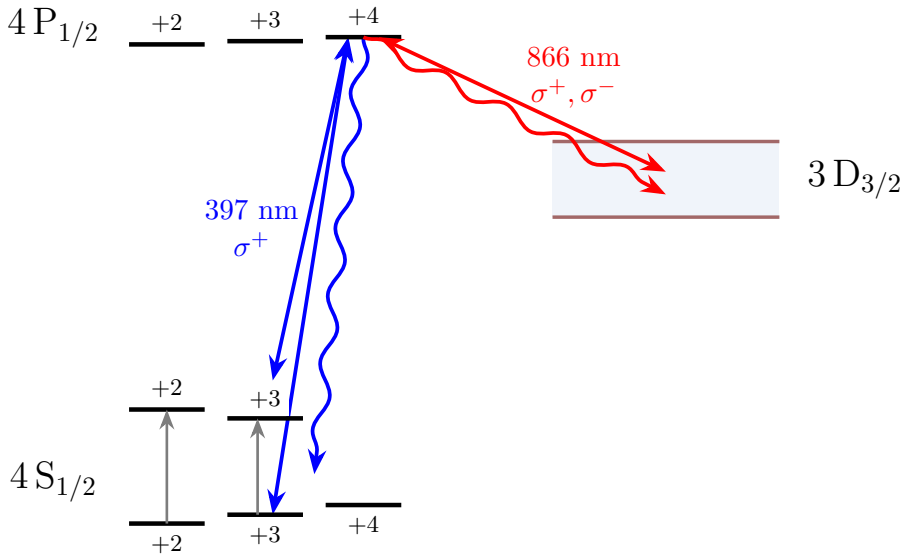


Figure 2.3: Optical pumping scheme used as part of qubit initialisation. A σ^+-polarised 397 nm beam containing two frequency components pumps into state $|4, +4\rangle$ of the ground level. Its intensity is chosen large enough that population in states with low m can be excited. Any population left in states with $m < 4$ due to polarisation impurities is subsequently recovered by applying microwave π-pulses and selectively addressing the $F = 3$ sublevel with a single-frequency 397 nm beam.

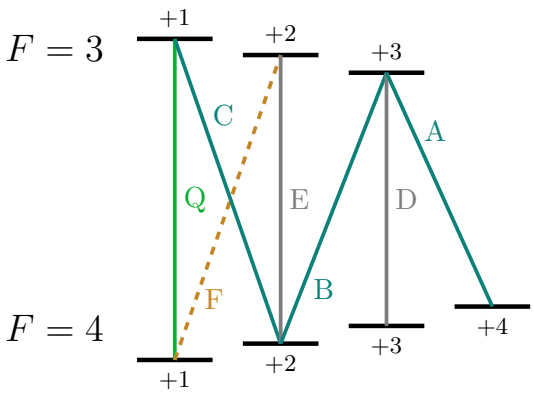


Figure 2.4: Microwave transitions in ground level relevant for qubit initialisation and readout.

2.6 Readout

A few methods for readout of trapped-ion qubits have been demonstrated, but the one most widely used — and the one we employ in our experiments — is state-dependent fluorescence detection. The underlying idea is simple: if a strong electric-dipole transition exclusively connects one of the qubit states to an auxiliary level, photons will only be scattered on that transition if the system is found in the corresponding qubit state. Observation of fluorescence while illuminating the ion with a laser driving the relevant transition thus leads to the conclusion that the wave function has collapsed to the state that is coupled to the auxiliary level, the *bright* state, whereas the absence of fluorescence indicates that the ion occupies the *dark* state, which is not connected to the auxiliary level. The method is inherently of the quantum-demolition kind as it projects the system onto one of the states constituting the qubit. This means that the cycle "state preparation - quantum circuit - readout" has to be repeated a large number of times while recording the occurrences of bright and dark events in order to infer the population in each qubit state and thus gain information about the underlying state vector.

Ideally, a closed cycling transition involving the bright state is desired so that the only possible decay route from the auxiliary level is back to the bright state, leading to a high scattering rate for fast readout with unambiguous state detection. However, this cannot always be achieved because couplings between states are dictated by atomic structure. For many choices of trapped-ion qubits, there is a possibility that the dark state is inadvertently excited to the auxiliary level or decay from the latter to a state other than the bright state may occur, both of which lead to readout errors. This would be the case if one attempted direct readout of the $|4,+1\rangle \leftrightarrow |3,+1\rangle$ hyperfine qubit on the 397 nm Doppler transition. While the hyperfine splitting is large enough that one of the qubit states can be addressed with a single 397 nm Doppler beam, spontaneous decay from the $4\,\mathrm{P}_{1/2}$ level can proceed to a variety of states in the ground level, including the intended dark state.

It turns out, however, that through slight modifications there is a way to achieve high-fidelity readout in $^{43}\mathrm{Ca}^{+}$. The scheme utilises the low-lying D levels and is an

example of the electron-shelving technique originally developed by Dehmelt [NSD86]. It has been investigated in detail in our group at lower magnetic fields before [Szw09] and, as applied to our clock qubit at 288 G, is summarised as follows. Instead of illuminating ions with the cooling laser immediately after quantum gates have been performed, we first map one of the qubit states to the $D_{5/2}$ level. States in that level do not participate in the cooling cycle driven by the 397 nm and 866 nm beams (in fact, this is the very reason why that cooling cycle was chosen in the first place). This means that if the ion has been transferred to the $D_{5/2}$ level, it will appear dark when the cooling lasers are subsequently turned on. Conversely, if the wave function collapses to the state that is not mapped to the $D_{5/2}$ level, the ion will scatter 397 nm light and appear bright. The $D_{5/2}$ level thus acts as the shelf in our scheme. The complete readout process consists of several steps: transfer of population from the clock qubit states to other states in the ground level in preparation for shelving, selective shelving to the $D_{5/2}$ level and finally state-dependent fluorescence detection. I will now describe each step in more detail.

2.6.1 Microwave transfer pulses for readout

The population of only one of the qubit states should be mapped to the shelf level, while the population of the other should remain in the ground level so as to scatter photons when the 397 nm laser is applied later. As will become clear in the next section, selectively transferring population from only one of the two qubit states, $|4,+1\rangle$ or $|3,+1\rangle$, to the shelf directly is not possible. Selective shelving can, however, be achieved from the $|4,+4\rangle$ stretch state, which is why we start the readout process by mapping population from one of the qubit states to $|4,+4\rangle$ through a series of resonant microwave pulses. We choose the $|3,+1\rangle$ state as it requires only three transfer pulses. With reference to fig. 2.4 defining the labels of microwave transitions, the exact sequence used is

$$\{\mathrm{C}(\pi/2),\, \mathbb{W}(\tau),\, \mathrm{C}(\pi/2),\, B(\pi),\, A(\pi),\, Q(\pi)\} \tag{2.6}$$

where $\mathbb{W}(\tau)$ represents free evolution (no microwaves applied) for a wait duration τ. We split the transfer on transition C over two pulses in order to prevent inadvertent transfer from $|4,+1\rangle$ to $|3,+2\rangle$. As shown in appendix A, the two transitions C and F are separated in frequency by only 165 kHz, so a direct π-pulse on the former at typical microwave powers would cause significant off-resonant excitation on the latter. This might subsequently lead to shelving of population that was initially in the $|4,+1\rangle$ state, which represents an error. We avoid this by instead using a Ramsey sequence consisting of two $\pi/2$-pulses resonant with transition C that are separated by free evolution of duration $\tau = \pi/\delta_{\mathrm{F}}$, where δ_F is the detuning of the $C(\pi/2)$-pulses from the resonance frequency of transition F. The second $\pi/2$-pulse thus returns any population that ended up in $|3,+2\rangle$ to $|4,+1\rangle$, while completing the transfer from $|3,+1\rangle$ to $|4,+2\rangle$. The last step of the transfer sequence, a π-pulse on the qubit transition Q, moves the population residing in $|4,+1\rangle$ out of the $F = 4$ sublevel. This is done because the 393 nm laser used for shelving addresses the $|4,+4\rangle$ state, which means that other states in the $F = 4$ sublevel are more susceptible to incorrect off-resonant shelving than states in the $F = 3$ sublevel. The overall mapping of the transfer sequence may thus be represented as $|3,+1\rangle \mapsto |4,+4\rangle$ and $|4,+1\rangle \mapsto |3,+1\rangle$.

2.6.2 Shelving to $\mathrm{D}_{5/2}$ level

After these microwave manipulations, we apply a pulse of σ^+-polarised light at 393 nm, resonant with the $4\,\mathrm{S}_{1/2}^{4,+4} \leftrightarrow 4\,\mathrm{P}_{3/2}^{5,+5}$ transition. As long as the polarisation of the 393 nm beam is pure, no other states in the $4\,\mathrm{P}_{3/2}$ level can be excited. This step is state-selective since states with $F = 3$ in the ground level are far off-resonant owing to the large hyperfine splitting. The scheme is depicted in fig. 2.5. Decay from $4\,\mathrm{P}_{3/2}^{5,+5}$ may occur either to states in the $\mathrm{D}_{5/2}$ level, in which case shelving was successful, back to $4\,\mathrm{S}_{1/2}^{4,+4}$, in which case the cycle starts anew, or to one of three states in the $3\,\mathrm{D}_{3/2}$ level. The 393 nm pulse is applied long enough that steady state is reached, at which point the $4\,\mathrm{S}_{1/2}^{4,+4}$ state has been emptied and population been moved either to the shelf or the $3\,\mathrm{D}_{3/2}$ level. The branching fraction for decay from $4\,\mathrm{P}_{3/2}^{5,+5}$ to $3\,\mathrm{D}_{3/2}$ is $f(4\,\mathrm{P}_{3/2} \to 3\,\mathrm{D}_{3/2}) = 0.00661$, while for decay to $3\,\mathrm{D}_{5/2}$ it is $f(4\,\mathrm{P}_{3/2} \to 3\,\mathrm{D}_{5/2}) = 0.0587$. If the shelving fidelity for the state that is to be

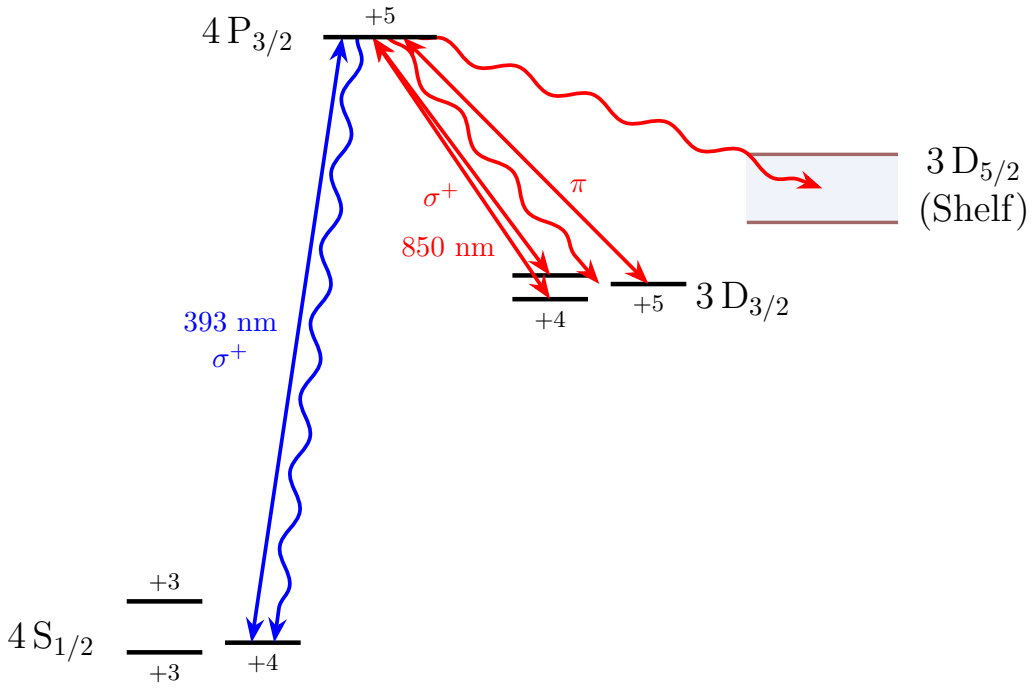


Figure 2.5: Shelving scheme for $^{43}Ca^+$. A pulse of σ^+-polarised 393 nm light is initially applied to excite population from $4\,S_{1/2}^{4,+4}$ to $4\,P_{3/2}^{5,+5}$. After steady state has been reached, the ion either occupies the $3\,D_{5/2}$ shelf level or one of the states in the $3\,D_{3/2}$ level indicated. For high-fidelity shelving, sequential pulses of 850 nm beams of suitable polarisation are then used to repump from the latter, resulting either in decay back to $4\,S_{1/2}^{4,+4}$ or additional transfer to the shelf. The 393 – 850 sequence is repeated several times, each step increasing population in the shelf. Off-resonant excitation from states in the $4\,S_{1/2}^{3}$ hyperfine sublevel is suppressed by the large hyperfine splitting.

shelved is defined as the probability that the ion ends up in the dark shelf level, given that it started in $4\,S_{1/2}^{4,+4}$, one finds $P(\mathrm{d}|S^{4,+4}) = 0.0587/(0.00661 + 0.0587) = 0.899$ after a single 393 nm pulse. The corresponding shelving error is defined as $\epsilon_{\mathrm{d,shelving}} = 1 - P(\mathrm{d}|S^{4,+4})$. Unless additional measures for repumping from $3\,D_{3/2}$ are taken, this is the best one can do.

We may also define an error for the state that is not to be shelved. We take this to be the probability that the ion ends up in the shelf, given that it started in the intended bright state in the $F = 3$ sublevel. We therefore have $\epsilon_{\mathrm{b,shelving}} = P(\mathrm{d}|S^{3,m})$.

2.6.2.1 High-fidelity shelving

Use of an 850 nm laser for repumping enables much higher shelving fidelities, as described in [Szw09]. Assuming pure σ^+-polarisation for the 393 nm beam, the only states in the $3\,\mathrm{D}_{3/2}$ level that may be occupied after the initial 393 nm pulse are the two states with $m = +4$ and the state with $m = +5$. Efficient repumping thus requires three frequency components. Assuming the 850 nm beam is turned on long enough that the $3\,\mathrm{D}_{3/2}$ level is depleted, population ends up in either the shelf or the ground level via decay from $4\,\mathrm{P}_{3/2}$. However, it is important to ensure that decay to any state other than $4\,\mathrm{S}_{1/2}^{4,+4}$ is prevented, since otherwise erroneous bright events would later be detected. This means that only the $4\,\mathrm{P}_{3/2}^{5,+5}$ state should be addressed by the repumper, which requires that no σ^- component be present in the 850 nm laser and furthermore that the σ^+ beams be applied before the π beam. After the repumping pulses, the population contained in the $3\,\mathrm{D}_{3/2}$ level has either been transferred to the shelf or been moved back to $4\,\mathrm{S}_{1/2}^{4,+4}$. When the sequence is repeated several times, more and more population will accumulate in $3\,\mathrm{D}_{5/2}$ and high shelving fidelity may be achieved. We therefore use a scheme of the form

$$\left\{\{393\,\sigma^+, 850\,\sigma^+, 850\,\pi\}^n,\, 393\,\sigma^+\right\}\ , \tag{2.7}$$

where n denotes the number of repeats of the subsequence.

If decay from the metastable shelf level could be ignored, arbitrarily precise shelving of $4\,\mathrm{S}_{1/2}^{4,+4}$ would be possible. In practice, however, the finite lifetime of the shelf causes a small fraction of population to be lost back to the ground level, which at some point balances the increase in population from the shelving lasers.

As mentioned above, there are two contributions to the overall error of the shelving process. One is the error caused by unsuccessful shelving of the state $|4, +4\rangle$ of the ground level, which should end up dark, and the other is the error caused by inadvertently shelving the intended bright state in the $F = 3$ sublevel. We define the overall shelving error as the average of these two, so

$$\epsilon_{\mathrm{shelving}} = \frac{1}{2}\left(\epsilon_{\mathrm{d,shelving}} + \epsilon_{\mathrm{b,shelving}}\right)\ . \tag{2.8}$$

At the time when most of the experiments described in the following chapters were conducted, the 850 nm repumping laser had not been set up yet, which means that the shelving fidelity was limited to 0.9. The high-fidelity method, the implementation of which is described for our apparatus in [Web22], was only used for the experiment presented in section 8.3.2.

2.6.3 State-dependent fluorescence detection

The readout process concludes by turning on the Doppler cooling beams while simultaneously monitoring fluorescence from the ion. We use a photon multiplier tube (PMT) to record the number of photons that are detected within a certain readout bin time, which are then compared to threshold values to distinguish between qubit states. Details of the model used to calculate optimal settings for bin time and threshold values such that the detection fidelity is maximised while the readout time kept short can be found in [Bur10]. The outcome of a single readout acquisition is either the event "ion dark" or the event "ion bright". By repeating the experimental procedure under investigation several times and counting the number of occurrences of each event out of the total number of repetitions, we infer the corresponding probabilities $P(\mathrm{d})$ and $P(\mathrm{b})$. To describe the uncertainty in these estimates, we use the Pearson-Clopper 68 %-confidence interval for a binomial proportion. Wherever errorbars for populations or transition probabilities are shown in the following chapters, they are based on this confidence interval.

The quantities of interest in most experiments are usually not the probabilities $P(\mathrm{d})$ and $P(\mathrm{b})$, but rather the populations $P(\uparrow)$ and $P(\downarrow)$ of the qubit states. The relationship between these variables depends on the state preparation and measurement errors arising from qubit initialisation, microwave transfer pulses (if relevant for the particular qubit), shelving and fluorescence detection. Letting $p = P(\mathrm{b}|\downarrow)$ denote the probability that an ion initialised in state $|\downarrow\rangle$ ends up bright and $q = P(\mathrm{d}|\uparrow)$ the probability that an ion initialised in state $|\uparrow\rangle$ ends up dark [Hom06], then the qubit

populations may be inferred from the observed quantities $P(\mathrm{d})$ and $P(\mathrm{b})$ through

$$\begin{pmatrix} P(\uparrow) \\ P(\downarrow) \end{pmatrix} = \frac{1}{p+q-1} \begin{pmatrix} p & p-1 \\ q-1 & q \end{pmatrix} \begin{pmatrix} P(\mathrm{d}) \\ P(\mathrm{b}) \end{pmatrix} . \tag{2.9}$$

Defining analogous variables for two ions, one finds that $p^2 = P(\mathrm{bb}|\downarrow\downarrow)$ and $q^2 = P(\mathrm{dd}|\uparrow\uparrow)$ [Hom06]. When a PMT is used for readout, such that one cannot observe which ion fluoresces, only the total number of bright ions, the populations may be obtained through

$$\begin{pmatrix} P(\uparrow\uparrow) \\ P(\uparrow\downarrow + \downarrow\uparrow) \\ P(\downarrow\downarrow) \end{pmatrix} = \frac{1}{(p+q-1)^2} \begin{pmatrix} p^2 & p(p-1) & (1-p)^2 \\ 2p(q-1) & 2pq-p-q+1 & 2q(p-1) \\ (q-1)^2 & (q-1)q & q^2 \end{pmatrix} \begin{pmatrix} P(\mathrm{dd}) \\ P(\mathrm{db}+\mathrm{bd}) \\ P(\mathrm{bb}) \end{pmatrix} . \tag{2.10}$$

For the experiments described in this thesis, an exact characterisation of state preparation and measurement errors was not required. However, we ensured that relevant parameters, for instance laser polarisations and durations of microwave transfer pulses, were optimised such that the observed error was consistent with the limit set by shelving when no 850 nm beam is used for repumping. In particular, from calibration experiments that involve repeated state preparation and readout without gate pulses we may bound the error caused by operations other than shelving to be less than 1 %.

Chapter 3

Apparatus

Trapping an ion and controlling its quantum state requires a range of experimental techniques and equipment. This chapter focuses on a technical description of the parts that make up the apparatus in which experiments have been carried out, explaining key performance requirements and giving an account of how different subsystems relate to each other. Some aspects of our apparatus have already been described in depth in other publications; where this is the case, I will only give a brief review that supplies the information necessary for understanding the experiments described in this thesis and will refer to the original source for details. Figure 3.1 contains a block diagram of our experimental arrangement, while a photograph of the central part of our apparatus is depicted in figure 3.2.

3.1 Vacuum system

A detailed account of the design of our trap and vacuum system has been given in ref. [Wol19]. Also included therein is a thorough description of the fabrication process of the trap chip and the steps taken in assembling the vacuum chamber. After the initial experiments described in that reference had been carried out, we encountered problems when we first tried to cool down the trap to cryogenic temperatures. Some of the electrical components on the in-vacuum printed circuit boards (PCBs) failed, presumably due to incompatibility with the solder that we had used. Additionally, we found that thermal contraction during cooldown caused the trap to move by a

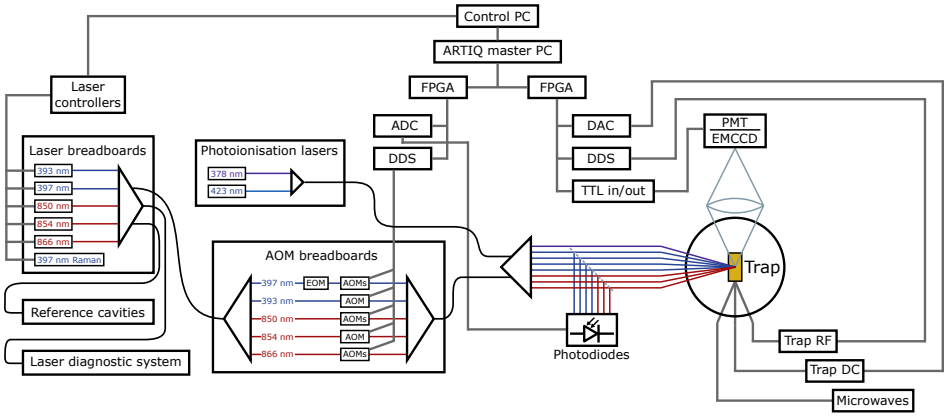


Figure 3.1: Block diagram of apparatus highlighting the relations between the various subsystems

much larger amount than expected. It was therefore necessary to open the vacuum chamber again to fix these issues and we replaced some components during this process. As part of the following presentation, I will mention any modifications that we made for the new version of our apparatus compared to the description in ref. [Wol19].

3.1.1 Trap chip

At the centre of our experiments lies a surface-electrode ion trap formed by 4 µm-thick patterned gold electrodes deposited on a 430 µm-thick substrate of sapphire. This trap chip follows the general "symmetric five-wire trap" geometry for surface Paul traps, but additionally contains a microwave electrode that generates the magnetic field required for the implementation of single- and two-qubit gates via magnetic-dipole transitions. A rendering of the chip is shown in figure 3.3 alongside a schematic illustration of the different types of electrodes. Electrical signals are supplied through wire bonds that are connected to PCBs mounted on the main support structure inside the vacuum chamber (see also fig. 3.7).

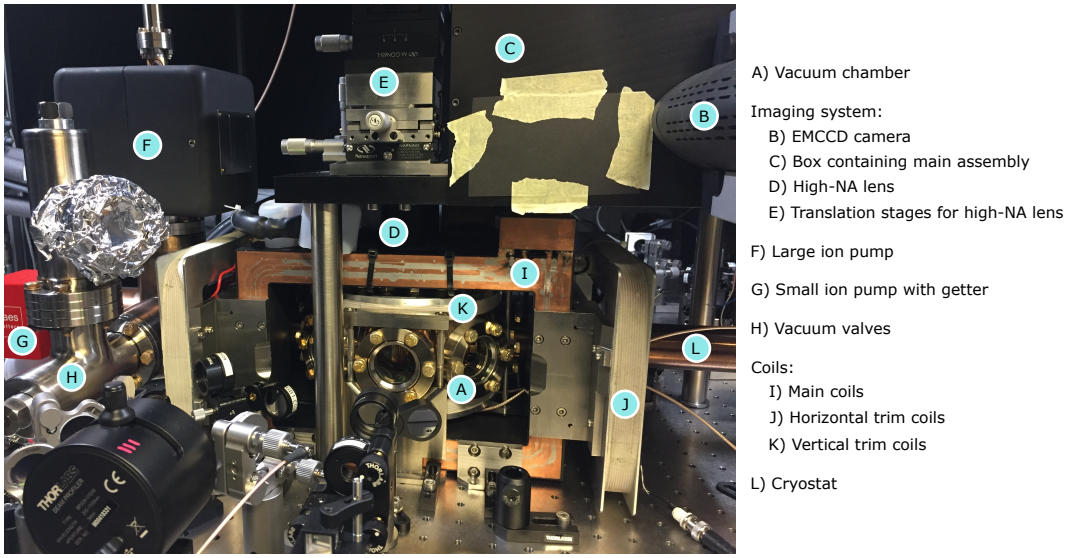


Figure 3.2: Photograph of main equipment located on trap table

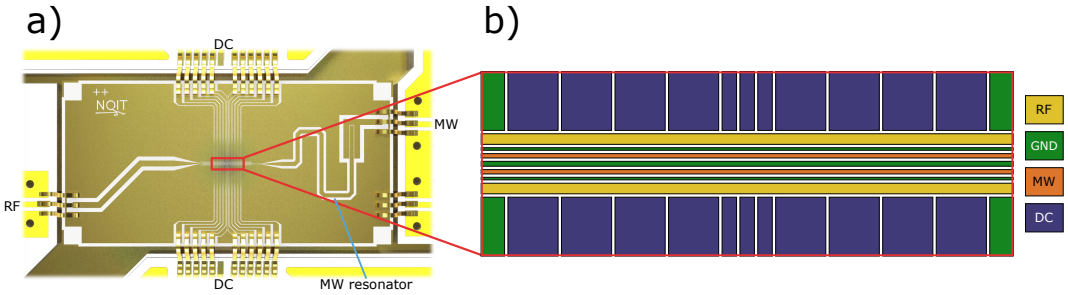


Figure 3.3: a) Rendering of trap chip showing signal connections and overall geometry b) Schematic of central region of trap chip with colour-coded electrodes. The relative size of electrodes is to scale.

3.1.1.1 Rf electrodes

Two radio-frequency (rf) electrodes generate an electric field that provides confinement along an axis lying half-way between the electrodes at a height of 40 µm above the surface of the chip. The electrodes are not driven independently, but rather derive from one common electrode that splits into two prongs close to the centre of the chip. The corresponding voltage signal is supplied via the rf PCB, the layout of which underwent one significant change compared to the version described in ref. [Wol19]: solder pads for the inductive choke were added to ease the mounting process. After we had completed assembly of the updated version of the vacuum part of the apparatus, the system was heated in a bakeout oven to reduce the base pressure that could be achieved. Unfortunately, during this step the newly installed rf PCB

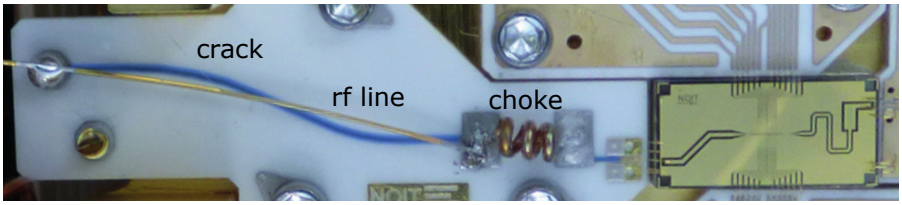


Figure 3.4: Photograph of rf PCB and trap chip. The crack in the PCB, which cuts the trace for the electric signal, is visible faintly on the left. A beryllium-copper wire has been soldered by hand to bridge the gap.

cracked in half. We had to open the vacuum chamber yet again, but rather than replacing the PCB completely, which would have required breaking the wirebonds and thus risking damage to the trap chip, we decided to solder a beryllium-copper wire across the crack, a few millimetres above the surface of the PCB. A photograph of the relevant section is shown in fig. 3.4. No further problems were encountered in the subsequent bake.

3.1.1.2 Dc electrodes

Several direct-current (dc) electrodes allow production of a static electric field. This is used to achieve confinement in the axial direction, cancel stray electric fields to eliminate excess micromotion and shuttle ions around the trap. There are 22 dc electrodes in total, 11 on each side of the trap axis. The width of the three central electrodes is a third of that of the remaining electrodes to facilitate shuttling operations. In order to reduce voltage noise at frequencies comparable to the motional frequencies of the ions, which causes undesirable motional heating, the dc signals are low-pass filtered on the in-vacuum dc PCBs. Their design has been updated slightly: each dc line now only contains a one-pole filter comprised of a 1 kΩ resistor[1] and a 1 nF capacitor[2]. The particular components were chosen so as to ensure that they were suitable for use in UHV conditions and that their solder pads, the solder and the solder pads of the PCB traces were all compatible.

[1] Part CHR 0603 HT from SRT Resistor Technology
[2] Part 0603A102JBCVN from SRT Microceramique

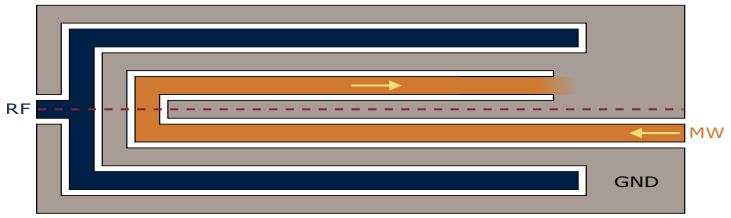


Figure 3.5: Schematic illustration of U-shaped microwave electrode (orange) and rf electrode (blue). The trap axis is shown as a dashed red line. One end of the microwave electrode is shorted to the ground plane of the trap chip, while the other is capacitively coupled to the input transmission line. Reproduced from [WLW+22].

3.1.1.3 Microwave electrode

A microwave (mw) electrode carrying current oscillating at microwave frequencies produces the magnetic field used to implement single- and two-qubit gates. Our trap chip is based on a novel design for the geometry of this mw electrode: an elongated U-shape leads by spatial symmetry to a vertical plane in which the microwave field is directed predominantly normal to the trap surface. Given the orientation of the static magnetic field that sets the quantisation axis in our trap, this means that the π-component of the microwave field, which couples the two states of the $|F = 4, m = +1\rangle \leftrightarrow |F = 3, m = +1\rangle$ clock qubit in the ground level, is thus by geometry strongly reduced in that plane. Figure 3.5 contains an illustration of the layout. One end of the mw electrode is shorted to the ground plane of the trap chip to prevent charging effects, while the other has an open termination, taking the form of a gap in the transmission line. The length of the electrode was chosen such that this arrangement forms a $\lambda/4$ resonator for the 3.1 GHz transition frequency of the clock qubit. This resonator ensures impedance matching to the $50\,\Omega$ characteristic impedance of the input feedline coming from the mw PCB, thus reducing the power reflected from the chip and leading to a build-up in current that increases the magnetic field gradient. The overall Q-factor of the resonator is affected by two contributions: the internal quality factor Q_{int}, which is mainly determined by resistive losses within the electrode, and the external quality factor Q_{ext}, which depends on the capacitive coupling between electrode and input transmission line [Poz11]. They are related through $Q^{-1} = Q_{\text{int}}^{-1} + Q_{\text{ext}}^{-1}$.

Figure 3.6 contains a plot of the S_{11} power reflection parameter as a function of

frequency and temperature for the particular chip that was used for the experiments described in this work. Data was acquired with a vector network analyser, see ref. [WLW+22] for details about the measurement setup. The main resonance close to the clock qubit frequency of 3.1 GHz is clearly visible. We observe additional dips at other frequencies, which we believe to be caused by inadvertent resonant coupling between mw and rf electrodes (see section 7.8.2.1). As the temperature of the trap is lowered, the resistance of the gold layer constituting the electrode decreases, which enhances Q_{int}. The factor Q_{ext} is mainly determined by the geometry of the junction between resonator and feedline, but also depends on the dielectric constant of the sapphire substrate. The latter will vary slightly with temperature, but any changes in Q_{ext} due to temperature should be negligible compared to those in Q_{int}. At room temperature, the resonator is under-coupled ($Q_{\text{int}} < Q_{\text{ext}}$), but as the trap chip is cooled, critical coupling ($Q_{\text{int}} = Q_{\text{ext}}$) is reached between 190 K and 50 K, at which point the power coupled onto the mw electrode is maximised. As the temperature is reduced further, the resonator becomes over-coupled ($Q_{\text{int}} > Q_{\text{ext}}$) and the amount of reflected power increases again. Ideally, the capacitance between resonator and feedline should be chosen such that critical coupling is achieved at the desired operating temperature, in our case approximately 20 K. However, this is hard to achieve in practice, since the residual resistivity ratio of gold, which depends on its purity and temperature, is usually not exactly known in advance.

As far as concerns the maximum power that may be coupled into the resonator at the frequency of the clock qubit, a high total Q is advantageous. However, we also need to be able to implement the microwave transfer pulses for state preparation with reasonable speed. Since these pulses use frequencies as low as 2.5 GHz, the resonance should not be too narrow. We therefore decided to limit Q to < 17 by an appropriate choice of input capacitance. From data taken with the previous iteration of the apparatus, which did not suffer from strong subsidiary peaks and thus allowed more accurate fits, we infer that $Q \approx 10$ is experimentally observed at cryogenic temperatures [WLW+22].

Another noteworthy feature of the plot in fig. 3.6 is a shift in resonance frequency of approximately 100 MHz between room temperature and 24 K. This can

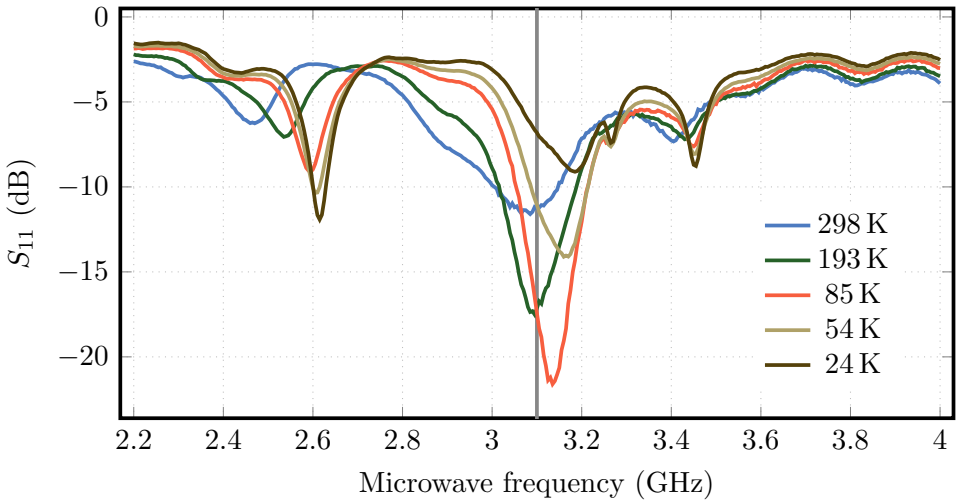


Figure 3.6: Fraction of input microwave power reflected from trap chip as function of frequency. The grey vertical line corresponds to the transition frequency of the clock qubit at a static field of 28.8 mT.

partially be attributed to the change in dielectric constant of sapphire, the reduction in resistance of gold and the decrease in length of the resonator due to thermal contraction. We find, however, that the observed shift is larger than what would be expected from a simplified circuit model [WLW+22]. Compared to the previous version of the apparatus, we used a trap chip with a microwave resonator of slightly different length. Its resonance occurred closer to the clock qubit frequency at cryogenic temperatures, thus increasing the microwave power that could be coupled onto the trap chip.

3.1.2 Vacuum equipment

The trap resides in a stainless steel ultra-high vacuum (UHV) system built around an octagonal vacuum chamber[3]. Two CF100 flanges attach to the chamber on top and bottom and eight CF40 flanges, equally spaced, on its sides. The bottom flange takes the form of a solid base plate containing feedthroughs for various electrical signals, while six AR-coated viewports[4] made of fused silica occupy the sides of the chamber for laser access. The remaining two side openings are used for vacuum equipment and the cryostat, respectively. The top flange houses a custom recessed

[3]MCF600-SphOct-F2C8 from Kimball Physics

[4]Custom-manufactured by Allectra, reflection $\leq 1\%$ at 393/397 nm and $\approx 5\%$ at 850/854/866 nm

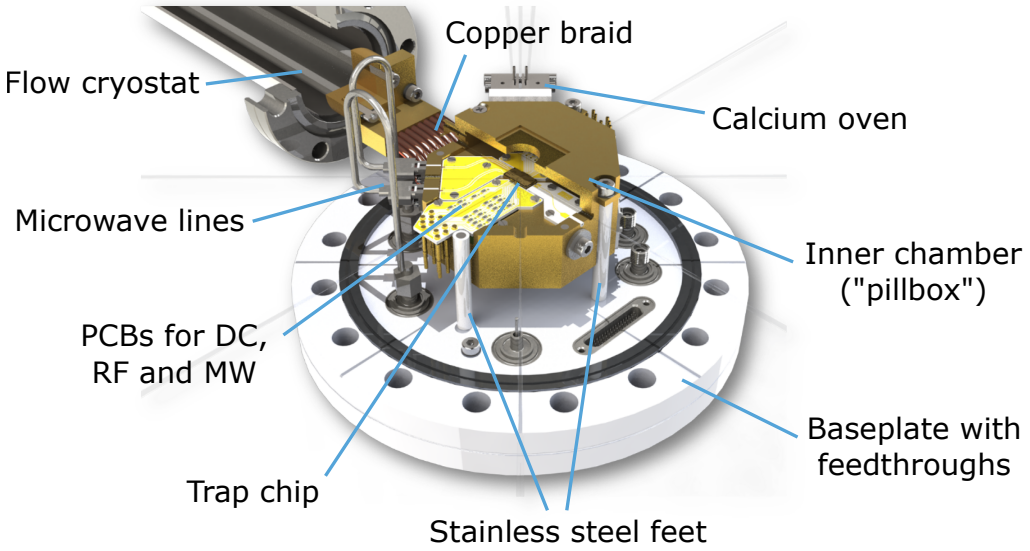


Figure 3.7: Rendering of the interior of the vacuum chamber, reproduced from [Wol19]. The copper braid has been replaced by copper sheets in the updated version described here.

viewport[5] that allows an imaging lens to be brought close to the ion for the collection of scattered light at high numerical aperture. Vacuum is maintained by two pumps: one is a combination of non-evaporable getter and small diode pump[6], while the other is a larger ion pump[7] to increase the pumping speed of gases that are not efficiently absorbed by the getter. An ion gauge monitors the pressure inside the system, which we measure to be $< 10^{-11}$ mbar.

Figure 3.7 contains an annotated rendering of the interior of the vacuum chamber. The trap chip is mounted on a pedestal — which I will refer to as "the pillbox" — made from oxygen-free high-conductivity copper. They are bonded together via eutectic solder to ensure very good thermal contact, which is essential for efficient cooling to cryogenic temperatures and dissipation of heat generated when applying high microwave powers. An oven consisting of a stainless steel tube crimped at both ends and electrical contacts provided by clamps is the source of calcium for our experiments [BGN+18]. When freshly filled, it holds approximately 2.5 mg of calcium granules[8] that have been isotopically enriched to contain about 25% ^{43}Ca and 75%

[5] Manufactured by UK Atomic Energy Authority, reflection $\approx 1\%$ at 360 – 430 nm
[6] NEXTorr D200-5 from SAES Getters
[7] StarCell VacIon Plus 20 from Agilent Technologies
[8] produced by the National Isotope Development Center

^{40}Ca. The tube contains a 0.5 mm hole in the centre through which atoms effuse when the oven is heated resistively. It is attached to the baseflange via an electrically and thermally insulating holder that includes a 2 mm aperture for collimation of the atomic beam. The oven is positioned such that the effused atoms propagate at $\approx 90°$ relative to the photoionising (PI) laser beams to minimise Doppler shifts. Thermocouple junctions allow monitoring of the oven temperature. In combination with a digital feedback loop implemented on a microcontroller located outside the vacuum system, this enables fast control of the temperature with minimal overshoot. It has been shown [BGN+18] that a stable atomic flux can be obtained in less than 15 s with this oven design.

3.2 Magnetic field coils

Three orthogonal pairs of coils, each in Helmholtz configuration, generate the static magnetic field that sets the quantisation axis for the atoms and ensures that the $|F = 4, M = +1\rangle$ and $|F = 3, M = +1\rangle$ states form a clock qubit. The largest field component, directed parallel to the trap surface and perpendicular to the trap axis, comes from the two rectangular main coils. They require a current of approximately 147 A to produce a field of 28.8 mT and are driven by two power supplies connected in parallel. One of them[9] is a high-current power supply that provides the bulk of the current, while the other[10] is used for fine adjustments in the milliampere range. Additionally, there are two sets of smaller trim coils: a vertical pair producing a field normal to the trap surface and a horizontal pair producing a field parallel to the trap axis. These are used for fine adjustments to align the magnetic field vector along the propagation axis of the blue sigma beams and thus increase the purity of the sigma polarisation seen by the ion for improved state preparation and readout.

[9] 6671A from Agilent Technologies
[10] QL355TP from Thurlby Thandar Instruments

3.3 Laser systems

Even though high-fidelity qubit gates are implemented via microwave magnetic fields in our experiments, we still need lasers for photoionisation, Doppler cooling, Raman sideband cooling, state preparation and readout. One advantage of calcium as a species for trapped-ion quantum computing is that the wavelengths of the lasers required fall into two narrow ranges: 378 — 423 nm ("blue lasers") and 850 — 866 nm ("red lasers"). This is convenient since diode lasers, which are relatively cheap and easy to operate, are readily available at these wavelengths, as are low-loss optical fibres. Additionally, optical components with design wavelengths around 400 nm or 850 nm can be bought off-the-shelf and their performance varies only very little over our narrow wavelength ranges, which allows standardisation into two sets of optics.

3.3.1 Photoionisation lasers

We use two lasers, with wavelengths of 423 nm and 378 nm respectively, to implement the two-step photoionisation process mentioned in section 2.3. The 423 nm laser is an external cavity diode laser[11] that produces an output of approximately 50 mW and is monitored via our laser diagnostics system. Its frequency is not stabilised via a reference cavity, but locked coarsely through software by measuring its wavelength with a wavemeter and feeding back on the piezo voltage of the laser to achieve the desired frequency setpoint. Selecting between isotopes is done by changing this setpoint. The 378 nm laser is a free-running diode laser[12] with an output power of 60 mW. We pick off the desired optical power from each laser, then combine the beams with a dichroic mirror[13] and deliver them to the trap table through a single-mode fibre[14]. Mechanical shutters are used to switch the PI beams on and off. During the loading process, we typically use 40 µW of 423 nm light and 3 mW of 378 nm light.

[11] DL pro HP from Toptica
[12] iBeam smart from Toptica
[13] FF414-Di01-25X36 from Semrock
[14] PMC-360Si-2.3-NA012-3-APC-xxx-P from Schäfter+Kirchhoff

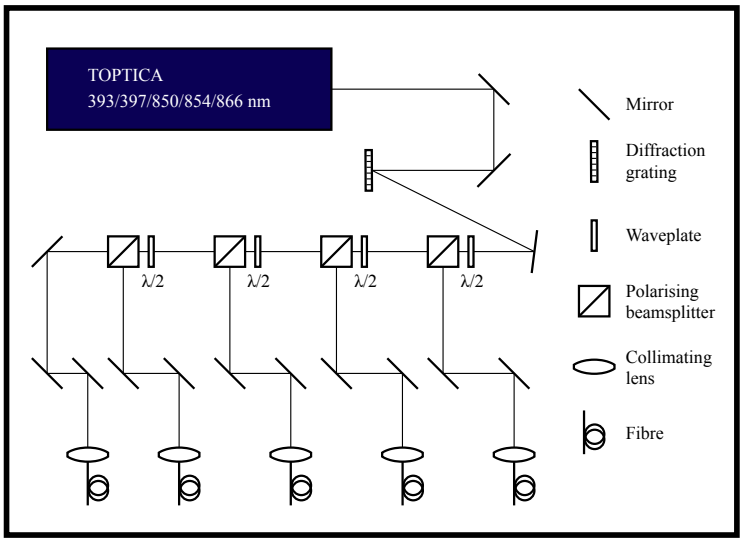


Figure 3.8: Arrangement of optical components on laser breadboards. The laser head contains optical isolators.

3.3.2 Ca^+ lasers

All the lasers used to drive transitions between the 4 S, 4 P and 3 D levels in Ca^+ at wavelengths of 393 nm, 397 nm, 850 nm, 854 nm and 866 nm are external cavity diode lasers[15]. We use optical isolators placed straight after each diode to suppress optical feedback caused by reflections from optical components further downstream in the beam path. For the red lasers, we found that one single-stage isolator[16] was enough for this purpose, but for the blue lasers we use two single-stage isolators[17] in series.

3.3.2.1 Laser breadboards

Instead of setting up the laser heads on separate optics tables, where space is at a premium, our lab has recently started to move the Ca^+ lasers to dedicated laser breadboards placed in drawers in a standard 19" server rack. The general layout of these breadboards is the same for all lasers and is depicted in figure 3.8.

A blazed diffraction grating[18] on each breadboard ensures that no amplified spontaneous emission at undesirable wavelengths reaches the ion. Repeated stacks of

[15] DL pro HP from Toptica
[16] #OK-001236 from Toptica
[17] #OK-001092 from Toptica followed by IO-3D-405-PBS from Thorlabs
[18] Item 48464 from Edmund Optics for blue lasers, GR13-0610 from Thorlabs for red lasers

half-waveplates[19] and polarising beam splitters[20] allow picking off varying amounts of optical power so as to split light between the optical diagnostics system, reference cavities and experiment table. The different beams are then coupled into optical fibres. For the red lasers, we achieve this with fixed-focus collimators[21], while for the blue lasers, which we found to require more adjustability and stability, we use variable-focus collimators[22]. A half-waveplate before polarisation-maintaining fibres allows us to align the plane of linear polarisation with the slow axis of the fibre to maximise the polarisation extinction ratio of the light exiting from the output end of the fibre.

3.3.2.2 Reference cavities

The frequencies of the 393 nm, 397 nm, 850 nm and 866 nm lasers are stabilised by locking to low-drift reference cavities[23] through the Pound-Drever-Hall (PDH) technique [DHK+83]. In the case of the blue lasers, the required sidebands are generated by passing the beam on the cavity table through an electro-optic modulator[24] (EOM). For the IR lasers, the sidebands are generated directly in the laser diode by modulating the diode current. This means that all 850 nm and 866 nm light contains sidebands at this frequency, but this should not have a negative effect since these lasers are only used as repumpers. Commercial PID boxes[25] produce the modulation signals applied to EOMs and diodes (50 MHz for both) and also the error signals that feed back to the laser controller to lock the frequencies. Varying the lengths of the cavities through built-in piezo elements allows us to change the frequencies of the locked lasers. For the 854 nm laser, the frequency stability of which is not as critical, we do not employ a reference cavity, but rather use a wavemeter lock in a similar way as described for the 423 nm PI laser.

[19] Custom item designed for 393 – 422 nm from Altechna for blue lasers, WPH05M-850 from Thorlabs for red lasers
[20] Custom item designed for 393-422 nm from Altechna for blue lasers, PBS122 for red lasers
[21] F240APC-850 from Thorlabs
[22] PAF-X-5-A from Thorlabs
[23] Custom item manufactured by StableLaserSystems
[24] EO-50M3-VIS from Qubig
[25] PDD 110 from Toptica

3.3.2.3 AOM breadboards

We make use of acousto-optic modulators (AOMs) to switch beams used for Ca^+ on and off, fine-tune their frequency and stabilise their intensity. With the exception of the Raman beams, the AOMs are set up on separate custom-machined AOM breadboards made from solid slabs of aluminium, which are stored away on rack-mounted shelves to save space on the optics tables. Light from the laser breadboards is delivered via optical fibres to the AOM breadboards, where it is manipulated as desired and then sent through another set of optical fibres to the trap table. The AOM breadboards were designed for pre-determined beam paths to achieve a high density of optical components while offering the possibility to combine beams with different frequencies into the same fibre. The general layout is the same for all AOM breadboards, details about the design can be found in [Ste19]. However, not all our breadboards are fully populated with optical components, see figs. 3.9 and 3.10 for the actual configurations realised. Generally, the purpose of the double-pass AOMs is frequency adjustment, while the single-pass AOMs are used to turn individual beams on and off and control their intensity.

The breadboard dedicated to the blue lasers (fig. 3.9) is the most complex. Light at 397 nm from the respective laser breadboard is launched through one of the input couplers and passes through an EOM[26] that generates the sidebands needed to allow addressing of states in the two hyperfine sublevels when trapping $^{43}Ca^+$. It is turned off when we work with $^{40}Ca^+$. After the double-pass AOM, the beam is split into three. One beam, the "397 Doppler", propagates further through a single-pass AOM and is then coupled into a fibre that delivers it to the trap table. Another beam, the "397 detuned Doppler", is steered through a different single-pass AOM, which is set up in such a way that a frequency difference of -400 MHz is introduced relative to the 397 Doppler beam. It is then combined with the latter on a R10:T90 beamsplitter[27]. The 397 detuned Doppler beam is intended to cool ions in highly excited motional states, which can help in preventing ion loss caused by collisions with residual background gas particles. We do not usually make use

[26] EO-T2700M3-VIS from Qubig
[27] BSN04 from Thorlabs

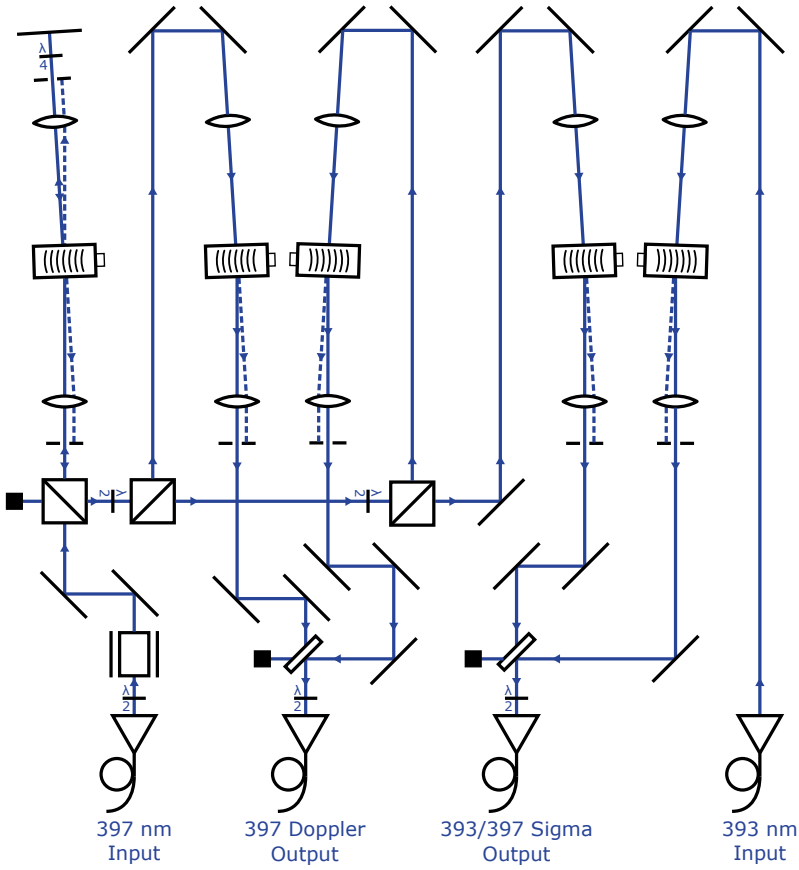
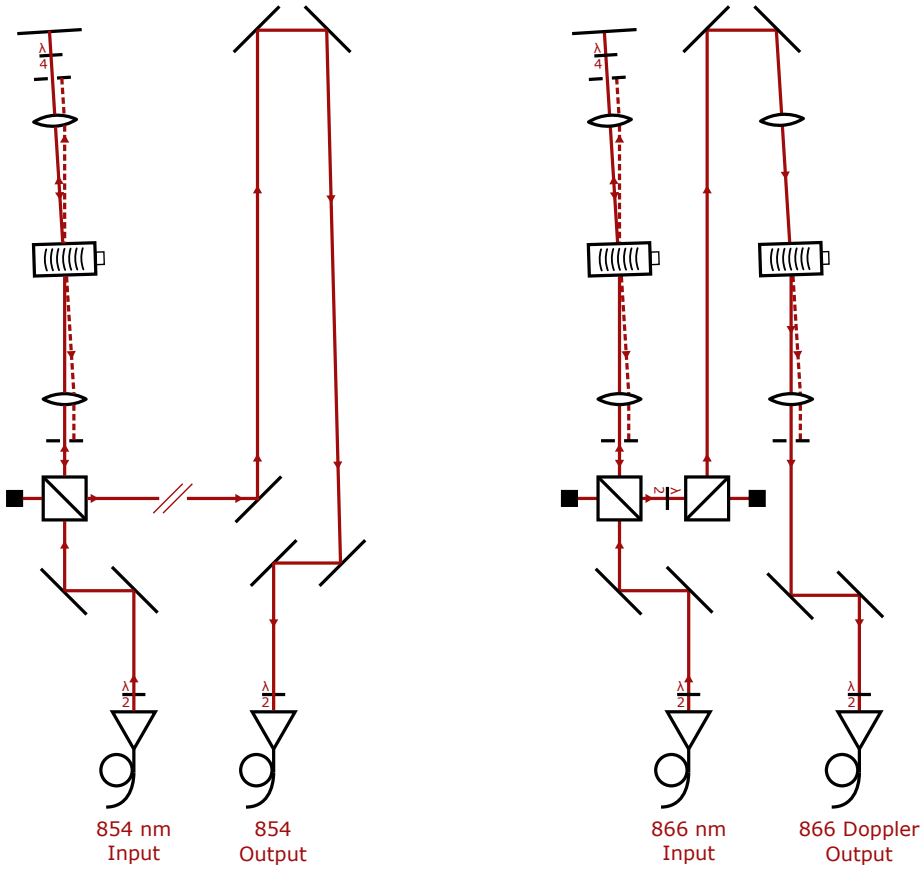


Figure 3.9: Configuration of optical components on 397/393 nm AOM breadboard

of it for a single ion, but we find that it has a noticeable effect for two ions, where it increases the average lifetime at room temperature from approximately one to four minutes. The third beam, the “397 sigma”, goes through a different single-pass AOM and is then combined via a R10:T90 beamsplitter[28] with the ”393 sigma” beam that enters through the second input of the breadboard and is modulated by another single-pass AOM. All AOMs on this breadboard are ISOMET model 1250C-829A, while for the collimators we use PAFA-X-4-A FibrePorts from Thorlabs. The lenses, half-waveplates and PBSs were custom-manufactured by Altechna, whereas the quarter-waveplate is a standard component[29]. Output and input fibres are type PMC-360Si-2.3-NA012-3-APC-xxx-P from Schäfter+Kirchhoff.

Since there is only a single 854 nm beam required in our trapping scheme, the corresponding breadboard (fig. 3.10a) is sparsely populated and contains only one

[28] BSN04 from Thorlabs
[29] WPQ05M-405 from Thorlabs



(a) (b)

Figure 3.10: Configuration of optical components on a) 854 nm AOM breadboard and b) 866 nm AOM breadboard

Isomet 1205C-1 AOM in double-pass configuration, which is used for both frequency tuning and intensity stabilisation. The resulting output beam is combined via a fiberised power splitter[30] with an 850 nm beam originating from the corresponding breadboard.

The 866 nm breadboard (fig. 3.10b) features one Isomet 1205C-1 AOM in double-pass configuration and a single-pass Isomet 1206C AOM, generating the 866 nm beam used for Doppler cooling.

The configuration of the 850 nm breadboard is similar to that of the 397 nm breadboard insofar as the 850 nm input is split into three separate beams. The beams propagating through the first two single-pass AOMs are combined and coupled into one fibre. They serve as the $850\sigma^+$ components for high-fidelity shelving. The beam

[30] PN850R5A2 from Thorlabs

passing through the third single-pass AOM, which acts as the 850π component for shelving, is sent down a separate fibre that delivers it to the 854 nm breadboard. There it is combined with the 854 nm beam.

On all IR breadboards we use PAFA-X-4-B FibrePort collimators, WPH05M-850 half-waveplates, WPQ05M-850 quarter-waveplates and PBS122 polarising beam-splitters from Thorlabs, while the lenses are part KPX064AR.16 from Newport.

3.3.3 Trap table optics

The arrangement of laser beams launched into the vacuum chamber on the trap table is depicted in fig. 3.11. I will discuss the various beam paths separately, but here want to highlight features common to almost all of them. Polarising beam splitters[31] straight after the collimators ensure a well-defined state of linear polarisation to start with. Fluctuations in polarisation are thus turned into intensity noise; we use polarisation-maintaining fibres to reduce the size of these fluctuations. Combinations of pick-offs and photodiodes (PD) after the beamsplitters enable monitoring of the beam powers and form part of a noise-eating system to stabilise optical intensity at the ion (see section 3.5.4). In each beam path, the last mirror mount before the viewport contains piezoelectric actuators that allow us to electronically servo the alignment of our lasers onto the ion in horizontal and vertical directions through our experimental control system.

3.3.3.1 Focussing and spot sizes

Several points need to be considered when deciding on suitable spot sizes at the trap centre for the laser beams. Firstly, background scatter from the trap surface should be minimised for the blue beams to ensure a high signal-to-noise ratio for state-dependent fluorescence detection and avoid charging of the dielectric substrate. Secondly, the edge of the trap chip should not clip the beam, otherwise the resulting diffraction effects would distort the beam profile and thus affect the laser intensity at the position of the ion. Thirdly, the smaller the beam diameter, the more sensitive

[31] Custom item designed for 393 - 422 nm from Altechna for blue lasers, PBS122 from Thorlabs for red lasers

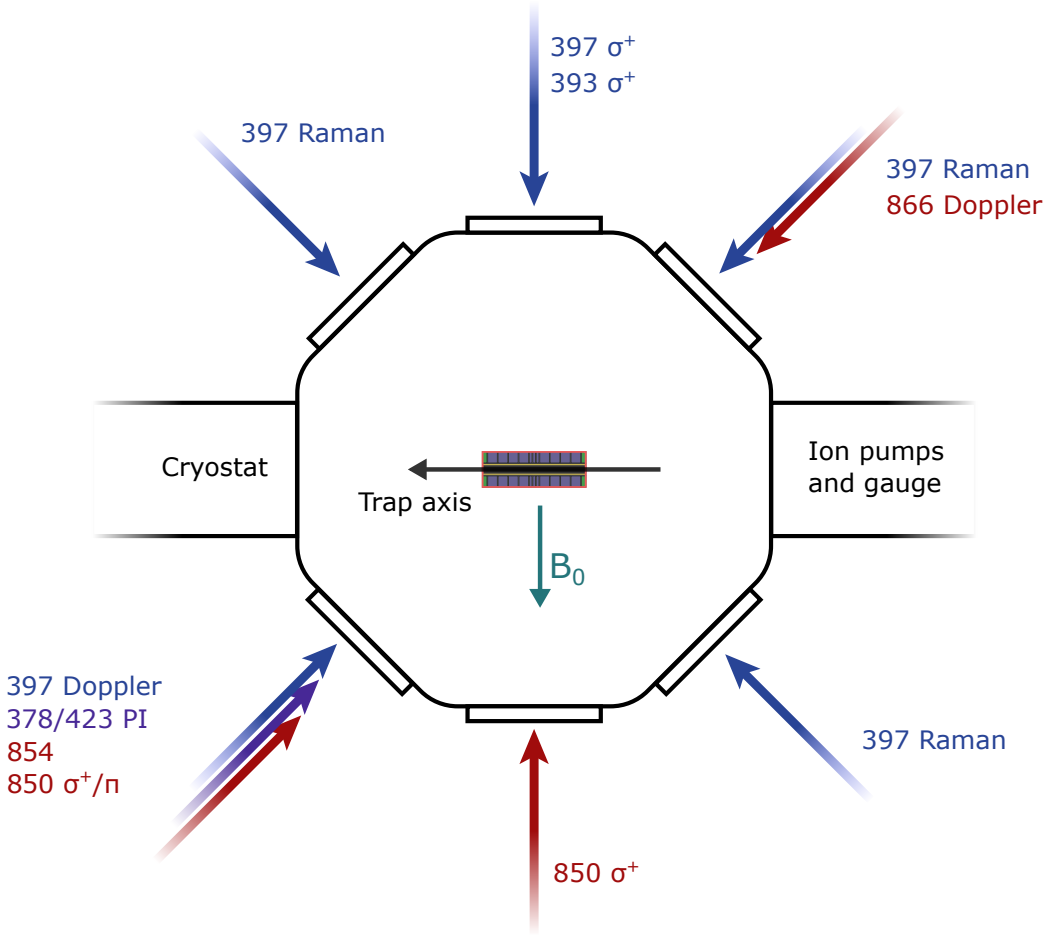


Figure 3.11: Configuration of laser beams launched into vacuum chamber

Wavelength (nm)	Beam waist radius (μm)	P_0 (nW)
397	16	377
393	16	396
866	28	113
850	28	121
854	28	118
423	16	493

Table 3.1: Measured waist radii at the trap centre for different laser beams. The quantity P_0 represents the beam power required to achieve one saturation intensity I_0 for the given beam size.

the intensity at the trap centre becomes to drifts in beam pointing. We tried to balance these competing effects by choosing the smallest beam waist radius possible while ensuring that the edge of the trap chip only clips the beam outside the $1/e^2$ radius. Based on a plot of beam radius at the edge of the trap chip as a function of beam waist at the trap centre, we decided to use a beam waist radius of approximately 15 µm for the blue and 30 µm for the red beams. We achieve these radii with 10:1 and 8:1 lens telescopes, respectively, formed by a f = 200 mm focussing lens and an appropriate collimator for each beam since the mode field diameters of our fibres are about 3.3 µm for the blue and 7.5 µm for the red.

The measured spot sizes for each beam are listed in table 3.1, along with the power P_0 required to achieve one saturation intensity. For these measurements, we first optimised the alignment of each beam onto the ion by maximising the ratio of fluorescence signal to background scatter; this should place the beam waist at the trap centre. We then deflected the beam with a flip mirror after the focussing lens and placed a beam profiler[32] at the waist of the deflected beam.

3.3.3.2 Doppler and PI beams

Figure 3.12 contains the beam paths of the Doppler beams used for cooling and fluorescence detection and of the PI beams used for photoionisation. They enter the chamber at 45° to the trap axis to ensure that axial and radial modes are cooled. Adjustable-focus collimators are used for the 397 nm[33] and 850/854 nm[34] beams.

[32] BP209-VIS/M from Thorlabs
[33] 60FC-T-4-M20L-01 from Schäfter+Kirchhoff
[34] 60FC-T-4-M25-02 from Schäfter+Kirchhoff

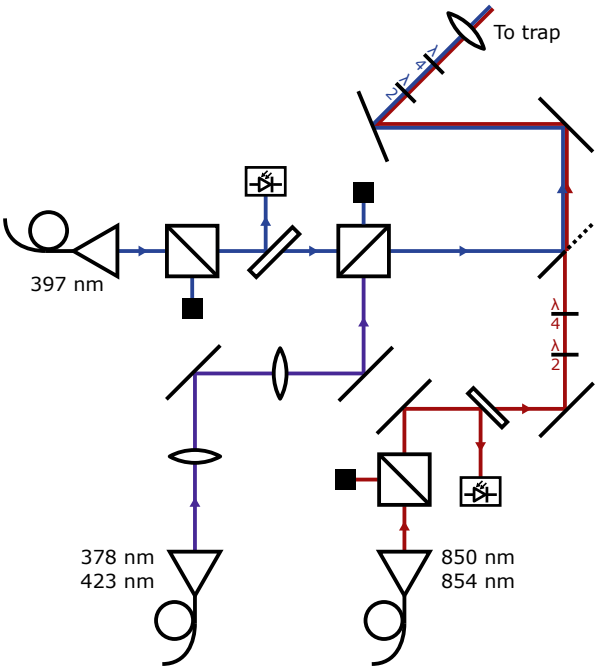


Figure 3.12: Beam path for Doppler and photoionisation beams. The 866 Doppler beam propagates in the opposite direction, as illustrated in the diagram for the Raman beam paths.

For the 378/423 nm PI beams, we found that the chromatic aberration over this wavelength range present in standard refractive components, in combination with our low ion height, meant that one of the beams would clip significantly on the trap chip. We therefore chose to use a reflective collimator[35] for the PI beams. To achieve the target waist radius of 16 µm, we had to insert an additional telescope formed by one f=-100 mm and one f=300 mm lens[36] in the PI beam path. The 397 nm Doppler beam and the PI beams have orthogonal polarisations and are combined on a PBS. The 850 nm and 854 nm beams reach the trap table via the same fibre and are combined with the blue beams through a dichroic mirror[37]. We use an air-spaced achromatic doublet[38] as the final focussing lens because of its lower chromatic aberration over the critical blue wavelength range compared to standard cemented achromatic doublets.

[35] RC04APC-F01 from Thorlabs
[36] ACN254-100-A and AC254-300-A from Thorlabs
[37] DMLP567 from Thorlabs
[38] ACA254-200-UV

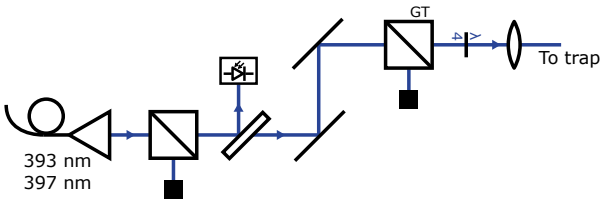


Figure 3.13: Beam path for blue sigma beams. An analogous arrangement applies to the counter-propagating 850 sigma beam.

3.3.3.3 Sigma beams

Beams with pure circular polarisation that drive σ^+ transitions form the basis for state preparation and shelving in our experiments. In order to achieve the desired polarisation, these beams are required to propagate parallel to the static magnetic field, which we achieve for the 393 nm and 397 nm beams through the arrangement shown in figure 3.13. The 850 nm sigma beam follows an analogous path on the opposite side of the vacuum chamber. We use Glan-Taylor (GT) prisms[39] in these beam paths to achieve a state of highly pure linear polarisation that is then transformed by a quarter-waveplate[40] mounted in a tip/tilt stage. The tip/tilt degrees of freedom allow us to correct for birefringence in the viewport and the fact that the waveplates were not designed for the exact wavelengths we are using (see [Har13] for further details).

3.3.3.4 866 nm Doppler and Raman beams

Figure 3.14 contains the beam paths of the 866 nm Doppler beam and the 397 nm Raman beams used for sideband cooling. We set up the 866 nm beam in a counter-propagating direction relative to the other Doppler beams for two reasons. Firstly, a lower temperature can be achieved in dark-resonance cooling with this geometry. Secondly, a substantial amount of 866 intensity is required at the ion and choosing a separate beam path allowed us to reduce power losses from fibre coupling and reflections at optical interfaces. The two Raman beams are derived from a common laser source. We introduce a frequency difference of 128 MHz between them via AOMs

[39] GT10-A and GT10-B from Thorlabs, respectively
[40] WPQ05M-405 and WPQ05M-850 from Thorlabs, respectively

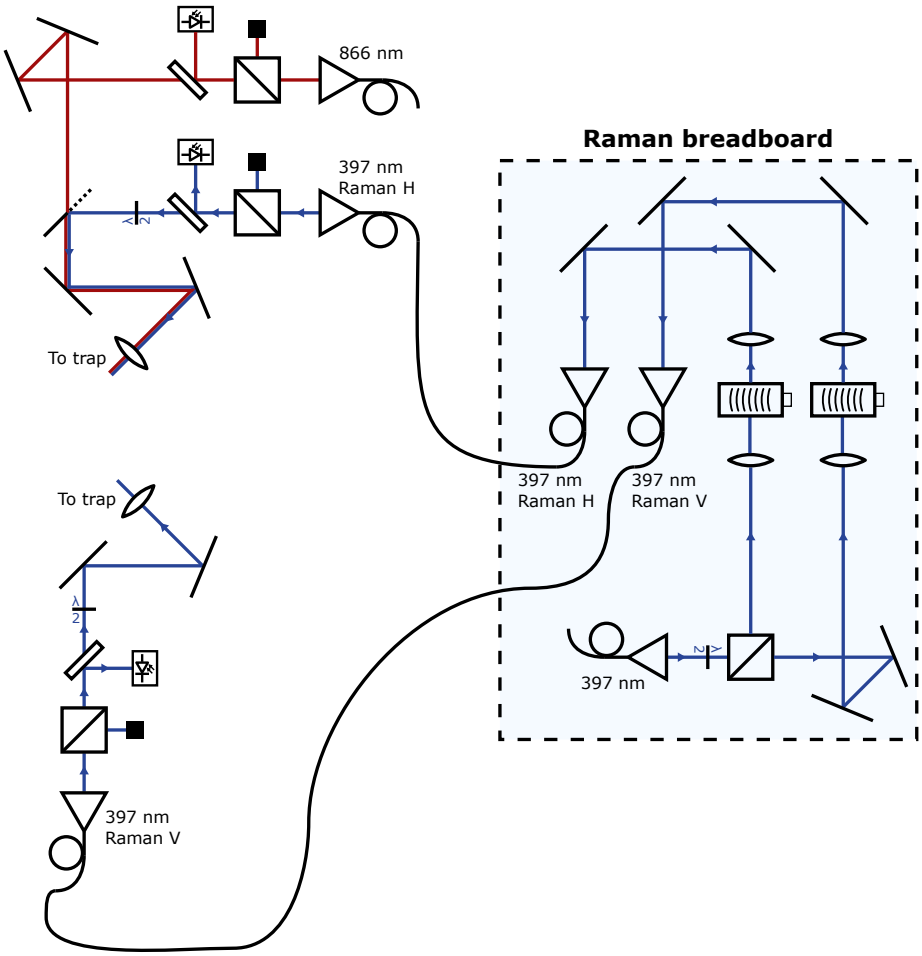


Figure 3.14: Beam path for 397 nm Raman beams

located on a breadboard directly on the trap table. Their geometry is dictated by the requirement that the difference in their wave vectors should have no component along the trap axis. They are sent into the trap with orthogonal polarisations; one of them is combined with the 866 nm beam through a dichroic mirror[41].

3.3.4 Imaging system

Detecting fluorescence from an ion illuminated by laser light is an important tool for inferring its state. In our experiments, the ion scatters light at 397 nm from transitions between the $4\,S_{1/2}$ and $4\,P_{1/2}$ levels. We observe the resulting fluorescence with the imaging system illustrated in figure 3.15. A custom multi-element primary lens designed and manufactured by Photon Gear Inc with a numerical aperture (NA)

[41] DMLP805 from Thorlabs

of 0.6 in the object plane collects photons scattered by the ion and brings them to a primary focus. This lens was designed to produce a diffraction-limited image with an optical path distance error of $< 0.075\lambda$ at a wavelength of 422 nm for a point source viewed through a 4 mm thick window of fused silica. Its performance was tested to be similarly high also at lower wavelengths. When set to its optimum working distance (ion-to-barrel separation, including window) of ≈ 17 mm, the lens forms an image at a barrel-to-image separation of approximately 153 mm with an NA of 0.09 in the image plane, thus having a magnification of 6.7. It is equipped with a dual AR coating for 397 nm and 422 nm, the transmission of which was measured to be 98% close to 400 nm.

The final image is produced by a relay consisting of one aspheric[42] and one achromatic lens[43]. This relay enables us to ensure that the final focus lies in the detection plane when the primary lens is at its optimum working distance from the ion. Additionally, it lets us change the overall magnification by choosing between achromats of different focal length. A 50:50 beamsplitter after the aspheric lens allows simultaneous detection of fluorescence with a photomultiplier tube[44] (PMT) and an electron multiplying charge-coupled device (EMCCD) camera[45]. The system also contains two shutters. One is an iris located directly after the primary lens that acts mainly as an aperture stop to reduce the effective NA of the lens (and thus the effects of aberrations) for initial alignment. The other is an adjustable rectangular aperture that is placed in the plane of the primary focus and forms a field stop to block out stray scatter from the trap surface, reducing the background counts detected by the PMT. To minimise background counts from ambient light, interference filters are installed before the detection devices: a narrow bandpass filter[46] in front of the PMT and a shortpass filter[47] before the EMCCD camera.

The position of the primary lens is controlled via a three-axis precision stage for translational and two goniometers for rotational adjustments, whereas the re-

[42] AL1225G-A from Thorlabs
[43] We typically use AC254-100-A from Thorlabs
[44] H10682-210 MOD from Hamamatsu
[45] iXonUltra897 from Andor
[46] FF01-400/12-25 from Semrock
[47] FF01-468/SP-25 from Semrock

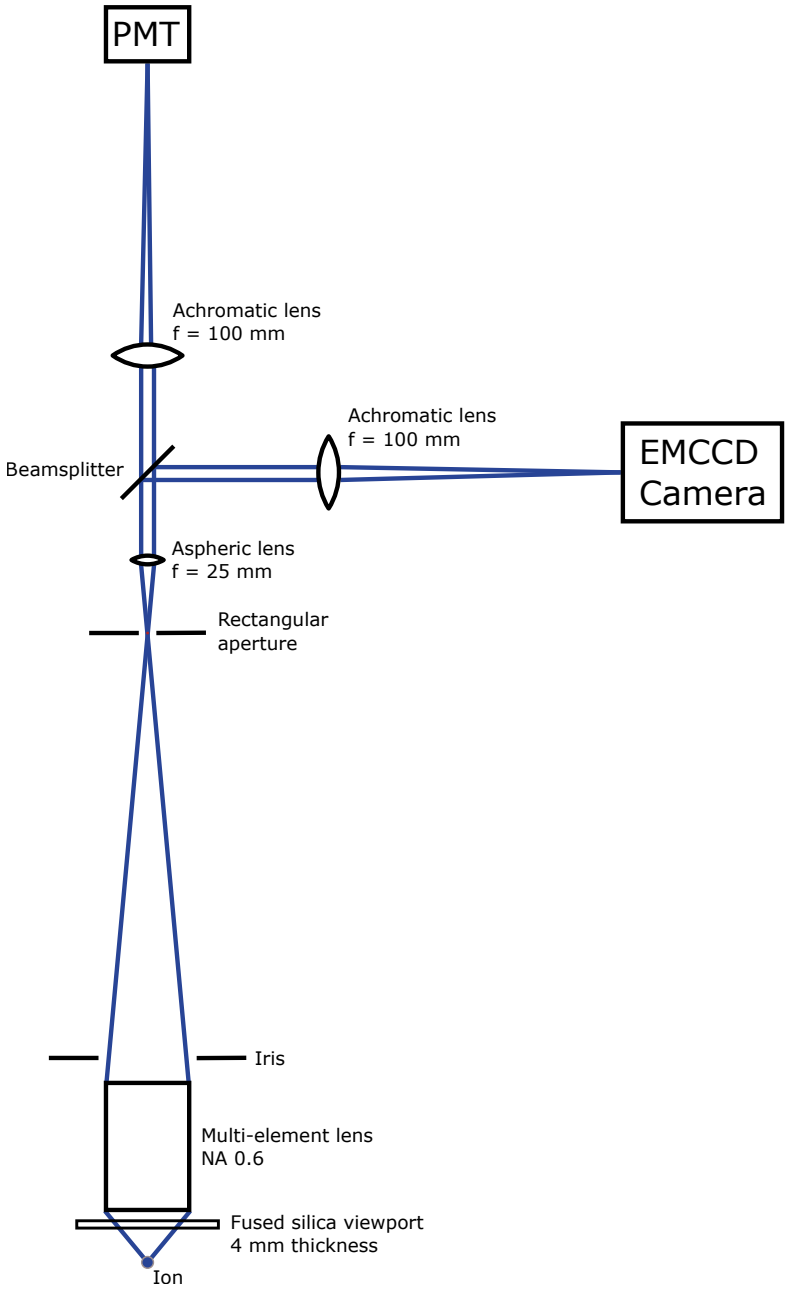


Figure 3.15: Imaging system used for detection of fluorescence at 397 nm. The relative scale of focal lengths of all lenses involved is accurate, but other distances and the sizes of some components have been reduced to fit the page.

collimating asphere is mounted on a five-axis translation stage that offers similar functionality. While having all these degrees of freedom makes the alignment process non-trivial, it is a necessity since obtaining a diffraction-limited image at such high NA is very sensitive to misalignments. With this imaging system we achieve a detection efficiency — defined as the fraction of photons scattered by the ion that are registered as pulses by the PMT, with the beamsplitter placed in the beam path — of 1.1%, as measured via a method that involves shelving to the $3\,D_{3/2}$ states [Bur10].

3.3.5 Laser diagnostic system

It is essential for the diode lasers to operate in single mode so as to obtain coherent light with a well-defined frequency and constant intensity. We cannot check single-mode behaviour with the locking cavities as this would require scanning the cavities over their free spectral range, which would defeat the point of having a stable reference cavity. Instead, we use a diagnostics system that continuously monitors the spectrum of light emitted by the laser diodes. It consists of a multi-channel fibre switch[48] in combination with optical spectrum analysers[49] and a wavelength meter[50]. In order to ensure accurate measurements, we calibrate the wavemeter regularly with a stable He-Ne reference. The system is controlled by software written in Python that automatically cycles through the different lasers at regular intervals with the switch and includes a GUI that plots the transmission signal as the length of the OSA cavity is scanned [Ste19]. The laser spectrum and mode behaviour can then be deduced by visual inspection. The absolute wavelength measured by the wavemeter is also displayed in the GUI.

3.4 Cryogenic equipment

We use a flow cryostat to cool the trap chip to cryogenic temperatures. A detailed description can be found in [Wol19]. The cryogen is stored in a pressurised dewar

[48] LEONI FiberSwitch mol 1x16
[49] SA200-3B and SA200-8B from Thorlabs
[50] WS7-PID2-MC8 from HighFinesse

next to the trap table and propagates through a transfer line to the cold plate at the end of the cryostat, where it evaporates and then leaves the lab through a return line. Compared to a closed-cycle cryostat, this allows the design of the vacuum system to be less complex, avoiding multiple cryogenic stages. Additionally, no special measures for vibration isolation are required. However, cooling with a flow cryostat is less efficient, in particular because the additional heat ingress between dewar and cold plate of the cryostat is substantial. Furthermore, we find that the seal rings at junctions between pipes may cease to function properly below a certain temperature, resulting in leaks that significantly increase cryogen consumption. The limited efficiency is highlighted by the fact that junctions are prone to icing up. For these reasons, we usually do not cool the trap chip below 20 K.

Thermal contact between the in-vacuum side of the cold plate and the pillbox is provided by a flexible copper band. During cooldown, the cryostat contracts by $\approx 0.9\,\mathrm{mm}$, which would lead to a large displacement of the pillbox if the two were rigidly connected. This would ruin the alignment with respect to laser beams and imaging system and would put significant strain on the legs supporting the pillbox. In the previous iteration, a copper braid was intended to prevent this, but we found that movement was larger than expected due to slight deficiencies with the original design. In the updated version, we instead make use of a thermal strap[51] consisting of 205 sheets of 25 µm-thick copper foil. It is mounted in such a way that it forms an S-shape between cold plate and pillbox, which ensures sufficient slack to counter thermal contraction.

Initial cooldown testing was carried out with liquid nitrogen, but in standard operation liquid helium acts as the coolant. We typically limit the rate of temperature changes to $2\,\mathrm{K\,min^{-1}}$ during cooldown and warmup. For the relevant experiments described in this thesis, two cooldowns were conducted on different days. However, for future operation we expect that the pillbox will be kept at cryogenic temperatures continuously, only warming up by a few tens of degrees during inactive periods to reduce helium consumption and when exchanging dewars.

[51] Custom part from Thermotive

3.5 Control software and electronics

We use ARTIQ (Advanced Real-Time Infrastructure for Quantum Physics) as the control software in our lab. It was developed to allow research groups to replace their in-house control systems, which would often be built ad-hoc and were thus limited in scope and hard to maintain, with a high-performance, versatile and scalable platform for the control of complex experiments. To that end, ARTIQ seamlessly combines the execution of code on normal PCs, which support a wide variety of hardware and software, with the execution of instructions on dedicated FPGAs and circuit boards, which are able to achieve nanosecond timing resolution and sub-microsecond latency. In the ARTIQ framework, experiments are described by programming scripts containing two types of instructions: normal Python code to be interpreted on a standard PC ("host") and ARTIQ kernels that are compiled for execution on an FPGA ("core device") connected to special-purpose peripherals. Several core devices can be chained together for parallel operation. A special "distributed real-time input and output" (DRTIO) protocol ensures that they are correctly synchronised and share a common timeline for events programmed through experiment scripts. Additionally, ARTIQ features the concept of controllers, which represent interfaces for controlling the operation of external devices reachable from the host (locally or via the network) such as piezo drivers, signal generators or power supplies.

3.5.1 Sinara hardware

For applications that require fine timing control and high-speed real-time processing, which includes most operations involving ions, we make use of the core device and peripheral extension boards connected to it in order to generate the desired signals. These circuit boards are part of the Sinara hardware ecosystem, which is a family of devices developed specifically for use with the ARTIQ control software. The following list contains brief descriptions of the main devices used in our apparatus, more information can be found in ref. [Sin22].

Kasli This is the core device in our ARTIQ setup, an FPGA carrier that implements

the DRTIO protocol and controls up to 12 peripheral devices connected as Eurocard extension modules (EEM). It determines the ultimate timing resolution in our experiments.

Urukul 4-channel 1 GS/s DDS frequency synthesiser board with an output frequency range of $<1\,\mathrm{MHz}$ to $\approx 400\,\mathrm{MHz}$. We use the version based on AD9910 chips, which offers control parameters for frequency (32 bits), phase (16 bits) and amplitude (14 bits), giving a resolution of 0.23 Hz in frequency, 0.005° in phase and 6×10^{-5} in amplitude scale factor. Each Urukul channel also contains an independent digital step attenuator to limit the maximum output power. All four output channels can be synchronised relative to each other and the Kasli master clock for deterministic phase control.

Sampler 8-channel ADC (LTC2320-16) board with 16-bit precision, an update rate of up to 1.5 MS/s (all channels simultaneously) and a bandwidth of up to 200 kHz. It includes programmable-gain instrumentation amplifiers (AD8253), leading to input voltage ranges from $\pm 10\,\mathrm{V}$ (with gain = 1) to $\pm 10\,\mathrm{mV}$ (with gain = 1000).

Fastino 32-channel DAC (AD5372) board with 16-bit precision and an update rate of 2.55 MS/s for all channels simultaneously. It offers an output voltage range of $\pm 10\,\mathrm{V}$.

Phaser 4-channel rf generator card with dual upconverter. Each channel supports up to 5 tones in gateware, which are converted to an analog signal using a 16-bit parallel DAC (DAC34H84) and then shifted to higher frequencies through a dual mixer (TRF372017). The frequency, amplitude and phase of each tone can be updated at a rate of 25 Ms/s, which enables the generation of complex pulse shapes.

A schematic overview of our experimental control system is contained in fig. 3.1. One Kasli acts as the master that sets the reference DRTIO timeline for all experiments. To ensure frequency and phase stability, we provide it with an input

clock signal from an external 10 MHz rubidium reference[52], which is multiplied to 125 MHz inside Kasli to generate its system clock. For the timing of output events, this clock is further multiplied to enable the production of timestamps at a rate of 1 GHz, resulting in a timing resolution of 1 ns. Other Kaslis are connected as satellites to this master via fibre-optic links and inherit clock and timeline from the master Kasli.

The main program, the ARTIQ master that is responsible for scheduling and running experiments and storing their results, runs on a dedicated computer. Any kernel code in experiment scripts is compiled on this PC and sent via Ethernet to the Kasli core devices. The master PC also controls the piezo drivers of the reference cavities and those of the steering mirrors on the trap table. Another machine, the control PC, is used for interaction with the ARTIQ master. It runs the ARTIQ dashboard, which is a graphical user interface that allows the user to submit experiments to the master and retrieve the corresponding results from it, offering plotting capabilities for immediate analysis. There are two additional computers worth mentioning. One PC hosts the server which broadcasts data from our optical diagnostics system, including the OSA traces and wavemeter measurements. Additionally, there is a general-purpose PC that is typically used for calibration and monitoring and runs, for example, software for the beam profiler or the EMCCD camera of the imaging system.

3.5.2 Trap rf signal

The initial signal is provided by a DDS channel of an Urukul card. However, the output is not connected to the baseflange of the vacuum chamber directly since we find that variations in the amplitude of the DDS output are large enough that they would lead to substantial fluctuations in the secular frequencies of the ions. Instead, the DDS signal is fed into an additional electronic circuit that we refer to as "squareatron", which contains a signal buffer[53] that converts the input sine wave into a digital logic-level signal of the same frequency. The amplitude of the

[52] FS725 from SRS
[53] LTC6957IDD-3 from Analog Devices

digital square wave is set by the supply voltage of the buffer chip, which is stabilised through a series of voltage regulators. A subsequent bandpass filter[54] attenuates higher harmonics, resulting in a sine wave of very stable amplitude. The schematic of the circuit can be found in ref. [Gro22]. After squareatron, the rf signal is fed into an rf amplifier[55] and subsequently into a toroidal resonator, which is attached to the bottom of the baseflange of the vacuum chamber. The resonator, described in ref. [Wol19], provides a voltage step-up by a factor of ≈ 15.

3.5.2.1 Temperature stabilisation

For the vast majority of experiments described in this work, none of the electronic components used in the generation of the rf trapping signal had their temperature actively stabilised. As discussed in sections 7.2.5.4 and 8.4.2, however, we found that for high-fidelity two-qubit gates to be realised in our trap, it will not be sufficient to rely on passive temperature stability. In preparation for high-fidelity gates, active stabilisation was therefore later added by housing squareatron and rf amplifier in a separate box, the temperature of which is regulated via thermoelectric elements. Additionally, we try to improve passive temperature stability of the rf resonator board attached to the baseflange of the vacuum chamber by wrapping it in insulating material. Restricted access to the rf resonator prevents us from installing an active stabilisation circuit there. The improved arrangement is described in more detail in ref. [Web22]. It was only used for the experiment presented in section 8.3.2.

3.5.3 Trap dc signals

A Fastino board generates the voltages applied to the dc electrodes. We find that the voltage range of $\pm 10\,\mathrm{V}$ which this device offers is sufficient to achieve the desired trapping parameters in our surface trap. Before being delivered into the vacuum chamber, all channels are filtered through common-mode chokes on a separate circuit board located in a screened box directly on the trap table.

[54] BPF-C45+ from Mini-Circuits
[55] ZHL-03-5WF+ from Mini-Circuits

3.5.4 Stabilisation of laser intensities ("noise-eating" system)

We use a noise-eating system to drive all AOMs on the AOM breadboards in order to reduce fluctuations in optical intensity at the ion, which are caused by several factors: noise in output power of the laser head, changes in fibre coupling efficiency due to vibrations and thermally induced deformation of components and drifts in the polarisation of light transmitted through fibres, which are converted to power fluctuations by polarisation-sensitive optical components. The noise-eater employs one Sampler and two Urukul boards in what is called SUServo configuration in ARTIQ. For each beam, the signal from the monitoring photodiode on the trap table is connected to one channel on Sampler and the AOM controlling the intensity of that beam to one channel on Urukul. When noise-eating is activated, the SUServo core on the Kasli FPGA reads the PD input and implements a digital IIR filter to feed back on the drive power of the AOM until the desired intensity setpoint is reached. Each servo channel offers several profiles with independent IIR states, which allows the intensity to be switched quickly between different levels without having to wait for the integrator to settle.

3.5.5 Microwave electronics

3.5.5.1 Standard setup

Our arrangement for the production of microwaves is a generalisation of the setup described in ref. [Wol19]. The four output channels of an Urukul card are grouped into two pairs, each of which is fed into a modulator. There each channel of a given pair is mixed with a local oscillator and the two channels are then summed, resulting in a single up-converted microwave tone if the phases and amplitudes of the input channels are chosen correctly. The output frequency of the tone is varied by changing the frequency of the corresponding pair of DDS output channels. The amplitudes and phases required to cancel the unwanted sideband have been calibrated individually for each modulator. When trying to generate signals that contain multiple frequencies with stable amplitudes, it is in general desirable to combine all tones before increasing signal power through a single amplifier. However, at the time when

most experiments described in this work were carried out, we did not yet have an amplifier available that would have been able to handle the microwave powers of 1 W and more per tone that we intended to use. We therefore instead send the outputs from the two independent modulators to separate amplifiers before combinining[56] the tones on a single microwave line, which connects through a circulator with the vacuum chamber. The circulator ensures that any power reflected from the trap chip that reaches the amplifiers is strongly attenuated so as to prevent reverse power from affecting operation of the amplifiers adversely. For all operations requiring a driving field with a single frequency component, only one microwave output channel is used.

3.5.5.2 Improved setup

The microwave power contained in one tone relative to the other is prone to drifts in the standard arrangement described in the previous subsection since separate DDS channels and amplifiers are involved. No active amplitude stabilisation had been set up for the experiments presented in this thesis. Consequently, the changing ac Zeeman shifts resulting from drifts in relative power limited the calibration of two-qubit gate parameters. For future work on high-fidelity gates, a different setup will therefore be used, in which the different microwave tones are generated directly within the same output channel of a Phaser board and only a single high-power microwave amplifier is included. Details can be found in ref. [Web22]. This arrangement, still without active stabilisation, was used for the experiment discussed in section 8.3.2.

[56] part 4033 from narda

Chapter 4

Motion of a single ion in a surface trap

Trapping a particle around a point in three-dimensional space requires a restoring force in all directions. For charged particles, the electromagnetic force presents itself as an obvious candidate. However, it is a basic fact that confinement cannot be achieved by a static electric field alone. This is sometimes called Earnshaw's theorem and is a straightforward consequence of the Maxwell equation $\nabla \cdot \mathbf{E} = 0$ in vacuum, where $\mathbf{E}$ denotes the electric field felt by the particle. Nevertheless, it turns out that one solution to this problem lies in the use of an inhomogeneous, oscillating electric field which, under suitable conditions, may give rise to a time-averaged effective confining force along all spatial axes. This insight forms the basis for the operation of Paul traps, which have enabled the study of atomic phenomena with unprecedented precision in the last few decades.

This chapter contains a thorough description of the motion of a single ion under the influence of the electric field generated by the electrodes in a surface trap. I start with a discussion of the classical equations of motion of a charged particle subjected to a combination of static and sinusoidally varying electric fields. This is followed by a treatment of the corresponding quantum mechanical expressions. In both descriptions I will at first set up the equations for the general case, in which motion along different spatial axes may be coupled, but subsequently restrict our

attention to the case when the motion is decoupled and provide the corresponding solution for the position of a particle as a function of time. I will treat homogeneous and inhomogeneous equations of motion. The latter applies when there are uncompensated static electric fields present at the trap centre.

It should be noted that motion of an ion in a Paul trap has been discussed by several authors [LBM+03; WMI+98]. Nevertheless, I find it worthwhile to present a thorough treatment here because the expressions obtained will be used repeatedly in later chapters. I will go into more detail than most reviews available in the literature, indicated for example by the fact that I include the quantum mechanical solution for excess micromotion.

In the last section I explain how the topics discussed relate to the operation of our surface trap. Whenever the derivation of a result is not directly included in this chapter, it can be found in appendix B or a reference is provided. I will not explicitly point the reader to the appendix in most instances, but instead stress at this point that mathematical details and additional information can be found there.

4.1 Classical description

In order to keep the motion of a particle as simple as possible, it is usually advantageous to apply forces that are linear functions of its coordinates. In the case of electric fields, this requires generating electric potentials that are purely quadratic in the coordinates, often referred to as quadrupole potentials. However, creation of a true quadrupole potential requires the use of electrodes that are hyperbolic in shape. While historically the first Paul traps were based on hyperbolic electrodes, modern traps use other electrode geometries, which offer advantages with regards to ease of fabrication, access of laser beams, possibility of ion transport and scalability. Underlying this development is the realisation that even if the electric potential generated in the trap is not purely quadratic, but instead also depends on higher powers of the coordinates, then as long as the distance of the particle from the trap centre remains small enough its motion will nevertheless be mainly determined by the quadratic terms. The potential can then be approximated as quadratic, assuming

the ion stays close enough to the trap centre. This consideration forms the basis for most modern ion traps, in particular surface traps, in which all trapping electrodes are arranged flat in planes and may sometimes even be stacked to form different layers.

I will consider a total electric potential $\Phi(\mathbf{x}, t)$ that is the sum of a static potential $\Phi_{\mathrm{dc}}(\mathbf{x})$ and an oscillating potential $\Phi_{\mathrm{rf}}(\mathbf{x}) \cos \omega_{\mathrm{rf}} t$. I denote the position of the desired trap centre by $\mathbf{x}_0$ and take it as the origin of the coordinate system, so $\mathbf{x}_0 = \mathbf{0}$. A Taylor expansion of the potential around this trap centre then leads to an expression for $\Phi(\mathbf{x}, t)$ as a function of the various powers of the coordinates x_i. I make the assumption, mentioned above, that the ion moves within such distances from $\mathbf{x}_0$ that the third-order terms $(1/6)\, k^{(3)}_{ijk}\, x_i x_j x_k$ and all higher-order terms, which take analogous forms, are small and can be neglected. The size of the spatial region over which this approximation holds is determined by the magnitude of the coefficients $k^{(n)}$ for $n \geq 3$ compared to $k^{(2)}$. I additionally assume that the gradient of the rf potential $\Phi_{\mathrm{rf}}(\mathbf{x}, t)$ vanishes at $\mathbf{x}_0$. However, I will not require the dc potential to fulfil this condition and thus allow for the possibility that the extrema of the rf and dc potentials may not coincide. Furthermore, I discard the constant terms $\Phi_{\mathrm{rf}}(\mathbf{x}_0)$ and $\Phi_{\mathrm{dc}}(\mathbf{x}_0)$ as they do not affect the resultant equations of motion.

Under these conditions, the overall electric potential can be written in the form

$$\Phi(\mathbf{x}, t) = \sum_i \frac{\partial \Phi_{\mathrm{dc}}}{\partial x_i}\Big|_{\mathbf{x}_0} x_i + \frac{1}{2} \sum_{i,j} \left(\frac{\partial^2 \Phi_{\mathrm{dc}}}{\partial x_i x_j}\Big|_{\mathbf{x}_0} + \frac{\partial^2 \Phi_{\mathrm{rf}}}{\partial x_i \partial x_j}\Big|_{\mathbf{x}_0} \cos \omega_{\mathrm{rf}} t \right) x_i x_j \ , \qquad (4.1)$$

for $i, j \in \{1, 2, 3\}$.

It follows that the motion of the centre of mass of a particle of mass m and charge Ze under the influence of the corresponding total electric field is described by

$$\frac{d^2 x_i(t)}{dt^2} + \frac{Ze}{m} \sum_j \left(\frac{\partial^2 \Phi_{\mathrm{dc}}}{\partial x_i \partial x_j}\Big|_{\mathbf{x}_0} + \frac{\partial^2 \Phi_{\mathrm{rf}}}{\partial x_i \partial x_j}\Big|_{\mathbf{x}_0} \cos \omega_{\mathrm{rf}} t \right) x_j(t) = -\frac{Ze}{m} \frac{\partial \Phi_{\mathrm{dc}}}{\partial x_i}\Big|_{\mathbf{x}_0} \ . \qquad (4.2)$$

The motion along different axes is coupled if the mixed derivatives $\partial^2_{x_i x_j} \Phi(\mathbf{x}_0)$ do not vanish. If one performs a change of variable to $\tau = \omega_{\mathrm{rf}} t/2$ and introduces two

matrices A, Q and a vector $\mathbf{s}$ with components

$$A_{ij} = \frac{4Ze}{m\omega_{\mathrm{rf}}^2} \frac{\partial^2 \Phi_{\mathrm{dc}}}{\partial x_i \partial x_j}\Big|_{\mathbf{x}_0} \tag{4.3}$$

$$Q_{ij} = -\frac{2Ze}{m\omega_{\mathrm{rf}}^2} \frac{\partial^2 \Phi_{\mathrm{rf}}}{\partial x_i \partial x_j}\Big|_{\mathbf{x}_0} \tag{4.4}$$

$$s_i = -\frac{4Ze}{m\omega_{\mathrm{rf}}^2} \frac{\partial \Phi_{\mathrm{dc}}}{\partial x_i}\Big|_{\mathbf{x}_0} , \tag{4.5}$$

then the equation of motion can be written in matrix form as

$$\frac{d^2\mathbf{x}(\tau)}{d\tau^2} + (A - 2Q\cos 2\tau)\ \mathbf{x}(\tau) = \mathbf{s} . \tag{4.6}$$

This may be recognised as the canonical form of inhomogeneous coupled Mathieu equations. There is a substantial literature on the Mathieu equation, ranging from treatments from a general mathematical point of view [Chi06] to descriptions of the main features relevant for ion trapping [Gho95]. I have included a brief overview of solutions to the Mathieu equation in appendix B.

The matrices A and Q depend on the electric potentials generated by the trap electrodes. In free space, these potentials have to satisfy Laplace's equation, which leads to the relations $\mathrm{tr}\, A = 0$ and $\mathrm{tr}\, Q = 0$, where tr denotes the trace of a matrix. Certain trap geometries or combinations of voltages applied to the electrodes may cause some of the off-diagonal elements of these matrices to vanish because of symmetry constraints. In that case, the relevant matrix does not couple motion along the corresponding coordinate axes. While this situation often occurs in practice, I will keep the treatment general and will not assume that any of the elements of A or Q are zero.

In preparation for the quantum mechanical description presented further down, I note that the equation of motion (4.2) can be derived from a classical Hamiltonian of the general form

$$H(t) = \sum_i \frac{p_i^2}{2m} + \frac{m}{2} \sum_{i,j} W_{ij}(t)\, x_i x_j - \sum_i f_i(t)\, x_i , \tag{4.7}$$

with time-dependent symmetric matrix $W_{ij}(t)$ and vector $\mathbf{f}(t)$. The latter may be

considered to represent a time-dependent driving force. In our case, this force arises from the gradient of the dc potential at $\mathbf{x}_0$ and is therefore time-independent. One finds

$$W(t) = \frac{\omega_{\mathrm{rf}}^2}{4}\left(A - 2Q\cos\omega_{\mathrm{rf}}t\right) \tag{4.8}$$

$$\mathbf{f} = \frac{m\omega_{\mathrm{rf}}^2}{4}\,\mathbf{s} \tag{4.9}$$

in terms of the quantities A, Q and $\mathbf{s}$ introduced earlier. The classical equation of motion resulting from the general Hamiltonian is given by

$$\frac{d^2\mathbf{x}(t)}{dt^2} + W(t)\,\mathbf{x}(t) = \mathbf{f}(t)/m\ . \tag{4.10}$$

This equation may be regarded as describing the dynamics of a driven harmonic oscillator with time-dependent natural frequency.

In the following sections I discuss the solutions to the classical equation of motion (4.2) describing a charged particle in a Paul trap. Two cases may be distinguished: if A and Q commute, one may find a set of eigenvectors common to both matrices. In the basis formed by these eigenvectors, both A and Q are simultaneously diagonal, with elements a_i and q_i. The eigenvectors thus correspond to a set of three principal axes, labelled by i, along which the motion decouples. Conversely, if A and Q do not commute, the principal axes of dc and rf potentials differ and motion in three-dimensional space is strictly coupled. I do not consider this general case here, the reader is referred to [LDR+12] for details. Instead, I make the simplifying assumption that approximate solutions to the equations of motion may be obtained by treating the motion as decoupled. Specifically, A and Q are replaced with the diagonal matrices that result when each is diagonalised separately and adopt the coordinate system defined by the eigenvectors of the dc potential. This approximation has been investigated before and found to be valid in many situations [SO12]. One may expect it to be accurate when the mismatch between principal axes of rf and dc potentials is small, as is the case in our surface trap.

4.1.1 Homogeneous case

When A and Q are diagonal, the dynamics along each axis may be treated independently and are described by

$$\frac{d^2x_i(\tau)}{d\tau^2} + (a_i - 2q_i\cos 2\tau)\; x_i(\tau) = 0\;. \tag{4.11}$$

I am considering the homogeneous case $s_i = 0$ for now since it forms the basis for the treatment of the inhomogeneous case. For ease of notation, I will drop the subscript i in the following and consider one-dimensional motion along a particular axis, using $x(t)$ for the position of the particle. The complete three-dimensional motion is constructed by combining this with the solutions for the other axes, which are treated in exactly the same way, but with different a_i and q_i in general.

A set of two linearly independent solutions to the decoupled Mathieu equation (4.11), in terms of the original variable t, is given by

$$u_1(t) = \mathrm{e}^{\mathrm{i}\nu t}\sum_{n\in\mathbb{Z}} c_{2n}\,\mathrm{e}^{\mathrm{i}n\omega_{\mathrm{rf}}t} \tag{4.12}$$

$$u_2(t) = \mathrm{e}^{-\mathrm{i}\nu t}\sum_{n\in\mathbb{Z}} c_{2n}\,\mathrm{e}^{-\mathrm{i}n\omega_{\mathrm{rf}}t}\;. \tag{4.13}$$

The quantity ν, called the secular frequency, is a function of a and q and thus depends on the electric potentials in the trap. In particular, ν has to be real for the motion of the particle to be bounded and it is found that only certain regions in the parameter space spanned by a and q result in real ν. Trapping a particle thus requires operating the trap with parameters that lie in such a stability region. I stress that ν denotes an angular frequency. The real coefficients c_{2n} are the same for both $u_1(t)$ and $u_2(t)$. The ratios c_{2n}/c_{2n-2} of successive coefficients are fixed for given values of a and q, but the overall normalisation $\sum_n c_{2n}$ can be chosen freely. Unless explicitly stated otherwise, I will not assume any particular choice of normalisation.

The general solution to the decoupled Mathieu equation (4.11) is obtained as a

suitable linear combination of the two basis solutions and may be written

$$x(t) = \sigma \sum_{n\in\mathbb{Z}} c_{2n} \cos\left[(\nu + n\omega_{\mathrm{rf}})\, t + \phi\right] \ . \tag{4.14}$$

The constants σ and ϕ depend on initial conditions. In almost all ion trapping experiments – in particular, our surface trap – the voltages applied to the trap electrodes are chosen to give parameters a and q that are small, in which case $\nu \ll \omega_{\mathrm{rf}}$ and the c_{2n} decrease quickly with $|n|$. The term varying as $\cos \nu t$ then dominates, representing a relatively slow oscillation of the particle around the trap centre, which is called the secular motion. The higher frequencies $\nu + n\omega_{\mathrm{rf}}$ correspond to faster oscillations with smaller amplitude, which are collectively referred to as micromotion.

For $|a|,\ q^2 \ll 1$, which holds in our and most other traps, it is found that the motion can be approximated by neglecting terms with $|n| > 1$. The coefficients in this lowest-order approximation are given by $c_{\pm 2} \simeq -(q/4)\, c_0$ and $c_{2n} \simeq 0$ for $|n| > 1$. Micromotion then occurs only at the frequencies $\omega_{\mathrm{rf}} \pm \nu$ and the position varies as

$$x(t) = r\cos(\nu t + \phi)\left(1 - \frac{q}{2}\cos\omega_{\mathrm{rf}} t\right) \ , \tag{4.15}$$

where the amplitude r and phase ϕ depend on conditions at $t = 0$. It is clear from this expression that the absolute magnitude $rq/2$ of micromotion oscillations in the homogeneous case is tied to the amplitude r of the secular motion. This type of micromotion is therefore called intrinsic micromotion. It cannot be avoided for a particle moving in the trap and can only be reduced by decreasing the secular amplitude.

4.1.2 Inhomogeneous case

If the gradient of the total electric potential does not vanish at the trap centre, the equation of motion takes the form of the inhomogeneous Mathieu equation

$$\frac{d^2 x_i(\tau)}{d\tau^2} + (a_i - 2q_i \cos 2\tau)\ x_i(\tau) = s_i \ . \tag{4.16}$$

Non-zero s_i may arise from stray static background fields at the intended trap centre that are outside experimental control. It may also come from imperfections in the geometry of the dc electrodes themselves, which may cause a spatially uniform field to be present at the trap centre even though none would be expected for ideal shapes of the electrodes. Regardless of the underlying reason, inclusion of this term can also just be based on empirical observation of its effects on the motion of the particle, as will be explained shortly.

In deriving an expression for the total potential $\Phi(\mathbf{x}, t)$ earlier, I assumed that the rf potential had a true extremum at $\mathbf{x}_0$. This meant that $\mathbf{s}$ was time-independent and only arose from the gradient of the dc potential. More generally, the rf potential may also contain a term linear in x_i, which leads to a time-varying contribution to $\mathbf{s}$. This can be caused, for example, by a phase difference between the oscillating voltages on the rf electrodes [BMB+98]. While a time-dependent $\mathbf{s}(t)$ could be included in the treatment of the inhomogenous case with only minor modifications, I will not explore this possibility in the following. We expect any phase difference to be negligible in our trap since the two rf rails in the trapping region are highly symmetric and derived from a common rf electrode. The latter splits into two only very close to the trap centre, which means that any difference in impedance between the two rf prongs that could result in a phase difference should be vanishingly small.

I will again omit the label i in what follows. Equipped with the linearly independent solutions $u_1(t)$ and $u_2(t)$ to the homogeneous case, one may construct a particular solution to the inhomogeneous equation by the method of variation of constants. This gives

$$\tilde{u}_\mathrm{p}(t) = -u_1(t) \int \frac{u_2(t)}{u_1(t)\dot{u}_2(t) - \dot{u}_1(t)u_2(t)} \frac{\omega_\mathrm{rf}^2}{4}\, s\, dt + u_2(t) \int \frac{u_1(t)}{u_1(t)\dot{u}_2(t) - \dot{u}_1(t)u_2(t)} \frac{\omega_\mathrm{rf}^2}{4}\, s\, dt\ . \tag{4.17}$$

The quantity $u_1(t)\dot{u}_2(t) - u_2(t)\dot{u}_1(t)$ may be shown to be constant in the case of the Mathieu equation and therefore equals its value at $t = 0$ at all times. One thus

obtains

$$\tilde{u}_{\mathrm{p}}(t) = \frac{\omega_{\mathrm{rf}}^2}{4} \frac{s}{u_1(0)\dot{u}_2(0) - \dot{u}_1(0)u_2(0)} \left[-u_1(t) \int u_2(t)\, dt + u_2(t) \int u_1(t)\, dt \right] . \tag{4.18}$$

Inserting the explicit expressions for $u_1(t)$ and $u_2(t)$ from eq. (4.12) results in

$$\tilde{u}_{\mathrm{p}}(t) = \frac{1}{4} \frac{s}{\sum\limits_{m,n\in\mathbb{Z}} c_{2m}c_{2n}(\nu/\omega_{\mathrm{rf}} + n)} \left(\sum_{m,n\in\mathbb{Z}} \frac{c_{2m}c_{2n}}{\nu/\omega_{\mathrm{rf}} + n} \cos\left[(m-n)\omega_{\mathrm{rf}}t\right] \right) . \tag{4.19}$$

It is important to note that this particular solution $\tilde{u}_{\mathrm{p}}(t)$ is periodic, with the same period $T = 2\pi/\omega_{\mathrm{rf}}$ as the applied rf field.

The general solution to eq. (4.16) is obtained by adding the general solution of the homogeneous equation to $\tilde{u}_{\mathrm{p}}(t)$ and may be written

$$\tilde{x}(t) = \tilde{u}_{\mathrm{p}}(t) + \tilde{\sigma} \sum_{n\in\mathbb{Z}} c_{2n} \cos\left[(\nu + n\omega_{\mathrm{rf}})\, t + \tilde{\phi} \right] . \tag{4.20}$$

The constants $\tilde{\sigma}$ and $\tilde{\phi}$ are again fixed by initial conditions. While the effects of the inhomogenous term resulting from the presence of an uncompensated dc electric field may already be inferred from this expression, they become more apparent in the lowest-order approximation. As before, when $|a|, q^2 \ll 1$, one may use the approximate values $c_{\pm 2} \simeq -(q/4)\, c_0$ and $c_{2n} \simeq 0$ for $|n| > 1$. Inserting these in eqs. (4.19) and (4.20) results in

$$\tilde{x}(t) \approx \left[r_0 \cos(\nu t + \tilde{\phi}) + r_1 \right] \left(1 - \frac{q}{2} \cos \omega_{\mathrm{rf}} t \right) , \tag{4.21}$$

where the secular amplitude r_0 depends on initial conditions and

$$r_1 = \frac{s\, \omega_{\mathrm{rf}}^2}{4\nu^2(1-q)} = \frac{ZeE_{\mathrm{emm}}}{m\nu^2(1-q)} . \tag{4.22}$$

The quantity $E_{\mathrm{emm}} = -\partial_{x_i} \Phi_{\mathrm{dc}}(\mathbf{x}_0)$ is the electric field at the intended trap centre $\mathbf{x}_0$, arising from the gradient term of the dc potential along the direction considered. It should be noted that, apart from the factor $1 - q$ in the denominator of r_1, the expression for $\tilde{x}(t)$ obtained here coincides with that given in ref. [BMB+98], which

was derived in the pseudopotential approximation. The first term within the square brackets in eq. (4.21), when multiplied with the factor on the right, represents the usual combination of secular motion and intrinsic micromotion also present in the homogeneous case. It is centred on the position $x = 0$ of the nominal trap centre. However, the second term in the square brackets arises from the uncompensated electric field E_{emm} and, in combination with the factor on the right, causes micromotion oscillations at the rf frequency around the position $x = r_1$. Overall, it is thus seen that the field E_{emm} shifts the average position of the particle away from the intended trap centre and induces additional micromotion. This kind of micromotion is called excess micromotion because it is absent when there are no uncompensated electric fields. It is usually undesired as it may have several negative effects (see section 7.2.6). Fortunately, excess micromotion can be eliminated by modifying the voltages applied to the trap electrodes so as to cancel the unwanted electric field E_{emm}.

4.2 Quantum description

The transition to a quantum mechanical description is as usual made by promoting the classical dynamical variables $\mathbf{x}$ and $\mathbf{p}$ describing the centre-of-mass motion to operators in the appropriate Hilbert space. The Hamiltonian in the Schrödinger picture is then given by

$$H_{\mathrm{mot}}^{(\mathrm{S})}(t) = \sum_{i=1}^{3} \frac{\left(p_i^{(\mathrm{S})}\right)^2}{2m} + \frac{m}{2} \sum_{i=1}^{3} \sum_{j=1}^{3} W_{ij}(t)\, x_i^{(\mathrm{S})} x_j^{(\mathrm{S})} - \sum_{i=1}^{3} f_i(t)\, x_i^{(\mathrm{S})} \,, \tag{4.23}$$

where $x_i^{(\mathrm{S})}$ and $p_i^{(\mathrm{S})}$ are the time-independent position and momentum operators in that picture. Letting $|\psi(t)\rangle^{(\mathrm{S})}$ denote the state vector corresponding to the centre-of-mass motion in the Schrödinger picture, then its evolution from some initial time t_0 to later time t is determined by the time-evolution operator $U_{\mathrm{mot}}(t;t_0)$ through $|\psi(t)\rangle^{(\mathrm{S})} = U_{\mathrm{mot}}(t;t_0)\,|\psi(t_0)\rangle^{(\mathrm{S})}$. The operator $U_{\mathrm{mot}}(t;t_0)$ is the solution to the equation

$$\mathrm{i}\hbar \frac{dU_{\mathrm{mot}}(t;t_0)}{dt} = H_{\mathrm{mot}}^{(\mathrm{S})} U_{\mathrm{mot}}(t;t_0), \qquad U_{\mathrm{mot}}(t_0;t_0) = \mathbb{I}\,. \tag{4.24}$$

I will, without loss of generality, take $t_0 = 0$ from now on and use $U_{\rm mot}(t)$ as shorthand for $U_{\rm mot}(t;0)$. I am not including an explicit superscript on $U_{\rm mot}(t)$ because the time-evolution operator in the Schrödinger picture is the only one that I will be considering here.

While it is in principle possible to solve for $|\psi(t)\rangle^{(\rm S)}$ in the Schrödinger representation, it turns out that a treatment in terms of the Heisenberg picture is more convenient for the time-dependent Hamiltonian considered here. I will be explicit about which picture is being referred to by writing $A^{(\rm S)}(t)$ for an operator in the Schrödinger picture and $A^{(\rm H)}(t)$ for the corresponding operator in the Heisenberg picture. The former, being in general a function of the time-independent operators $x_i^{(\rm S)}$ and $p_i^{(\rm S)}$, may still have time dependence since any coefficients multiplying $x_i^{(\rm S)}$ and $p_i^{(\rm S)}$ may be functions of time. Operators in the two pictures are related through $A^{(\rm H)}(t) = U^\dagger(t) A^{(\rm S)}(t) U(t)$ and the time evolution of an operator in the Heisenberg picture is given by

$$\frac{dA^{(\rm H)}(t)}{dt} = -\frac{\rm i}{\hbar}\left[A^{(\rm H)}(t), H^{(\rm H)}(t)\right] + U^\dagger(t)\frac{\partial A^{(\rm S)}(t)}{\partial t}U(t)\ . \tag{4.25}$$

I therefore introduce the transformations

$$x_i^{(\rm H)}(t) = U_{\rm mot}^\dagger(t) x_i^{(\rm S)} U_{\rm mot}(t) \tag{4.26}$$

$$p_i^{(\rm H)}(t) = U_{\rm mot}^\dagger(t) p_i^{(\rm S)} U_{\rm mot}(t) \tag{4.27}$$

and, using eq. (4.25), find that the position operators $x_i^{(\rm H)}(t)$ have to satisfy

$$\frac{d^2 x_i^{(\rm H)}(t)}{dt^2} + \sum_j W_{ij}(t)\, x_j^{(\rm H)}(t) = f_i(t)/m\ , \tag{4.28}$$

subject to the initial conditions $x_i^{(\rm H)}(0) = x_i^{(\rm S)}$ and $dx_i^{(\rm H)}/dt(0) = p_i^{(\rm S)}/m$. The form of this equation is exactly the same as that of its classical analogue eq. (4.10), but $x_i^{(\rm H)}(t)$ here describe operators rather than functions.

The treatment in the following is based on the elegant approach by Glauber [Gla92], which I extend to cover the case when the equation of motion for a particle

in a Paul trap contains a constant inhomogeneous term.

4.2.1 Homogeneous case

If the matrix $W_{ij}(t)$ can be diagonalised, one obtains decoupled equations of motion along three principal axes in the same way as in the classical case[1]. Letting $w_i(t)$ denote the elements of $W(t)$ in the basis in which it is diagonal, one finds

$$\frac{d^2 x_i^{(\mathrm{H})}(t)}{dt^2} + w_i(t)\, x_i^{(\mathrm{H})}(t) = 0 \; . \tag{4.29}$$

The variables $x_i^{(\mathrm{H})}(t)$ then represent the position operators along the principal axes. I will again omit the label i in the following.

Let $u_a(t)$ and $u_b(t)$ be two arbitrary solutions to the classical equation

$$\ddot{x} + w(t)\, x = 0 \tag{4.30}$$

corresponding to eq. (4.29). Then one may verify that they obey the identity

$$u_a(t)\dot{u}_b(t) - \dot{u}_a(t)u_b(t) = \text{constant} \; . \tag{4.31}$$

Since the equations for the classical and quantum variables take the same form, one might expect that the above relation also holds for a combination of classical and quantum-mechanical solutions $u(t)$ and $x^{(\mathrm{H})}(t)$. One may thus be led to form the operator

$$C^{(\mathrm{H})}(t) = \frac{\mathrm{i}}{\sqrt{2m\hbar\omega_{\mathrm{r}}}} \left[u(t)\, p^{(\mathrm{H})}(t) - m\dot{u}(t)\, x^{(\mathrm{H})}(t) \right] \; , \tag{4.32}$$

where $u(t)$ is any solution to the classical equation and ω_{r} is a real constant that is otherwise unspecified at this point. When this operator $C^{(\mathrm{H})}(t)$ is inserted into the Heisenberg evolution equation (4.25), one finds indeed that $dC^{(\mathrm{H})}(t)/dt = 0$, whence it follows that $C^{(\mathrm{H})}(t)$ is a constant operator in the Heisenberg picture and

$$C^{(\mathrm{H})}(t) = C^{(\mathrm{H})}(0) = \frac{\mathrm{i}}{\sqrt{2m\hbar\omega_{\mathrm{r}}}} \left[u(0)\, p^{(\mathrm{H})}(0) - m\dot{u}(0)\, x^{(\mathrm{H})}(0) \right] \; . \tag{4.33}$$

[1] If W is not diagonalisable because A and Q do not commute, one invokes the same approximation as in the classical description presented earlier to replace A and Q with diagonal matrices.

The solution $u(t)$ has so far been arbitrary, but inspection of the above equation shows that a specific choice for $u(t)$ may lead to simplifications for $C^{(\mathrm{H})}(t)$. In particular, taking $u(t)$ such that it satisfies the initial conditions $u(0) = 1$ and $\dot{u}(0) = \mathrm{i}\omega_\mathrm{r}$ and furthermore noting that $p^{(\mathrm{H})}(0) = p^{(\mathrm{S})}$ and $x^{(\mathrm{H})}(0) = x^{(\mathrm{S})}$, one finds that

$$C^{(\mathrm{H})}(t) = \sqrt{\frac{m\omega_\mathrm{r}}{2\hbar}} \left(x^{(\mathrm{S})} + \frac{\mathrm{i}}{m\omega_\mathrm{r}} p^{(\mathrm{S})} \right) . \tag{4.34}$$

This may be recognised as the annihilation operator $a = a^{(\mathrm{S})}$ for a reference harmonic oscillator with mass m and frequency ω_r. The particular value of ω_r is still arbitrary at this point, but its choice determines which harmonic oscillator is used as the reference. One therefore arrives at the relations

$$C^{(\mathrm{H})}(t) = a \tag{4.35}$$

$$C^{(\mathrm{H})\dagger}(t) = a^\dagger . \tag{4.36}$$

By combining expressions (4.32) and (4.35), an explicit solution for the position operator in the Heisenberg picture may now be obtained in the form

$$x^{(\mathrm{H})}(t) = -\mathrm{i}\sqrt{\frac{2\hbar\omega_\mathrm{r}}{m}} \frac{u(t)\, a^\dagger + u^*(t)\, a}{u(t)\dot{u}^*(t) - \dot{u}(t)u^*(t)} . \tag{4.37}$$

Since $w(t)$ is real, it follows that if $u(t)$ is a solution to (4.30), so is $u^*(t)$. This means that eq. (4.31) applies to the denominator in the expression above and taking into account the initial conditions for $u(t)$ one finds that $u(0)\dot{u}^*(0) - \dot{u}(0)u^*(0) = -2\mathrm{i}\omega_\mathrm{r}$. Therefore

$$x^{(\mathrm{H})}(t) = \sqrt{\frac{\hbar}{2m\omega_\mathrm{r}}} \left[u(t)\, a^\dagger + u^*(t)\, a \right] . \tag{4.38}$$

It follows that once the classical solution $u(t)$ satisfying $u(0) = 1$ and $\dot{u}(0) = \mathrm{i}\omega_\mathrm{r}$ has been found, the solution for the operator $x^{(\mathrm{H})}(t)$ can immediately be constructed.

No particular functional dependence has so far been assumed for $w(t)$. However, I will now specialise to the decoupled Mathieu equation relevant for ion trapping, for which $w(t)$ is periodic and $w(t) = \left(\omega_\mathrm{rf}^2/4\right)(a - 2q\cos\omega_\mathrm{rf} t)$. The corresponding classical equation was discussed in section 4.1.1, where a set of Floquet solutions

$u_1(t)$ and $u_2(t)$ was presented in eq. (4.12) that may be used as a basis to form arbitrary solutions. The classical solution $u(t)$ used in the construction of $x^{(\mathrm{H})}(t)$ can thus be written $u(t) = k_1 u_1(t) + k_2 u_2(t)$ for some constants k_1, k_2. I will now assume that the Floquet solutions have been normalised such that $u_1(0) = u_2(0) = 1$, which requires $\sum_n c_{2n} = 1$. Noting that $\dot{u}_1(0) = -\dot{u}_2(0)$, the initial conditions on $u(t)$ introduced earlier translate to

$$u(0) = k_1 + k_2 = 1 \tag{4.39}$$

$$\dot{u}(0) = (k_1 - k_2)\, \dot{u}_1(0) = \mathrm{i}\omega_{\mathrm{r}} \, . \tag{4.40}$$

This makes it evident that it is possible to reduce $u(t)$ to one of the Floquet solutions by a certain choice of ω_{r}. If one takes $\omega_{\mathrm{r}} = -\mathrm{i}\dot{u}_1(0)$, then it follows that $u(t) = u_1(t)$, resulting in a relatively simple function for $u(t)$. From the explicit expression for $u_1(t)$ in (4.12), it can be seen that this choice requires

$$\omega_{\mathrm{r}} = \sum_{n\in\mathbb{Z}} c_{2n} \left(\nu + n\omega_{\mathrm{rf}}\right) \, . \tag{4.41}$$

I should point out that the frequency ω_{r} of the reference harmonic oscillator is in general not quite the same as the secular frequency ν, but rather contains contributions from micromotion frequencies. However, if the lowest-order approximation for $u_1(t)$ that was introduced in section 4.1.1 holds, then one finds

$$\omega_{\mathrm{r}} \simeq c_{-2} \left(\nu - \omega_{\mathrm{rf}}\right) + c_0 \nu + c_2 \left(\nu + \omega_{\mathrm{rf}}\right) = c_0 \left(1 - \frac{q}{2}\right) \nu \, . \tag{4.42}$$

It is worth noting that in this approximation, the initial condition $\sum_n c_{2n} = 1$ translates to $c_0 \left(1 - q/2\right) = 1$. Inserting this in the expression above, one sees that $\omega_{\mathrm{r}} \simeq \nu$, which means that in the lowest-order approximation the frequency of the reference oscillator coincides with the secular frequency.

In conclusion, the solution for $x^{(\mathrm{H})}(t)$ that I will be using in later sections is given by eq. (4.38) in the homogeneous case, where the function $u(t)$ is the classical solution $u_1(t)$ to the Mathieu equation contained in (4.12).

4.2.2 Inhomogeneous case

In the presence of an external driving force, the Heisenberg evolution equation for the position operator becomes

$$\frac{d^2 x_i^{(\mathrm{H})}(t)}{dt^2} + w_i(t)\, x_i^{(\mathrm{H})}(t) = f_i(t)/m \; . \tag{4.43}$$

It is then found that the operator $C^{(\mathrm{H})}(t)$ used in the homogeneous case and defined in (4.32) is no longer a constant operator, but rather changes with time according to

$$\frac{dC^{(\mathrm{H})}(t)}{dt} = \frac{\mathrm{i}}{\sqrt{2\hbar m\omega_{\mathrm{r}}}}\, u(t) f(t) \; . \tag{4.44}$$

However, this suggests that a different constant operator $C'^{(\mathrm{H})}(t)$ may be introduced for the inhomogeneous case, given by

$$C'^{(\mathrm{H})}(t) = C^{(\mathrm{H})}(t) - \frac{\mathrm{i}}{\sqrt{2\hbar m\omega_{\mathrm{r}}}} \int_0^t u(s) f(s)\, ds \; . \tag{4.45}$$

This operator satisfies $dC'^{(\mathrm{H})}(t)/dt = 0$ with $C'^{(\mathrm{H})}(0) = C^{(\mathrm{H})}(0) = a$ so that one finds $C'^{(\mathrm{H})}(t) = a$. The solution $\tilde{x}^{(\mathrm{H})}(t)$ for the position operator in the inhomogeneous case may therefore be expressed as

$$\tilde{x}^{(\mathrm{H})}(t) = \sqrt{\frac{\hbar}{2m\omega_{\mathrm{r}}}} \left[u(t)\, a^\dagger + u^*(t)\, a \right] + \frac{\mathrm{i}}{2\omega_{\mathrm{r}}} \left[-u(t) \int_0^t u^*(s) f(s)\, ds + u^*(t) \int_0^t u(s) f(s)\, ds \right] \; . \tag{4.46}$$

The above equation holds for any solution $u(t)$ to the classical equation (4.30) subject to $u(0) = 1$ and $\dot{u}(0) = \mathrm{i}\omega_{\mathrm{r}}$ and arbitrary $f(t)$. I now specialise to motion in a trap in the presence of an uncompensated static electric field and thus $w(t) = \left(\omega_{\mathrm{rf}}^2/4\right)(a - 2q\cos\omega_{\mathrm{rf}} t)$ and $f(t) = \left(m\omega_{\mathrm{rf}}^2/4\right) s$. I make the particular choice $u(t) = u_1(t)$ with the normalisation $u_1(0) = 1$ and set the reference frequency such that $\dot{u}_1(0) = \mathrm{i}\omega_{\mathrm{r}}$. It follows that with this choice $u^*(t) = u_2(t)$. Denoting

$g(t) = \int u_1(t)\,dt$, one obtains

$$\tilde{x}^{(\mathrm{H})}(t) = \sqrt{\frac{\hbar}{2m\omega_\mathrm{r}}}\left(u_1(t)\left[a^\dagger + \frac{\mathrm{i}}{\sqrt{2\hbar m\omega_\mathrm{r}}}\frac{\omega_\mathrm{rf}^2}{4}s\,g^*(0)\right] + u_2(t)\left[a - \frac{\mathrm{i}}{\sqrt{2\hbar m\omega_\mathrm{r}}}\frac{\omega_\mathrm{rf}^2}{4}s\,g(0)\right]\right) + \frac{\omega_\mathrm{rf}^2}{4}s\,\frac{1}{(-2i\omega_\mathrm{r})}\left[-u_1(t)\int u_2(t)\,dt + u_2(t)\int u_1(t)\,dt\right]\,. \tag{4.48}$$

I now define $\kappa = -\mathrm{i}\omega_\mathrm{rf}^2\,s\,g(0)/\left(4\sqrt{2\hbar m\omega_\mathrm{r}}\right)$ and introduce

$$b = a + \kappa \tag{4.49}$$

$$b^\dagger = a^\dagger + \kappa^*\,. \tag{4.50}$$

These operators satisfy the commutation relation $[b, b^\dagger] = \mathbb{I}$ and therefore form ladder operators of a harmonic oscillator. They differ, however, from the operators a and $a^\dagger$ that occur in the homogeneous case. I note that a similar expression for $\tilde{x}^{(\mathrm{H})}(t)$ has been presented in [BSM+17]. However, the authors of that paper seem to have discarded the boundary term $g(0)$ of the integral and consequently did not distinguish between the ladder operators a and b.

By comparison with eq. (4.18), it is seen that when the initial conditions imposed on $u_1(t)$ are taken into account, the last term in the expression for $\tilde{x}^{(\mathrm{H})}(t)$ is just the particular solution $\tilde{u}_\mathrm{p}(t)$ of the classical inhomogeneous equation. One can therefore write the position operator in the form

$$\tilde{x}^{(\mathrm{H})}(t) = \sqrt{\frac{\hbar}{2m\omega_\mathrm{r}}}\left[u_1(t)\,b^\dagger + u_2(t)\,b\right] + \tilde{u}_\mathrm{p}(t)\,\mathbb{I}\,. \tag{4.51}$$

The solution $\tilde{x}^{(\mathrm{H})}(t)$ for the inhomogeneous case consists of two terms. The first involves ladder operators b and $b^\dagger$ and thus corresponds to the quantised motion under the influence of the trapping potential. It includes secular motion and intrinsic micromotion, with amplitude dependent on the oscillator state $|n\rangle$ of the particle. The second part, containing the identity operator, results from the driving force and corresponds to motion that is independent of $|n\rangle$. This term describes the shift of the average position away from the rf null and also excess micromotion.

4.3 Pseudopotential approximation

I explained in the previous sections that under the trapping conditions $|a|, q^2 \ll 1$ used in our experiments, the motion of the ion along a given spatial axis may be approximated to consist of secular motion of frequency ν, onto which micromotion with smaller amplitude is superposed, see for example eq. (4.15). The ratio of micromotion and secular components is determined by the ratio of the Mathieu coefficients $c_{\pm 2}/c_0$, which is $-q/4 \ll 1$ in the lowest-order approximation. This suggests that an even cruder approximation, in which micromotion is neglected completely and only the secular term retained, may be used. Considering for convenience the decoupled case, the motion of the ion is then the same as would result from a pure harmonic oscillator potential of natural frequency $\nu = (\omega_{\mathrm{rf}}/2)\sqrt{a + q^2/2}$. This is called the *pseudopotential approximation*. For many purposes, such a treatment is sufficient and effects caused by micromotion only give small corrections. I will make use of this approximation at several points in subsequent chapters.

The pseudopotential approximation may also be introduced in a different way by starting from the classical equations of motion and making certain assumptions about the resulting solutions [Deh68]. It is then found that motion in a pure rf potential $\Phi_{\mathrm{rf}}(\mathbf{x}) \cos \omega_{\mathrm{rf}} t$ can be derived from an effective pseudopotential energy

$$V_{\mathrm{ps}}(\mathbf{x}) = \frac{Z^2 e^2}{4 m \omega_{\mathrm{rf}}^2} \left| \nabla \Phi_{\mathrm{rf}}(\mathbf{x}) \right|^2 . \tag{4.52}$$

This expression is useful for the approximate description of electric fields used in trapping. It also allows us to obtain an estimate for the trap depth, which I regard as the minimum kinetic energy a particle needs to have at $\mathbf{x}_0$ to escape the trap. For the fictitious case of a purely quadratic rf potential with sharp drop to zero at some distance from the trap centre, the trap depth would be easy to calculate. The electric potentials realised in practice, however, contain higher-order terms that start to become important when the distance of the particle from the trap centre is sufficiently large, resulting in non-linear equations of motion. The trap depth could then in principle be estimated by Monte Carlo simulations that start the particle off with different initial velocities. More crudely, one could take the description in

terms of the pseudopotential energy to hold even in regions where $\nabla\Phi_{\mathrm{rf}}(\mathbf{x})$ is not linear in the coordinates. The potential energy $V_{\mathrm{ps}}(\mathbf{x})$ may then contain at least one local maximum or saddle point beyond which the particle is no longer confined. The value of V_{ps} at the position of the lowest such point can be taken as an estimate of the trap depth.

4.4 Operation of our surface trap

4.4.1 Trap geometry

I will now apply the results of the preceding sections to our surface trap. Figure 4.1 contains a schematic picture of the central region of the trap chip. The gaps that separate electrodes in the physical trap have been omitted and instead the electrodes extended symmetrically to fill the plane. The rf electrode, to which the oscillating voltage is applied, splits into two prongs in a region of the trap chip far away from the trap centre. These two prongs then run in parallel along the length of the chip, extending significantly past the trapping region. As far as the electric field generated by them in the trapping region is concerned, they can be modelled like infinite straight parallel conductors to a good approximation. By symmetry, the resulting rf electric field therefore does not have a component along the direction parallel to the two rf electrodes. Furthermore, it is found that the field in the remaining two directions vanishes on a line running parallel to the rf electrodes halfway between them at a height of approximately 40 µm above the trap surface. I will refer to this rf null line as the *trap axis* as it provides the extremum in the rf potential around which the particle can be trapped. The rf null thus defines the *axial* direction, while the two directions orthogonal to it will be called the *radial* directions.

The rf field may only provide confinement in the radial directions, motion along the trap axis is not affected by it because the corresponding component vanishes. Creating a trapping potential along the axial direction is achieved through the dc electrodes instead. These allow the axial position of the trap centre to be set and control the strength of the confinement in that direction. They also contribute to

the potential in the radial directions in general.

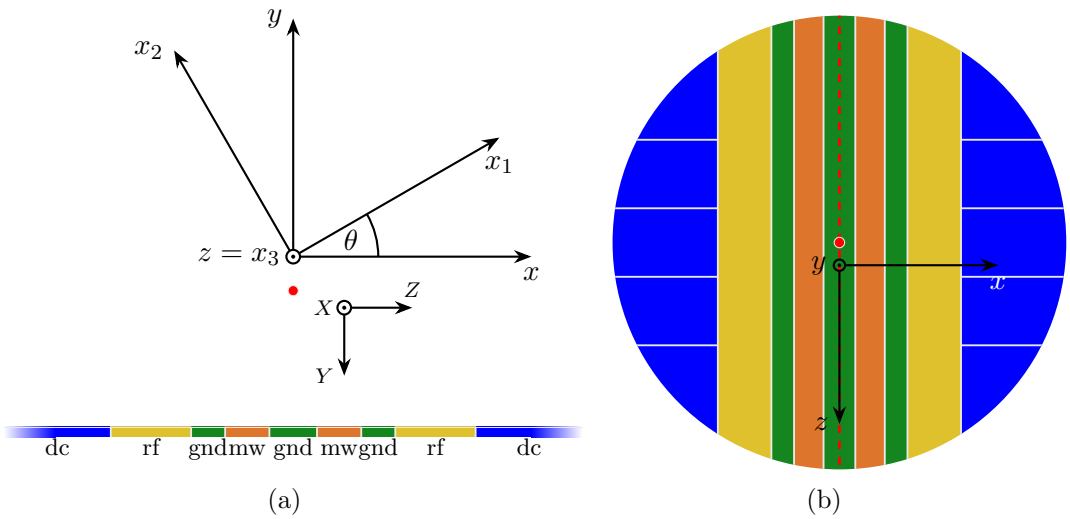


Figure 4.1: Schematic of trap with relevant coordinate systems. The view in a) is along the trap axis, in b) from above the trap chip. The position of the trap centre on the rf null 40 µm above the surface is marked by a red circle, while the rf null is shown as a dashed red line. Distances within each image are to scale, but a different absolute scale has been used in a) and b). The trap coordinate system is labelled by $\{x, y, z\}$, the motional coordinate system, with its axes along the directions of the secular modes of motion, by $\{x_1, x_2, x_3\}$ and the atomic coordinate system, defined by the atomic quantisation axis, by $\{X, Y, Z\}$.

I introduce in figure 4.1 the various coordinate systems that will be used in later chapters. The *trap coordinate system* is defined with reference to the physical structure of the trap chip. It is oriented such that the z-axis coincides with the trap axis, the x-axis is aligned parallel to the plane of the electrodes and orthogonal to the trap axis, while the y-axis extends vertically upward from the trap surface.

The *motional coordinate system*, the axes of which I label $\{x_1, x_2, x_3\}$, has its x_3-axis lying along the trap axis. The axes in the radial plane are chosen to coincide with the directions of the secular modes of motion. The angle of rotation of the x_1-axis of the motional coordinate system relative to the x-axis of the trap coordinate system is denoted by θ, which I take to lie in the interval $[-\pi/4, \pi/4]$. I will often refer to the x_1-axis as the *in-plane* (ip) direction and the x_2-axis as the *out-of-plane* (oop) direction. In the pseudopotential approximation, the directions of the secular modes coincide with the principal axes of the dc potential (see next subsection) and A is then diagonal in this coordinate system.

The *atomic coordinate system*, with axes labelled by $\{X, Y, Z\}$, is defined with respect to the atomic quantisation axis. Its Z-axis coincides with the quantisation axis set by the direction of the strong static magnetic field generated by the main coils. I choose the X-axis to lie in a plane parallel to the trap surface. The Y-axis is then determined as the remaining direction required to form a right-handed orthogonal coordinate system. Operators acting on the internal atomic degrees of freedom such as the magnetic dipole moment $\boldsymbol{\mu}$ are expressed in this coordinate system. The relation between the trap and atomic coordinate systems depends on the alignment of the main coils relative to the trap chip and also on the exact spatial variation of the magnetic field generated by the coils around the trap centre. For ideal vertical coils positioned symmetrically around the trap centre and exactly aligned with the trap chip, one would find that $x = Z$, $y = -Y$ and $z = X$. In practice, however, a slight mismatch is to be expected as fabrication tolerances mean that real coils are never quite ideal. More importantly, alignment of the main coils is done by hand, which we estimate to be only accurate to $\leq 5°$. We therefore use pairs of vertical and horizontal trim coils to optimise alignment of the atomic quantisation axis relative to the laser beams propagating along the x-axis, as required for high-fidelity shelving.

The origin of every coordinate system coincides with the position of the intended trap centre on the rf null. They are shown with offsets in fig. 4.1 only to avoid cluttering the illustration.

4.4.2 Trapping potentials

As far as terms higher than quadratic in the coordinates can be neglected, the motion of a charged particle is determined by the positions of the extrema of the rf and dc potentials, any inhomogeneous terms $\mathbf{s}$ that may be present and the matrices A and Q. All these factors depend on the electric potentials Φ_{rf} and Φ_{dc} in the trap, which arise from the superposition of all the individual potentials of the trap electrodes. Calculating the voltages necessary to achieve a desired trapping configuration thus requires knowledge of the electric potential resulting from each particular electrode. This may in principle be modelled numerically using specialised software packages

that solve Maxwell's equations for arbitrary arrangements of conductors and dielectrics. However, for our purposes it is not necessary to make use of such methods when calculating the voltages to be applied to the electrodes. This is because we are not interested in setting, for example, the secular frequencies with high precision, but rather our aim is to approximately achieve target values for the trapping parameters. The important point is that the values of all relevant parameters have to be measured experimentally in any case, so as long as the discrepancy between target and measured values is not too large, using simple means of calculating the potentials is sufficient.

We therefore use an analytic model [Hou08] to calculate the potentials generated by the various electrodes. This model assumes ideal rectangular electrodes in a gapless-plane approximation and ignores any effects that might result from nearby dielectrics, such as the substrate that the electrodes are placed on. Despite these limitations, I find that the differences between parameter values predicted using this model and measured values are less than 3 %.

I will first consider the rf potential Φ_{rf} generated by the two rf electrodes. Since the voltage on each rf electrode varies with the same amplitude as $V_{\mathrm{rf},0}\cos\omega_{\mathrm{rf}}t$ and they are both of the same width, the resulting rf potential is symmetric about the yz-plane. It contains an extremum at a point in the yz-plane 40 µm above the trap surface, which is independent of position along z and forms the rf null. This fixes the trap centre $\mathbf{x}_0$ in the radial plane. By symmetry, Q is therefore diagonal in the trap coordinate system and can be written

$$Q = q \begin{pmatrix} 1 & 0 & 0 \\ 0 & -1 & 0 \\ 0 & 0 & 0 \end{pmatrix} , \tag{4.53}$$

where $q = -2Ze\,\partial^2_{xx}\Phi_{\mathrm{rf}}(\mathbf{x}_0)/(m\omega^2_{\mathrm{rf}})$ and is proportional to $V_{\mathrm{rf},0}$.

The dc potential Φ_{dc} offers more flexibility since the voltage of each dc electrode can be controlled independently. All elements of the resulting matrix A may be made non-zero in general. The trap centre along the axial direction is determined

only by the dc potential and is set by making $\partial_z \Phi_{\rm dc} = 0$ at the desired z-position. Additionally, it is advantageous to leave axial and radial motion uncoupled, which requires $\partial^2_{xz}\Phi_{\rm dc}(\mathbf{x}_0) = 0$ and $\partial^2_{yz}\Phi_{\rm dc}(\mathbf{x}_0) = 0$. In this case, axial motion becomes particularly simple and is described by

$$\frac{d^2 z(t)}{dt^2} + \frac{\omega_{\rm rf}^2}{4} A_{zz}\, z(t) = 0 \,, \tag{4.54}$$

which is just harmonic motion with natural frequency $\nu_z = \omega_{\rm rf}\sqrt{A_{zz}}/2$.

If the dc voltages are chosen such that A is diagonal in the trap coordinate system, then the principal axes of A and Q coincide and the motion is decoupled along the x- and y-axes. However, this means that the Doppler cooling lasers, which propagate in the xz-plane, cannot cool motion along the y-axis. In fact, since spontaneous emission along that direction may still occur, scattering of light would effectively heat the mode corresponding to the y-axis on average. To avoid this, we set the dc voltages such that A contains off-diagonal elements in the radial directions of the trap coordinate system. The principal axes of the dc potential in the radial plane are thus tilted and the secular modes, which define the motional coordinate system, no longer lie along the x- and y-axes. The cooling lasers then have a non-zero projection along each secular mode, enabling cooling in all three dimensions. With these considerations, one can write A in the trap coordinate system as

$$A = \begin{pmatrix} A_{xx} & A_{xy} & 0 \\ A_{xy} & A_{yy} & 0 \\ 0 & 0 & A_{zz} \end{pmatrix} . \tag{4.55}$$

It may be seen that for $A_{xy} \neq 0$, as assumed here, the matrices A and Q given by eq. (4.55) and (4.53) do not commute. It follows that strictly speaking a description involving coupled equations of motion is required. However, in such an analysis it is found that for $A_{ij} \ll 1$ and $q < 0.4$, which corresponds to conditions in our trap, the directions of the secular modes lie very close to the principal axes of the dc potential. In practice the angle θ determining the rotation of the secular modes relative to the trap coordinate system can therefore be identified with the angle of

rotation of the principal axes of the dc potential. This is also the result obtained through a treatment in terms of the pseudopotential approximation.

4.4.3 Trapping under pseudopotential approximation

If I assume for a moment that there are no static fields applied in the trap, the motion of the ion can be described by means of the pseudopotential energy

$$V_{\mathrm{ps}}(\mathbf{x}) = \frac{m\omega_{\mathrm{rf}}^2}{16}\, q^2\,(x^2 + y^2)\ . \tag{4.56}$$

In deriving this equation, I have made use of the Taylor expansion of $\Phi_{\mathrm{rf}}(\mathbf{x})$ up to second order and taken into account expressions (4.52) and (4.53). The pseudopotential is seen to be symmetric with respect to rotation about the trap axis. It follows that if one now introduces static fields and superposes the dc potential on this pseudopotential, then the principal axes of motion in the radial plane are purely determined by the dc potential. In the coordinate system formed by these principal axes, which is the same as the motional coordinate system in this approximation, one may write the dc potential energy as

$$V_{\mathrm{dc}}(\mathbf{x}) = \frac{m\omega_{\mathrm{rf}}^2}{8}\,\left(a_1\, x_1^2 + a_2\, x_2^2 + a_3\, x_3^2\right)\ , \tag{4.57}$$

where a_1, a_2 and a_3 are the respective elements of A, which is diagonal in this coordinate system. Owing to the rotational symmetry of V_{ps}, the equations of motion along the principal radial axes in the pseudopotential approximation are given by

$$\frac{d^2x_i(t)}{dt^2} + \frac{\omega_{\mathrm{rf}}^2}{4}\left(a_i + \frac{q^2}{2}\right) x_i(t) = 0, \qquad i \in \{1, 2\}\ , \tag{4.58}$$

assuming there are no uncompensated electric fields and thus $s_i = 0$. This describes harmonic motion with angular frequency $\nu_i = (\omega_{\mathrm{rf}}/2)\sqrt{a_i + q^2/2}$.

From the expressions for the natural frequencies ν_i, a useful relation for q may be obtained by considering

$$\nu_1^2 + \nu_2^2 + \nu_3^2 = \frac{\omega_{\mathrm{rf}}^2}{4}\left(a_1 + \frac{q^2}{2} + a_2 + \frac{q^2}{2} + a_3\right) = \frac{\omega_{\mathrm{rf}}^2}{4}\left(\mathrm{tr}\, A + q^2\right)\ . \tag{4.59}$$

Recalling that $\mathrm{tr}\, A = 0$ leads to

$$q = \frac{2}{\omega_{\mathrm{rf}}} \sqrt{\nu_1^2 + \nu_2^2 + \nu_3^2} \,. \tag{4.60}$$

This allows estimating q in the pseudopotential approximation from the secular frequencies, which can be measured accurately.

4.4.4 Calculation of voltage sets

The voltages applied to the rf and dc electrodes have to be chosen such that they lead to matrices A and Q that give real secular frequencies ν_i in the solutions (4.12) to the Mathieu equation. Otherwise the motion of the particle would not be bounded. A given trapping configuration thus leads to a system of equations for the unknown electrode voltages. Under standard operation, we trap in the centre of the trap chip on the rf null and keep motion in the axial and radial directions decoupled. We achieve this by creating a dc potential that has a minimum at $z = 0$ and is symmetric about the xy-plane. For that purpose, we constrain the electrodes on opposite sides of the xy-plane along the z-axis to be held at the same voltage. Since this leads to simple harmonic motion along the trap axis, setting a target axial frequency ν_z corresponds to the constraint $A_{zz} = (2\nu_z/\omega_{\mathrm{rf}})^2$.

As regards motion in the radial plane, we aim to eliminate any offset from the rf null in order to avoid excess micromotion. In the ideal case, this requires $s_x = 0$ and $s_y = 0$, which we use for initial trapping attempts. Once this has succeeded and an ion is available for observation, however, we vary these two parameters to empirically find the optimal settings that minimise excess micromotion.

The parameters left are then q, A_{xx}, A_{xy} (or, more conveniently, θ) and A_{yy}, which have to be chosen such that the resulting solutions to the Mathieu equation are stable. Since we use $A_{xy} \neq 0$, rigorous determination of stability requires numerical simulations of coupled Mathieu equations to find which regions in the corresponding parameter space give rise to real secular frequencies ν_i. It is found that off-diagonal terms typically do not negatively affect the size of the stability regions compared to the decoupled case, especially when the motion is only weakly coupled [SO12]. One

may thus invoke the by-now familiar approximation of replacing coupled equations of motion by a decoupled version such that in the latter the a_i take the same values as in the coordinate system in which A is diagonal and the q_i as in the coordinate system in which Q is diagonal. The stability conditions for the one-dimensional Mathieu equation then apply separately to each axis. The same conclusion is reached in the pseudopotential approximation, as follows from the discussion in the previous section. Our main interest then lies in setting q and the tilt angle θ. We keep the former in the range[2] $0.2 < q < 0.3$. The only degree of freedom here is the rf voltage amplitude $V_{\mathrm{rf},0}$, which we cannot measure directly as there are no accessible electric contacts after the rf resonator PCB attached to the bottom of the vacuum chamber. Nevertheless, for initial trapping, we obtained an estimate for the voltage step-up factor of the PCB by taking measurements of rf power after the resonator when connected to a load with similar impedance as the trap chip. Once the secular frequencies have been measured, it is possible to infer an accurate value for q through relation (4.60). The angle θ is set by rotating the principal axes of the dc potential by the desired amount. Considering the effect of a rotation between coordinate systems, this leads to the constraint $(A_{xx} - A_{yy}) \sin 2\theta = 2A_{xy} \cos 2\theta$.

The total dc potential at the trap centre is given by $\Phi_{\mathrm{dc}}(\mathbf{x}_0) = \sum_i \Phi_{\mathrm{dc},i}(\mathbf{x}_0)$, where $\Phi_{\mathrm{dc},i}$ is the contribution from an individual dc electrode labelled by i. All relevant derivatives of Φ_{dc} at $\mathbf{x}_0$ can be written in a similar form. We model each dc electrode as extending infinitely either along the $+x$ or the $-x$ direction, depending on which side of the trap chip it is located on. In combination with the known trap dimensions, each $\Phi_{\mathrm{dc},i}(\mathbf{x}_0)$ can then be calculated from the analytic expression for the potential generated by an electrode of corresponding shape [Hou08]. It takes the form $\Phi_{\mathrm{dc},i}(\mathbf{x}_0) = V_i f_i(\mathbf{x}_0)$, where V_i is the voltage applied to the ith electrode and $f_i(\mathbf{x}_0)$ is a geometric factor resulting from the spatial dependence of the potential and the position of the electrode relative to the trap centre. The equations determining the voltages required to achieve desired values for the trapping

[2] I note that validity of the lowest-order approximation presented earlier requires $q^2 \ll 1$, which means that this approximation should be applicable as long as q is not significantly larger than 0.3.

parameters can therefore be written in matrix form as

$$\begin{pmatrix} \partial_x f_1(\mathbf{x}_0) & \partial_x f_2(\mathbf{x}_0) & \dots & \partial_x f_n(\mathbf{x}_0) \\ \partial_y f_2(\mathbf{x}_0) & \partial_y f_2(\mathbf{x}_0) & \dots & \partial_y f_n(\mathbf{x}_0) \\ \partial_{zz} f_1(\mathbf{x}_0) & \partial_{zz} f_2(\mathbf{x}_0) & \dots & \partial_{zz} f_n(\mathbf{x}_0) \\ k_1 & k_2 & \dots & k_n \end{pmatrix} \begin{pmatrix} V_1 \\ V_2 \\ \vdots \\ V_n \end{pmatrix} = \begin{pmatrix} -E_x \\ -E_y \\ \frac{m\nu_z^2}{Ze} \\ 0 \end{pmatrix}, \tag{4.61}$$

where E_x and E_y are the spatially uniform fields at $\mathbf{x}_0$ required to cancel any uncompensated stray fields. I have defined $k_i = \left(\partial_{xx}^2 f_i - \partial_{yy}^2 f_i\right) \sin 2\theta - 2\cos 2\theta\, \partial_{xy}^2 f_i$. The voltages V_i, with $i \in \{1, 2, \dots, n\}$, represent the independent dc voltages that may be set in the trap. In case the ith electrode is to be kept at ground, we fix $V_i = 0$ and the terms $f_i(\mathbf{x}_0)$ and V_i are simply removed from the system of equations. If certain electrodes should be held at the same voltage V_i, then $f_i(\mathbf{x}_0)$ corresponding to this independent voltage no longer arises from a single electrode, but is replaced with $f_i(\mathbf{x}_0) = \sum_j f_j^{(i)}(\mathbf{x}_0)$, where j runs over all electrodes that should be kept at the same voltage. The individual V_j and $f_j(\mathbf{x}_0)$ then do not enter the equations, but instead V_i and $f_i(\mathbf{x}_0) = \sum_j f_j^{(i)}(\mathbf{x}_0)$ are used.

Letting G denote the matrix of coefficients, $\mathbf{v}$ the vector of unknown voltages and $\mathbf{b}$ the vector of target values, the system of equations may be expressed in matrix form as $G\mathbf{v} = \mathbf{b}$. The length n of $\mathbf{v}$ corresponds to the number of voltages available in the trap and the length m of $\mathbf{b}$ to the number of constraints to achieve desired trapping parameters. We solve the system numerically to find the required voltage set through $\mathbf{v} = G^{-1}\mathbf{b}$. Assuming that the equations are linearly independent, a necessary condition for the inverse to exist is $n \geq m$. For $n = m$, the standard inverse, if it exists, is unique and provides the required solution. For $n > m$, we use the pseudoinverse, which results in the voltage set that satisfies the equations and is characterised by minimal $|\mathbf{v}|$.

During standard trapping operation, we only constrain the dc potential through the four equations contained in (4.61). We use the minimum set of four independent voltages to fulfil these constraints. The twelve dc electrodes in the outer trapping zones are fixed at ground and only the ten electrodes of the central zone are used.

While keeping the dc electrodes on either side of the yz-plane independent, we tie the three smaller electrodes together at one voltage and similarly for the two larger electrodes. This ensures symmetry about the xy-plane while leaving the possibility for asymmetry about the yz-plane to tilt the principal axes. It is straightforward to extend the method to a larger number of independent voltages and include, for example, conditions fixing the magnitude of one of the radial secular frequencies or higher-order derivatives of the dc potential at the trap centre. However, when only steady confinement of ions around the trap centre is needed, we do not make use of this option for ease of maintenance and because we find that the dc parameters a_2 and a_3 that result from constraining only ν_z and θ are already suitable for stable ion motion.

Whenever shuttling of ions is required, such as during loading of a two-ion crystal or for experiments that involve displacing an ion by a controlled amount, we make use of more complex routines for the calculation of electric potentials and corresponding voltage sets. The software library that has been developed in our group for this purpose is described elsewhere [Web22].

4.4.5 Trapping parameters

The total electric potential in the pseudopotential approximation $\Phi(\mathbf{x}) = V_{\mathrm{ps}}(\mathbf{x})/(Ze) + \Phi_{\mathrm{dc}}(\mathbf{x})$ that arises from the voltage set typically used for the experiments described in this work is shown in figure 4.2. The trap depth can be estimated as the value of the potential energy at the saddle point in the radial plane, which is found to be approximately 27 meV.

We usually use an rf frequency $\omega_{\mathrm{rf}} = 2\pi \times 61.4\,\mathrm{MHz}$ and $q \approx 0.25$. The latter is found indirectly from measurements of the three secular frequencies. The corresponding rf voltage is inferred to be approximately 78 V. We fix the target axial trap frequency at $\nu_z = 2\pi \times 1.1\,\mathrm{MHz}$ and mode angle at $\theta = 15°$. With this setting, an axial frequency of 1.12 MHz is experimentally observed, sufficiently close to the target value. We find that our choice of mode angle allows sufficient cooling of all motional modes, but is small enough so as not to destabilise motion in the radial directions or lead to excessive voltages for the dc electrodes. The compensation

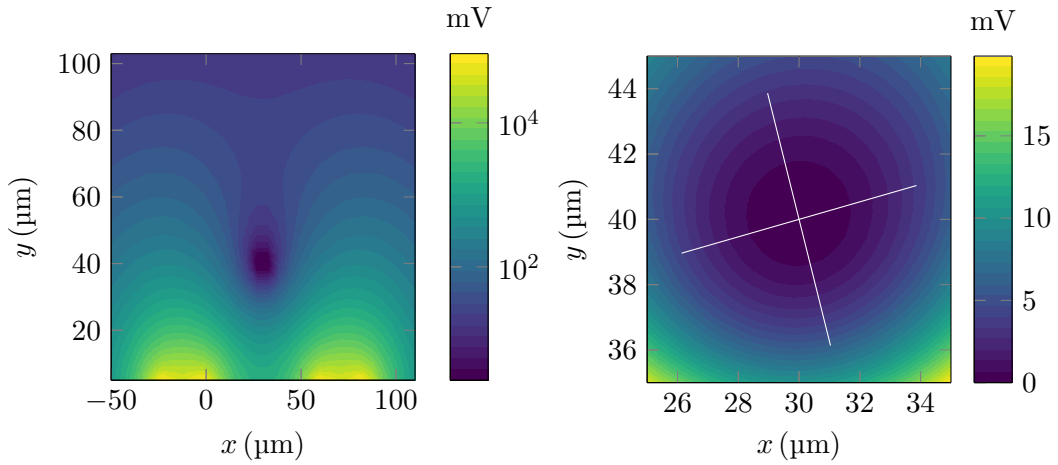


Figure 4.2: Electric potentials in radial plane assuming standard trapping parameters. a) Rf pseudopotential. b) Total potential resulting from rf and dc electrodes in the vicinity of the trap centre. The principal axes of the potential are indicated as white lines.

fields required to minimise excess micromotion are of the order of $100\,\mathrm{V\,m^{-1}}$. The secular frequencies in the radial directions resulting from these dc parameters are typically $\nu_{\mathrm{ip}} = 2\pi \times 5.2\,\mathrm{MHz}$ and $\nu_{\mathrm{oop}} = 2\pi \times 5.6\,\mathrm{MHz}$.

Chapter 5

Interaction of a single ion with external fields

In this chapter I present the theory underlying the coherent manipulation of the quantum state of a single ion confined in our surface trap. This is relevant for single-qubit gates on the clock qubit in particular, but the basic principles apply more generally to arbitrary transitions between states in the ground level. I separately discuss two types of interactions: magnetic-dipole interactions for direct transitions between states in the ground level and Raman interactions that couple two states in the ground level indirectly via an intermediate third state in the $4\,\mathrm{P}_{1/2}$ level. There is significant overlap in the description of both types of interactions. I therefore provide a thorough treatment of the magnetic-dipole interaction, while keeping the discussion of Raman transitions briefer as several results can be obtained analogously. I will assume that incoherent relaxation processes, which would require a formulation based on the density operator, can be neglected throughout and that it is therefore sufficient to describe the atomic system by means of a wavefunction $|\psi(t)\rangle$. With regards to spontaneous decay from states with $F = 3$ in the ground level, this assumption holds to an excellent approximation due to the long natural lifetime of these states.

The approach may be outlined as follows. I start by writing down the complete Hamiltonian that includes all internal electronic states, quantised centre-of-mass

motion in the rf trapping potential and their interaction with a position-dependent magnetic or electric field that varies sinusoidally with time. Then I assume that the relevant driving frequency of the field is such that only transitions between one pair of internal states are near resonance, which allows us to eliminate all other internal states and effectively reduce the Hilbert space of the system. It is found that an inhomogeneous field leads to the appearance of sideband transitions, which can be used to change the motional state of the particle. In this chapter, I will only consider the situation where a single driving frequency is present and consequently only one sideband may be addressed at a time. In a more general case, two frequency tones may be applied, which makes it possible to produce a spin-dependent force that operates in a basis of rotated spin states. This case will be treated in chapter 8.

It should be noted that the interaction of a trapped ion with lasers has been discussed in several review articles, see for example refs. [WMI+98] and [LBM+03]. This is another reason why I will only give a relatively short description of Raman transitions. Instead, the focus lies on the magnetic-dipole interaction and its dependence on the microwave magnetic field generated in our trap.

5.1 Making use of the interaction picture

The Hamiltonian $H_0(t)$ describing a single ion bound in the trap in the Schrödinger picture consists of a time-independent part H_{itl} due to the internal electronic state and a time-dependent part $H_{\mathrm{mot}}(t)$ arising from the motion of the centre of mass of the particle in the three-dimensional trapping potential,

$$H_0(t) = H_{\mathrm{itl}} + H_{\mathrm{mot}}(t) \ . \tag{5.1}$$

The internal Hamiltonian, which was discussed in chapter 2, includes the effects of the static magnetic field produced by the main coils. Letting $\{|i\rangle\}$ denote the set of eigenstates of H_{itl} with energies $E_i = \hbar\omega_i$, it may be written

$$H_{\mathrm{itl}} = \sum_i \hbar\omega_i |i\rangle\langle i| \ . \tag{5.2}$$

The contribution $H_{\rm mot}(t)$ was presented in chapter 4 and is explicitly time-dependent because of the oscillating rf trapping potential. It takes the form

$$H_{\rm mot}(t) = \sum_m \frac{p_m^2}{2M} + \frac{M}{2}\frac{\omega_{\rm rf}^2}{4}\sum_{m,n}(A_{mn} - 2Q_{mn}\cos\omega_{\rm rf}t)\,x_m x_n - M\frac{\omega_{\rm rf}^2}{4}\sum_m s_m\,x_m \tag{5.3}$$

for a particle of mass M.

Application of an external electromagnetic field – in addition to those already included in $H_0(t)$ – gives rise to an interaction Hamiltonian $H_{\rm int}(t)$. The total Hamiltonian in the Schrödinger picture is then

$$H(t) = H_0(t) + H_{\rm int}(t)\ . \tag{5.4}$$

The exact form of $H_{\rm int}(t)$ depends on the details of the applied field, but in general it will act on both the internal and and the centre-of-mass degrees of freedom of the system. Regardless of the specific expression for $H_{\rm int}(t)$, it will prove useful to transform to the interaction picture with respect to the Hamiltonian $H_0(t)$. This is achieved by applying the unitary transformation

$$|\psi(t)\rangle^{(\rm I)} = U_0^\dagger(t;t_0)\,|\psi(t)\rangle \tag{5.5}$$

to each Schrödinger-picture state $|\psi(t)\rangle$ in the Hilbert space, where $U_0(t;t_0)$ satisfies

$$\mathrm{i}\hbar\frac{dU_0(t;t_0)}{dt} = H_0(t)\,U_0(t;t_0), \qquad U_0(t_0;t_0) = \mathbb{I} \tag{5.6}$$

and is thus the time-evolution operator for the system in the absence of the interaction $H_{\rm int}(t)$. I will take $t_0 = 0$ without loss of generality and write $U(t) = U(t;0)$. Since internal and centre-of-mass operators act on different degrees of freedom, $U_0(t)$ factors as $U_0(t) = U_{\rm itl}(t)\otimes U_{\rm mot}(t)$, where $U_{\rm itl}$ ($U_{\rm mot}$) satisfies an equation analogous to (5.6), with H_0 replaced by $H_{\rm itl}$ ($H_{\rm mot}$). The interaction Hamiltonian in the interaction picture, which I will denote by $H_{\rm int}^{(\rm I)}(t)$, is given by

$$H_{\rm int}^{(\rm I)}(t) = U_0^\dagger(t)H_{\rm int}(t)U_0(t)\ . \tag{5.7}$$

Since H_{itl}, as evident from eq. (5.2), is time-independent, the corresponding propagator can be written down explicitly in the form

$$U_{\mathrm{itl}}(t) = \mathrm{e}^{-\mathrm{i}H_{\mathrm{itl}}t/\hbar} = \mathrm{e}^{-\mathrm{i}\sum_i \omega_i t|i\rangle\langle i|} \,. \tag{5.8}$$

5.2 Magnetic-dipole transitions

The magnetic-dipole interaction is described in the Schrödinger picture by the interaction Hamiltonian

$$H_{\mathrm{int}}(t) = H_{\mathrm{M2}}(t) = -\boldsymbol{\mu} \cdot \mathbf{B}_{\mathrm{mw}}(\mathbf{x}, t) \,, \tag{5.9}$$

where $\boldsymbol{\mu}$ is the magnetic dipole moment of the atom and $\mathbf{B}_{\mathrm{mw}}(\mathbf{x}, t)$ is the microwave magnetic field at position $\mathbf{x}$ of the centre of mass of the ion. For the moment, I will assume $\mathbf{x}$ is a classical variable and will only promote it to an operator later. I will omit the explicit label on the magnetic field in the following.

It is convenient at this point to introduce the spherical basis for three-dimensional vectors. To this end, one extends the vector space from $\mathbb{R}^3$ to $\mathbb{C}^3$ and defines the spherical basis vectors

$$\mathbf{e}_{+1} = -\frac{1}{\sqrt{2}} (\mathbf{e}_x + \mathrm{i}\mathbf{e}_y) \tag{5.10}$$

$$\mathbf{e}_0 = \mathbf{e}_z \tag{5.11}$$

$$\mathbf{e}_{-1} = \frac{1}{\sqrt{2}} (\mathbf{e}_x - \mathrm{i}\mathbf{e}_y) \tag{5.12}$$

in terms of their Cartesian analogues $\mathbf{e}_x$, $\mathbf{e}_y$, $\mathbf{e}_z$. Physically valid vectors are taken to be the subset comprised of those vectors that have real Cartesian components. Every vector $\mathbf{v}$ can then be expanded in the spherical basis as $\mathbf{v} = \sum_q v^q \mathbf{e}_q$, with

contravariant components v^q given by

$$v^{+1} = -\frac{1}{\sqrt{2}}\left(v^x - \mathrm{i}\, v^y\right) \tag{5.13}$$

$$v^0 = v^z \tag{5.14}$$

$$v^{-1} = \frac{1}{\sqrt{2}}\left(v^x + \mathrm{i}\, v^y\right) \ , \tag{5.15}$$

where v^i denote the usual Cartesian components. The *covariant* components v_q are consequently found to be $v_q = (-1)^q v^{-q}$. The scalar product in the spherical basis, applied to the magnetic-dipole Hamiltonian, becomes

$$H_{\mathrm{int}} = -\boldsymbol{\mu} \cdot \mathbf{B} = -\sum_q \mu_q B^q = \sum_q (-1)^{q+1} \mu_q B_{-q} \ . \tag{5.16}$$

Here, the spherical components are taken with respect to the *atomic* coordinate system[1], in which the z-axis is the quantisation axis defined by the strong static magnetic field generated by the main coils. The reason for using the covariant components in this expression lies in the fact that the spherical atomic operators μ_q resulting from the covariant combinations of Cartesian operators μ_i, $i \in \{x, y, z\}$, form a rank-one irreducible spherical tensor operator. In general, this allows using the Wigner-Eckart theorem for calculation of matrix elements between atomic states. For the magnetic-dipole Hamiltonian, however, use of this theorem is not required as the operators μ_q can be directly expressed in terms of angular momentum operators, as will become clear in the next section.

I assume that the magnetic field $\mathbf{B}(\mathbf{x}, t)$ generated by the microwave current contains a single frequency component ω and thus takes the form

$$B_k(\mathbf{x}, t) = B_{k,0}(\mathbf{x}) \cos\left[\omega t - \phi_k(\mathbf{x})\right] \tag{5.17}$$

along each Cartesian axis k. I allow for the possibility that the field may not necessarily be linearly polarised at a given position. Furthermore, amplitude and phase for each component may have spatial dependence. The field can also be written

[1] I will denote components in any coordinate system with lower-case letters in this chapter. It should be clear from context which particular one, such as the atomic or the motional coordinate system, is relevant.

$B_k(\mathbf{x},t) = B_k^{(\mathrm{c})}(\mathbf{x})\cos\omega t + B_k^{(\mathrm{s})}(\mathbf{x})\sin\omega t$, which enables us to perform a Taylor expansion around the trap centre $\mathbf{x}_0$ to obtain

$$\begin{aligned} B_k(\mathbf{x},t) = \Bigg[& B_k^{(\mathrm{c})}(\mathbf{x}_0) + \sum_{m=1}^{3} \left.\frac{\partial B_k^{(\mathrm{c})}}{\partial x_m}\right|_{\mathbf{x}_0} (x_m - x_{0,m}) \\ & + \sum_{m=1}^{3}\sum_{n=1}^{3} \frac{1}{2} \left.\frac{\partial^2 B_k^{(\mathrm{c})}}{\partial x_m \partial x_n}\right|_{\mathbf{x}_0} (x_m - x_{0,m})(x_n - x_{0,n}) + O\left(\mathbf{x}^3\right) \Bigg] \cos\omega t \\ + \Bigg[& B_k^{(\mathrm{s})}(\mathbf{x}_0) + \sum_{m=1}^{3} \left.\frac{\partial B_k^{(\mathrm{s})}}{\partial x_m}\right|_{\mathbf{x}_0} (x_m - x_{0,m}) \\ & + \sum_{m=1}^{3}\sum_{n=1}^{3} \frac{1}{2} \left.\frac{\partial^2 B_k^{(\mathrm{s})}}{\partial x_m \partial x_n}\right|_{\mathbf{x}_0} (x_m - x_{0,m})(x_n - x_{0,n}) + O\left(\mathbf{x}^3\right) \Bigg] \sin\omega t \end{aligned} \tag{5.18}$$

The coordinates in this expansion are taken with respect to an arbitrary Cartesian coordinate system. I will take the trap centre as the origin of the coordinate system, so $\mathbf{x}_0 = \mathbf{0}$. When this expansion is inserted in the expressions for the spherical components of $\mathbf{B}(\mathbf{x},t)$ and the sinusoids written in terms of complex exponentials, one finds that

$$B_q(\mathbf{x},t) = \frac{1}{2}\left[B_q^{+}(\mathbf{x})\,\mathrm{e}^{-\mathrm{i}\omega t} + B_q^{-}(\mathbf{x})\,\mathrm{e}^{\mathrm{i}\omega t}\right] \tag{5.19}$$

with

$$B_q^{\rho}(\mathbf{x}) = B_q^{\rho}(\mathbf{x}_0) + \sum_{m=1}^{3} \left.\frac{\partial B_q^{\rho}}{\partial x_m}\right|_{\mathbf{x}_0} x_m + \sum_{m=1}^{3}\sum_{n=1}^{3} \frac{1}{2} \left.\frac{\partial^2 B_q^{\rho}}{\partial x_m \partial x_n}\right|_{\mathbf{x}_0} x_m\, x_n + O\left(\mathbf{x}^3\right) \tag{5.20}$$

for $\rho \in \{+,-\}$. The variables B_q^{ρ} can be expressed in terms of the various components $B_k^{(\mathrm{c})}$ and $B_k^{(\mathrm{s})}$ (or alternatively in terms of $B_{k,0}$ and ϕ_k). I note that $\left(B_q^{\rho}\right)^* = (-1)^q B_{-q}^{-\rho}$ and that in general $\left|B_q^{\rho}\right|^2 \neq \left|B_q^{-\rho}\right|^2$. The components $B_q^{\rho}(\mathbf{x})$ are constrained by the requirement that the magnetic field has to satisfy the Maxwell's equations $\nabla\cdot\mathbf{B}(\mathbf{x},t) = 0$ and $\nabla\times\mathbf{B}(\mathbf{x},t) = \mathbf{0}$ for all t, where the latter holds because I am considering the near-field regime of the conductor [WHZ17]. In the following, I will switch to the more compact notation $\partial_m B_q^{\rho}(\mathbf{x}_0)$ for the partial derivatives of the magnetic field at the trap centre.

I now proceed to a quantum mechanical description of the interaction and henceforth let $\mathbf{x}$ represent an operator. Consequently, the quantities $B_q^{\rho}(\mathbf{x})$ now denote functions of the centre-of-mass position operators x_m. The Hamiltonian $H_{\mathrm{int}}(t)$ is

transformed into the interaction picture with respect to $H_0(t)$ through eq. (5.7). Since the magnetic-dipole operators μ_q act on the internal state, while the field $\mathbf{B}(\mathbf{x},t)$ depends on the centre-of-mass degree of freedom, the resulting Hamiltonian can be grouped into two terms:

$$H_{\mathrm{int}}^{(\mathrm{I})}(t) = \sum_q (-1)^{q+1} \left[\mathrm{e}^{\mathrm{i}\sum_i \omega_i t |i\rangle\langle i|} \, \mu_q \, \mathrm{e}^{-\mathrm{i}\sum_j \omega_j t |j\rangle\langle j|} \right] \left[U_{\mathrm{mot}}^\dagger(t) B_{-q}(\mathbf{x},t) U_{\mathrm{mot}}(t) \right] . \tag{5.21}$$

I have made use of the fact that $U_{\mathrm{itl}}(t)$ and $U_{\mathrm{mot}}(t)$ commute. The Hamiltonian may be simplified to

$$H_{\mathrm{int}}^{(\mathrm{I})}(t) = \sum_q (-1)^{q+1} \left[\sum_{i,j} \mathrm{e}^{\mathrm{i}(\omega_i - \omega_j)t} \langle i|\mu_q|j\rangle |i\rangle\langle j| \right] \left[U_{\mathrm{mot}}^\dagger(t) B_{-q}(\mathbf{x},t) U_{\mathrm{mot}}(t) \right] . \tag{5.22}$$

The interaction with the time-varying magnetic field thus depends on the matrix elements $\langle i|\mu_q|j\rangle$ of the magnetic dipole operator between the various internal atomic states and the spatial variation of the field. I will now consider these two contributions separately.

5.2.1 Magnetic-dipole matrix elements

Every energy eigenstate of the internal atomic Hamiltonian H_{itl} is also an eigenstate of F_z and thus characterised by a definite value of the quantum number m. I will hereafter focus on magnetic-dipole transitions within the ground level of $^{43}\mathrm{Ca}^+$ and write a general internal state as $|i\rangle = |m_i, \chi_i\rangle$, where $\chi \in \{\mathrm{F3}, \mathrm{F4}\}$ indicates whether I am referring to the state $|F=4,m\rangle$ in the $F=4$ sublevel or the state $|F=3,m\rangle$ in the $F=3$ sublevel. The spherical components of the magnetic-dipole operator are given by

$$\mu_{+1} = -\frac{1}{\sqrt{2}} (\mu_x + \mathrm{i}\,\mu_y) = \frac{1}{\sqrt{2}} (g_J \mu_{\mathrm{B}} J_+ - g_I \mu_{\mathrm{N}} I_+) , \tag{5.22a}$$

$$\mu_0 = \mu_z = -(g_J \mu_{\mathrm{B}} J_z - g_I \mu_{\mathrm{N}} I_z) , \tag{5.23}$$

$$\mu_{-1} = \frac{1}{\sqrt{2}} (\mu_x - \mathrm{i}\,\mu_y) = -\frac{1}{\sqrt{2}} (g_J \mu_{\mathrm{B}} J_- - \mu_{\mathrm{N}} g_I I_-) , \tag{5.24}$$

where $J_\pm = J_x \pm \mathrm{i}\, J_y$ (similarly for $I_\pm$) are the standard ladder operators for angular momentum. One observes that $\mu_q^\dagger = (-1)^q \mu_{-q}$. By noting that $[F_z, \mu_q] = q\mu_q$, one may conclude that[2] application of μ_q to a vector from the subspace corresponding to m results in a vector lying in the subspace $m + q$. It follows that the operator μ_q drives transitions from an initial state with m to a final state with $m + q$. Given two internal states $|m_i, \chi_i\rangle$ and $|m_j, \chi_j\rangle$, only the matrix element $\langle m_i, \chi_i|\mu_q|m_j, \chi_j\rangle$ for the particular component $q(i, j) = m_i - m_j$ is therefore non-zero.

I label the different spherical components according to the following convention: for a higher-energy state with quantum number m_i and a lower-energy state with m_j, I refer to the transition characterised by

- $m_i = m_j - 1$ as σ^-,
- $m_i = m_j$ as π,
- $m_i = m_j + 1$ as σ^+.

Note that the field component driving a transition from m to $m + q$ is $B_{-q}(\mathbf{x}, t)$. I use the same convention for electric-dipole transitions.

Since the spherical component q that can couple two states $|i\rangle$ and $|j\rangle$ is unique, I define a matrix element $R_{ij,q(i,j)}$ representing the strength of the transition magnetic dipole moment as

$$R_{ij,q(i,j)} = (-1)^{q(i,j)+1} \langle m_i, \chi_i|\mu_{q(i,j)}|m_j, \chi_j\rangle \qquad \text{with } q = m_i - m_j \,. \tag{5.25}$$

I have tabulated the values of these matrix elements for an ion in a static magnetic field of 288 G in appendix A. As shown there, all elements $R_{ij,q(i,j)}$ are real. It is worth noting that $R_{ji,q(j,i)} = (-1)^{q(i,j)+1} R_{ij,q(i,j)}$.

Since the matrix element of only one spherical component of $\boldsymbol{\mu}$ can be non-zero for a given pair of internal states, the sum over q in eq. (5.22) reduces to a single

[2] Alternatively, one may also directly consider the action of μ_q in the basis $\{|I, m_I, J, m_J\rangle\}$ using eq. (5.23).

term for each combination of i and j. One hence writes

$$H_{\rm int}^{(\rm I)}(t) = \sum_{i,j} R_{ij,q(i,j)}\, {\rm e}^{{\rm i}\omega_{ij}t}\, |i\rangle\langle j|\, U_{\rm mot}^{\dagger}(t) B_{-q(i,j)}(\mathbf{x},t) U_{\rm mot}(t)\ , \tag{5.26}$$

where I have introduced the bare transition frequencies $\omega_{ij} = \omega_i - \omega_j$. I will omit the dependence of q on i, j in the following, but it should be borne in mind that the q to be used in each respective term of the sum is a function of the corresponding combination of internal states.

5.2.2 Dependence of magnetic field on position operator

I next turn attention to the second term of the interaction Hamiltonian, containing the centre-of-mass position operator $\mathbf{x}$. Making use of expression (5.19) for the spherical components $B_{-q}(\mathbf{x},t)$, one obtains

$$H_{\rm int}^{(\rm I)}(t) = \frac{1}{2}\sum_{i,j} {\rm e}^{{\rm i}\omega_{ij}t} R_{ij,q}\, |i\rangle\langle j|\, U_{\rm mot}^{\dagger}(t) \left[B_{-q}^{+}(\mathbf{x})\, {\rm e}^{-{\rm i}\omega t} + B_{-q}^{-}(\mathbf{x})\, {\rm e}^{{\rm i}\omega t}\right] U_{\rm mot}(t)\ . \tag{5.27}$$

I now insert the Taylor expansion for $B_{-q}^{\rho}(\mathbf{x})$ and introduce the short-hand notation

$$\begin{aligned} B_{-q}^{\rho}(\mathbf{x}^{(\rm I)}) &= U_{\rm mot}^{\dagger}(t) B_{-q}^{\rho}(\mathbf{x}) U_{\rm mot}(t) \\ &= B_{-q}^{\rho}(\mathbf{x}_0) + \sum_m \partial_m B_{-q}^{\rho}(\mathbf{x}_0)\, x_m^{(\rm I)}(t) + \sum_{m,n} \frac{1}{2}\partial_{mn}^2 B_{-q}^{\rho}(\mathbf{x}_0)\, x_m^{(\rm I)}(t)\, x_n^{(\rm I)}(t) + \ldots \end{aligned} \tag{5.28}$$

which involves the position operators in the interaction picture, given by $x_m^{(\rm I)}(t) = U_{\rm mot}^{\dagger}(t) x_m U_{\rm mot}(t)$. The operator $U_{\rm mot}(t)$ satisfies the equation ${\rm i}\hbar\, dU_{\rm mot}(t)/dt = H_{\rm mot}(t) U_{\rm mot}(t)$, subject to the condition $U_{\rm mot}(0) = \mathbb{I}$. It therefore induces on x_m exactly the kind of transformation that was presented in section 4.2. There the transformation produced by $U_{\rm mot}(t)$ corresponded to the transition to the Heisenberg picture. Here it only moves us into the interaction picture because there is an additional $H_{\rm int}(t)$. Nevertheless, the expressions $U_{\rm mot}^{\dagger}(t) x_m U_{\rm mot}(t)$ are identical and one may therefore use the solutions $x_m^{(\rm H)}(t)$ found in section 4.2 for the operators $x_m^{(\rm I)}(t)$ here.

I will consider the case when the motion of the ion is decoupled along three

orthogonal axes. In the absence of excess micromotion, the position operator along each principal axis in the interaction picture then takes the form

$$x_m^{(\mathrm{I})}(t) = x_{m,0}\left[u_m(t)\, a_m^\dagger + u_m^*(t)\, a_m\right] , \tag{5.29}$$

with $x_{m,0} = \sqrt{\hbar/\left(2M\nu_m\right)}$ for a particle of mass M moving with secular frequency ν_m. The operators $a_m^\dagger$ and a_m are creation and annihilation operators for the reference harmonic oscillator along the respective principal axis. I stress again that ν_m is used here to denote an angular frequency. A separate Floquet solution $u_m(t)$, as introduced in section 4.1.1, applies to each axis and is given by

$$u_m(t) = \sum_{r\in\mathbb{Z}} c_{2r,m}\, \mathrm{e}^{\mathrm{i}(\nu_m + r\omega_{\mathrm{rf}})t} , \tag{5.30}$$

which I require to satisfy the initial condition $u_m(0) = 1$.

5.2.3 Coupling internal and external degrees of freedom

Making use of expression (5.29) for $x_m^{(\mathrm{I})}(t)$, one finds that the interaction of the atom with the time-varying magnetic field is described by

$$\begin{aligned} H_{\mathrm{int}}^{(\mathrm{I})}(t) = \frac{1}{2}\sum_{i,j} \mathrm{e}^{\mathrm{i}\omega_{ij}t}\, R_{ij,q}\, |i\rangle\langle j| \\ \times\Bigg[\left(B_{-q}^{+}(\mathbf{x}_0) + \sum_m \partial_m B_{-q}^{+}(\mathbf{x}_0)\, x_{m,0}\left[u_m(t)\, a_m^\dagger + u_m^*(t)\, a_m\right] + \ldots\right)\mathrm{e}^{-\mathrm{i}\omega t} \\ + \left(B_{-q}^{-}(\mathbf{x}_0) + \sum_m \partial_m B_{-q}^{-}(\mathbf{x}_0)\, x_{m,0}\left[u_m(t)\, a_m^\dagger + u_m^*(t)\, a_m\right] + \ldots\right)\mathrm{e}^{\mathrm{i}\omega t}\Bigg] \end{aligned} \tag{5.31}$$

The interaction Hamiltonian at this point is exact. To find the time evolution of the wavefunction $|\psi(t)\rangle^{(\mathrm{I})}$ in the interaction picture, one introduces a suitable basis for the Hilbert space. The appearance of $a_m^\dagger$ and a_m in the interaction Hamiltonian suggests using the basis formed by the internal states $\{|i\rangle\}$ and the number states $\{|n_m\rangle\}$ of the reference harmonic oscillators along the different spatial axes. One

thus takes

$$|\psi(t)\rangle^{(\mathrm{I})} = \sum_i \sum_{n_1} \sum_{n_2} \sum_{n_3} c_{i,n_1,n_2,n_3}(t)\, |i\rangle \otimes |n_1\rangle \otimes |n_2\rangle \otimes |n_3\rangle \ , \tag{5.32}$$

which highlights that to each internal state $|i\rangle$ corresponds a ladder of three-dimensional harmonic oscillator states.

When the evolution equation for $|\psi(t)\rangle^{(\mathrm{I})}$ is projected onto this basis, a set of coupled differential equations for the coefficients $c_{i,n_1,n_2,n_3}(t)$ is obtained. In light of expression (5.30) for $u_m(t)$ and taking into account the action of the ladder operators on the number states, it can be seen that when all the various factors have been multiplied out, the expansion coefficients are coupled by terms of the form

$$\Omega^{(\gamma)} \exp\left[\mathrm{i}\left(\omega_{ij}^{(\gamma)} + \sum_m s_m^{(\gamma)} \nu_m + s_{\mathrm{rf}}^{(\gamma)}\, \omega_{\mathrm{rf}} \pm \omega\right) t\right] = \Omega^{(\gamma)} \exp(\mathrm{i}\omega^{(\gamma)} t) \tag{5.33}$$

The coupling strength is determined by $\Omega^{(\gamma)}$, while $s_m^{(\gamma)}$ and $s_{\mathrm{rf}}^{(\gamma)}$ are integers. These quantities depend on the particular term in question, denoted by γ, which is a composite label containing information about the internal and motional states involved.

While the time evolution is in principle determined by the complete set of equations involving all coefficients $c_{i,n_1,n_2,n_3}(t)$ and terms γ, in practice only a few terms contribute significantly. I therefore now introduce a few approximations that greatly simplify the description. I assume that the driving frequency ω is tuned such that only a transition involving one particular pair of internal states, which I label $|\mathrm{g}\rangle$ and $|\mathrm{e}\rangle$ with $E_{\mathrm{e}} > E_{\mathrm{g}}$, is driven close to resonance. This means that the detuning $\omega - \omega_{\mathrm{eg}}$ will be small compared to $\omega + \omega_{ij}$ and $\omega - \omega_{ij}$ of the remaining internal states. It follows that the complex exponentials corresponding to the near-resonant states $|\mathrm{g}\rangle$ and $|\mathrm{e}\rangle$ will be oscillating much more slowly than those corresponding to the off-resonant states. I additionally make the assumption that for all these fast-oscillating terms, $\Omega^{(\gamma)} \ll \omega^{(\gamma)}$ holds. Under these conditions, it is found that essentially no population transfer occurs between the set of relevant states $\{|g\rangle, |e\rangle\}$ and the off-resonant states. One may then restrict attention to the space spanned by the relevant states and adiabatically eliminate the off-resonant states, as explained

in appendix C. In this procedure, an effective Hamiltonian acting on the reduced space is derived that includes the effects of coupling of $|\mathrm{g}\rangle$ and $|\mathrm{e}\rangle$ to far-detuned states. The main consequence is an effective shift in the energy of each of the two near-resonant states, which in the case of a time-varying magnetic field is called the ac Zeeman shift.

The method of adiabatic elimination removes all off-resonant internal states and the ladder of motional states attached to each of them from the description. It leaves a reduced Hilbert space, spanned by the states $|\mathrm{g}\rangle\,|\mathbf{n}\rangle$ and $|\mathrm{e}\rangle\,|\mathbf{n}\rangle$, where the vector $\mathbf{n} = (n_1, n_2, n_3)$ represents the motional part. This represents an effective system with two internal states moving in the three-dimensional trapping potential.

It is found that the effective Hamiltonian acting in the reduced Hilbert space takes the form

$$\begin{aligned} H_{\mathrm{int}}^{(\mathrm{I})}(t) = \hbar\Delta_{\mathrm{g}}^{\mathrm{ac}}|\mathrm{g}\rangle\langle\mathrm{g}| + \hbar\Delta_{\mathrm{e}}^{\mathrm{ac}}|\mathrm{e}\rangle\langle\mathrm{e}| - \Big(\langle\mathrm{g}|\mu_0|\mathrm{g}\rangle\,|\mathrm{g}\rangle\langle\mathrm{g}| + \langle\mathrm{e}|\mu_0|\mathrm{e}\rangle\,|\mathrm{e}\rangle\langle\mathrm{e}|\Big)\,B_0\big(\mathbf{x}^{(\mathrm{I})},t\big) \\ + R_{\mathrm{eg},q}\,\mathrm{e}^{\mathrm{i}\omega_{\mathrm{eg}}t}\,|\mathrm{e}\rangle\langle\mathrm{g}|\,B_{-q}\big(\mathbf{x}^{(\mathrm{I})},t\big) + (-1)^q R_{\mathrm{eg},q}\,\mathrm{e}^{-\mathrm{i}\omega_{\mathrm{eg}}t}\,|\mathrm{g}\rangle\langle\mathrm{e}|\,B_q\big(\mathbf{x}^{(\mathrm{I})},t\big)\ , \end{aligned} \tag{5.34}$$

where the symbol Δ_i^{ac} refers to the ac Zeeman shift of each individual level and

$$B_q(\mathbf{x}^{(\mathrm{I})},t) = \frac{1}{2}\left[B_q^+(\mathbf{x}^{(\mathrm{I})})\,\mathrm{e}^{-\mathrm{i}\omega t} + B_q^-(\mathbf{x}^{(\mathrm{I})})\,\mathrm{e}^{\mathrm{i}\omega t}\right]\ . \tag{5.35}$$

The relevant spherical component q is uniquely determined by the quantum numbers m_{g} and m_{e} of the near-resonant internal states $|\mathrm{g}\rangle$ and $|\mathrm{e}\rangle$.

The method of adiabatic elimination has removed all states $|j\rangle\,|n_1', n_2', n_3'\rangle$ involved in transitions that are not close to resonance with the applied radiation. The reduced internal space is spanned by the two states $|\mathrm{g}\rangle$ and $|\mathrm{e}\rangle$, which can be mapped onto the two-dimensional Hilbert space connected with a spin-1/2 system. One therefore introduces pseudo-spin states through the map $|\mathrm{e}\rangle \mapsto |\uparrow\rangle$ and $|\mathrm{g}\rangle \mapsto |\downarrow\rangle$. This allows operators acting in the internal space to be represented as a combination of the Pauli matrices and the identity matrix. The wavefunction is

then expanded in the form

$$|\widetilde{\psi}(t)\rangle = \sum_{i\in\{\uparrow,\downarrow\}} \sum_{n_1,n_2,n_3} c_{i,\mathbf{n}}(t)\,|i\rangle\,|\mathbf{n}\rangle \ . \tag{5.36}$$

I now move to a different frame via the unitary transformation $R(t) = \exp\left(\mathrm{i}\Delta_{\mathrm{g}}^{\mathrm{ac}}t\right)|\mathrm{g}\rangle\langle\mathrm{g}| + \exp\left(\mathrm{i}\Delta_{\mathrm{e}}^{\mathrm{ac}}t\right)|\mathrm{e}\rangle\langle\mathrm{e}|$ to remove the constant ac shifts. Using eqs. (5.28), (5.30) and (5.35), one finds that the interaction Hamiltonian $\widetilde{H}_{\mathrm{int}}$ in that frame may to first order in x_m be written

$$\begin{aligned}
\widetilde{H}_{\mathrm{int}}(t) = -\frac{1}{2}\Big(\frac{\mu_{\mathrm{e}}+\mu_{\mathrm{g}}}{2}\,\mathbb{I} + \frac{\mu_{\mathrm{e}}-\mu_{\mathrm{g}}}{2}\,\sigma_z\Big)\Bigg(& B_{0,0}(\mathbf{x}_0)\cos[\omega t - \phi(\mathbf{x}_0)] \\
&+ \sum_m \sum_r \big|\partial_m B_0^+(\mathbf{x}_0)\big|\, x_{m,0}\, c_{2r,m}\Big[\mathrm{e}^{\mathrm{i}(\nu_m + r\omega_{\mathrm{rf}} - \omega)t}\,\mathrm{e}^{\mathrm{i}\phi^+}\,a_m^\dagger + \mathrm{e}^{-\mathrm{i}(\nu_m + r\omega_{\mathrm{rf}} - \omega)t}\,\mathrm{e}^{-\mathrm{i}\phi^+}\,a_m\Big]\Bigg) \\
&+ \frac{1}{2}R_{\mathrm{eg},q}\,\sigma_+\Bigg(B_{-q}^+(\mathbf{x}_0)\,\mathrm{e}^{\mathrm{i}(\bar{\omega}_{\mathrm{eg}} - \omega)t} \\
&+ \sum_m \sum_r \partial_m B_{-q}^+(\mathbf{x}_0)\, x_{m,0}\, c_{2r,m}\Big[\mathrm{e}^{\mathrm{i}(\bar{\omega}_{\mathrm{eg}} + \nu_m + r\omega_{\mathrm{rf}} - \omega)t}\,a_m^\dagger + \mathrm{e}^{\mathrm{i}(\bar{\omega}_{\mathrm{eg}} - \nu_m - r\omega_{\mathrm{rf}} - \omega)t}\,a_m\Big]\Bigg) \\
&+ \mathrm{H.c.}
\end{aligned} \tag{5.37}$$

with $\mu_{\mathrm{g}} = \langle\mathrm{g}|\mu_0|\mathrm{g}\rangle$, $\mu_{\mathrm{e}} = \langle\mathrm{e}|\mu_0|\mathrm{e}\rangle$ and $\phi^+ = \arg\big[\partial_m B_0^+(\mathbf{x}_0)\big]$. I have defined $\bar{\omega}_{\mathrm{eg}} = \omega_{\mathrm{e}} + \Delta_{\mathrm{e}}^{\mathrm{ac}} - \big(\omega_{\mathrm{g}} + \Delta_{\mathrm{g}}^{\mathrm{ac}}\big)$, which is the effective transition frequency between the two internal states after adjusting for ac Zeeman shifts. The Hermitian conjugate is to be taken with respect to the whole preceding expression, resulting in multiplication by a factor of 2 for the diagonal term. In deriving $\widetilde{H}_{\mathrm{int}}(t)$, I have applied a rotating-wave approximation, which consists in neglecting all terms oscillating at $\pm(\nu_m + r\omega_{\mathrm{rf}} + \omega)$, $\pm(\bar{\omega}_{\mathrm{eg}} + \omega)$ and $\pm[\bar{\omega}_{\mathrm{eg}} \pm (\nu_m + r\omega_{\mathrm{rf}}) + \omega]$. This is justified as long as the coupling strengths of the various terms (proportional to $B_{-q}^{\rho}(\mathbf{x}_0)$ and $\partial_m B_{-q}^{\rho}(\mathbf{x}_0)$) are sufficiently small, so that the fast-oscillating exponentials only lead to low-amplitude modulations on timescales much shorter than those that one is interested in. By adjusting the frequency ω of the applied magnetic field, one may selectively cause a certain term of $\widetilde{H}_{\mathrm{int}}(t)$ to be near-resonant, which will then contain an exponential that oscillates slowly compared to the exponentials connected with other terms.

I will first focus on the part of $\widetilde{H}_{\mathrm{int}}$ that is diagonal between internal states. The

term containing the identity operator may be interpreted as an energy modulation common to both states. I will neglect it since it leads to the same evolution for both states. However, the term involving σ_z leads to evolution that is dependent on the spin state. In combination with $B_{z,0}(\mathbf{x}_0)\cos[\omega t - \phi(\mathbf{x}_0)]$, it represents a time-dependent differential change in the energies of the two states. The factor $\cos\omega t$ will only vary slowly in the limit when the driving field becomes static. In all other situations, when ω is close to resonance with a different term in the Hamiltonian, $\cos\omega t$ oscillates rapidly and I neglect its effect by means of a rotating-wave approximation. More interesting is the combination of σ_z with the second motional term, containing the ladder operators a_m and $a_m^\dagger$. This part, which is near resonance when $\omega \approx \nu_m$, does not lead to a transition between internal states either, but represents a spin-dependent force that drives the centre-of-mass motion around in phase space. I will have more to say about this kind of interaction in chapter 8.

The diagonal part does not play an important role for our purposes because $\mu_\mathrm{e} - \mu_\mathrm{g}$ is very small for clock qubits, as discussed in appendix A. Instead, I will consider the off-diagonal part and assume that ω is close to $\bar{\omega}_\mathrm{eg}$. For states in the ground level of $^{43}\mathrm{Ca}^+$ one has $\nu_m \ll \bar{\omega}_\mathrm{eg}$, which means that all diagonal terms will be oscillating relatively fast and may be neglected in yet another application of the rotating-wave approximation.

The final interaction Hamiltonian to first order in x_m thus becomes

$$\begin{aligned}\widetilde{H}_\mathrm{int}(t) = \frac{1}{2}R_{\mathrm{eg},q}\,\sigma_+ \Bigg(& B^+_{-q}(\mathbf{x}_0)\,\mathrm{e}^{-\mathrm{i}\delta t} \\ & + \sum_m \sum_r \partial_m B^+_{-q}(\mathbf{x}_0)\, x_{m,0}\, c_{2r,m} \left[\mathrm{e}^{-\mathrm{i}(\delta-\nu_m-r\omega_\mathrm{rf})t}\, a_m^\dagger + \mathrm{e}^{-\mathrm{i}(\delta+\nu_m+r\omega_\mathrm{rf})t}\, a_m\right]\Bigg) \\ & + \mathrm{H.c.}\end{aligned} \tag{5.38}$$

I have introduced the detuning $\delta = \omega - \bar{\omega}_\mathrm{eg}$ of the microwave field from the effective transition frequency between the internal states, after adjusting for ac Zeeman shifts. This Hamiltonian represents a coupling between internal states, induced by the interaction of the transition dipole moment $\langle \mathrm{e}|\mu_q|\mathrm{g}\rangle$ with the microwave magnetic field and modified by the motional state of the atom. It is evident from the expression above that by choosing the detuning δ appropriately, one may selectively place a

particular term in this Hamiltonian close to resonance.

Carrier transitions: If $\delta \approx 0$, the resonant part of $\widetilde{H}_{\mathrm{int}}(t)$ is given by

$$\widetilde{H}_{\mathrm{car}}(t) = \frac{1}{2} R_{\mathrm{eg},q}\, \sigma_+\, B^+_{-q}(\mathbf{x}_0)\, \mathrm{e}^{-\mathrm{i}\delta t} + \mathrm{H.c.}\,. \tag{5.39}$$

It will drive transitions $|\downarrow\rangle\,|\mathbf{n}\rangle \leftrightarrow |\uparrow\rangle\,|\mathbf{n}\rangle$, such that the internal state changes while the motional state remains unaffected. This is referred to as a *carrier* transition. Let us assume that the atom starts in a definite eigenstate of the three-dimensional oscillator, for example $|\downarrow\rangle\,|\mathbf{n}\rangle$ for some $\mathbf{n}$. If the carrier contribution $\widetilde{H}_{\mathrm{car}}(t)$ is close to resonance, it will vary slowly with time, while the other parts of the total Hamiltonian $\widetilde{H}_{\mathrm{int}}(t)$, as given in eq. (5.38), contain exponentials that oscillate quickly since they are off-resonant. By considering the action of a_m, $a_m^\dagger$ in the $\{|n_m\rangle\}$ basis, it can be seen that the off-resonant terms couple the state $|\downarrow\rangle\,|\mathbf{n}\rangle$ to states $|\uparrow\rangle\,|\mathbf{n'}\rangle$ that differ in occupation of the motional modes. With the same reasoning as used earlier to adiabatically eliminate off-resonant internal states, one may now remove the off-resonant motional states from the description of the dynamics. It should be noted that this procedure requires the couplings to off-resonant states to be much smaller than the detunings from the respective resonance frequencies. As a result of the elimination procedure, the Hilbert space is further reduced and now only contains the two states $|\downarrow\rangle\,|\mathbf{n}\rangle$ and $|\uparrow\rangle\,|\mathbf{n}\rangle$. However, the transition frequency of this effective two-state system is modified slightly by additional ac Zeeman shifts due to the coupling to off-resonant motional states. In the $\{|i\rangle\,|\mathbf{n}\rangle\}$ basis, the components of the two states evolve as

$$\frac{d}{dt} C_{\uparrow,n_1,n_2,n_3} = \hbar \Delta_{\mathrm{e}}^{\mathrm{ac,car}}\, C_{\uparrow,n_1,n_2,n_3} + \frac{\hbar}{2} \Omega_{\mathrm{car}}\, \mathrm{e}^{\mathrm{i}\phi_{\mathrm{car}}}\, \mathrm{e}^{-\mathrm{i}\delta t}\, C_{\downarrow,n_1,n_2,n_3} \tag{5.40}$$

$$\frac{d}{dt} C_{\downarrow,n_1,n_2,n_3} = \hbar \Delta_{\mathrm{g}}^{\mathrm{ac,car}}\, C_{\downarrow,n_1,n_2,n_3} + \frac{\hbar}{2} \Omega_{\mathrm{car}}\, \mathrm{e}^{-\mathrm{i}\phi_{\mathrm{car}}}\, \mathrm{e}^{\mathrm{i}\delta t} C_{\uparrow,n_1,n_2,n_3}\,, \tag{5.41}$$

where $\Delta_i^{\mathrm{ac,car}}$ denotes the ac Zeeman shift relevant for a carrier transition. The evolution can be expressed by means of an effective interaction Hamiltonian for the two-state system. After removal of the ac shifts from the diagonal elements, it takes

the form

$$\widetilde{H}_{\rm car}(t) = \frac{\hbar}{2}\,\Omega_{\rm car}\,{\rm e}^{{\rm i}\phi_{\rm car}}\,\sigma_+\,{\rm e}^{-{\rm i}\epsilon_{\rm car}t} + \text{ H.c. }, \tag{5.42}$$

where the Rabi frequency $\Omega_{\rm car}$, phase $\phi_{\rm car}$ and relevant detuning $\epsilon_{\rm car}$ are defined as

$$\hbar\Omega_{\rm car} = |R_{{\rm eg},q}|\,\left|B^+_{-q}(\mathbf{x}_0)\right|, \tag{5.42a}$$

$$\phi_{\rm car} = \arg\left(R_{{\rm eg},q}\right) + \arg\left[B^+_{-q}(\mathbf{x}_0)\right], \tag{5.43}$$

$$\epsilon_{\rm car} = \delta - \Delta_{\rm eg}^{\rm ac,car}\ . \tag{5.44}$$

With the convention used here, all Rabi frequencies are real nonnegative numbers. The quantity $\Delta_{\rm eg}^{\rm ac,car} = \Delta_{\rm e}^{\rm ac,car} - \Delta_{\rm g}^{\rm ac,car}$ denotes the differential ac Zeeman shift induced on the two relevant states.

Red sideband transitions: If $\delta \approx -\nu_m - s_{\rm rf}\,\omega_{\rm rf}$, with $s_{\rm rf}$ integer, the atom will undergo an internal transition accompanied by a simultaneous decrease in occupation number for mode m from $|n_m\rangle$ to $|n_m - 1\rangle$, driven by the term

$$\widetilde{H}_{\rm rsb}(t) = \frac{1}{2}R_{{\rm eg},q}\,\sigma_+\,\partial_m B^+_{-q}(\mathbf{x}_0)\,x_{m,0}\,c_{2s_{\rm rf},m}\,{\rm e}^{-{\rm i}(\delta+\nu_m+s_{\rm rf}\omega_{\rm rf})t}\,a_m + \text{ H.c. }. \tag{5.45}$$

One speaks of the transition as proceeding via the first-order *red secular sideband* of mode m and $|s_{\rm rf}|$-th order red ($s_{\rm rf} > 0$) or blue ($s_{\rm rf} < 0$) *micromotion sideband*. To first order in x_m, the occupation number of only one mode may change by one motional quantum. When $\widetilde{H}_{\rm rsb}(t)$ for mode m is near-resonant, one may obtain an effective two-state system formed by the states $|{\downarrow}\rangle\,|n_m\rangle\,|\mathbf{n}_0\rangle$ and $|{\uparrow}\rangle\,|n_m - 1\rangle\,|\mathbf{n}_0\rangle$ by eliminating motional states coupled by the off-resonant contributions of the interaction Hamiltonian. The term $|n_m\rangle$ here represents the mode of which the sideband is driven near resonance, while $|\mathbf{n}_0\rangle$ corresponds to the remaining modes. Using the action of ladder operators on number states,

$$a_m\,|n_m\rangle = \sqrt{n_m}\,|n_m - 1\rangle\,, \tag{5.45a}$$

$$a_m^\dagger\,|n_m\rangle = \sqrt{n_m + 1}\,|n_m + 1\rangle\ , \tag{5.46}$$

the Hamiltonian for the two-state system may be expressed as

$$\widetilde{H}_{\mathrm{rsb}}(t) = \frac{\hbar}{2}\,\Omega_{\mathrm{rsb}}\,\mathrm{e}^{\mathrm{i}\phi_{\mathrm{rsb}}}\,\sigma_+\,\mathrm{e}^{-\mathrm{i}\epsilon_{\mathrm{rsb}}t} + \mathrm{H.c.}\,, \tag{5.47}$$

where for pure secular sidebands ($s_{\mathrm{rf}} = 0$) the relevant parameters are given by

$$\hbar\Omega_{\mathrm{rsb}} = \sqrt{n_m}\;|R_{\mathrm{eg},q}|\;\left|\partial_m B^+_{-q}(\mathbf{x}_0)\right| x_{m,0}\,c_{0,m}, \tag{5.48}$$

$$\phi_{\mathrm{rsb}} = \arg\left(R_{\mathrm{eg},q}\right) + \arg\left[\partial_m B^+_{-q}(\mathbf{x}_0)\right], \tag{5.49}$$

$$\epsilon_{\mathrm{rsb}} = \delta - \Delta_{\mathrm{eg}}^{\mathrm{ac,rsb}} + \nu_m\,. \tag{5.50}$$

Blue sideband transitions: Similarly, if $\delta \approx \nu_m + s_{\mathrm{rf}}\,\omega_{\mathrm{rf}}$, an internal transition occurs with a simultaneous increase in occupation number of one mode from $|n_m\rangle$ to $|n_m+1\rangle$, caused by the resonant contribution

$$\widetilde{H}_{\mathrm{bsb}}(t) = \frac{1}{2}R_{\mathrm{eg},q}\,\sigma_+\,\partial_m B^+_{-q}(\mathbf{x}_0)\,x_{m,0}\,c_{2s_{\mathrm{rf}},m}\,\mathrm{e}^{-\mathrm{i}(\delta-\nu_m-s_{\mathrm{rf}}\omega_{\mathrm{rf}})t}\,a_m^\dagger + \mathrm{H.c.}\,. \tag{5.51}$$

This is called a transition on the first-order blue secular sideband of mode m and $|s_{\mathrm{rf}}|$-th order blue ($s_{\mathrm{rf}} > 0$) or red ($s_{\mathrm{rf}} < 0$) micromotion sideband. After elimination of off-resonant motional states, the effective two-state system is now formed by $|\downarrow\rangle\,|n_m\rangle\,|\mathbf{n}_0\rangle$ and $|\uparrow\rangle\,|n_m+1\rangle\,|\mathbf{n}_0\rangle$, which are coupled by the Hamiltonian

$$\widetilde{H}_{\mathrm{bsb}}(t) = \frac{\hbar}{2}\,\Omega_{\mathrm{bsb}}\,\mathrm{e}^{\mathrm{i}\phi_{\mathrm{bsb}}}\,\sigma_+\,\mathrm{e}^{-\mathrm{i}\epsilon_{\mathrm{bsb}}t} + \mathrm{H.c.}\,. \tag{5.52}$$

For pure secular sidebands, one finds

$$\hbar\Omega_{\mathrm{bsb}} = \sqrt{n_m+1}\;|R_{\mathrm{eg},q}|\;\left|\partial_m B^+_{-q}(\mathbf{x}_0)\right| x_{m,0}\,c_{0,m}, \tag{5.53}$$

$$\phi_{\mathrm{bsb}} = \arg\left(R_{\mathrm{eg},q}\right) + \phi_{\mathrm{rsb}} = \arg\left[\partial_m B^+_{-q}(\mathbf{x}_0)\right], \tag{5.54}$$

$$\epsilon_{\mathrm{bsb}} = \delta - \Delta_{\mathrm{eg}}^{\mathrm{ac,bsb}} - \nu_m\,. \tag{5.55}$$

The three different types of transitions are pictured in figure 5.1. Note that, to first order in x_m, the carrier Rabi frequency does not depend on the initial motional state $|\mathbf{n}\rangle$. The Rabi frequencies for sideband transitions do of course depend on

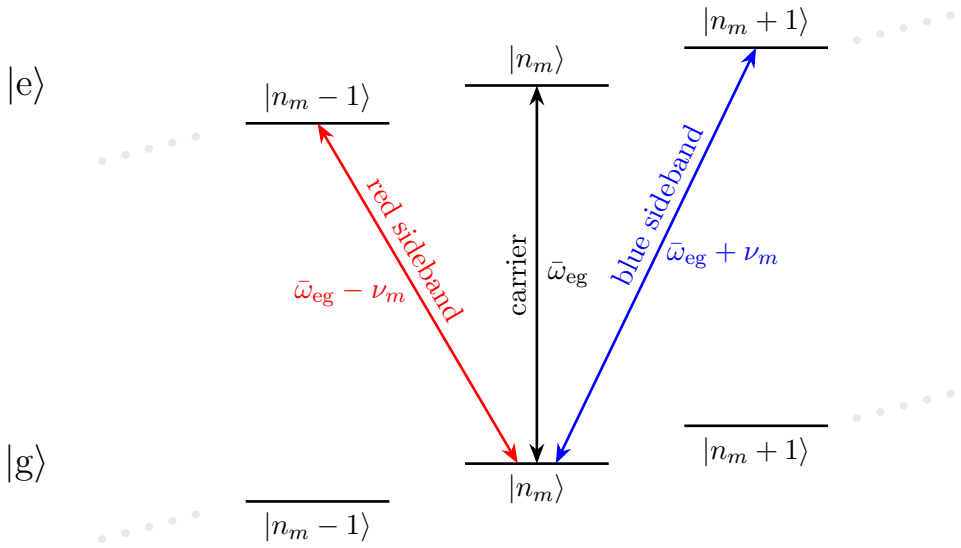


Figure 5.1: Possible transitions between internal and motional states to first order in x_m. Only the motional states corresponding to the mode undergoing a change in occupation number are shown. The resonance frequencies indicated omit additional Zeeman shifts arising from couplings to off-resonant motional states.

$|\mathbf{n}\rangle$, but they only involve the occupation number of the relevant mode m that the sideband is driven on, not the occupation numbers of the spectator modes.

It is evident that the coupling strength of the carrier transition depends on the amplitude of the relevant component of the microwave magnetic field at the trap centre, while the sideband coupling depends on the gradient of the field component. In analogy with laser-mediated transitions, one may introduce an effective Lamb-Dicke parameter

$$\bar{\eta}_m = \sqrt{\frac{\hbar}{2M\nu_m}}\, c_{0,m}\, \frac{\left|\partial_m B^+_{-q}(\mathbf{x}_0)\right|}{\left|B_{-q}(\mathbf{x}_0)\right|}\,, \tag{5.56}$$

so that the sideband Rabi frequencies can be written

$$\Omega_{\mathrm{rsb}} = \sqrt{n_m}\,\bar{\eta}_m\,\Omega_{\mathrm{car}} \tag{5.56a}$$

$$\Omega_{\mathrm{bsb}} = \sqrt{n_m+1}\,\bar{\eta}_m\,\Omega_{\mathrm{car}}\,. \tag{5.57}$$

The treatment so far has assumed that any stray dc electric fields have been completely compensated so that the equilibrium position of the ion coincides with the rf null and no excess micromotion is present. This is why I have been using expression (5.30) for $u_m(t)$, which is a solution of the classical homogeneous Math-

ieu equation. The modulation of $u_m(t)$ at the rf frequency ω_{rf} and all the effects resulting from it, such as the appearance of additional resonances in the form of micromotion sidebands, are therefore induced by the *intrinsic* micromotion of the trapped particle.

5.2.3.1 Effects of higher orders in position operator

I have only included terms linear in x_m in (5.38), so one might wonder what effects higher-order terms have and under what conditions ignoring them is justified. Inspection of (5.28) shows that the second-order contribution to $\widetilde{H}_{\mathrm{int}}(t)$ takes the form

$$\frac{1}{2}R_{\mathrm{eg},q}\,\sigma_+\,\mathrm{e}^{-\mathrm{i}\delta t}\sum_{i,j}\partial^2_{ij}B^+_{-q}(\mathbf{x}_0)\,x_{i,0}\,x_{j,0}\big[u_i(t)\,a_i^\dagger+u_i^*(t)\,a_i\big]\big[u_j(t)\,a_j^\dagger+u_j^*(t)\,a_j\big]\ . \tag{5.58}$$

Terms containing $a_i^\dagger a_j^\dagger$ represent couplings between $|n_i\rangle\,|n_j\rangle$ and $|n_i+1\rangle\,|n_j+1\rangle$ and thus lead to transitions during which two motional modes undergo an increase in occupation number or, for $i=j$, couplings between $|n_i\rangle$ and $|n_i+2\rangle$, which cause a mode to gain two quanta of motion. In the terminology introduced earlier, the latter case would be referred to as a second-order blue sideband. Similarly, terms with $a_i a_j$ lead to higher-order red sidebands. For the mixed terms $a_i^\dagger a_j$, two cases may be distinguished: if $i\neq j$, they cause transitions during which the occupation number of one mode increases while that of another decreases. If $i=j$, they represent a carrier transition. Each term in (5.58) oscillates at the respective sum or difference of secular frequencies, which may be further affected by micromotion. I will not treat second-order effects in detail, but it is instructive to look at the last case mentioned. Its contribution is given by

$$\frac{1}{2}R_{\mathrm{eg},q}\,\sigma_+\sum_i\sum_{r_1,r_2}\partial^2_{ii}B^+_{-q}(\mathbf{x}_0)\,x^2_{i,0}\,c_{2r_1,i}\,c_{2r_2,i}\,\mathrm{e}^{-\mathrm{i}[\delta-(r_1-r_2)\omega_{\mathrm{rf}}]t}\left(a_i^\dagger a_i+a_i a_i^\dagger\right)\ , \tag{5.59}$$

or, in the $\{|\mathbf{n}\rangle\}$ basis,

$$\frac{1}{2}R_{\mathrm{eg},q}\,\sigma_+\sum_i\sum_{r_1,r_2}\partial_{ii}^2 B_{-q}^+(\mathbf{x}_0)\,x_{i,0}^2\,c_{2r_1,i}\,c_{2r_2,i}\,(2n_i+1)\,\mathrm{e}^{-\mathrm{i}[\delta-(r_1-r_2)\omega_{\mathrm{rf}}]t}\,|n_i\rangle\langle n_i|\;. \tag{5.60}$$

The terms for which $r_1 = r_2$ will be close to resonance when $\delta \approx 0$ and therefore result in a correction to the carrier Rabi frequency:

$$\hbar\Omega_{\mathrm{car}}^{(2)} = R_{\mathrm{eg},q}\sum_i\sum_r \partial_{ii}^2 B_{-q}^+(\mathbf{x}_0)\,x_{i,0}^2\,c_{2r,i}\,c_{-2r,i}\,(2n_i+1)\;. \tag{5.61}$$

Additionally, pure micromotion sidebands can be driven whenever $\delta \approx s_{\mathrm{rf}}\,\omega_{\mathrm{rf}}$, with s_{rf} integer. Contrary to secular sidebands, they couple the internal states but do not lead to a change in motional state. This is further reflected by the fact that the secular frequencies ν_i do not appear in (5.60) and terms from all three modes will therefore be on resonance at the same time. The corresponding Rabi frequencies are found to be

$$\hbar\Omega_{\mathrm{imm}}^{(s_{\mathrm{rf}})} = \sum_i\sum_r \partial_{ii}^2 B_{-q}^+(\mathbf{x}_0)\,x_{i,0}^2\,c_{2r,i}\,c_{2r+2s_{\mathrm{rf}},i}\,(2n_i+1)\;. \tag{5.62}$$

5.2.3.2 Excess micromotion

If the extremum of the dc potential does not lie on the rf null, then the dc electric field around the trap centre $\mathbf{x}_0$ will contain a spatially uniform contribution, which leads to the appearance of an inhomogeneous term in the equations of motion. This situation was discussed in section 4.2.2, where it was found that the position operator then takes the form

$$x_m^{(\mathrm{I})}(t) = x_{m,0}\big[u_m(t)\,b_m^\dagger + u_m^*(t)\,b_m\big] + \tilde{u}_{\mathrm{p},m}(t)\,\mathbb{I}\;, \tag{5.63}$$

where $\tilde{u}_{\mathrm{p},m}(t)$, as given in eq. (4.19), is a particular solution to the classical inhomogeneous equation and is periodic with period $T = 2\pi/\omega_{\mathrm{rf}}$. Owing to its periodicity,

$\tilde{u}_{\mathrm{p},m}(t)$ may be written as a Fourier series in the form

$$\tilde{u}_{\mathrm{p},m}(t) = \sum_{r\in\mathbb{Z}} d_{2r,m}\, \mathrm{e}^{\mathrm{i}r\omega_{\mathrm{rf}}t} \,. \tag{5.64}$$

The interaction Hamiltonian in the presence of excess micromotion still takes the same form as in eq. (5.31), but $x_m^{(\mathrm{I})}(t)$ is now given by expression (5.63). The treatment otherwise proceeds in the same way as for the homogeneous case and one finds that the interaction Hamiltonian acting in the space of the resonant internal states becomes

$$\begin{aligned}\widetilde{H}_{\mathrm{int}}(t) = \frac{1}{2}R_{\mathrm{eg},q}\,\sigma_+ \Bigg(& B^+_{-q}(\mathbf{x}_0)\,\mathrm{e}^{-\mathrm{i}\delta t} \\ & + \sum_m \sum_r \partial_m B^+_{-q}(\mathbf{x}_0) x_{m,0}\, c_{2r,m} \left[\mathrm{e}^{-\mathrm{i}(\delta-\nu_m-r\omega_{\mathrm{rf}})t}\, a_m^\dagger + \mathrm{e}^{-\mathrm{i}(\delta+\nu_m+r\omega_{\mathrm{rf}})t}\, a_m\right] \\ & + \sum_m \sum_r \partial_m B^+_{-q}(\mathbf{x}_0)\, d_{2r,m}\, \mathrm{e}^{-\mathrm{i}(\delta-r\omega_{\mathrm{rf}})t} \Bigg) \\ & + \text{H.c.} \,.\end{aligned} \tag{5.65}$$

One observes that excess micromotion gives rise to an additional term in the interaction Hamiltonian, contained in the third line of eq. (5.65). This term does not change the motional state, but causes a transition between internal states. It may be driven resonantly whenever the detuning is adjusted such that $\delta \approx s_{\mathrm{rf}}\omega_{\mathrm{rf}}$, with s_{rf} integer. I will refer to such a transition as an excess micromotion sideband. The Rabi frequency for the first-order sideband is given by

$$\hbar\Omega_{\mathrm{emm}} = R_{\mathrm{eg},q} \sum_m \partial_m B^+_{-q}(\mathbf{x}_0)\, d_{2,m} \,. \tag{5.66}$$

In the lowest-order approximation for motion in the rf trapping potential, one finds that

$$d_{2,m} = -\frac{Ze}{M\nu_m^2} \frac{q_m}{4\,(1-q_m)} E_{\mathrm{emm},m}(\mathbf{x}_0) \,, \tag{5.67}$$

where q_m is the Mathieu q parameter for motion along the principal axis labelled by m and $E_{\mathrm{emm},m}(\mathbf{x}_0)$ is the component along that axis of the uncompensated electric field $\mathbf{E}_{\mathrm{emm}}$ at the trap centre causing excess micromotion. This shows that Ω_{emm} depends on $\mathbf{E}_{\mathrm{emm}}$, which means that micromotion sideband transitions may be used

to probe the strength of any uncompensated fields. As long as the component of the magnetic field responsible for the coupling between internal states has a non-zero gradient along principal axis m, micromotion along that axis may be detected.

5.2.4 Ac Zeeman shifts

When an ideal two-state system, comprised of a ground state with energy E_{g} and an excited state with energy E_{e}, is driven by a sinusoidal perturbation of frequency ω, the transition probability reaches unity when $\omega = \omega_{\mathrm{eg}} = (E_{\mathrm{e}} - E_{\mathrm{e}})/\hbar$. At this point, the driving frequency is exactly equal to the Bohr frequency between the two states[3]. The situation is different if the system is made up of multiple states, as is the case for an atom, which contains states corresponding to the internal and the centre-of-mass degrees of freedom. Applying a driving field to such a system results in various couplings between states, determined by the polarisation of the field and the matrix elements between atomic states. If one is only interested in the dynamics for a particular pair of states, it is often possible to find an effective Hamiltonian by adiabatic elimination of the remaining states, as explained in the previous section. The effect of couplings of the two states of interest to eliminated states then results in an apparent shift of the resonance frequency of the former, so that maximum transition probability no longer occurs at $\omega = \omega_{\mathrm{eg}}$.

I will illustrate this effect on the clock qubit in $^{43}\mathrm{Ca}^{+}$, as shown in fig. 5.2. In this case $|\mathrm{g}\rangle = |4, +1\rangle$ and $|\mathrm{e}\rangle = |3, +1\rangle$. When a sinusoidal magnetic field $\mathbf{B}_\omega$ of frequency ω is applied to the ion, each qubit state may couple to a number of other states, depending on the components B_q of the field. To first order in x_m, couplings caused by both carrier and sideband terms in the Hamiltonian will be present. If the detunings $\omega - \omega_{\mathrm{e}j}$ and $\omega - \omega_{\mathrm{g}j}$ for all possible transitions out of the qubit states are much larger than the corresponding Rabi frequencies, one may eliminate all states other than the qubit states. In most cases, couplings via sidebands are much smaller than couplings via the carrier and one may neglect contributions to the shift resulting from the former. As shown in appendix C, the ac Zeeman shift induced on

[3] I neglect the Bloch-Siegert shift, by which I mean the shift in resonance frequency due to the counter-rotating term of the near-resonant driving field, as it is very small if the transition is weakly driven.

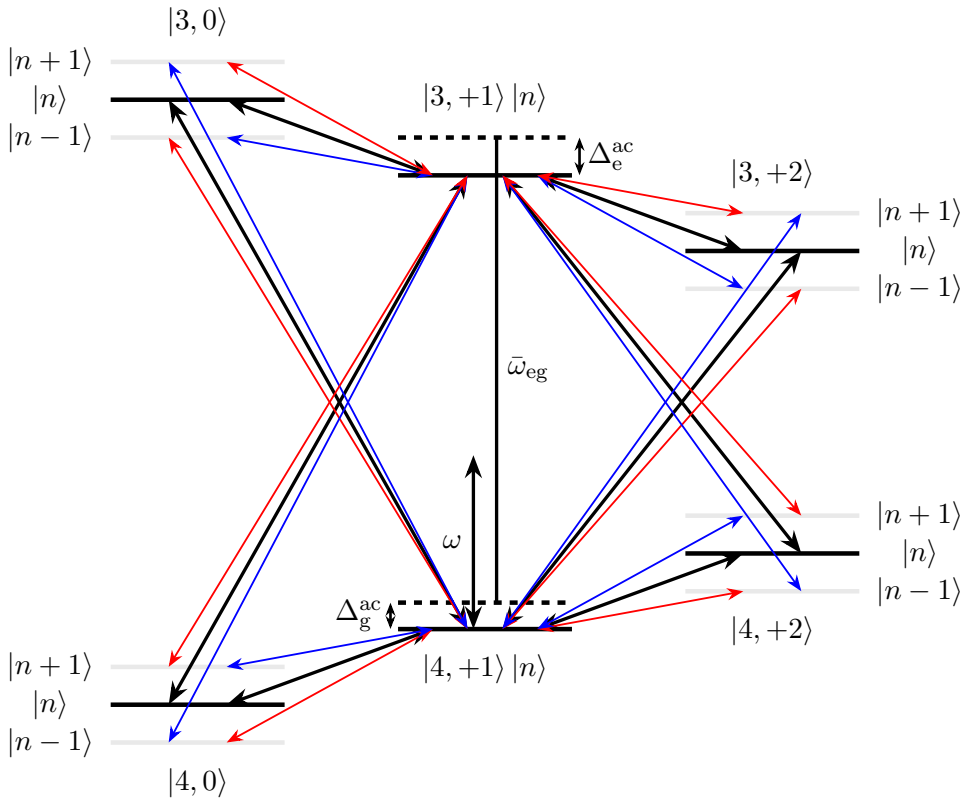


Figure 5.2: Ac Zeeman shifts on clock qubit resulting from adiabatic elimination of off-resonant internal states. Only one motional mode is shown. A magnetic field of frequency ω leads to couplings between states in the ground level that depend on the polarisation of the field. As long as the respective detuning $\omega - \omega_{ij}$ is much larger than the Rabi frequency for transitions from the qubit to adjacent states, the effect of the field is only to cause a shift $\Delta_{\mathrm{e}}^{\mathrm{ac}} - \Delta_{\mathrm{g}}^{\mathrm{ac}}$ in the resonance frequency of the qubit.

internal state $|i\rangle$, with $i \in \{\mathrm{g}, \mathrm{e}\}$ is then given by

$$\Delta_i^{\mathrm{ac}} = -\frac{1}{4} \sum_k R_{q,ki}^2 \left[\frac{\left|B_{-q}^{+}(\mathbf{x}_0)\right|^2}{\omega_{ki} - \omega} + \frac{\left|B_{-q}^{-}(\mathbf{x}_0)\right|^2}{\omega_{ki} + \omega} \right], \tag{5.68}$$

where the sum runs over all eliminated internal states $|k\rangle$ and $\omega_{ki} = (E_k - E_i)/\hbar$ as before.

The origin of the magnetic field $\mathbf{B}_\omega$ was left unspecified. It may be a background field that is always present, such as the magnetic field resulting from the small but finite current flowing through the rf trap electrodes. Such a field is usually far detuned from the bare qubit frequency ω_{eg} itself and the frequencies $\omega_{\mathrm{e}j}$, $\omega_{\mathrm{g}j}$. Its only effect is then to induce a small shift in the qubit states. However, $\mathbf{B}_\omega$ may also

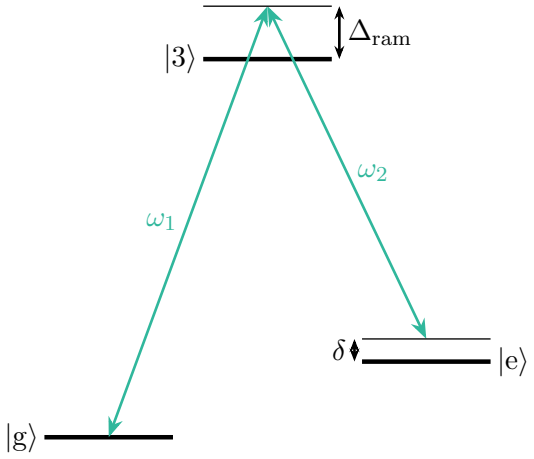


Figure 5.3: Raman transition.

represent the field used to drive transitions between the qubit states, in which case its frequency will be close to ω_{eg}. Its effect is then two-fold: it shifts the effective qubit resonance frequency to $\bar{\omega}_{\mathrm{eg}}$ via couplings from off-resonant spectator transitions and, having adjusted for this shift, drives the evolution within the subspace spanned by the qubit and their attached motional states. In general, there may be several background and driving fields present. Since adiabatic elimination is a perturbative method, the total ac Zeeman shift in this case is just the sum over the shifts induced by the individual fields.

5.3 Raman transitions

Instead of a magnetic field, it is possible to use a time-dependent electric field to drive transitions between states within a fine-structure level. However, the selection rule $\Delta l = 1$ for the electric-dipole interaction forbids direct single-photon transitions. The desired coupling between two states may nevertheless be achieved indirectly by means of a two-photon Raman transition mediated by a third state, which requires the total electric field to be a superposition of two individual fields of suitable frequencies. Historically, the first demonstrations of qubit gate operations used this laser-based approach [TWK+98].

The method is illustrated in fig. 5.3. A three-state system formed by $|\mathrm{g}\rangle$, $|\mathrm{e}\rangle$, $|3\rangle$, with $E_{\mathrm{g}} < E_{\mathrm{e}} < E_3$, interacts with two electric fields of wave vectors $\mathbf{k}_1$, $\mathbf{k}_2$ and

frequencies ω_1, ω_2 respectively. Each field can be written as

$$\mathbf{E}_a(\mathbf{x},t) = \frac{1}{2}E_{a,0}\left[\boldsymbol{\epsilon}_a\,\mathrm{e}^{\mathrm{i}(\mathbf{k}_a\cdot\mathbf{x}-\omega_a t+\phi_a)} + \boldsymbol{\epsilon}_a^*\,\mathrm{e}^{-\mathrm{i}(\mathbf{k}_a\cdot\mathbf{x}-\omega_a t+\phi_a)}\right], \tag{5.69}$$

where $\boldsymbol{\epsilon}$ is a unit polarisation vector[4]. In the absence of any driving fields, the Hamiltonian $H_0(t)$ is given by eq. 5.1 as before. When the Raman beams are applied to the ion, there arises an additional interaction represented by the Schrödinger-picture Hamiltonian

$$H_{\mathrm{int}}(t) = H_{\mathrm{ram}}(t) = -\mathbf{d}\cdot\left[\mathbf{E}_1(\mathbf{x},t)+\mathbf{E}_2(\mathbf{x},t)\right]. \tag{5.70}$$

The variable $\mathbf{d}$ is the total electric dipole moment of the atom. For an atom with a single valence electron outside closed subshells, $\mathbf{d} = -e\mathbf{r}$, where $\mathbf{r}$ is the position vector of the electron relative to the nucleus.

I will follow the same steps as I did earlier for the magnetic-dipole interaction. In the interaction picture with respect to $H_0(t)$, one finds

$$\begin{aligned} H_{\mathrm{int}}^{(\mathrm{I})}(t) = \frac{1}{2}\sum_{i,j}\mathrm{e}^{\mathrm{i}\omega_{ij}t}\,|i\rangle\langle j| \\ \times\left[eE_{1,0}\langle i|\mathbf{r}\cdot\boldsymbol{\epsilon}_1|j\rangle\,\mathrm{e}^{\mathrm{i}\mathbf{k}_1\cdot\mathbf{x}^{(\mathrm{I})}(t)}\,\mathrm{e}^{-\mathrm{i}\omega_1 t}\,\mathrm{e}^{\mathrm{i}\phi_1} + eE_{2,0}\langle i|\mathbf{r}\cdot\boldsymbol{\epsilon}_2|j\rangle\,\mathrm{e}^{\mathrm{i}\mathbf{k}_2\cdot\mathbf{x}^{(\mathrm{I})}(t)}\,\mathrm{e}^{-\mathrm{i}\omega_2 t}\,\mathrm{e}^{\mathrm{i}\phi_2} + \mathrm{H.c.}\right], \end{aligned} \tag{5.71}$$

The components $x_m^{(\mathrm{I})}(t)$ of the position operator in the interaction picture are given by eq. (5.63).

For simplicity, I will assume that laser 1 only couples states $|\mathrm{g}\rangle$ and $|3\rangle$, while laser 2 only couples $|\mathrm{e}\rangle$ and $|3\rangle$. After adiabatic elimination of the third state [WMI+98], the effective Raman Hamiltonian is obtained in the form[5]

$$\begin{aligned} H_{\mathrm{int}}^{(\mathrm{I})}(t) = \hbar\Delta_{\mathrm{g}}^{\mathrm{ac}}\,|\mathrm{g}\rangle\langle\mathrm{g}| + \hbar\Delta_{\mathrm{e}}^{\mathrm{ac}}\,|\mathrm{e}\rangle\langle\mathrm{e}| \\ + \left[\frac{\hbar}{2}\Omega_{\mathrm{ram}}\,\mathrm{e}^{\mathrm{i}\mathbf{k}_{\mathrm{ram}}\cdot\mathbf{x}^{(\mathrm{I})}(t)}\,\mathrm{e}^{-\mathrm{i}(\omega_{\mathrm{ram}}-\omega_{\mathrm{eg}})t}\,\mathrm{e}^{\mathrm{i}\phi_{\mathrm{ram}}}|\mathrm{e}\rangle\langle\mathrm{g}| + \mathrm{H.c.}\right], \end{aligned} \tag{5.72}$$

[4] Unit vector with respect to the norm $|\boldsymbol{\epsilon}|^2 = \sum_i \epsilon_i\epsilon_i^*$.

[5] More generally, the system may contain several higher-energy intermediate states through which Raman transitions proceed. The method of adiabatic elimination can still be applied in this case, but the expressions for Ω_{ram} and Δ_i^{ac} will be more complicated, containing contributions from couplings to all intermediate states.

where $\mathbf{k}_{\mathrm{ram}} = \mathbf{k}_1 - \mathbf{k}_2$, $\omega_{\mathrm{ram}} = \omega_1 - \omega_2$ and $\phi_{\mathrm{ram}} = \phi_1 - \phi_2$. The Rabi frequency Ω_{ram} and ac Stark shifts Δ_i^{ac} are given by

$$\Omega_{\mathrm{ram}} = \frac{|\Omega_1||\Omega_2|}{2\Delta_{\mathrm{ram}}}, \tag{5.73}$$

$$\Delta_{\mathrm{g}}^{\mathrm{ac}} = -\frac{|\Omega_1|^2}{4\Delta_{\mathrm{ram}}}, \tag{5.74}$$

$$\Delta_{\mathrm{e}}^{\mathrm{ac}} = -\frac{|\Omega_2|^2}{4\Delta_{\mathrm{ram}}}, \tag{5.75}$$

in terms of the single-photon Rabi frequencies $\Omega_1 = eE_{1,0}\langle 3|\mathbf{r}\cdot\boldsymbol{\epsilon}_1|\mathrm{g}\rangle/\hbar$ and $\Omega_2 = eE_{2,0}\langle 3|\mathbf{r}\cdot\boldsymbol{\epsilon}_2|\mathrm{e}\rangle/\hbar$. The Raman interaction thus results in a Hamiltonian that takes the same form as if the transition between internal states $|\mathrm{g}\rangle$ and $|\mathrm{e}\rangle$ was driven directly. Analogous to the case of magnetic-dipole transitions, the interaction Hamiltonian couples different motional states owing to the exponential factor containing the position operator. In general, both secular and micromotion has to be considered. However, I will neglect the effects of the latter in this section and assume that the trapping potential can be approximated as that of a pure three-dimensional harmonic oscillator. This corresponds to the pseudopotential approximation discussed in section 4.3. The components of the position operator along the three principal axes are then given by $x_m^{(\mathrm{I})}(t) = x_{m,0}\big[\exp(\mathrm{i}\nu_m t)\, a_m^\dagger + \exp(-\mathrm{i}\nu_m t)\, a_m\big]$. After transformation to another rotating frame to remove the constant ac shifts, the interaction Hamiltonian can be written

$$\widetilde{H}_{\mathrm{int}}(t) = \frac{\hbar}{2}\Omega_{\mathrm{ram}}\, \mathrm{e}^{-\mathrm{i}\delta t}\, \mathrm{e}^{\mathrm{i}\phi_{\mathrm{ram}}}\, \sigma_+ \, \exp\left[\mathrm{i}\sum_m k_m\, x_{m,0}\left(\mathrm{e}^{\mathrm{i}\nu_m t}a_m^\dagger + \mathrm{e}^{-\mathrm{i}\nu_m t}a_m\right)\right] + \mathrm{H.c.}\,, \tag{5.76}$$

where I have introduced the detuning $\delta = \omega_{\mathrm{ram}} - \left(\omega_{\mathrm{eg}} + \Delta_{\mathrm{eg}}^{\mathrm{ac}}\right)$ from the effective resonance frequency of the internal states. I will focus on the motional term of the interaction Hamiltonian, containing the various ladder operators $a_m^\dagger$ and a_m. Since ladder operators of different harmonic-oscillator modes commute, the motional term can be transformed into a product of three individual exponential factors, each of the form

$$D_m\big[\alpha_m(t)\big] = \exp\Big[\mathrm{i}k_m\, x_{m,0}\left(\mathrm{e}^{\mathrm{i}\nu_m t}a_m^\dagger + \mathrm{e}^{-\mathrm{i}\nu_m t}a_m\right)\Big] = \mathrm{e}^{\alpha_m(t)a_m^\dagger - \alpha_m^*(t)a_m} \tag{5.77}$$

with

$$\alpha_m(t) = \mathrm{i}\eta_m \mathrm{e}^{\mathrm{i}\nu_m t} \; . \tag{5.78}$$

I have introduced the Lamb-Dicke parameters $\eta_m = k_m x_{m,0}$, which are a measure of the extent of the ground-state wave packet relative to the wavelength of the coupling radiation. The operator $D_m\big[\alpha_m(t)\big]$ represents a displacement operator for the harmonic oscillator corresponding to mode m.

To determine the time evolution of the system, the state vector is expanded in the basis $\{|i\rangle\,|\mathbf{n}\rangle\}$, as was done in eq. (5.36). The differential equations for the coefficients $c_{i,\mathbf{n}}(t)$ then involve the matrix elements of $\widetilde{H}_{\mathrm{int}}(t)$ between these states. One finds

$$\langle \mathbf{n}'|\langle\uparrow|\widetilde{H}_{\mathrm{int}}(t)|\downarrow\rangle|\mathbf{n}\rangle = \frac{\hbar}{2}\Omega_{\mathrm{ram}} \Big(\prod_m \langle n'_m|D_m\big[\alpha_m(t)\big]|n_m\rangle\Big)\, \mathrm{e}^{-\mathrm{i}\delta t}\, \mathrm{e}^{\mathrm{i}\phi_{\mathrm{ram}}} \; . \tag{5.79}$$

The matrix elements of the displacement operator between number states may be obtained analytically through use of [CG69]

$$\langle n'|D(\alpha)|n\rangle = \sqrt{\frac{n_<!}{n_>!}}\, \chi^{n_>-n_<}\, \mathrm{e}^{-|\alpha|^2/2}\, L_{n_<}^{(n_>-n_<)}\big(|\alpha|^2\big) \; , \tag{5.80}$$

where $L_k^{(m)}(x)$ denotes a generalised Laguerre polynomial, $n_> = \max(n', n)$, $n_< = \min(n', n)$ and $\chi = \alpha$ if $n' \geq n$, while $\chi = -\alpha^*$ if $n' \leq n$. Inserting eq. (5.78), one may write $\langle n'|D(\alpha)|n\rangle = K_{n',n}(\eta)\exp[\mathrm{i}(n'-n)\nu t]$, with

$$K_{n'n}(\eta) = \sqrt{\frac{n_<!}{n_>!}}\, \big[\mathrm{sgn}(n'-n)\big]^{|n'-n|}\, \mathrm{i}^{n'-n}\, \eta^{|n'-n|}\, \mathrm{e}^{-\eta^2/2}\, L_{n_<}^{(|n'-n|)}\big(\eta^2\big) \; . \tag{5.81}$$

The matrix elements are therefore given by

$$\langle \mathbf{n}'|\langle\uparrow|\widetilde{H}_{\mathrm{int}}(t)|\downarrow\rangle|\mathbf{n}\rangle = \frac{\hbar}{2}\Omega_{\mathrm{ram}} \Big[\prod_m K_{n'_m n_m}(\eta_m)\Big]\, \mathrm{e}^{-\mathrm{i}[\delta - \sum_m (n'_m - n_m)]t}\, \mathrm{e}^{\mathrm{i}\phi_{\mathrm{ram}}} \; . \tag{5.82}$$

One deduces that the Raman interaction Hamiltonian is capable of driving transitions between motional states differing by an arbitrary number of oscillator quanta, with coupling strengths that depend on the occupation numbers of the modes in

each state and the Lamb-Dicke parameters. By choosing the detuning δ appropriately, a transition between a particular pair $|\downarrow\rangle|\mathbf{n}\rangle$ and $|\uparrow\rangle|\mathbf{n'}\rangle$ may be driven near resonance. The Hilbert space is then reduced to an effective two-state system formed by these two states, analogous to the treatment of magnetic-dipole transitions considered earlier. There is, however, a difference between the two cases: the change in magnetic field as a function of distance from the trap centre is small, so that it is sufficient to retain only the term linear in the position operator in the Taylor expansion. Conversely, the electric field relevant for Raman transitions varies much more strongly with position due to the short wavelength of free-space radiation at optical frequencies. The complete expression (5.69) for the electric field of a plane wave was therefore used, which essentially amounts to including all terms in the Taylor expansion.

The effective Hamiltonian for the two near-resonant states may be written

$$\widetilde{H}_{\mathrm{int}}(t) = \frac{\hbar}{2}\,\Omega(\mathbf{n'},\mathbf{n})\,\mathrm{e}^{-\mathrm{i}\epsilon t}\,\mathrm{e}^{\mathrm{i}\kappa}\,\sigma_+ + \mathrm{H.c.}\,, \tag{5.83}$$

where the Rabi frequency $\Omega(\mathbf{n'},\mathbf{n})$, detuning ϵ and phase ϕ depend on the motional states involved as

$$\Omega(\mathbf{n'},\mathbf{n}) = \Omega_{\mathrm{ram}} \prod_m \left|K_{n'_m n_m}(\eta_m)\right|, \tag{5.84}$$

$$\kappa = \phi_{\mathrm{ram}} + \sum_m \arg\left[K_{n'_m n_m}(\eta_m)\right], \tag{5.85}$$

$$\epsilon = \delta - \sum_m \left(n'_m - n_m\right)\ . \tag{5.86}$$

In our convention, the Rabi frequency is real and non-negative, while any phases arising from the matrix elements have been absorbed into κ.

5.4 Rabi pulses

I explained in the previous two sections how the coherent evolution of a trapped atomic system interacting with time-varying external fields can be greatly simplified under certain conditions. Rather than having to take into account all internal

and motional states with their various couplings, one may restrict attention to a subspace of the total Hilbert space, containing those states that are connected by transition frequencies close to the driving frequency of the external perturbation. In the simplest case, the description reduces to an effective two-state system (or a collection of several independent two-state systems) comprised of the two states $|\downarrow\rangle\,|\mathbf{n}\rangle$ and $|\uparrow\rangle\,|\mathbf{n'}\rangle$ that are coupled by the near-resonant term in the Hamiltonian.

For both magnetic-dipole and Raman transitions, it was found that in some suitable rotating frame the interaction Hamiltonian $\widetilde{H}_{\mathrm{int}}(t)$ for the effective two-state system can be brought into the form

$$\widetilde{H}_{\mathrm{int}}(t) = \frac{\hbar}{2}\,\Omega(\mathbf{n'},\mathbf{n})\,\mathrm{e}^{-\mathrm{i}\epsilon t}\,\mathrm{e}^{\mathrm{i}\phi}\,\sigma_+ + \mathrm{H.c.}\,. \tag{5.87}$$

The Rabi frequencies $\Omega(\mathbf{n'},\mathbf{n})$ are defined such that they are real and may in general be a function of the motional states involved. The phase ϕ depends on the absolute phase of the applied electric or magnetic field and possibly also on any phases of matrix elements between atomic or motional states.

Transforming to a different frame via $R(t) = \exp(\mathrm{i}\epsilon t\sigma_z/2)$ results in a time-independent Hamiltonian. In the basis in which $|\uparrow\rangle\,|\mathbf{n'}\rangle = (1,0)^T$ and $|\downarrow\rangle\,|\mathbf{n}\rangle = (0,1)^T$, the time-dependent Schrödinger equation is given by

$$\mathrm{i}\hbar\frac{d}{dt}\begin{pmatrix}\tilde{c}_{\uparrow,\mathbf{n'}}(t)\\ \tilde{c}_{\downarrow,\mathbf{n}}(t)\end{pmatrix} = \frac{\hbar}{2}\begin{pmatrix}-\epsilon & \Omega\,\mathrm{e}^{\mathrm{i}\phi}\\ \Omega\,\mathrm{e}^{-\mathrm{i}\phi} & \epsilon\end{pmatrix}\begin{pmatrix}\tilde{c}_{\uparrow,\mathbf{n'}}(t)\\ \tilde{c}_{\downarrow,\mathbf{n}}(t)\end{pmatrix}. \tag{5.88}$$

The time-evolution operator $U_{\mathrm{rabi}}(t;t_0)$ for this Schrödinger equation is derived in appendix C. In particular, the probability for a system prepared in either the ground or excited state at $t_0 = 0$ to be found in the other after application of a Rabi pulse from t_0 to t is given by the familiar expression

$$P_{\downarrow\to\uparrow}(t) = P_{\uparrow\to\downarrow}(t) = \frac{\Omega^2}{\Omega^2+\epsilon^2}\,\sin^2\!\left[\frac{\sqrt{\Omega^2+\epsilon^2}}{2}\,(t-t_0)\right]. \tag{5.89}$$

This gives rise to Rabi oscillations between the two involved states $|\downarrow\rangle\,|\mathbf{n}\rangle$ and $|\uparrow\rangle\,|\mathbf{n'}\rangle$.

We use microwave Rabi pulses for the transfer sequences required as part of our

qubit initialisation and readout procedure, in addition to the actual single-qubit gates implemented on the clock qubit. Furthermore, we use Rabi pulses of our Raman lasers for the coherent part of our resolved sideband cooling scheme.

5.5 Ramsey interferometry

Another standard method to measure the resonance frequency of the transition between a pair of states is the Ramsey sequence. In this scheme, the atom is irradiated by two pulses of equal frequency ω, duration T and Rabi frequency Ω that are separated by an interval τ during which no driving field is applied. While the driving field is off, the ion evolves freely and the resonance frequency between the two states takes the value $\bar{\omega}_{\mathrm{off}} = \omega_{\mathrm{eg}} + \Delta_{\mathrm{e}}^{\mathrm{ac,off}} - \Delta_{\mathrm{g}}^{\mathrm{ac,off}}$. The transition frequency may in general be slightly different from the nominal Bohr frequency ω_{eg} due to ac shifts caused by background fields that are always present (such as the ac Zeeman shift induced by the currents in the rf electrodes or a shift due to blackbody radiation). In a frame rotating at the frequency ω of the driving radiation, the state of the system precesses at the rate given by $\delta_{\mathrm{off}} = \omega - \bar{\omega}_{\mathrm{off}}$. While the pulses are applied, off-resonant coupling through the driving field leads to an additional ac shift and the resonance frequency of the two states is given by $\bar{\omega}_{\mathrm{on}} = \omega_{\mathrm{eg}} + \Delta_{\mathrm{e}}^{\mathrm{ac,on}} - \Delta_{\mathrm{g}}^{\mathrm{ac,on}}$, resulting in a corresponding detuning $\delta_{\mathrm{on}} = \omega - \bar{\omega}_{\mathrm{on}}$.

The total time-evolution operator U_{ramsey} of the sequence may be obtained in a straightforward manner by multiplying the time-evolution operators for each step, so that $U_{\mathrm{ramsey}} = U_{\mathrm{rabi},2} U_{\mathrm{free}} U_{\mathrm{rabi},1}$. For a system initially prepared in state $|\downarrow\rangle$, the probability of making a transition to $|\uparrow\rangle$ is given by $|\langle\uparrow| U_{\mathrm{ramsey}} |\downarrow\rangle|^2$, which is found to be

$$P_{\mathrm{g}\to\mathrm{e}} = 2\left(\frac{\Omega}{\widetilde{\Omega}}\right)^2 \sin^2\theta \left[\cos^2\theta + \left(\frac{\delta_{\mathrm{on}}}{\widetilde{\Omega}}\right)^2 \sin^2\theta\right] \left[1 + \cos\left(\phi_1 - \phi_2 + \delta_{\mathrm{off}}\tau + 2\gamma\right)\right] \tag{5.90}$$

with

$$\widetilde{\Omega} = \sqrt{\Omega^2 + \delta_{\text{on}}^2}, \tag{5.91}$$

$$\theta = \frac{\widetilde{\Omega} T}{2}, \tag{5.92}$$

$$\gamma = \arctan\left(\frac{\delta_{\text{on}}}{\widetilde{\Omega}} \tan\theta\right) . \tag{5.93}$$

The parameters that are usually varied in a Ramsey-type experiment are either the frequency ω of the driving field (which changes δ_{off} and δ_{on}) or the interval τ between pulses. As is evident from expression (5.90) for the transition probability, the detunings enter in both factors, while the time τ only affects the second term.

Chapter 6

Laser cooling of $^{43}Ca^{+}$ in a static magnetic field of 28.8 mT

Laser cooling refers to the reduction in kinetic energy of an atom through interaction with an electromagnetic wave. First demonstrated for trapped ions decades ago, it is nowadays routinely used in laboratories to control their motional state. By decreasing the energy of an ion in the trap, its velocity is diminished and it becomes confined to an ever smaller region around the trap centre. This means that anharmonicities in the electric potential may be neglected if the ion can be made sufficiently cold, justifying the treatment used in chapter 4. A smaller amplitude of secular motion also reduces the magnitude of intrinsic micromotion. Furthermore, it allows one to assign a concrete position to each particle and makes it possible to perform spatially resolved readout of several ions. A lower velocity reduces the impact of Doppler shifts on the fluorescence spectrum, which leads to narrower resonances and allows more precise control over the scattering rate. In its most effective form, laser cooling provides a way to place atoms in the ground state of motion within the trapping potential. This is a prerequisite for some two-qubit gate schemes based on the coupling of internal to motional degrees of freedom. The Mølmer-Sørensen scheme, which we use for entangling operations, is not subject to this requirement, but certain gate errors caused by other factors are amplified when the ion does not start out in the motional ground state [SM00]. It is therefore important to reduce

the vibrational energy of the particle as much as possible. In this chapter, I discuss our approach to achieve this. I was responsible for carrying out the investigation presented here, which included finding optimal cooling parameters and characterising the temperatures of the different motional modes at the end of the different cooling stages.

6.1 Theoretical considerations

Interaction of an atom with near-resonant laser light leads to excitation of its internal state and exchange of momentum between atom and radiation field. This results in the scattering of photons by the atom, at a rate proportional to the populations of excited internal states. The probability of excitation to higher-energy internal states is affected by the motional state of the atom, which is itself changed by each scattering event. The scattering process thus leads to coupling between internal and external atomic degrees of freedom. A rigorous treatment of the resulting dynamics requires use of the density matrix such that both internal and centre-of-mass degrees of freedom are described by means of quantised variables. While such a formulation has been described theoretically before [CBZ+92; JY93; RLB96], it becomes exceedingly complex as the number of internal atomic states grows. Besides, it is possible in many cases to gain a qualitative understanding of the interplay between internal populations, fluorescence rate and vibrational energy of the centre-of-mass motion through models that make certain simplifying assumptions about the dynamics. Even quantitative predictions of such treatments are often sufficiently accurate. We have therefore chosen not to invest time in developing exact simulations based on a master equation, but instead rely on insights from a semiclassical model the group has previously used [Jan15]. Before discussing the cooling scheme for $^{43}Ca^{+}$ in detail, I will briefly review the key features of laser cooling for a two-state system since this model provides guidance as to which parameters are relevant for the cooling process.

6.1.1 Two-state model

I consider a particle containing two internal states that moves in one dimension in a pure harmonic potential and interacts with a plane electromagnetic wave. As the theory of cooling for such a system has been established for a while [Ste85; Ste86; EMS+03], I will only highlight points relevant for this thesis. The system is characterised by the internal resonance frequency ω_{eg} determined by the energy difference between the ground state and the excited state, the spontaneous decay rate Γ from the excited state, the (angular) natural frequency ν of the harmonic oscillator potential and the frequency ω of the incident radiation. The energy eigenstates take the form $|i\rangle \otimes |n\rangle$, where $|i\rangle \in \{|\mathrm{g}\rangle, |\mathrm{e}\rangle\}$ refers to the internal state and $\{|n\rangle\}$ are the number states of the harmonic oscillator. The energy spectrum of the moving particle is thus given by two ladders, with energies $E_{\mathrm{g},n} = \hbar\left[\omega_{\mathrm{g}} + \nu(n + 1/2)\right]$ and $E_{\mathrm{e},n} = \hbar\left[\omega_{\mathrm{e}} + \nu(n + 1/2)\right]$.

If spontaneous emission were absent, the dynamics would be fully coherent and could be described by an interaction Hamiltonian of the form given in section 5.3. In this idealised situation, the spatially varying field induces transitions $|\mathrm{g}\rangle\,|n\rangle \leftrightarrow |\mathrm{e}\rangle\,|n'\rangle$ between different motional states, which can be driven selectively by adjusting the frequency of the radiation such that $\omega = \omega_{\mathrm{eg}} + (n' - n)\nu$. This means that distinct resonances are observed in the excitation spectrum as ω is varied. The strength of the coupling between internal and external degrees of freedom depends on the Lamb-Dicke parameter

$$\eta = kx_0 = k\sqrt{\frac{\hbar}{2M\nu}}\,, \tag{6.1}$$

where k denotes the magnitude of the wave vector of the plane wave and x_0 is the spatial extent of the wavefunction of the particle when in the ground state of the oscillator potential. The Lamb-Dicke parameter enters the description through its influence on the motional matrix elements $\langle n'|\exp\left[\mathrm{i}\eta\left(a^\dagger + a\right)\right]|n\rangle$. If the particle is cold enough that it only occupies number states for which $\sqrt{\langle n|k^2x^2|n\rangle} = \eta\sqrt{2n+1} \ll 1$, these matrix elements may be obtained to a very good approximation by expanding the exponential in a power series and retaining only the term linear in η. For this to hold on average thus requires $\eta\sqrt{2\bar{n}+1} \ll 1$, where $\bar{n}$ is the average occupation

number of the particle in the harmonic oscillator. The bar accent here denotes an ensemble average over a large number of independent realisations of the cooling process. The particle is then said to be in the Lamb-Dicke regime. Note that a small value of the Lamb-Dicke parameter is a necessary, but not a sufficient condition for this regime to hold [WMI+98].

When spontaneous emission is included, the description has to be modified. The finite lifetime of the excited state leads to broadening of each resonance, resulting in a width proportional to Γ. Two limiting cases may then be considered.

6.1.1.1 Weak-confinement limit

When $\nu \ll \Gamma$ (weak-confinement limit), resonances corresponding to different motional transitions overlap strongly and therefore one cannot exclusively drive a certain kind of motional transition. For example, if the frequency of the radiation is adjusted to $\omega_{\mathrm{eg}} - \nu$, which would correspond to addressing the first red sideband and thus decreasing the motional energy in a coherent treatment, there is now due to the large natural linewidth a significant probability that instead a scattering event on the carrier or first blue sideband occurs, which does not lead to a reduction in motional energy. Nevertheless, the particle will still be cooled on average if the laser frequency is set below ω_{eg} as transitions on red sidebands are then favoured. I will refer to cooling in the weak-confinement limit as Doppler cooling. Assuming that the particle is in the Lamb-Dicke regime and that the intensity of the incident radiation is such that the transition between internal states is driven far below saturation, the minimum average mechanical energy (kinetic plus potential energy) $\bar{E}_{\mathrm{min}}$ of the particle in the harmonic potential is obtained for $\omega = \omega_{\mathrm{eg}} - \Gamma/2$, at which point

$$\bar{E}_{\mathrm{min}} = \frac{\hbar\Gamma}{4}(1+\alpha) \,, \tag{6.2}$$

where α is a geometric factor of order unity that depends on the spatial pattern of spontaneous emission [Ste86]. For the fictitious case of isotropic scattering, $\alpha = 1/3$ and thus $\bar{E}_{\mathrm{min}} = \hbar\Gamma/3$. If the mechanical energy is converted to an effective temperature, one thus finds that the Doppler limit temperature T_{D} set by $\bar{E}_{\mathrm{min}}$ is

given by $k_{\mathrm{B}}T_{\mathrm{D}} = \hbar\Gamma/3$ for isotropic scattering. Assuming a two-state system with the same $\Gamma = 2\pi \times 23\,\mathrm{MHz}$ as the total decay rate of the $4\,\mathrm{P}_{1/2}$ level in $^{43}\mathrm{Ca}^{+}$, one obtains $T_{\mathrm{D}} = 0.4\,\mathrm{mK}$. Alternatively, one may infer an average occupation number of the harmonic oscillator through

$$\bar{n}_{\mathrm{min}} = \frac{\bar{E}_{\mathrm{min}}}{\hbar\nu} - 1/2\,. \tag{6.3}$$

With $\Gamma = 2\pi \times 23\,\mathrm{MHz}$ and $\nu = 2\pi \times 5\,\mathrm{MHz}$, one finds $\bar{n}_{\mathrm{min}} \approx 1$ for isotropic scattering.

Cooling in the weak confinement limit can also be viewed from a different angle. When a pure two-state system, having no external degrees of freedom, interacts with electromagnetic radiation, the populations of the two internal states reach steady state within a time of order Γ^{-1}. The steady-state populations depend on the detuning of the radiation from the internal resonance frequency. If the description is now expanded to include centre-of-mass motion and the particle placed in a harmonic potential, the detuning observed in the rest frame of the particle will vary with time as the oscillating velocity of the particle leads to a time-dependent Doppler shift. The characteristic timescale for changes in detuning is of order ν^{-1}. For $\nu \ll \Gamma$, the internal part of the density matrix therefore evolves much faster than the detuning varies, which means that at each point in the oscillation cycle the internal populations approximately take the steady-state values corresponding to the respective detuning at that point. In this case, a description similar to the cooling of free particles applies [Ste86]. Each cycle of absorption and spontaneous re-emission on average imparts a momentum kick of $\hbar k$ in the direction of propagation of the laser beam. When a red-detuned laser with detuning $\delta = \omega - \omega_{\mathrm{eg}}$ in the lab frame is incident on the system, the atom scatters more photons when it moves towards the laser source than when it moves away from it and thus, averaged over one oscillation in the trap, loses energy. The strength of the cooling depends on the difference in scattering rates between points with different Doppler shifts. For a particle with low velocity, this difference is approximately given by the gradient of fluorescence with respect to detuning, calculated at the detuning δ that would be observed by a

stationary particle. Motional energy is extracted until the cooling effect is balanced by heating arising from the stochastic nature of spontaneous emission. The latter is proportional to the rate at which a stationary particle would scatter photons for the given laser detuning. Denoting the scattering rate for a hypothetical stationary particle by R and its gradient with respect to frequency (and thus detuning) as $\partial_\omega R$, it follows that the average energy reached at the end of the cooling process is expected to be proportional to $R/\partial_\omega R$. This view on Doppler cooling generalises more easily to systems containing multiple internal states and I will make use of it in later sections.

6.1.1.2 Strong-confinement limit

When $\nu \gg \Gamma$ (strong-confinement limit), resonances corresponding to different motional transitions are clearly resolved and the behaviour is not too dissimilar from the case where spontaneous emission is ignored. It becomes possible to efficiently address individual sidebands, with only a slight probability of scattering to undesired motional states. This means that tuning the cooling laser to a red sideband allows driving predominantly transitions where motional quanta are extracted and the ion is driven towards the ground state of motion. Cooling is then mainly limited by off-resonant excitation on the carrier and blue sidebands. I use the term sideband cooling to refer to cooling in the strong-confinement limit. For a particle in the Lamb-Dicke regime driven on the first red sideband ($\omega = \omega_{\mathrm{eg}} - \nu$) by radiation far below saturation, the vibrational energy reached is found [Ste86] to be

$$\bar{E}_{\mathrm{min}} = \hbar\nu \left[\left(\frac{\Gamma}{2\nu} \right)^2 \left(\alpha + \frac{1}{4} \right) + \frac{1}{2} \right] . \tag{6.4}$$

Regardless of which confinement limit is assumed, the particle will not always occupy the same motional state $|n\rangle$ when cooling has finished. Rather, the probability of finding the particle in a certain number state will be described by a probability distribution $P(n)$. The quantity $\bar{n} = \sum_{n=0}^{\infty} nP(n)$ is the average occupation number observed if the cooling process is repeated a large number of times. It may be shown [Ste86] that in the Lamb-Dicke regime $P(n)$ is given by a thermal distribution such

that

$$P(n) = \frac{1}{\bar{n}+1}\left(\frac{\bar{n}}{\bar{n}+1}\right)^n \quad . \tag{6.5}$$

6.1.2 Cooling scheme for $^{43}Ca^+$

I will neglect any effects due to micromotion in this chapter and instead make the pseudopotential approximation, so that the trapping potential is modelled as purely harmonic in all three dimensions. Motion is then decoupled along the three principal axes of the dc potential. In the radial plane, the oscillator frequencies are given by the secular frequencies ν_{ip} and ν_{oop}, where the subscripts refer to the in-plane and out-of-plane directions. The component of the rf field along the trap axis vanishes, which means that motion in this direction is always strictly harmonic, with corresponding frequency ν_z.

After an atom has initially been ionised and trapped, it usually occupies a highly excited motional state in the trapping potential. We use two steps to reduce the mechanical energy of ions. The first step is Doppler cooling via strong electric-dipole transitions. This removes the bulk of the energy and leaves the particles in states corresponding to relatively low $\bar{n}$, such that the Lamb-Dicke regime holds for the radial modes. Any time that ions are not used for a specific experiment, the Doppler lasers are applied continuously to ensure the particles remain cold and are not lost due to heating processes such as electric field noise or collisions with background gas. Whenever an even lower motional energy is required, we perform resolved sideband cooling using two Raman beams in combination with a repumper. I will present the theory underlying these two methods in the following subsections.

6.1.2.1 Doppler cooling

It is obvious that $^{43}Ca^+$ is far from a two-state system. As a result, cooling is complicated by several factors. The first is the fact that the metastable $3\,\mathrm{D}$ levels lie lower in energy than the $4\,\mathrm{P}$ levels and thus provide additional channels for decay from the latter[1]. This means that the electric-dipole transitions from $4\,\mathrm{S}_{1/2}$ to $4\,\mathrm{P}_{1/2}$ or $4\,\mathrm{P}_{3/2}$ do not form a closed system. This is not a severe limitation, however, as

[1] The same situation is of course also encountered in $^{40}Ca^+$.

the addition of repumping lasers allows recovering population from the 3 D levels. Nevertheless, the dynamics of the Λ-system thus formed are more complex than those of the simple two-state system. In particular, there is a possibility for the appearance of dark states, which can have a significant impact on the fluorescence spectrum. As explained in chapter 2, the $3\,\mathrm{D}_{5/2}$ level is used as the shelf for state-dependent fluorescence detection during readout, which means that we have to choose a cooling cycle that does not involve this level. Our cooling scheme therefore utilises the $4\,\mathrm{S}_{1/2}$, $4\,\mathrm{P}_{1/2}$ and $3\,\mathrm{D}_{3/2}$ levels.

The second complication is the hyperfine splitting within the ground level, which is much larger than the 23 MHz linewidth of the 397 nm laser. A 397 nm beam with a single frequency component may only excite population from one of the two hyperfine sublevels effectively, which means that continuous scattering required for cooling cannot be sustained this way. We therefore add another frequency component to the 397 nm beam, so that both sublevels may be addressed.

Thirdly, the energies of states contained in a fine-structure level cover a wide range of values at a magnetic field of 288 G. As a result, the various transitions between different states from two given fine-structure levels may differ in frequency by several multiples of the linewidth of the relevant laser. One might therefore not necessarily expect that efficient cooling can be achieved with only a few laser beams.

There are two key processes in our experiments that rely on sustained scattering of light from the atom: Doppler cooling and readout via state-dependent fluorescence detection. Its purpose, however, is different in the two applications. For cooling, the focus is on the external state of the atom and the relevant quantity is thus the average mechanical energy $\bar{E}$ of the particle in the trap, which depends on $\bar{n}_{\mathrm{ip}}$, $\bar{n}_{\mathrm{oop}}$ and $\bar{n}_z$. The aim lies in achieving as low an $\bar{E}$ as possible and, more importantly, minimising $\bar{n}_{\mathrm{ip}}$ as it is the in-plane mode that we use for two-qubit gates. For readout, the goal is to maximise the rate of fluorescence from the ion while keeping the intensity as low as possible to avoid background scatter. The rate of scattering of photons at 397 nm is given by $R_{397} = \Gamma_{397}\, P\big(\mathrm{P}_{1/2}\big)$, where Γ_{397} is the rate of decay from $4\,\mathrm{P}_{1/2}$ to $4\,\mathrm{S}_{1/2}$ and $P\big(\mathrm{P}_{1/2}\big)$ is the population of the $4\,\mathrm{P}_{1/2}$ level. The aim is therefore to maximise this population. The optimal detunings, intensities and

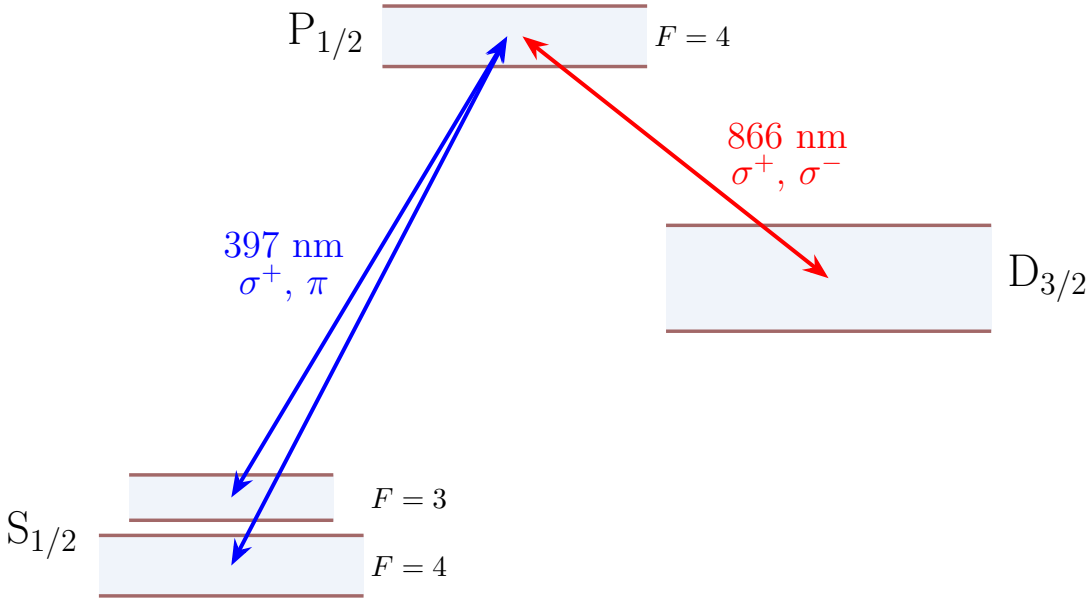


Figure 6.1: Scheme used for Doppler cooling. A 397 nm beam with two frequency components, each σ^+ and π polarised, optically pumps population towards the $|4, +4\rangle$ state in the ground level, while a single 866 nm beam repumps population lost to the $3\,D_{3/2}$ level back into the cooling cycle.

polarisations to use for the 397 nm and 866 nm beams will in general be different for each of these two applications. From a practical point of view, it is advantageous to find sets of parameters that are sufficiently similar so that it is possible to switch between fluorescence settings while keeping experimental complexity to a minimum.

Our group has previously invested considerable effort into devising a cooling scheme that achieves these goals in the intermediate-field regime at 146 G. A detailed theoretical investigation can be found in ref. [Jan15], while the experimental demonstration is described in refs. [Har13; Sep16]. We expected the main conclusions drawn there to hold also for an ion in a magnetic field of 288 G. However, it was not clear whether the significantly larger energy splittings at 288 G would prevent efficient cooling or cause a strong reduction in achievable population of the $4\,P_{1/2}$ level and thus degrade readout performance.

The basic idea of the cooling scheme is illustrated in fig. 6.1. A 397 nm laser driving transitions between the $4\,S_{1/2}$ and $4\,P_{1/2}$ levels concentrates population in the states with extremal values of m within the ground level. Either the $m = +4$ or the $m = -4$ end could be used, but they are not completely equivalent since the energies and transition frequencies are different for each. We choose to operate in the

$m = +4$ end because simulations showed that lower final temperatures could thus be obtained. It then follows that the 397 nm laser should not contain any σ^--component in order to achieve efficient optical pumping to states with positive values of m; this also turns out to be a requirement for the formation of strong dark resonances suitable for enhanced cooling. It is beneficial to have a strong σ^+-component to build up population in the $4\,S_{1/2}^{4,+4}$ state, but some π-light is also required since otherwise fluorescence would stop quickly due to the lack of states in the $4\,P_{1/2}$ level that $4\,S_{1/2}^{4,+4}$ could couple to. The main cooling cycle is therefore formed by the $4\,S_{1/2}^{4,+4} \leftrightarrow 4\,P_{1/2}^{4,+4}$ transition and any decays to states with $m < 4$ are counteracted by optical pumping through the σ^+-component. The large hyperfine splitting of the $4\,S_{1/2}$ ground level makes it necessary to use two frequency components in the 397 nm beam to address states derived from both the $F = 4$ and the $F = 3$ sublevels. The cooling scheme is not particularly sensitive to the polarisation of the 866 nm repumper and it is experimentally convenient to use σ^+-and σ^--components of equal strength.

This leaves frequencies and intensities as the remaining parameters. The two frequency components of the 397 nm beam must differ by ≈ 3 GHz to bridge the hyperfine splitting, but the exact position relative to the resonance frequencies of possible transitions from states in the ground level is harder to predict. The intensities must be large enough to enable sufficient off-resonant excitation when the ion happens to occupy a state with large negative m, but low enough so as not to broaden resonances too much and decrease the cooling rate. The frequency of the 866 nm beam is determined by the requirement that a strong dark resonance be formed that may be used for cooling, as explained in the next section. Its intensity must be relatively high to prevent population from getting trapped in the $3\,D_{3/2}$ level, which would result in reduced fluorescence. This is especially relevant for readout.

6.1.2.2 Cooling on a dark resonance

A quantum system with three or more states to which a time-dependent perturbation is applied exhibits features not observed in the simpler two-state system.

One of them is the interference of transition amplitudes, which may lead to the suppression of transitions to an excited state. In the context of laser cooling, this results in a sharp drop in fluorescence caused by coherent population trapping when a two-photon resonance condition is satisfied. Such dark resonances are usually very narrow, which makes them highly interesting for Doppler cooling because they combine a low scattering rate R with a strong gradient $\partial R/\partial\omega$, where ω is the frequency of one of the driving lasers. This provides a method to reach temperatures at or even below the Doppler limit despite a complex level structure.

I explain the concept using the three-state system in Λ-configuration shown in fig. 6.2a. Let the high-energy state $|3\rangle$ be characterised by a total decay rate $\Gamma = 2\pi \times 23\,\mathrm{MHz}$ and branching ratios $r_{3\mathrm{g}} = 0.94$, $r_{3\mathrm{e}} = 0.06$. These values correspond to the properties of the $4\,\mathrm{P}_{1/2}$ level in Ca^+. Two laser beams with frequencies ω_1 and ω_2 are applied, one of which drives $|\mathrm{g}\rangle \leftrightarrow |3\rangle$ with Rabi frequency Ω_1 and the other $|\mathrm{e}\rangle \leftrightarrow |3\rangle$ with Rabi frequency Ω_2. The rate of fluorescence is proportional to the steady-state population P_3 of state $|3\rangle$, which is a function of the detunings $\delta_1 = \omega_1 - \omega_{3\mathrm{g}}$ and $\delta_2 = \omega_2 - \omega_{3\mathrm{e}}$ of the two lasers. I assume in the following that laser 1 is red-detuned from the transition it drives, specifically $\delta_1 = 2\pi \times -10\,\mathrm{MHz}$. Figure 6.2b contains a plot of P_3 for a stationary atom as a function of the detuning δ_2 of the repumping laser when $\Omega_1 = r_{3\mathrm{g}}\Gamma/2$ and $\Omega_2 = 10 r_{3\mathrm{e}}\Gamma$. The population was calculated by numerically solving the optical Bloch equations in the form given in ref. [ZCA11] for the parameter values assumed. In this ideal case, fluorescence completely stops when $\delta_2 = \delta_1$.

I now include centre-of-mass motion and assume that the ion is confined in a harmonic potential, with a motional frequency of 5 MHz, for example. Since $\Gamma/\nu \approx 5$, one would expect that for a two-state system with the same decay rate the weak-confinement limit should provide a reasonable approximation. The situation is more complicated when three states and unequal branching ratios are involved, but I will assume that the main features of the cooling dynamics may be derived by taking the internal part of the density matrix to be approximately in steady state at each point of the oscillation cycle. The velocity of the particle then only enters the picture through Doppler shifts $-\mathbf{k}_i \cdot \mathbf{v}$ that change the detunings δ_1 and δ_2 as the

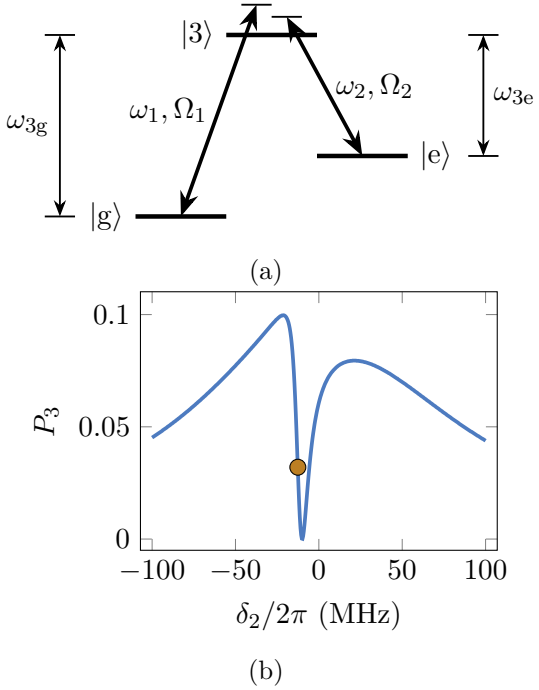


Figure 6.2: Dark resonance in a three-state system. a) Two lasers are incident, each of which is assumed to couple only one pair of states. b) Population of state $|3\rangle$ for a stationary atom as a function of detuning δ_2 of laser 2 when the detuning of laser 1 is fixed to $\delta_1 = 2\pi \times -10\,\mathrm{MHz}$. Coherent population trapping occurs when the resonance condition $\delta_2 = \delta_1$ is satisfied, at which point fluorescence drops sharply.

particle moves and the instantaneous fluorescence rate may be inferred from profiles analogous to that depicted in fig. 6.2b. Suppose the repumping laser is slightly detuned from the bottom of the dark resonance, such that a stationary ion would exhibit fluorescence at a rate indicated by the orange circle in fig. 6.2b. An ion with a small, but non-zero velocity moving towards the source of laser 1 will see a slightly less negative detuning $\delta_1' > \delta_1$ in its rest frame and therefore the dark resonance will appear further to the right on the δ_2'-axis. At the same time, δ_2' will of course also be shifted. If lasers 1 and 2 are co-propagating, $\delta_2' > \delta_2$, but $\left|\delta_2' - \delta_2\right| < \left|\delta_1' - \delta_1\right|$ since $k_1 > k_2$. If the lasers are counter-propagating, then $\delta_2' < \delta_2$. In both cases, one therefore finds that $\delta_1' - \delta_2' > \delta_1 - \delta_2$, which means that the ion sits further to the left on the dark resonance in its rest frame, where the scattering rate is higher. The converse applies for an ion moving away from the source of laser 1. It follows that over one period of oscillation there is a net force that reduces the vibrational energy, similar to the standard case of Doppler cooling in a two-state system. The

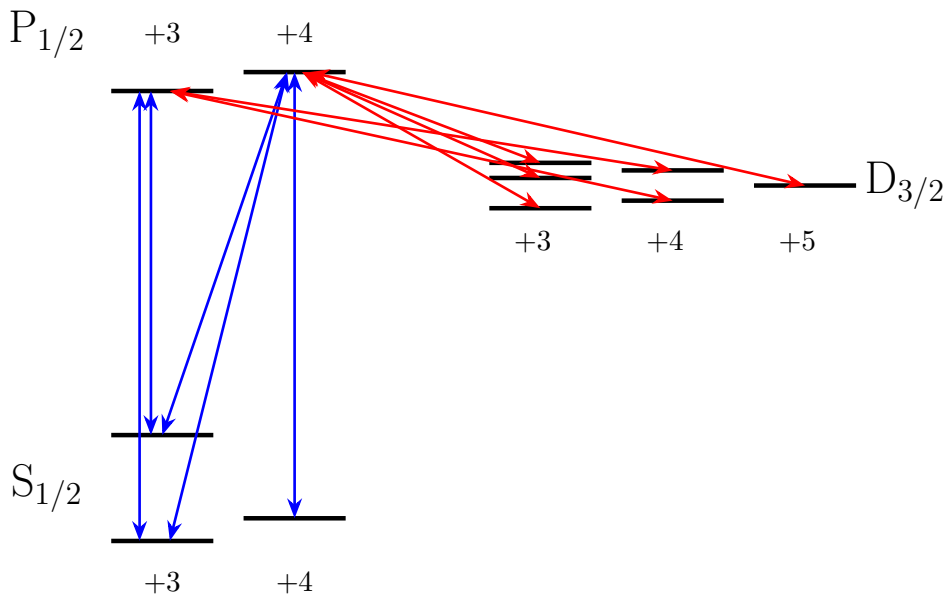


Figure 6.3: Transitions involved in main dark resonances arising in our cooling scheme. If the 397 nm beam contains no σ^- polarisation component, an ideal dark resonance involving the states $4\,S_{1/2}^{4,+4}$, $4\,P_{1/2}^{4,+4}$ and $3\,D_{3/2}^{5,+5}$ may be formed.

important point is that the fluorescence gradient of a dark resonance can be very steep and the scattering rate near the bottom rather low, resulting in strong cooling. Note that if the frequency of the repumping laser is scanned, the appropriate place to sit is the downward slope of the dark resonance. As follows from the discussion above, cooling strength is maximised if the two lasers involved propagate in opposite directions.

In a multi-state system like $^{43}Ca^+$, the evolution is more complicated, but one may roughly identify states in $4\,S_{1/2}$ with $|g\rangle$, in $3\,D_{3/2}$ with $|e\rangle$ and in $4\,P_{1/2}$ with $|3\rangle$. The presence and strength of dark resonances depends on the matrix elements between atomic states and is thus a function of laser polarisations and intensities. In general, there may not be pure dark states, but rather superpositions that have slightly reduced coupling to an excited state and will thus only cause a small reduction in fluorescence. Nevertheless, if the 397 nm beam contains no σ^- polarisation component, one finds that an ideal dark resonance may in fact be formed, involving the states $4\,S_{1/2}^{4,+4}$, $4\,P_{1/2}^{4,+4}$ and $3\,D_{3/2}^{5,+5}$. Additionally, a partial dark resonance occurs whenever the frequencies of the 397 nm and 866 nm beams are such that the respective detuning of each from some transition $4\,S_{1/2} \leftrightarrow 4\,P_{1/2}$ or $3\,D_{3/2} \leftrightarrow 4\,P_{1/2}$

is equal. Since in our cooling scheme most population resides in states near the $m = +4$ end of the ground level, the main dark resonances are expected to result from transitions out of these states, as shown in fig. 6.3. For purely monochromatic laser beams incident on a stationary atom, the fluorescence at the centre of an ideal dark resonance would in theory drop to zero, but in reality the depth is limited by several factors, including residual velocity of the ion, finite laser linewidths, polarisation impurities, decoherence and phase stability of the lasers. Based on the description just presented, one may therefore expect that scanning the frequency of the 866 nm laser while keeping the frequency of the 397 nm laser fixed should result in a fluorescence trace with a multitude of small dips and at least one clear drop.

6.1.3 Raman sideband cooling

Sideband cooling requires $\nu \gg \Gamma$, which cannot usually be achieved with electric dipole transitions in ion traps. In our surface trap, for instance, $\nu \approx 2\pi \times 1\,\mathrm{MHz}$ in the axial direction and $\nu \approx 2\pi \times 5\,\mathrm{MHz}$ in the radial directions under typical trapping conditions, while $\Gamma \approx 2\pi \times 23\,\mathrm{MHz}$ for decay from $4\,\mathrm{P}_{1/2}$ to $4\,\mathrm{S}_{1/2}$, resulting in $\nu/\Gamma \approx 0.04 - 0.22$. Instead, a narrow optical resonance such as a quadrupole transition could be used, but this requires a technically demanding laser. An easier option consists in engineering an effective two-state system with narrow linewidth through a Raman interaction [WMI+98]. This method uses two lasers to couple two low-energy states indirectly via a higher-energy intermediate state. As long as the detuning of the two Raman lasers from the auxiliary level is large enough that the population of the latter (and thus spontaneous emission) is negligible, the system can effectively be reduced to two states, with a Hamiltonian that is formally equivalent to that of direct coupling. The effective linewidth is of order

$$\Gamma_{\mathrm{ram}} \approx \Gamma \frac{\Omega_1^2 + \Omega_2^2}{\Delta_{\mathrm{ram}}^2} \,, \tag{6.6}$$

where Γ is the total decay rate of the auxiliary level and Ω_i is the Rabi frequency of an individual laser beam.

The coherent evolution of the effective two-state system under the influence of the

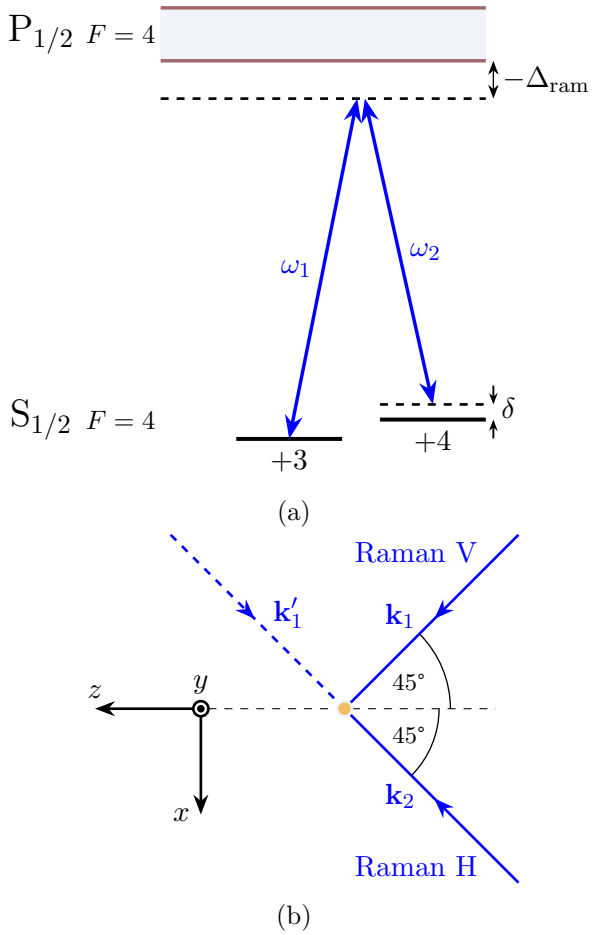


Figure 6.4: Raman transition used for sideband cooling and motional thermometry. a) Internal states involved. b) Arrangement of Raman beams relative to trap. The labels "V" and "H" refer to vertical and horizontal polarisation, respectively.

Raman interaction was discussed in section 5.3. It was found there that transitions involving a simultaneous change in internal and motional state may be driven. In particular, changes in occupation number for the motional modes may be induced selectively by appropriate adjustment of the frequency of the applied radiation. In the case of a Raman transition, the relevant parameter is the frequency difference between the two Raman beams. Resolved sideband cooling may therefore be realised by setting this difference to address the sideband transition that extracts energy from the mode of interest.

We use the states $|4, +3\rangle$ and $|4, +4\rangle$ in the ground level for this purpose, as illustrated in fig. 6.4a. The frequency difference between these states at a magnetic field of 288 G is 127.8 MHz. States in the $4\,P_{1/2}$ level mediate the Raman transition. The polarisations of the Raman beams have to be chosen such that both states in

the ground level couple to at least one common state in $4\,\mathrm{P}_{1/2}$. This means that some combination of π- and σ^+/σ^--polarisation components needs to be present in the beams. For simplicity, we choose one beam (Raman V) to be vertically polarised along the y-direction with respect to the trap coordinate system, so that it contains σ^+- and σ^--components, while we adjust the other beam (Raman H) to be horizontally polarised in the xz-plane, thus having σ^+-, π- and σ^--components. The Raman beams are detuned from the centre of mass of the $4\,\mathrm{P}_{1/2}$ level by $\Delta_{\mathrm{ram}} \approx 2\pi \times -30\,\mathrm{GHz}$, which is large compared to the energy differences between states in this level. It follows that both beams will lead to couplings between $|4,+3\rangle$, $|4,+4\rangle$ in the ground level and several states in the $4\,\mathrm{P}_{1/2}$ level and the effective Raman Rabi frequency Ω_{ram} is therefore not given by the simple expression (5.73). We might be able to increase Ω_{ram} by choosing the polarisations of the Raman beams more carefully, but we have not investigated this because the coupling strength obtained with vertical and horizontal polarisations is already sufficient for our purposes.

The arrangement of Raman beams in our apparatus is depicted in fig. 6.4b. During standard operation of our trap, the Raman V beam is set up according to the solid line in that figure. The Raman wavevector is given by $\mathbf{k}_{\mathrm{ram}} = \mathbf{k}_1 - \mathbf{k}_2 = \sqrt{2}k(\cos\theta, -\sin\theta, 0)$ with respect to the motional coordinate system (see section 4.4.1), where $k = |\mathbf{k}_1|$ and I have taken $|\mathbf{k}_1| \approx |\mathbf{k}_2|$ since the frequency difference between the Raman beams is negligible compared to their absolute frequencies. The variable θ denotes the mode angle. For the standard angle of $\theta = 15°$ and secular frequencies of $\nu_{\mathrm{ip}} = 2\pi \times 5.2\,\mathrm{MHz}$, $\nu_{\mathrm{oop}} = 2\pi \times 5.6\,\mathrm{MHz}$, $\nu_z = 2\pi \times 1.1\,\mathrm{MHz}$, the corresponding Lamb-Dicke parameters become $(\eta_{\mathrm{ip}}, \eta_{\mathrm{oop}}, \eta_z) = (0.10, 0.03, 0)$. In this configuration, the Raman transition is thus not sensitive to the motional state of the axial mode and no sideband cooling can be performed on this mode. Whenever we are interested in the state of the axial mode for diagnostic purposes, we temporarily switch to the arrangement given by the dashed line in fig. 6.4b. For this case we find $\mathbf{k}_{\mathrm{ram}} = \sqrt{2}k(\cos\theta, -\sin\theta, -1)$ and $(\eta_{\mathrm{ip}}, \eta_{\mathrm{oop}}, \eta_z) = (0.10, 0.03, 0.23)$.

After Doppler cooling has finished, we initialise the ion in $|\mathrm{e}\rangle = |4,+4\rangle$ through optical pumping with the 397 nm σ^+ beam. Suppose the motional state of mode m at this point is $|n_m\rangle$. We then drive a transition to the internal state $|\mathrm{g}\rangle = |4,+3\rangle$ in

combination with a change in motional state to $|n_m - 1\rangle$ through the Raman beams. Contrary to the usual discussion of sideband cooling, the ion here starts in the state that lies higher in energy, which means that we have to drive with Raman difference frequency $\omega_{\mathrm{ram}} = \omega_{\mathrm{eg}} + \nu_m$ for this purpose. While the Raman beams are applied, the system oscillates between $|\mathrm{e}\rangle\,|n_m\rangle$ and $|\mathrm{g}\rangle\,|n_m - 1\rangle$. Extraction of a motional quantum thus requires transferring the ion to $|\mathrm{g}\rangle\,|n_m - 1\rangle$, followed by resetting the internal state to $|\mathrm{e}\rangle$ without increasing the motional occupation number. Since the effective decay rate Γ_{ram} is very low, relying on spontaneous scattering for this purpose is inefficient. Instead, it is customary to use a repumper to speed up the process [WMI+98]. In our case, this is achieved by optically pumping the ion back to $|\mathrm{e}\rangle$ via the 397 nm σ^+ beam. As long as the ion is in the Lamb-Dicke regime with respect to mode m, excitation to $4\,\mathrm{P}_{1/2}$ and subsequent spontaneous decay occur predominantly on the carrier, which means that the motional state remains unchanged most of the time. The overall effect of one cycle of sideband cooling and repumping is therefore to change the state of the ion from $|\mathrm{e}\rangle\,|n_m\rangle$ to $|\mathrm{e}\rangle\,|n_m - 1\rangle$, resulting in a reduction in motional energy. Sideband cooling may be performed using either a continuous scheme, where Raman and repumping beams are both incident simultaneously, or a pulsed scheme, where the two kinds of beams alternate. We take the latter approach because we found it easier to optimise laser parameters in this way.

It should be noted that in principle we could also use microwaves to drive the sideband transitions required for cooling of the in-plane radial mode. However, the corresponding Rabi frequency is significantly lower than those for lasers because the effective Lamb-Dicke parameter for microwaves $\bar{\eta}_{\mathrm{ip}}$, as introduced in chapter 5, is smaller. With the microwave power currently available in our apparatus, it is therefore not feasible to perform sideband cooling via microwaves.

6.1.4 Thermometry of the motional state

Measuring the temperature of an ion in the trap requires a method that is sensitive to the motional state. For a crude estimate, we use the EMCCD camera of our imaging system to monitor the size of the region in which fluorescence from the ion is detected.

The larger this region, the larger is the amplitude of oscillations of the ion around the trap centre and the higher its mechanical energy. This allows us to quickly detect when the ion is not cooled efficiently at all, but does not provide a quantitative estimate of the occupation numbers of the motional modes. To obtain the latter, a different technique is used: we coherently drive Rabi oscillations for a pair of atomic states through application of an inhomogeneous sinusoidal electromagnetic field, as discussed in chapter 5. Since the field value depends on the position of the particle, the Rabi frequency depends on the number state of the harmonic oscillator that the ion happens to occupy, which means that average occupation numbers can be inferred from repeated observations of Rabi flopping.

To keep the following discussion in line with the usual treatment of sideband cooling, I will assume in this subsection that the ion starts in the lower-energy internal state $|\mathrm{g}\rangle$. The conclusions drawn are equally valid if the ion initially occupies the higher-energy state $|\mathrm{e}\rangle$, but the roles of sideband frequencies are then reversed. The latter case applies to the implementation of Raman sideband cooling in our trap.

Suppose the ion starts in state $|\mathrm{g}\rangle\,|\mathbf{n}\rangle$. I will not assume that any of the modes are in the Lamb-Dicke regime with respect to the Raman transition, although in practice this will often be the case. The frequency of applied radiation is adjusted such that[2] $\omega - (\omega_{\mathrm{eg}} + s\nu_m) = \epsilon$. This means we are driving either the carrier transition or a $|s|$-th order sideband of mode m and hence $|\mathrm{g}\rangle\,|\mathbf{n}\rangle$ near-resonantly couples to $|\mathrm{e}\rangle\,|\mathbf{n}'\rangle$, where $\mathbf{n}'$ is the same as $\mathbf{n}$ except that the occupation number of one mode m has changed to $n_m + s$. If the ion could always be prepared in state $|\mathbf{n}\rangle$ with certainty before the probe pulse was applied, the population of internal state $|\mathrm{e}\rangle$ would exhibit sinusoidal oscillations at the single frequency $\sqrt{[\Omega(\mathbf{n},\mathbf{n}')]^2 + \epsilon^2}$, where $\Omega(\mathbf{n},\mathbf{n}')$ is the Rabi frequency for the transition, as derived in section 5.3. In practice, however, each repetition of the cooling stage (Doppler cooling or sideband cooling) leaves the particle in a different motional state according to some underlying probability distribution. The vector $\mathbf{n}$ is therefore a random variable and each cooling step represents a sample drawn from this distribution. If the experiment is repeated a

[2] I will not explicitly write out ac shifts in this section, but instead absorb them into ω_{eg}.

large number of times, the observed population of $|\mathrm{e}\rangle$ will be the average over the probability distribution and thus

$$P_{\mathrm{g}\to\mathrm{e}}(t,\epsilon) = \sum_{n_1,n_2,n_3=0}^{\infty} P(\mathbf{n})\,\frac{[\Omega(\mathbf{n},\mathbf{n}')]^2}{[\Omega(\mathbf{n},\mathbf{n}')]^2+\epsilon^2}\,\sin^2\left(\frac{\sqrt{[\Omega(\mathbf{n},\mathbf{n}')]^2+\epsilon^2}}{2}t\right)\,. \qquad (6.7)$$

The probability distribution of the motional state is denoted by $P(\mathbf{n})$, which is a joint probability distribution for the occupation numbers n_m of the individual modes. If one assumes that the n_m are statistically independent, then the joint distribution becomes $P(\mathbf{n}) = P(n_1,n_2,n_3) = P_1(n_1)P_2(n_2)P_3(n_3)$, where $P_m(n_m)$ is the distribution for an individual mode. Note that even when driving a sideband on mode m, the observed flopping probability $P_{\mathrm{g}\to\mathrm{e}}(t,\epsilon)$ in general still depends on the occupation numbers of the spectator modes.

The function $\Omega(\mathbf{n},\mathbf{n}')$ depends on the spatial variation of the applied probing field. I assume that $\Omega(\mathbf{n},\mathbf{n}')$ is known. The change between $\mathbf{n}$ and $\mathbf{n}'$ is also known, since this is determined by the motional transition being addressed and thus controlled by the frequency of the probing pulse. The quantity of interest in (6.7) is then $P(\mathbf{n})$, either because the functional form of the probability distribution is not known at all or because, even though its form is known, values for the defining parameters are not available.

If the aim is to infer the coefficients $P(\mathbf{n})$ directly, one may drive Rabi flops on resonance as a function of pulse time t, followed by calculating the Fourier coefficients of the observed signal [WMI+98]. This may be useful if the probe field can be adjusted such that $\Omega(n_m,n_m')$ becomes sensitive only to a single motional mode.

In most situations, however, the form of the probability distribution may be derived theoretically and the interest lies not so much in the coefficients $P(\mathbf{n})$ themselves, but parameters characterising the distribution. This applies to Doppler cooling and sideband cooling, for which the probability distribution of each mode at the end of the cooling process is thermal and therefore given by eq. (6.5). The relevant parameters in this case are the average occupation numbers $\bar{n}_m$ of the modes. It is possible to estimate $\bar{n}_m$ by performing Rabi flopping resonant with the carrier transition as a function of t and fitting the resulting signal with a function of the

form (6.7), where the $\bar{n}_m$ are floated parameters. This fitting procedure will be most sensitive to that motional mode for which varying the occupation number leads to the largest change in $\Omega(\mathbf{n}, \mathbf{n}')$. This will be the mode with the largest Lamb-Dicke parameter η_m. We use carrier flops to deduce occupation numbers when $\bar{n}_m \gtrsim 5$ for the mode of interest.

If $\bar{n}_m \lesssim 5$ for a particular mode, another method is usually more accurate. The Rabi frequency for a transition on the s-th order red sideband of mode m ($s \geq 1$), vanishes if the particle starts in a motional state with $n_m < s$, while the strength of the s-th order blue sideband for the same initial state is non-zero. The transition probability for red and blue sidebands is thus not symmetric. Assuming a thermal distribution, this asymmetry may be exploited to extract information about the mean occupation number $\bar{n}_m$ of the motional mode in question. In typical presentations of this method it is shown that the asymmetry is independent of the duration or detuning used for the probe pulse [WMI+98]. Here I additionally point out that the asymmetry is also not affected by the occupation numbers of spectator modes. Inserting expression (5.84) for the Rabi frequency $\Omega(\mathbf{n}, \mathbf{n}')$ and taking into account that $K_{n,n-s} = 0$ for $n < s$, the transition probability when driving the s-th order red sideband of mode 1 may be written

$$P_{\mathrm{rsb}}(t,\epsilon) = \sum_{n_1=s}^{\infty} \sum_{n_2,n_3} P(n_1)P(n_2,n_3) \frac{|K_{n_1,n_1-s}|^2 \, |S(n_2,n_3)|^2}{|K_{n_1,n_1-s}|^2 \, |S(n_2,n_3)|^2 + \epsilon^2} \times \sin^2\left(\frac{\sqrt{|K_{n_1,n_1-s}|^2 \, |S(n_2,n_3)|^2 + \epsilon^2}}{2} t\right) , \tag{6.8}$$

where $S(n_2, n_3) = R_{\mathrm{eg}} K_{n_2,n_2} K_{n_3,n_3}$. Assuming a thermal distribution for $P(n)$ and using $K_{n_1,n_1'} = K_{n_1',n_1}$, one finds

$$\begin{aligned} P_{\mathrm{rsb}}(t,\epsilon) &= \sum_{n_1=0}^{\infty} \sum_{n_2,n_3} P(n_1+s)P(n_2,n_3) \frac{|K_{n_1+s,n_1}|^2 \, |S(n_2,n_3)|^2}{|K_{n_1+s,n_1}|^2 \, |S(n_2,n_3)|^2 + \epsilon^2} \\ &\qquad \times \sin^2\left(\frac{\sqrt{|K_{n_1+s,n_1}|^2 \, |S(n_2,n_3)|^2 + \epsilon^2}}{2} t\right) \\ &= \left(\frac{\bar{n}_1}{\bar{n}_1 + 1}\right)^s P_{\mathrm{bsb}}(t,\epsilon) \, . \end{aligned} \tag{6.9}$$

It follows that the ratio $r = P_{\mathrm{rsb}}(t,\epsilon)/P_{\mathrm{bsb}}(t,\epsilon) = [\bar{n}_1/(\bar{n}_1+1)]^s$ depends only on $\bar{n}_1$ and the chosen sideband, but is independent of pulse time, detuning and occupation numbers of the spectator modes. The same result would have been obtained if a sideband on any other mode had been chosen for the derivation, so this relation holds in general. Therefore,

$$\bar{n}_m = \frac{r_m^{1/s}}{1 - r_m^{1/s}} \,. \tag{6.10}$$

We make use of this technique to obtain estimates of the temperature of the ion after Doppler cooling and Raman sideband cooling.

In principle, the microwave magnetic field could be used for motional thermometry, but this approach has two drawbacks. Firstly, carrier transitions cannot really be used because the value of higher-order derivatives of the microwave field is not known accurately. More importantly, terms proportional to the square of the displacement operator are expected to be small and thus the dependence of Rabi frequency on motional state for carrier transitions is very weak. Secondly, microwave sideband transitions are slow enough that the heating rate causes a non-negligible change in motional state during the probe pulse. At the time of conducting the experiments described in this chapter, the available microwave power limited the π-time on the sidebands to $\approx 100\,\mu\mathrm{s}$, while we observed heating rates of up to $8000\,\mathrm{quanta\,s^{-1}}(\mathrm{q\,s^{-1}})$. This means the assumption that the occupation number is constant during the interrogation time would be inaccurate. For these reasons, we instead utilise the Raman transition described in the preceding subsection.

6.2 Experimental implementation

6.2.1 Doppler cooling

We choose the direction of propagation of the 397 nm Doppler beam such that the projection of its wave vector on every principal axis of the harmonic potential is non-zero. As long as the oscillation frequencies ν_m are all distinct , this ensures that motion in all three dimensions will be cooled. We let the 397 nm beam be incident at 45° to the trap axis in the xz-plane of the trap coordinate system, as shown

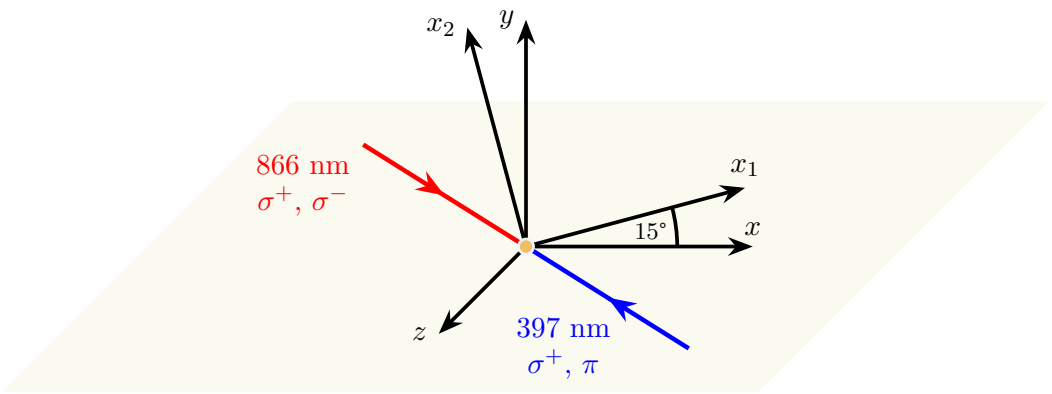


Figure 6.5: Arrangement used for Doppler cooling beams

in fig. 6.5. The atomic quantisation axis lies along the x-axis. We find that, for given wavevector, the condition that no σ^--polarisation component be present in the 397 nm beam uniquely fixes the state of polarisation the incident beam is required to have, in particular the relative magnitude of σ^+-and π-components. With our choice of propagation direction, the σ^+-component is then found to carry 2/3 of total power and the π-component 1/3. We use a half-waveplate and a quarter-waveplate just before the viewport of the vacuum chamber to set the polarisation of the 397 nm beam. The required rotation angles have been calculated theoretically by means of Jones matrices. We choose a counter-propagating geometry for the 866 nm beam as this maximises the change in relative detuning $\delta_{397} - \delta_{866}$ between the Doppler beams for a given velocity of the ion. The polarisation of this beam is less crucial; we choose vertical polarisation along the y-axis for simplicity, resulting in σ^+-and σ^--components of equal magnitude.

The two required frequency components of the 397 nm beam are generated via an EOM. We drive it at the power required for the carrier and first-order sidebands of the output beam to be equal in amplitude. This means that each of the components addressing different hyperfine sublevels carries the same intensity. We set the overall frequency of the 397 nm laser diode such that the carrier drives transitions from the $F = 3$ sublevel and the blue sideband transitions from the $F = 4$ sublevel. This allows us to selectively turn off the latter component for microwave-enhanced optical pumping by switching off the EOM. Additionally, it means that the remaining sideband is red-detuned from any transitions between $4\,S_{1/2}$ and $4\,P_{1/2}$, thus avoiding

possible heating effects that might otherwise arise for ions with large velocities. The optimum carrier frequency and EOM splitting to use for efficient cooling are not straightforward to estimate. Initial simulations for $^{43}Ca^{+}$ at 288 G indicated that a frequency splitting of 2652 MHz between the components of the 397 nm beam should be optimal [Jan15], so we choose to drive the EOM at this frequency.

For initial experiments, we set the carrier frequency of the 397 nm beam a few tens of megahertz to the red of the $4\,S_{1/2}^{3,+3} \leftrightarrow 4\,P_{1/2}^{4,+4}$ transition using a wavemeter and adjusted the power such that an intensity of $30\,I_0$ was available in each of the three components. We moved the frequency of the 866 nm beam so that it matched the frequency difference between the centres of mass of the $3\,D_{3/2}$ and $4\,P_{1/2}$ levels and used a beam power corresponding to $1000\,I_0$. This should ensure efficient repumping even when the frequency of the 397 nm beam was non-optimal. We had calculated the angles that the fast axes of the two 397 nm waveplates should make with the vertical, but in practice we could only easily determine the direction of some neutral axis. We therefore sequentially rotated each waveplate in steps of 90° until we found the orientation that maximised fluorescence from the ion. Given that the 397 nm laser was set close to resonance with transitions from the $m = +4$ end of the ground level, we assumed that strong fluorescence indicated pumping towards this end. We ultimately confirmed this by driving microwave transitions after Doppler cooling and checking that the resonance peak occured at the frequency expected for the $|4, +4\rangle \leftrightarrow |3, +3\rangle$ transition in the ground level.

We next worked on finding the optimal laser frequencies for cooling. Since fluorescence depends on the frequency of both the 397 nm and 866 nm beams, the corresponding parameter space is two-dimensional. However, the frequency of the former has got a much stronger impact on the cooling dynamics than the frequency of the latter because the recoil energy of 397 nm photons and the decay rate from $4\,P_{1/2}$ to the ground level are much larger. In particular, if the 397 nm laser is detuned to the blue from the main transitions responsible for cooling, the ion becomes very hot or may be even be lost, regardless of the frequency of the 866 nm beam. The same behaviour is in general not observed when the 866 nm laser is blue-detuned. We therefore find it advantageous to use scans of the frequency of the 866 nm beam

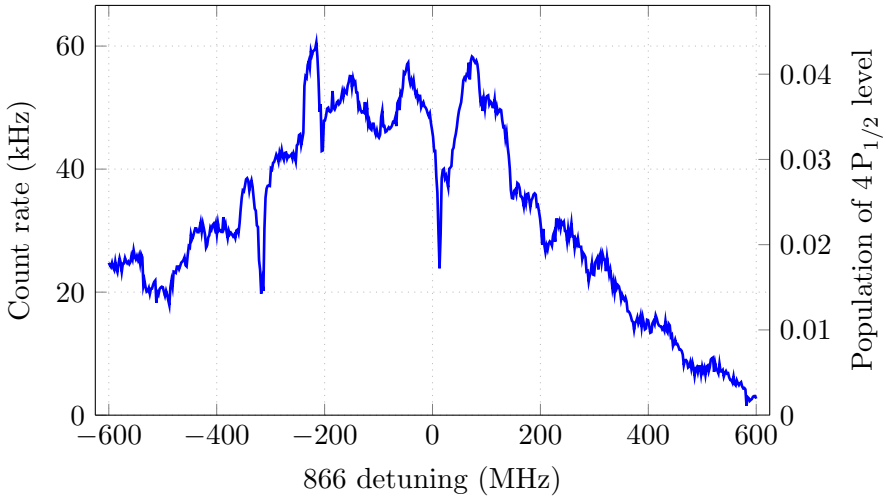


Figure 6.6: Rate of fluorescence collected from ion and inferred population of $4\,P_{1/2}$ level as function of frequency of 866 nm beam. The 866 detuning is measured relative to the reference set by the resonance frequency of the locking cavity.

as the main diagnostic of the cooling performance. During each 866 scan, the frequency of the 397 nm laser is fixed, but we vary the latter across scans to find the optimal value for cooling.

Figure 6.6 contains a typical 866 scan obtained when high laser intensities are used, specifically $33\,I_0$ per frequency component for the 397 nm beam and $1000\,I_0$ for the 866 nm beam. The x-axis corresponds to the detuning of the 866 nm beam relative to the reference frequency set by the position of the locking cavity when the scan was taken. The y-axis gives the population of the $4\,P_{1/2}$ level, as deduced from measured fluorescence rate and known detection efficiency. Two deep dark resonances are clearly visible. By comparison with numerical simulations [Jan15], we infer that the drop in fluorescence around -325 MHz results from destructive interference of the $4\,S_{1/2}^{4,+4} \leftrightarrow 4\,P_{1/2}^{4,+4}$ transition with the $3\,D_{3/2}^{+5} \leftrightarrow 4\,P_{1/2}^{4,+4}$ transition. This should in theory be an ideal dark resonance. The drop around 10 MHz is caused by interference of $4\,S_{1/2}^{4,+4} \leftrightarrow 4\,P_{1/2}^{4,+4}$ with the $3\,D_{3/2}^{+3,k=1} \leftrightarrow 4\,P_{1/2}^{4,+4}$ transition. We repeatedly performed 866 scans while stepping the 397 frequency by 50 MHz and checking for the presence and depth of dark resonances. This allowed us to narrow down the range of 397 frequencies that might lead to efficient cooling. For the particular scan shown in fig. 6.6, the frequency of the 397 nm carrier was set to the value that we later found to be optimal for cooling.

Either of the two strong dark resonances visible in fig. 6.6 is a candidate for cooling. The resonance around -325 MHz exhibits a lower scattering rate near the bottom, so might be expected to lead to slightly lower temperature. However, we choose to work with the resonance around 10 MHz because it enables us to obtain larger fluorescence rates when the 866 nm beam is moved slightly away from the dark resonance, by an amount within the reach of an AOM. This provides a significant advantage with regards to readout.

Having decided on the resonance to use, we then focussed on finding laser intensities for optimum cooling. We adjusted the 397 frequency such that the depth of the selected dark resonance was close to optimal and set the 866 frequency to sit a few megahertz to the red of the bottom. For different combinations of intensities of the 397 nm and 866 nm beams, we drove Rabi flopping on the motional carrier transition using the Raman beams and fitted the resulting curves to obtain estimates of the average occupation numbers of the motional modes. I stress that the arrangement of Raman beams was as given by the solid lines in figure 6.4b and thermometry was therefore only sensitive to the occupation numbers of the radial modes. The results of these fits are depicted in fig. 6.7. We find that the average occupation number of the in-plane mode is minimised when each frequency component of the 397 nm beam carries an intensity of $7 - 10\, I_0$ and the 866 nm beam an intensity of $1000\, I_0$. We focus on this motional mode since it is the one used for the implementation of entangling gates. To ensure robustness against drifts in beam pointing and thus unwanted decreases in intensity, we chose optimum cooling intensities to be $10\, I_0$ per component in the 397 nm beam and $1000\, I_0$ in the 866 nm beam.

As the final step, we optimised the frequencies of the 397 nm carrier and 866 nm beams more carefully. For this purpose, we observed the average occupation number of the in-plane mode for different settings of 397 and 866 frequencies. Since the occupation numbers at this point were relatively low, we estimated them by measuring the ratio of excitation probabilities on first-order red and blue sidebands driven by the Raman beams. For a given setting of the 397 frequency, we scanned the 866 frequency around the respective position of the bottom of the dark resonance. Two kinds of scans were performed: wide scans over ≈ 50 MHz, in which the fluorescence

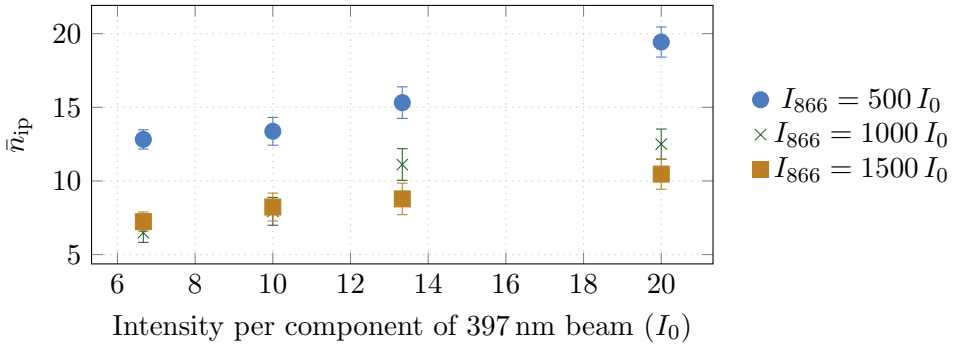


Figure 6.7: Average occupation number of in-plane mode for different intensities of the 397 nm and 866 nm beams.

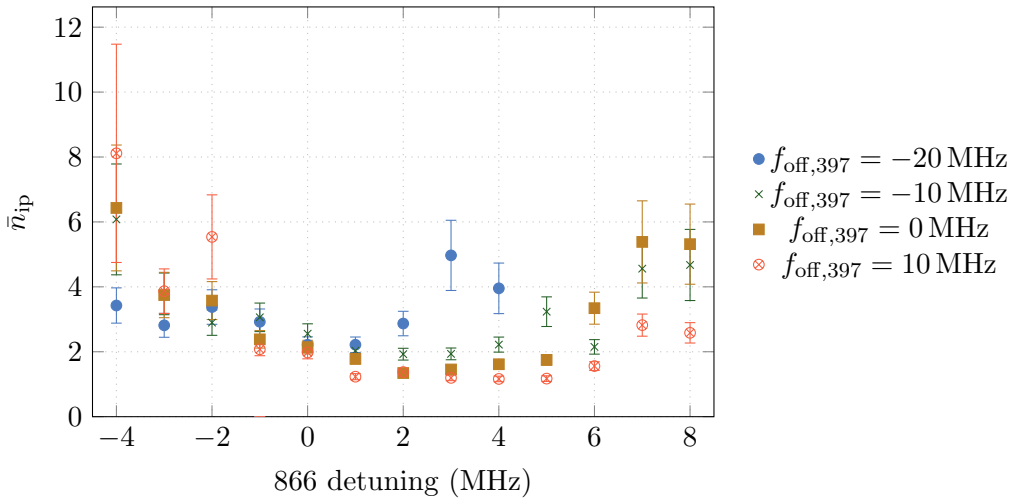


Figure 6.8: Average occupation number of in-plane mode as a function of frequencies of 397 nm and 866 nm beams. Optimal cooling intensities were used.

rate was monitored, and narrow scans over $\approx 12\,\mathrm{MHz}$, in which $\bar{n}_{\mathrm{ip}}$ was measured.

Our findings are shown in fig. 6.8. I have accounted for the fact that the dark resonance moves as the 397 frequency is varied[3]. For each data series, an 866 detuning of 5 MHz corresponds to the bottom of the dark resonance. Average occupation numbers of $\bar{n}_{\mathrm{ip}} < 4$ are obtained within a 10 MHz window for the 866 frequency, which is reliable over a range of 20 MHz in 397 frequency. The lowest values are reached at an 866 detuning of approximately -3 MHz to 1 MHz from the bottom.

The scans of fig. 6.8 provide a way to set reference positions for the Doppler

[3]The condition for a dark resonance is $\delta_{397} = \delta_{866}$, where δ_i is the detuning of the respective beam from the transition it drives. It follows that varying the 397 frequency changes the value of 866 frequency at which the resonance occurs.

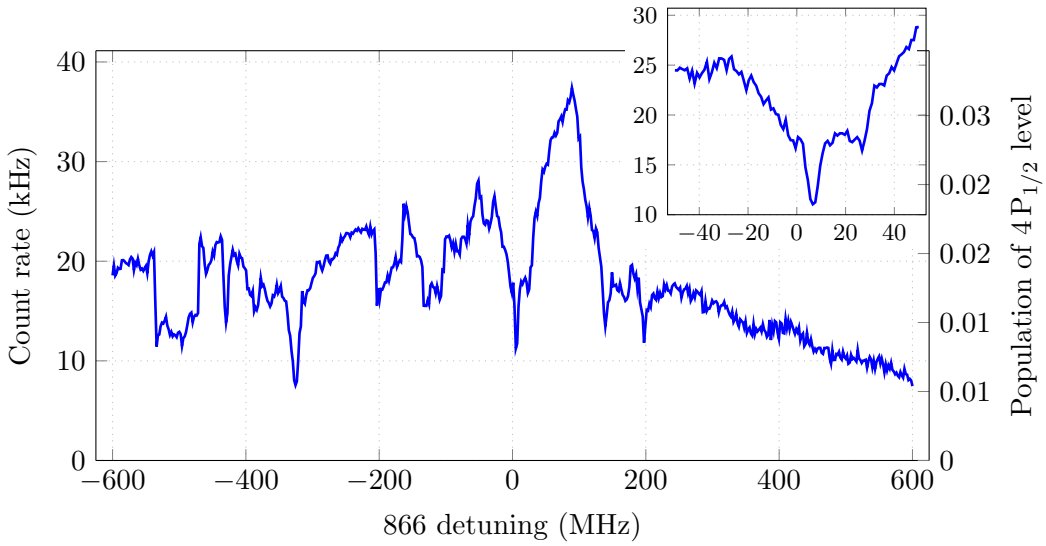


Figure 6.9: Fluorescence profile as a function of frequency of 866 nm beam that is obtained when the frequency of the 397 nm laser is set to the ideal value for cooling. Optimum cooling intensities have been applied. We use the dark resonance close to a detuning of 0 MHz for Doppler cooling. The inset shows a narrower scan around this resonance, which provides a reference for calibrating the frequency of the 397 laser at later times. The 866 detuning is measured relative to the reference set by the resonance frequency of the 866 locking cavity.

lasers in order to ensure that optimum cooling can be maintained reliably in our trap. The reference for the 397 nm beam is not set directly via a 397 frequency scan, but rather determined by that particular fluorescence profile observed during an 866 scan that corresponds to the 397 setting indicated by the brown squares in fig. 6.8. This reference profile is plotted in fig. 6.9. In practice we only use the portion from −50 MHz to 50 MHz around the dark resonance, which is shown as an inset. If the shape of the fluorescence trace obtained during an 866 scan at a later point looks different (and no changes to the imaging system have been made), we infer that the frequency of the 397 nm laser has drifted relative to the reference position. Once the 397 frequency has been set to the reference value, the reference frequency for the 866 nm laser is set to the point in the fluorescence trace that corresponds to a detuning of −3 MHz from the bottom of the dark resonance.

With these settings in place, we took measurements of the absolute frequencies of the 397 nm carrier beam and 866 nm beam using a high-accuracy wavemeter[4]. A summary of the cooling parameters that we found to be optimal and used in all later

[4]HighFinesse WS8-2

Cooling parameter	Value
Frequency of 397 nm carrier beam	755 221 624(30) MHz
Frequency of 866 nm beam	345 996 820(25) MHz
EOM drive frequency	2652.3 MHz
Intensity per frequency component of 397 nm beam	$10\,\mathrm{I}_0$
Intensity of 866 nm beam	$1000\,\mathrm{I}_0$

Table 6.1: Optimal laser parameters for Doppler cooling. The value in parentheses for the frequencies of the 397 nm and 866 nm laser beams represents the systematic uncertainty of the HighFinesse WS8-2 wavemeter.

experiments is contained in table 6.1.

A scan over the first-order red and blue sidebands of the in-plane mode obtained after Doppler cooling when optimal cooling parameters are used is shown further down in fig. 6.13. From the ratio of the two sidebands we infer $\bar{n}_{\mathrm{ip}} = 1.3(3)$, which corresponds to a temperature of 0.45(7) mK. Despite the complex atomic structure of $^{43}Ca^{+}$ at the magnetic field strength used, our cooling scheme enables the ion to reach temperatures close to the Doppler limit.

6.2.1.1 Temperature of out-of-plane mode

The average occupation number of the out-of-plane mode is expected to be much larger than that of the in-plane mode because the projection of the 397 nm cooling beam on the principal axis of the former is significantly smaller. The excitation probabilities on red and blue sidebands are so similar that we cannot obtain an estimate of $\bar{n}_{\mathrm{oop}}$ from their asymmetry, given the statistical uncertainty resulting from readout. Instead, we obtain an order-of-magnitude estimate from Rabi flopping on the motional carrier transition with the Raman beams. Figure 6.10 shows a plot of the transition probability from $|4, +4\rangle\,|\mathbf{n}\rangle$ to $|4, +3\rangle\,|\mathbf{n}\rangle$ as a function of pulse duration after Doppler cooling. The arrangement of the Raman beams corresponds to the solid lines in fig. 6.4b, which means that the transition probability is only sensitive to the occupation numbers of the radial modes. A function of the form

$$P(t) = \mathrm{e}^{-\gamma t} \sum_{n_{\mathrm{ip}}} \sum_{n_{\mathrm{oop}}} P(n_{\mathrm{ip}}) P(n_{\mathrm{oop}})\, \sin^2[\Omega(n_{\mathrm{ip}}, n_{\mathrm{oop}})t/2] \tag{6.11}$$

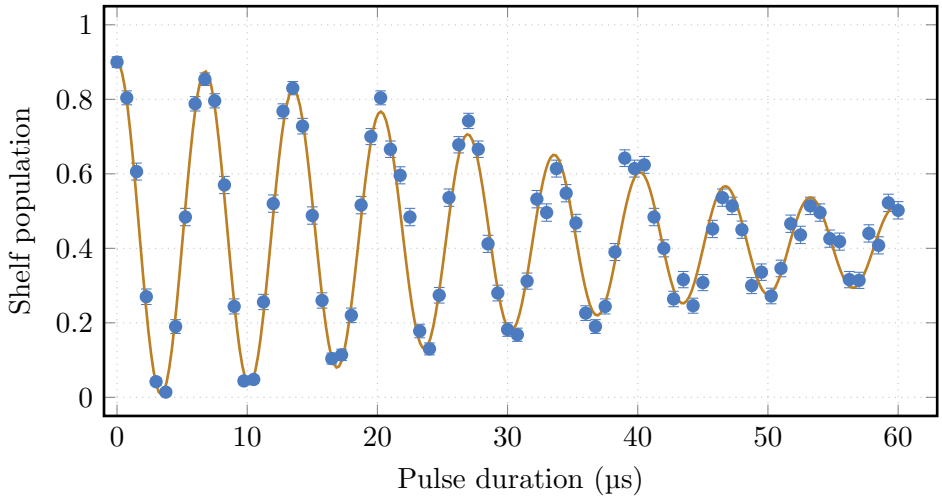


Figure 6.10: Probability of transition on the carrier, from $|4,+4\rangle|\mathbf{n}\rangle$ to $|4,+3\rangle|\mathbf{n}\rangle$, as a function of duration of Raman pulse on resonance. The arrangement of Raman beams was such that the Rabi frequency was only sensitive to the occupation numbers of the radial modes. An average occupation number of $\bar{n}_{\mathrm{oop}} = 37(14)$ is extracted from the fit.

is fitted, where each $P(n_m)$ is given by a thermal distribution (6.5) with parameter $\bar{n}_m$. A factor $\exp(-\gamma t)$ is included to allow for population leaving the subspace spanned by the states $|4,+3\rangle$ and $|4,+4\rangle$, which we believe is caused by spontaneous scattering from $4\,\mathrm{P}_{1/2}$ to other states in the ground level during the Raman transition. The internal coherence time between $|4,+3\rangle$ and $|4,+4\rangle$ may be estimated through eq. (7.3) by inserting the known field dependence of this transition. We find that the damping of Rabi oscillations in the carrier scan is dominated by the interference of transitions involving different motional states rather than decoherence between internal states. The parameter $\bar{n}_{\mathrm{ip}}$ was constrained to lie in the range $1.3 - 2.0$ during fitting. We obtain $\bar{n}_{\mathrm{oop}} = 37(14)$, $\Omega_{\mathrm{ram}} = 2\pi \times 156.1(3)\,\mathrm{kHz}$ and $\gamma = 1.8(4) \times 10^3\,\mathrm{s}^{-1}$.

6.2.1.2 Temperature of axial mode

The temperature of the axial mode may affect the fidelity of two-qubit entangling operations, even though it is not the main motional mode mediating the interaction. This results from cross-coupling to the in-plane mode caused by the non-linearity of the Coulomb potential for an ion crystal [NRJ09]. The error due to this coupling grows with the occupation number of the axial mode. It is therefore important that

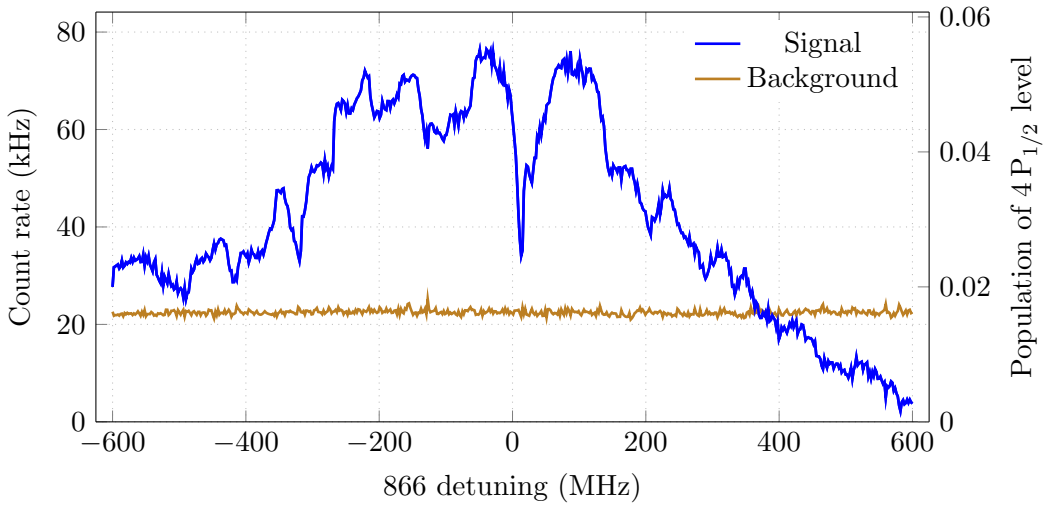


Figure 6.11: Population of $4\,P_{1/2}$ level and rate of fluorescence collected from ion as a function of frequency of 866 nm beam when laser parameters for readout are used. The 866 detuning is measured relative to the reference set by the resonance frequency of the locking cavity.

the axial mode is cold enough for the two-qubit gate fidelity not to be limited by this source of error.

We rearranged the path of the Raman V beam so as to be able to probe the average occupation number of the axial mode. We find that even though $\bar{n}_z$ is relatively high, thermometry based on the sideband method is nevertheless more accurate in this case than use of carrier flopping. From the ratio of sidebands we estimate $\bar{n}_z = 12(3)$.

6.2.1.3 Readout parameters

As pointed out earlier, the main advantage of using the deep dark resonance located at an 866 detuning of 0 MHz lies in the large fluorescence rate that may be obtained by slightly changing the detuning of the 866 nm beam. For readout, we use higher laser powers to maximise population in the $4\,P_{1/2}$ level and thus increase the scattering rate. This is evident in fig. 6.11, which shows a plot of population in $4\,P_{1/2}$ as a function of 866 frequency when our standard readout intensities of $150\,I_0$ for the 397 nm beam and $1500\,I_0$ for the 866 nm beam are used. For readout, we change the 866 detuning to −45 MHz.

6.2.2 Raman sideband cooling

At the end of the Doppler cooling stage, the ion is characterised by average occupation numbers $(\bar{n}_{\mathrm{ip}}, \bar{n}_{\mathrm{oop}}, \bar{n}_z) \approx (1.5, 35, 12)$. Given the standard arrangement of Raman beams indicated by the solid lines in 6.4b, it follows that the Lamb-Dicke regime with respect to the Raman interaction holds for the radial modes, but not the axial.

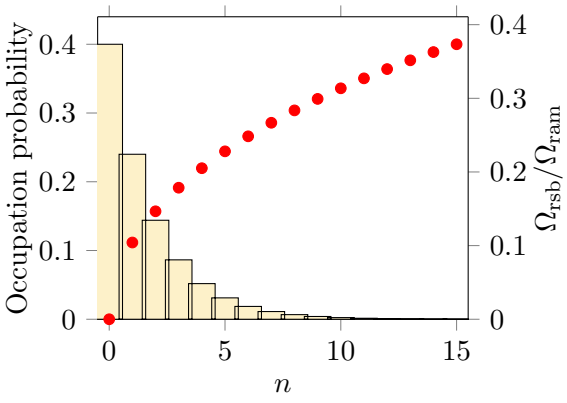


Figure 6.12: Occupation probabilities of different number states for a thermal ion with $\bar{n} = 1.5$ and Rabi frequency of that first-order sideband which extracts a motional quantum.

For two-ion entangling operations, it is desirable to start with ions as close as possible to the ground state of motion. We therefore reduce $\bar{n}_{\mathrm{ip}}$ further via pulsed Raman sideband cooling. The thermal distribution $P(n_{\mathrm{ip}})$ for a particle with $\bar{n}_{\mathrm{ip}} = 1.5$ is shown in fig. 6.12, along with the strength of the Rabi frequency of the first-order red sideband relative to Ω_{ram} for each number state. More than 99.9% of total population is contained within motional states with $n_{\mathrm{ip}} \leq 14$. In theory, the optimal approach to pulsed sideband cooling would thus be to start with a Raman pulse duration that results in a π-pulse for the transition $|4, +4\rangle\,|n_{\mathrm{ip}} = 14\rangle \rightarrow |4, +3\rangle\,|n_{\mathrm{ip}} = 13\rangle$, reset the internal state via the repumper and then repeat this procedure while sequentially adjusting the Raman pulse duration to implement a π-pulse for each motional state with lower occupation number. This method efficiently sweeps population from number states with high n_{ip} down to the ground state of motion. However, we adopted a slightly different approach that is simpler to implement. We used the same duration for all Raman pulses and empirically optimised the pulse duration and number of cooling cycles by measuring $\bar{n}_{\mathrm{ip}}$ for different parameter combinations. For an intensity of $1000\, I_0$ in each Raman beam, we find that the lowest $\bar{n}_{\mathrm{ip}}$ is obtained for a pulse duration of $t_{\mathrm{ram}} = 10\,\mu\mathrm{s}$ and 30 cycles of sideband pulse and repumping.

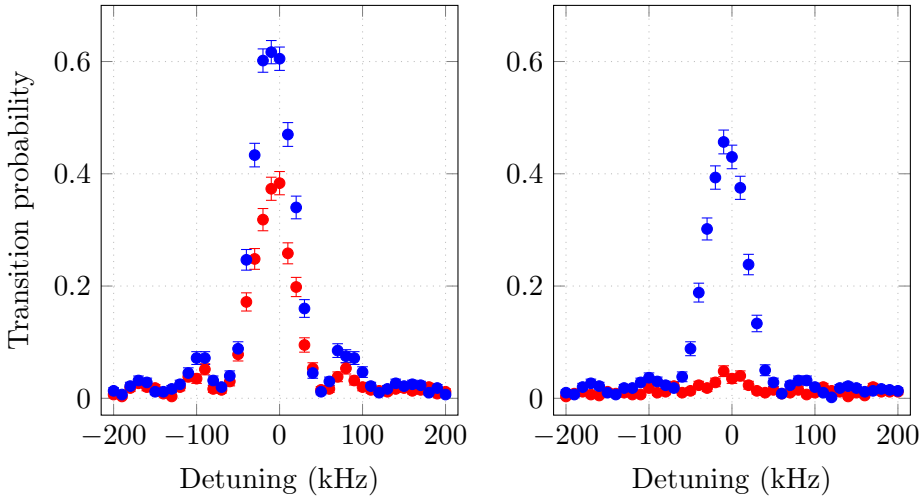


Figure 6.13: Transition probabilities on first-order red and blue sidebands of the in-plane mode for a single ion, driven by the Raman beams. The sideband that extracts a motional quantum is plotted in red, while the sideband that adds a motional quantum is plotted in blue. The detuning is measured relative to the nominal resonance frequency of the respective sideband. a) After Doppler cooling on a dark resonance. From the ratio of sidebands we infer $\bar{n}_{\mathrm{ip}} = 1.3(3)$. b) After 30 pulses of additional Raman sideband cooling. We find $\bar{n}_{\mathrm{ip}} = 0.09(2)$.

For the repumping step, we use the same intensity of $3\,\mathrm{I}_0$ in the 397 nm σ^+ beam as for initial optical state preparation. We find that a pulse time of $t_{\mathrm{pump}} = 20\,\mu\mathrm{s}$ is sufficient to ensure complete transfer of population back to $|4, +4\rangle$.

Transition probabilities on the first-order red and blue sidebands of the in-plane mode are depicted in fig. 6.13. The plot on the left corresponds to sidebands at the end of Doppler cooling, while the plot on the right shows sidebands after Raman sideband cooling, when optimal parameters for each cooling stage are used. From the sideband ratio we infer an average occupation number of $\bar{n}_{\mathrm{ip}} = 0.09(2)$ after sideband cooling. This corresponds to an occupation probability of 92% for the ground state of motion.

6.3 Laser cooling of two ions

We cool two ions using the same methods as for a single ion. An initial stage of Doppler cooling on a dark resonance reduces the vibrational energy of the particles such that the radial modes are placed in the Lamb-Dicke regime with respect to the

Raman lasers. Motional thermometry may be performed using Raman transitions, but the dependence of observed populations on parameters of the driving pulse and occupation numbers of the normal modes is more complicated than for a single ion. A detailed discussion of this topic may be found in [Hom06]. If $\bar{n}$ of the mode of interest is low enough, it may be estimated through the asymmetry of the transition probabilities $P_{\uparrow\uparrow,\mathrm{rsb}}$ and $P_{\uparrow\uparrow,\mathrm{bsb}}$ on the corresponding first-order red and blue sidebands. Here, $P_{\uparrow\uparrow}$ denotes the probability that a two-ion system which initially occupies $|\downarrow\downarrow\rangle$ is found in state $|\uparrow\uparrow\rangle$ after the driving pulse. Explicitly, one finds that

$$\bar{n} = \frac{\sqrt{r}}{1-\sqrt{r}} \,, \tag{6.12}$$

where $r = P_{\uparrow\uparrow,\mathrm{rsb}}/P_{\uparrow\uparrow,\mathrm{bsb}}$.

We have investigated the temperature achieved for the two-ion radial in-plane modes after Doppler cooling as a function of laser intensities and find that the parameters which result in optimum cooling are the same as for a single ion. From the asymmetry of sidebands, we infer average occupation numbers of $\bar{n}_{\mathrm{ip,com}}, \bar{n}_{\mathrm{ip,rocking}} \approx 2$ after dark-resonance cooling. A typical plot of the observed sideband asymmetry for the in-plane rocking mode is depicted in fig. 6.15. Since this is comparable to the temperature achieved for the in-plane mode of a single ion, we assume that the average occupation numbers of the two-ion out-of-plane radial and axial modes are also similar to the values obtained for a single atom.

After Doppler cooling has reached steady state, we lower the temperature of the in-plane rocking mode further via Raman sideband cooling. The theoretical treatment is analogous to the discussion presented in section 5.3 for a single particle, taking into account the normal modes of motion of the ion crystal discussed in 8.1. The Raman interaction Hamiltonian $\widetilde{H}_{\mathrm{int}}^{(i)}$ for each individual ion takes the form given in eq. (5.76), but the exponential now involves $\sum_m k_m x_m^{(i)}(t) = \sum_m k_m \bar{x}_m^{(i)} + \sum_m k_m \rho_m^{(i)}(t)$ in the interaction picture. The first term gives rise to a position-dependent constant phase factor, while the second may be expanded by means of the normal modes of the collective motion. The exponent thus becomes $\sum_{m,p} \eta_{m,p}^{(i)} \left[\exp(\mathrm{i}\nu_{m,p}t)\, a_{m,p}^\dagger + \exp(-\mathrm{i}\nu_{m,p}t)\, a_{m,p}\right]$, where the Lamb-Dicke parameters

for the different modes are defined as $\eta_{m,p}^{(i)} = k_m b_i^{(p)} q_0^{(m,p)}$.

The experimental implementation also mirrors the single-ion case. Both ions are prepared in state $|4,+4\rangle$ of the ground level via optical pumping with the 397 nm σ^+ beam. A Raman pulse resonant with the blue sideband of the in-plane rocking mode on the $|4,+4\rangle \leftrightarrow |4,+3\rangle$ transition is then applied to extract one motional quantum, followed by repumping back to $|4,+4\rangle$. Both ions are illuminated equally by the Raman and repumping beams. Cycles of sideband pulses with subsequent repumping are repeated until the average occupation number, as measured via sideband thermometry, cannot be decreased any further. We use an intensity of $1000\, I_0$ in each Raman beam and keep the duration of the Raman pulse fixed throughout the cooling process. The optimum duration was found empirically by observing the steady-state temperature reached at the end of sideband cooling as a function of pulse length. The same method was applied to determine the optimum number of cooling cycles. We find that the parameters which result in optimal cooling are the same as for a single ion.

When trying to infer the average occupation number for a two-ion mode that has been cooled close to the ground state via sideband thermometry, care has to be taken that the observed transition probability is not significantly affected by resonances arising from other modes nearby that are much higher in temperature. This is particularly relevant for the sideband that extracts a motional quantum since its height tends to zero as the atom approaches the ground state of the corresponding motional mode.

The issue is illustrated in fig. 6.14, where I have plotted the individual Rabi resonance curves for the blue sidebands of two fictitious modes of a single ion when different Raman beam powers and thus Rabi frequencies are used. The natural frequencies and Lamb-Dicke parameters of the modes were chosen to be equal to those observed for the in-plane centre-of-mass and rocking modes of two ions. In both plots, solid lines correspond to a base Raman Rabi frequency of $\Omega_{\mathrm{ram}} = 2\pi \times 42\,\mathrm{kHz}$, while dotted lines result from $\Omega_{\mathrm{ram}} = 2\pi \times 14\,\mathrm{kHz}$. In section 6.2.1.1 we inferred that using an intensity of $1000\, I_0$ in each Raman beam leads to $\Omega_{\mathrm{ram}} \approx 2\pi \times 160\,\mathrm{kHz}$. It follows that the solid lines correspond to an intensity of $\approx 300\, I_0$ in each beam

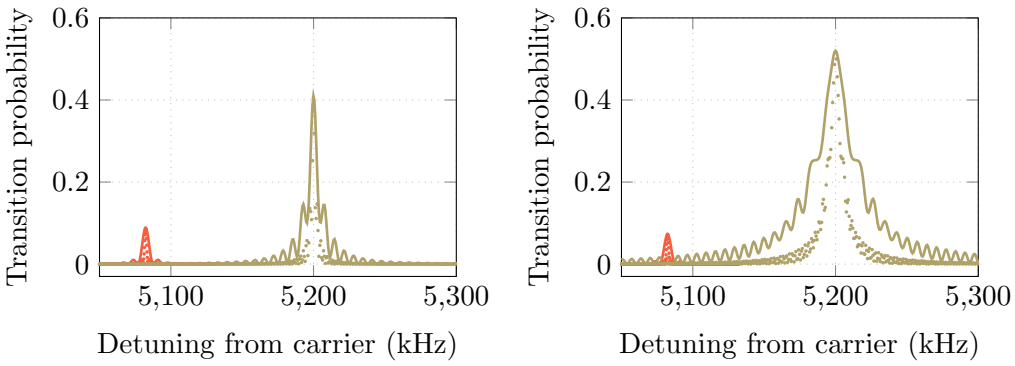


Figure 6.14: Influence of off-resonant spectator mode on the observed transition probability when probing the red sideband of the mode of interest. Resonance curves are calculated for a single ion, assuming two motional modes with frequencies and Lamb-Dicke parameters equal to those observed for the in-plane center-of-mass and rocking modes of two ions. Solid lines correspond to $\Omega_{\mathrm{ram}} = 2\pi \times 42\,\mathrm{kHz}$ and dotted lines to $\Omega_{\mathrm{ram}} = 2\pi \times 14\,\mathrm{kHz}$. The mode of interest, with $\nu_2 = 5.08\,\mathrm{MHz}$, is characterised by $\bar{n}_2 = 0.1$ in both subfigures. a) Off-resonant mode at $\bar{n}_1 = 2.0$. Its effect on transition probability when probing near ν_2 is seen to be negligible. b) Off-resonant mode at $\bar{n}_1 = 50.0$. Depending on the Raman beam power used, an incorrect estimate for the height of the red sideband might be obtained.

and the dotted lines to an intensity of $\approx 100\,I_0$. The average occupation number of mode 2 is $\bar{n}_2 = 0.1$ in both plots. Figure 6.14a assumes that mode 1 is relatively cold, with $\bar{n}_1 = 2.0$. It is clear that in this case off-resonant excitation of mode 1 is negligible compared to the height of the blue sideband of mode 2, even when large Raman beam powers are used. When the temperature of mode 1 is much larger, however, the transition probability arising from off-resonant driving of mode 1 may be significant relative to the excitation achieved on resonance for mode 2 unless the Raman beam powers are reduced sufficiently. This is shown in fig. 6.14b, in which $\bar{n}_1 = 50$. Assuming that the total transition probability observed is approximately the sum of the individual probabilities obtained for completely independent modes, it follows that the height of the blue sideband of mode 2 will be overestimated when the resonances overlap. The same reasoning holds when Raman transitions for two ions are considered. To ensure that estimates of $\bar{n}$ for two-ion modes that are close in frequency do not suffer from this systematic error, we therefore use an intensity of $100\,I_0$ in each Raman beam when performing sideband thermometry.

Scans over the red and blue sidebands of the two-ion in-plane rocking mode

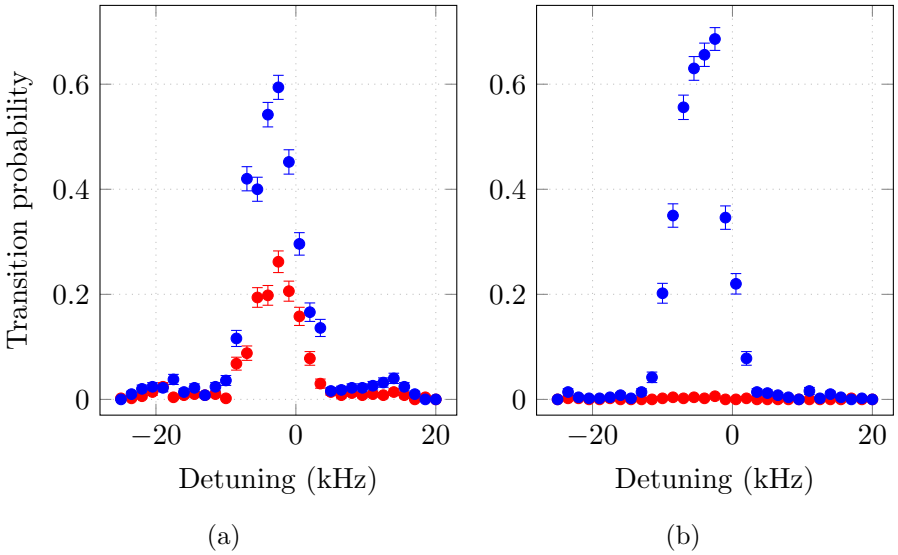


Figure 6.15: Transition probabilities on first-order red and blue sidebands of the radial in-plane rocking mode of two ions, driven by the Raman beams. The sideband that extracts a motional quantum is plotted in red, while the sideband that adds a motional quantum is plotted in blue. The detuning is measured relative to the nominal resonance frequency of the respective sideband. a) After Doppler cooling on a dark resonance. From the ratio of sidebands, $\bar{n}_{\mathrm{ip,rocking}} = 1.8(3)$ is inferred. b) After in-plane centre-of-mass mode and rocking mode have been further cooled via 30 pulses of Raman sideband cooling for each. We find $\bar{n}_{\mathrm{ip,rocking}} = 0.08(2)$.

after Doppler cooling on a dark resonance and sideband cooling, respectively, are contained in fig. 6.15. From the ratio of sidebands we calculate an average occupation number of $\bar{n}_{\mathrm{ip,rocking}} = 1.8(3)$ after Doppler cooling and $\bar{n}_{\mathrm{ip,rocking}} = 0.08(2)$ after sideband cooling. Both are comparable to the temperature achieved for a single ion.

Chapter 7

Trap characterisation and calibration experiments

Before progress towards two-qubit gates could be made, a number of auxiliary calibration routines had to be implemented that would enable reliable operation of our trap. These included experiments to set laser parameters, stabilise the static magnetic field, measure secular frequencies of motional modes and eliminate excess micromotion. With the required routines in place, we proceeded to characterise properties of our surface trap chip that would be relevant for the planned future realisation of high-fidelity two-qubit gates. In this chapter, I discuss the methods used and results obtained for these calibration and characterisation experiments. I collected most of the data presented here, but sections 7.2.5.4, 7.5 and 7.8.2 also contain results of measurements undertaken by other members of the lab. Nevertheless, I carried out the analysis for all data in this chapter.

7.1 Methods to measure transition frequencies

Determining the resonance frequency of the transition between a pair of states $|\downarrow\rangle$ and $|\uparrow\rangle$ is a prerequisite for many operations in our ion trap. I will distinguish between different definitions of transition frequency. There is the bare internal transition frequency $\omega_0 = \omega_{\uparrow\downarrow} = (E_\uparrow - E_\downarrow)/\hbar$, corresponding to the energy difference between internal states as determined by the atomic Hamiltonian. This is usually

taken as the reference transition frequency. However, when a near-resonant field of frequency ω is applied to drive a transition between these internal states, the ω at which resonance (peak population transfer) occurs is in general not ω_0 due to ac shifts induced by couplings to other atomic states that are off-resonant, as explained in chapter 5. Rather, resonance occurs at a frequency $\omega_{\text{eff}} = \omega_0 + \Delta^{\text{ac}}_{\uparrow\downarrow}$, where $\Delta^{\text{ac}}_{\uparrow\downarrow} = \Delta^{\text{ac}}_{\uparrow} - \Delta^{\text{ac}}_{\downarrow}$ is the differential ac shift between the two states. Similarly, if the treatment is extended to include motional states, resonance is not observed at the nominal value $\omega_0 + s\nu_m$, but rather at $\omega_{\text{eff}} = \omega_0 + s\nu_m + \Delta^{\text{ac}}_{\uparrow\downarrow,\text{s}}$, where $\Delta^{\text{ac}}_{\uparrow\downarrow,\text{s}}$ now in general depends on the type of motional transition. For example, the ac shift observed on a carrier transition is different from the ac shift on a first-order sideband. There are two contributions to $\Delta^{\text{ac}}_{\uparrow\downarrow,\text{s}}$: one from background fields that might be present, which I denote $\Delta^{\text{ac,bg}}_{\uparrow\downarrow,\text{s}}$, and one from the near-resonant driving field itself, which I call $\Delta^{\text{ac,drive}}_{\uparrow\downarrow,\text{s}}$.

Perhaps the most intuitive way of determining the position of a resonance is provided by Rabi flopping as a function of frequency ω for fixed pulse time T. The relevant resonance frequency in this case is $\omega_{\text{eff}} = \omega_0 + s\nu_m + \Delta^{\text{ac,bg}}_{\uparrow\downarrow,\text{s}} + \Delta^{\text{ac,drive}}_{\uparrow\downarrow,\text{s}}$ and the Rabi transition probability $P_{\downarrow\rightarrow\uparrow}$ is symmetric about ω_{eff}. The width of the central peak is proportional to the Rabi frequency Ω and inversely proportional to T, which means that, for given statistical uncertainty in measuring state populations, sensitivity may be enhanced by reducing Ω or increasing T. As sensitivity grows, however, the transition probability becomes more susceptible to fluctuations in Ω, which leads to increasingly stringent demands with regards to the stability of the amplitude of the driving field throughout the pulse. A fit to the Rabi curve allows extracting ω_{eff}. If one is only interested in finding the drive frequency ω that has to be used to achieve peak population transfer, this is sufficient. However, if the aim is to experimentally determine the underlying frequencies ω_0 or ν_m, it is necessary to obtain an estimate for $\Delta^{\text{ac}}_{\uparrow\downarrow,\text{s}}$ and use this to correct the measured ω_{eff} for ac shifts. Note that the magnitude of $\Delta^{\text{ac,drive}}_{\uparrow\downarrow,\text{s}}$ decreases as the strength of the drive field and thus the Rabi frequency is reduced. We make use of Rabi flopping for various purposes, including estimation of secular frequencies and the resonance frequency of the stretch qubit.

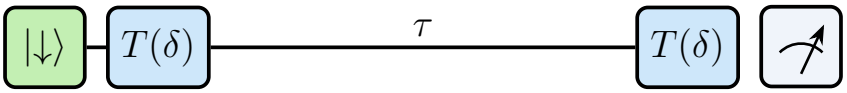


Figure 7.1: Pulse sequence in basic Ramsey scheme. The pulse time T of the two driving pulses is chosen such that $\Omega T = \pi/2$ on resonance. The detuning δ, determined by the frequency of the driving field, or the Ramsey delay time τ may be varied.

7.1.1 Ramsey spectroscopy

A different way of measuring resonance frequencies is offered by the Ramsey scheme [Ram50]. In its most basic form, the scheme is described by the pulse sequence shown in fig. 7.1. The ion is initially prepared in one of the basis states, let us say $|\downarrow\rangle$. It is then excited on the transition of interest by applying a driving field of frequency ω and phase offset ϕ_1 relative to some reference time t_0 for a duration T. During the pulse, the resonance frequency is given by $\omega_{\text{eff,on}} = \omega_0 + s\nu_m + \Delta^{\text{ac,bg}}_{\uparrow\downarrow,\text{s}} + \Delta^{\text{ac,drive}}_{\uparrow\downarrow,\text{s}}$. The strength of the driving field results in a Rabi frequency of Ω on resonance. The duration T is chosen such that on resonance a pulse area of $\Omega T = \pi/2$ is achieved. This moves the state vector of the ion to the equator of the Bloch sphere. After the pulse has ended, the resonance frequency is $\omega_{\text{eff,off}} = \omega_0 + s\nu_m + \Delta^{\text{ac,bg}}_{\uparrow\downarrow,\text{s}}$. The ion is then left to evolve freely for a Ramsey time delay τ, during which it precesses around the z-axis of the Bloch sphere at a rate $\delta_{\text{off}} = \omega - \omega_{\text{eff,off}}$ in a frame rotating at ω. The precession results from the fact that the ion accumulates phase at a different speed compared to the reference oscillator provided by the driving field. The latter is of course not incident on the ion at this point, but may be regarded as acquiring phase in the dark. When τ has passed, another pulse of the driving field is applied, with the same ω, Ω and T, but possibly different phase offset ϕ_2 relative to the same reference time t_0. After the second pulse, the probability that the ion occupies $|\uparrow\rangle$ is measured.

If one ignores the slight difference between $\omega_{\text{eff,on}}$ and $\omega_{\text{eff,off}}$ due to ac shifts from the driving field, the transition probability $P_{\downarrow\to\uparrow}(\tau, \delta)$ after the Ramsey sequence can be calculated from (5.90) by using $\delta = \delta_{\text{off}} = \delta_{\text{on}}$ and $\theta = (\pi/4)\sqrt{1 + (\delta/\Omega)^2}$. The transition probability in this scheme is a function of two parameters: the detuning δ (determined by the drive frequency ω) and the delay time τ. In practice, we

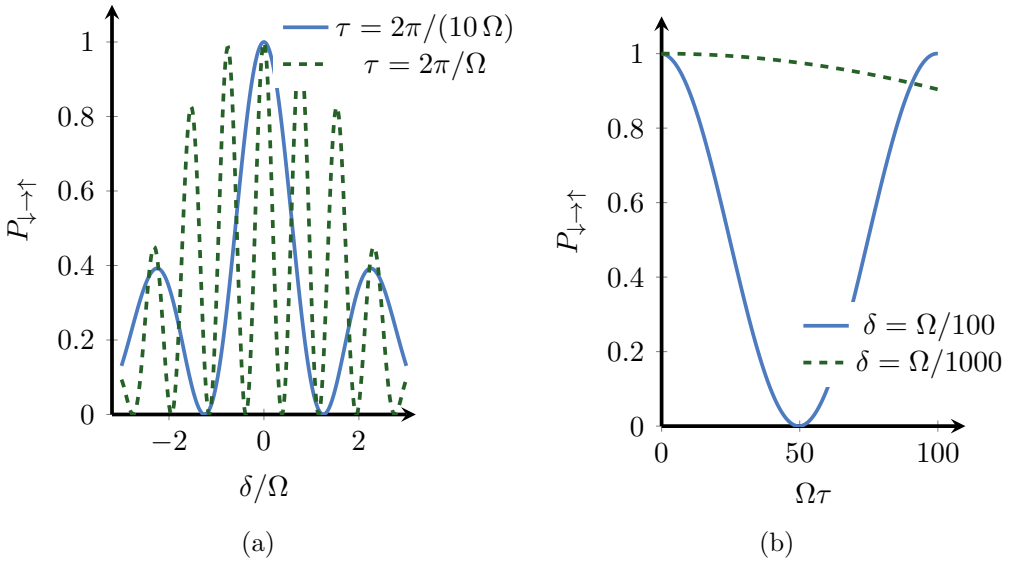


Figure 7.2: Variation of transition probability as a function of parameters in the Ramsey scheme. a) Detuning δ of $\pi/2$-pulses is varied, but Ramsey delay time τ is fixed. b) Detuning is fixed, but Ramsey delay is varied. In both types of Ramsey experiment, the ability to resolve the position of the resonance increases with Ramsey delay.

vary only one while keeping the other fixed, corresponding to two different kinds of Ramsey experiments. They are illustrated in fig. 7.2. If the detuning is varied for constant Ramsey delay, fringes are observed that decay in amplitude as the detuning increases. Under the assumption $\delta_{\text{off}} \approx \delta_{\text{on}}$, the fringes are symmetric and centred on $\delta = 0$, corresponding to the resonance frequency $\omega_{\text{eff,off}}$. The longer τ, the narrower the fringe spacing and thus the greater the ability to resolve the position of the resonance. We use this kind of Ramsey sequence to measure the transition frequency of the clock qubit for magnetic fields near 288 G, as discussed in section 7.5.

I now focus on the other type of sequence, in which the Ramsey delay is the scanned parameter. For fixed δ, the transition probability may be written $P_{\downarrow\to\uparrow}(\tau) = a\cos(\phi_1 - \phi_2 + \delta\tau) + b$, where I have assumed $\delta \ll \Omega$ and thus $\gamma \approx 0$ in eq. (5.90). When dephasing between the states involved is negligible, the basic method is as follows: one applies microwave pulses with a frequency ω close to the presumed resonance frequency of the transition of interest, observes $P_{\downarrow\to\uparrow}(\tau)$ while scanning the delay τ and fits the resulting population curve with a sinusoid. The frequency

of the sinusoid gives[1] δ, which is subtracted from ω to obtain an estimate of the resonance frequency $\omega_{\text{eff,off}}$. This estimate may then be used to update the drive frequency and the procedure repeated with longer delays to increase precision. For the initial estimate, the steps in τ have to be chosen small enough to avoid aliasing.

When decoherence caused by fluctuations in energies of the qubit states is significant, the observed transition probability will no longer be described by a pure sinusoid. Instead, the amplitude of oscillations will decay in time [BP03; LGR04] and thus

$$P_{\downarrow\to\uparrow}(\tau) = a(\tau)\cos(\phi_1 - \phi_2 + \delta\tau) + b\,. \tag{7.1}$$

If a specific form for $a(\tau)$ is assumed, it is possible to use a modified fit function to extract δ. The function $a(\tau)$ depends on the dominant mechanism for decoherence. Even if the functional form of $a(\tau)$ is known, an additional fit parameter has to be introduced. We find it more robust to use a slightly different approach. First we obtain an initial estimate for ω_{eff}, for example through Rabi flopping. Then we run the Ramsey sequence, with fixed ω and τ, but scanning the relative phase $\phi_1 - \phi_2$. The resulting population curve is a pure sinusoid, as is evident from eq. (7.1). Its frequency is known, while its phase $\kappa = \delta\tau$ is extracted from a fit. Scans over $\phi_1 - \phi_2$ are repeated for different Ramsey delays and thus κ as a function of τ may be inferred. The phase from the fit is of course only obtained within the principal range $[0, 2\pi)$, but we may account for phase wrapping by inferring the necessary multiples of 2π from the initial estimate for the detuning. This assumes that the initial estimate for ω is sufficiently close to the true resonance frequency. As the last step, we infer δ as the phase slew rate obtained from a linear fit to κ as a function of τ.

7.1.1.1 Ramsey sequence with spin-echo

A modified Ramsey sequence may be used to measure ac shifts induced by off-resonant pulses [HGR03]. The scheme is shown in fig. 7.3. The initial and final Rabi pulses are driven on resonance with a duration such that a $\pi/2$-pulse results.

[1] The relative phase should be chosen as $\phi_1 - \phi_2 = -\pi/2$ so that the sign of δ may be inferred.

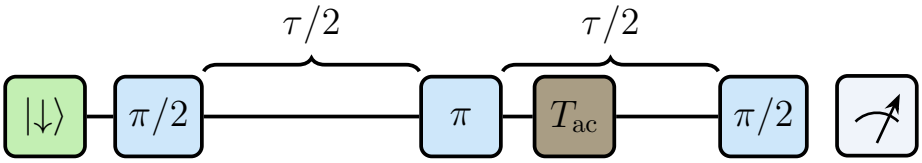


Figure 7.3: Ramsey sequence with spin-echo and off-resonant probe pulses. The duration T_{ac} of the probe pulse is varied.

During the first half of the sequence, the ion evolves freely with resonance frequency $\omega_{\mathrm{eff,off}} = \omega_0 + s\nu_m + \Delta^{\mathrm{ac,bg}}_{\uparrow\downarrow,\mathrm{s}}$ and precesses at a rate $\delta_{\mathrm{off}} = \omega - \omega_{\mathrm{eff,off}}$. Another resonant Rabi pulse is then applied, with pulse area of π, which reflects the state vector around the respective axis of the pulse on the Bloch sphere. In the second half, an off-resonant field is applied for a variable duration T_{ac}, which induces an additional ac shift $\Delta^{\mathrm{ac,probe}}_{\uparrow\downarrow,\mathrm{s}}$. During the probe pulse, the ion thus precesses at a rate $\delta_{\mathrm{off}} - \Delta^{\mathrm{ac,probe}}_{\uparrow\downarrow,\mathrm{s}}$. Because of the spin-echo pulse in the middle, precession due to δ_{off} in the two halves of the sequence cancels. The overall time-evolution operator may be obtained from multiplication of the individual propagators of each pulse and leads to the transition probability

$$P_{\downarrow\to\uparrow}(\tau) = a(\tau)\cos\left(\phi_1 - \phi_2 + \Delta^{\mathrm{ac,probe}}_{\uparrow\downarrow,\mathrm{s}}\, T_{\mathrm{ac}}\right) + b \tag{7.2}$$

when dephasing between the two states is included. The ac shift caused by the probe pulse may then be deduced from a fit to the observed population curve.

7.2 Calibration routines

7.2.1 Laser beam alignment

Slow temperature drifts in our laboratory cause slight deformations in optical components, which change the alignment of laser beams relative to the ion. We therefore re-optimise beam pointing in regular intervals by scanning the voltage applied to each piezoelectric mirror, fitting the response of the relevant experimental quantity with a Gaussian and finally updating the piezo voltage to the value required for peak response. This is particularly important for the Doppler cooling beams since the effectiveness of dark-resonance cooling depends on the intensities at the ion and

hence drifts caused by beam pointing may negatively impact the temperature. Furthermore, the fluorescence threshold levels for readout are also sensitive to Doppler beam alignment. The quantity used for optimisation in case of the Doppler beams is the rate of scattering of 397 nm photons from the ion. However, we find that simultaneous illumination with 397 nm and 866 nm light is not suitable for this purpose, because the presence and depth of the dark resonance depends on the intensities incident on the ion of these two beams. This means that the fluorescence rate is not strictly increasing with intensity and peak fluorescence does not necessarily correspond to optimum alignment. Instead, we use a scheme in which the 397 nm and 866 nm beams are switched on alternately, recording the number of scattered photons for each pulse. Since the two beams are never incident on the ion at the same time, no dark resonance can be formed in this case and, as long as the intensities and pulse times are kept low and short enough to avoid saturation, the number of photons detected always increases with growing intensity. In day-to-day operation, we typically optimise alignment of the Doppler beams every 3 hours, whereas for the remaining beams intervals of 24 hours or more are sufficient. During cooldown and warmup, we cycle through all laser beams repeatedly and adjust their pointing every few minutes to follow the ion.

7.2.2 Setting laser frequencies

The only lasers that we actively calibrate using an ion are those that are locked to optical reference cavities. The frequencies of the remaining lasers are set coarsely via the wavemeter. Adjusting the frequency of the 393 nm laser is relatively easy as we only need to measure the probability of shelving while the frequency of 393 nm light incident on the ion is scanned via the respective AOM. The number of shelving events is maximised when the light is resonant with the $4\,\mathrm{S}_{1/2}^{4,+4} \leftrightarrow 4\,\mathrm{P}_{3/2}^{5,+5}$ transition. We determine the offset of the resulting peak from the zero reference set by the current value of the locking cavity and, if necessary, feed back on the voltage applied to the cavity piezo so that the cavity is moved to resonance with the shelving transition. The same method is used for the 850 nm beam.

Setting the frequencies of the 397 nm and 866 nm Doppler cooling lasers is more

complicated. The temperature of the ion in the trap depends on the frequencies of both lasers, so in theory a 2D optimisation routine could be used. However, we find it easier in practice to vary only the frequency of the 866 nm beam while monitoring the rate of fluorescence from the ion. We then compare the resulting fluorescence curve by eye to reference 866 scans which had been taken for different frequencies of the 397 nm beam and for which the temperature of the ion had been measured with sideband thermometry. These reference scans were discussed in section 6.2.1. We can thus estimate the offset of the 397 nm carrier beam from the target value (corresponding to the reference scan for which the lowest average motional occupation number could be achieved) and adjust the 397 nm locking cavity accordingly. Once the 397 frequency has been calibrated, a narrow 866 scan around the bottom of the dark resonance is performed. We determine the position of the minimum in fluorescence and move the 866 nm cavity such that the light incident on the ion has a frequency corresponding to a detuning of -3 MHz from the bottom, which is the position that we previously found to result in reliable cooling.

7.2.3 Microwave transfer pulses

As described in chapter 2, initialisation of the clock qubit proceeds via two steps: optical pumping to $4\,S_{1/2}^{4,+4}$, followed by microwave transfer pulses. Achieving a low state preparation error therefore requires complete population transfer on each relevant microwave transition, which relies on an accurate estimate of the microwave pulse time necessary to implement a π-pulse for each respective transition. We obtain this calibration by resonantly driving Rabi flops between the relevant pairs of states as a function of pulse time, fitting a sinusoid to the resulting transition probability and extracting the π-time from the fit. When operating the apparatus at a fixed temperature, we find that these reference π-times do not change within statistical uncertainty between calibration runs. When the system is cooled down, however, we see substantial differences, caused by changes in the spatial dependence of the microwave field and an increase in the current flowing through the microwave electrode at lower temperatures. With the standard microwave setup described in section 3.5.5.1 and using an input power of ≈ 1 W, we find typical π-times of 0.3 µs

for the stretch qubit and 0.5 µs for the clock qubit.

7.2.4 Calibration of static magnetic field

The energy eigenstates of the atom depend on the strength of the static magnetic field that is generated by the strong current flowing through our set of main coils. In particular, a field strength of $B_0 = 287.7828\,\mathrm{G}$ is required for the transition frequency of the qubit formed by the pair of states $|4,+1\rangle$ and $|3,+1\rangle$ in the ground level to vary as $f(B) = f_0 + a(B - B_0)^2$ and thus to remain to first order unaffected by field fluctuations. It is therefore important to cancel slow drifts in the field at the ion, which ultimately means adjusting the current through the main coils in regular intervals.

For this purpose, we use Rabi spectroscopy on the stretch qubit, comprised of the states $|4,+4\rangle$ and $|3,+3\rangle$ in the ground level. The transition frequency f_0 of this qubit at the target field of 287.7828 G can be calculated from the Breit-Rabi formula. Measuring the observed resonance frequency f_{obs} for the stretch qubit and comparing with the target frequency f_0 thus allows one to detect any offset from the desired field strength. The method is illustrated in 7.4. We start by preparing the ion in state $|4,+4\rangle$ through optical pumping. Using relatively large microwave power in order to create a wide resonance, we then apply two separate microwave pulses with frequencies $f_0 \pm 0.8\Omega$, where Ω is the Rabi frequency at the given microwave power. The frequencies used correspond to the FWHM points of the central Rabi peak. The pulse duration is chosen such that a π-pulse would result on resonance. After each pulse we observe the probability that the ion occupies $|3,+3\rangle$. If the field strength is correct, the resonance will occur at the target frequency f_0 and the populations measured after each pulse will be the same, within statistical uncertainty. However, if the field strength is incorrect, the resonance will lie at f_{obs} away from the target frequency and the measured populations will be unequal. The observed imbalance can be used to estimate the position of the resonance f_{obs}. We then reduce the microwave power to obtain narrower Rabi features and repeat the procedure using appropriate pulse times and frequencies, where the latter are now calculated relative to the estimated f_{obs}. We continue thus until we reach a resolution of approximately

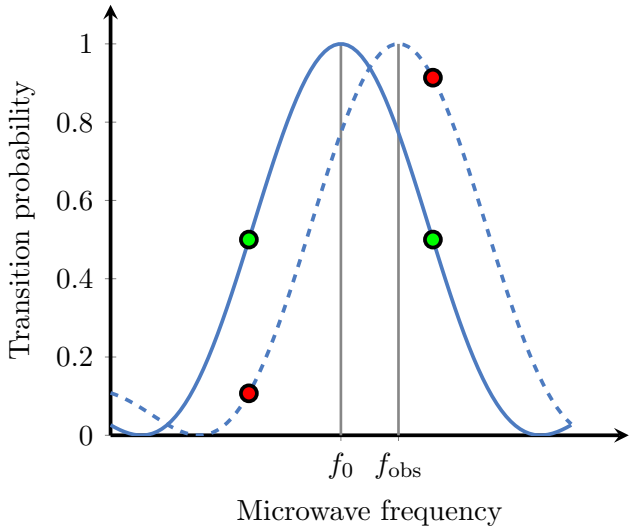


Figure 7.4: Method used to calibrate static magnetic field. Two microwave Rabi pulses, symmetrically spaced around the target frequency f_0 corresponding to the desired field strength, are applied on the stretch qubit. If the static field is correct, the transition probabilities for the two pulses are equal. Otherwise, the observed imbalance can be used to infer the required adjustment in current flowing through the coils.

$\pm 500\,\mathrm{Hz}$ for f_{obs}. The final estimate is then used to infer the offset $f_{\mathrm{obs}} - f_0$, which can be converted to a current correction that is subsequently applied to the coils. We typically run this calibration routine every ten minutes and observe drifts up to $\pm 10\,\mathrm{kHz}$ in the frequency of the stretch qubit between runs, corresponding to field drifts of $\pm 4\,\mathrm{mG}$.

The method just described allows us to cancel slow drifts in the mean strength of the static magnetic field between experiments. There are, however, also faster variations present in the field, caused by rapid fluctuations in the current flowing through the coils. These lead to changes in the energies of atomic states on timescales that are fast compared to the duration of an experiment, with a magnitude determined by the sensitivity df/dB of the respective transition at $288\,\mathrm{G}$. During all experiments described in this work, the current flowing through the main coils was not actively stabilised on fast timescales. Only slow drifts in the magnetic field were eliminated by changing the setpoint of the power supply for the main coils every few minutes.

7.2.5 Measurements of secular frequencies

7.2.5.1 Tickling

The quickest, but least accurate way to measure secular frequencies is provided by a method that we refer to as "tickling". It consists in applying a sinusoidal voltage from a signal generator to one of the dc electrodes while illuminating the ion with the Doppler cooling lasers and monitoring the fluorescence rate. As the frequency of the voltage signal is varied, spikes in fluorescence occur whenever the driving frequency is close to the secular frequency of one of the motional modes. The magnitude of the spike depends on the projection of the perturbing electric field on the principal axis of the respective mode and the projection of the cooling lasers on that axis. The change in fluorescence is therefore most pronounced for the in-plane radial and the axial mode. We find that this method allows a resolution of approximately 2 kHz on the axial mode and 20 kHz on the radial modes.

7.2.5.2 Sideband transitions

Once the secular frequencies have roughly been determined through tickling, the estimates may be refined by driving Rabi flopping on a sideband transition as a function of frequency for fixed pulse time. This method can be used as long as there is a gradient in the driving field along the principal axis corresponding to the mode of interest. When the frequency of the driving field is scanned, resonances appear whenever the driving frequency matches the relevant transition frequency, taking into account ac shifts induced by background fields or the driving field itself. The resonance frequency therefore does not provide a direct estimate of the secular frequency, but rather includes a systematic shift that may be relatively large. For example, we observe an ac Zeeman shift of up to 150 kHz when microwaves are used to drive the sideband. We therefore prefer to use Raman transitions, for which we only find ac Stark shifts of approximately 2 kHz at typical intensities of $300\,I_0$ in each beam. The precision of this method is limited by the width of the resonance and thus the Rabi frequency used. We typically obtain a resolution of 300 Hz. In principle, we could measure the resonance frequency for different drive powers and

extrapolate to zero power to obtain an estimate of the secular frequency without the ac Stark shift caused by the driving field, but at this point it is usually easier to use the method described in the next subsection.

7.2.5.3 Coherent driving of harmonic oscillator

If the mode of interest can be cooled close to the ground state of motion, it is possible to measure its secular frequency by monitoring the height of its red sideband while varying the frequency of a weak sinusoidal voltage applied to one of the dc electrodes. The procedure starts by cooling the mode to $\bar{n} \ll 1$, at which point the red sideband approximately vanishes. The perturbing voltage is then pulsed on for some time, followed by interrogation of the red sideband. If the frequency of the voltage signal is close to the secular frequency, the motional state will be excited coherently[2], resulting in an increase in average occupation number and therefore in the height of the red sideband. The mechanism is essentially the same as for background heating caused by environmental electric noise, except that here the heating is induced in a controlled manner. As long as the environmental heating rate is low enough so as not to swamp the "artificial heating" resulting from the applied voltage signal, there will be a clear resonance at the secular frequency. Using this method, we typically achieve a resolution of 60 Hz. The last two methods mentioned are compared in fig. 7.5.

7.2.5.4 Stability of secular frequency of in-plane mode

Slow drifts in the voltages sustained by the trap electrodes result in gradual changes of the secular frequencies. Since two-qubit gates based on the entanglement of spin and motion rely on correct values for the motional frequencies, such drifts can lead to significant gate errors [SM00; Sep16]. We therefore measure the secular frequency of the in-plane mode of a single ion in regular intervals to monitor the magnitude and timescale of frequency drifts in our apparatus. We use the method presented in section 7.2.5.3 for this purpose. When the temperature of electronic devices generating the rf trapping voltage is not actively stabilised, we observe drifts of

[2]The ion behaves like a driven harmonic oscillator.

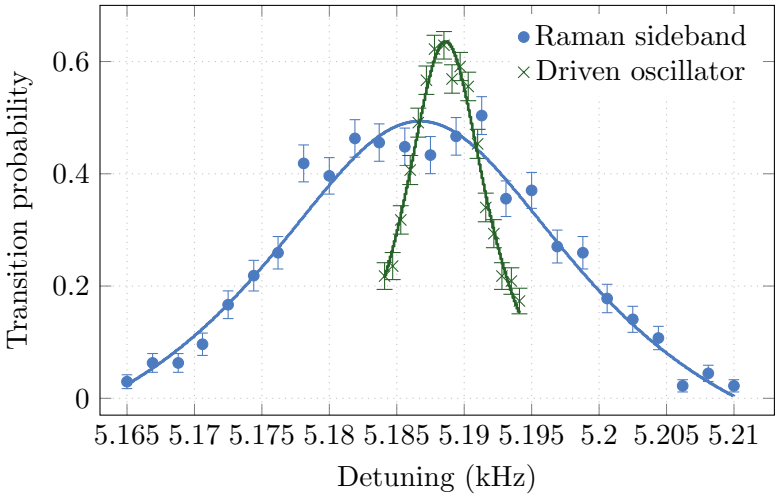


Figure 7.5: Measurements of secular frequency of in-plane mode for a single ion. The blue line shows the transition probability when exciting the first-order blue sideband of the in-plane mode with Raman beams. The position of the resonance is influenced by the systematic error caused by the ac Stark shift induced by the Raman beams. The green line shows the transition probability on the red sideband after the harmonic oscillator corresponding to the in-plane mode has been driven by a weak sinusoidal voltage signal applied to one of the dc electrodes.

up to 2 kHz over tens of minutes. Given that a typical experiment involving spin-motion entanglement runs for a few minutes, these drifts are significant and would result in unacceptably high two-qubit gate errors. We therefore find it necessary to use active temperature stabilisation for the squareatron circuit board and the subsequent rf amplifier and have tried to improve the passive temperature stability of the rf resonator board attached to the baseflange of the vacuum chamber, as described in chapter 3. We checked the passive stability of the output voltages of the DACs providing the dc signals and deduced that they were not the limiting factor. With these measures in place, we find drifts in secular frequency of 300 Hz over roughly half an hour. We believe that the stability at this point is limited by changes in temperature of the rf resonator. Measurements of the secular frequency of the in-plane mode of a single ion over time, with and without active temperature stabilisation, are shown in fig. 7.6. When this data was taken, the trap was operated with a slightly higher rf voltage, which explains the larger secular frequency of the in-plane mode.

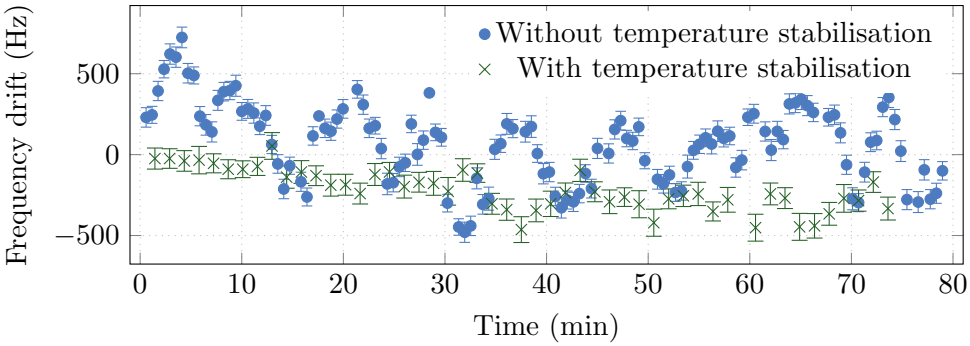


Figure 7.6: Drift in secular frequency of radial in-plane mode for a single ion over time relative to a reference of 5.631 MHz.

7.2.6 Micromotion compensation

The motion of an ion in the trap is determined by both oscillating and static electric fields. The resulting dynamics have been described in detail in chapter 4, where it was found that the trajectory of the ion contains components at frequencies ν (secular motion) and $\nu + n\omega_{\mathrm{rf}}$ (intrinsic micromotion). In the presence of excess micromotion, there are additional components at frequencies $n\omega_{\mathrm{rf}}$. This kind of micromotion is caused by the presence of oscillating rf electric fields at the average position of the ion. This may be due to static fields at the rf null, which shift the equilibrium position of the ion – the trap centre – away from the null. Secular motion then occurs around the shifted trap centre, but may still be cooled. The micromotion amplitude, however, becomes limited to a certain minimum value because the ion no longer approaches the rf node as the magnitude of secular motion is reduced. Rather, it settles around the shifted trap centre, where a non-zero rf field is present that continuously drives micromotion oscillations.

Significant micromotion is undesirable since it changes the fluorescence spectrum of an atomic transition and produces both second-order Doppler and ac Stark shifts [BMB+98]. Additionally, for multi-ion crystals in a trap, excess micromotion affecting one ion may couple to the secular motion of other ions and thus limit the temperature that can be achieved through cooling [KPB+15]. The contribution from intrinsic micromotion is unavoidable, but excess micromotion can be minimised by compensating any stray electric fields at the rf null through application of suitable voltages to the dc electrodes.

Several methods exist for the detection of excess micromotion [BMB+98], two of which we use in our surface trap. The first technique, usually called the rf correlation method, exploits the modulation of fluorescence from the ion due to a time-varying Doppler shift induced by micromotion. The fluorescence signal exhibits a sinusoidal component at the rf frequency, the amplitude of which depends on the magnitude of micromotion and thus the offset from the rf null. As this method relies on Doppler shifts, only micromotion along the direction of propagation of the 397 nm cooling beam can be detected. Given the arrangement of laser beams and trap geometry in our apparatus, this means that we are only sensitive to displacements from the rf null in the xz-plane of the trap coordinate system. We implement the rf correlation method in our trap using a single ion as follows. The instantaneous scattering rate from the ion is not available for us to observe directly, only the arrival times of individual photons at 397 nm. To detect a sinusoidal component, we therefore record photons for a certain duration and correlate the observed arrival times with sine and cosine functions oscillating at the rf frequency. We repeat this procedure for different compensation voltages E_x along the x-direction of the trap coordinate system to find the voltage at which the correlation amplitude is minimised. A typical plot of such a scan is shown in figure 7.7a. We achieve a resolution of approximately $1.5\,\mathrm{V\,m^{-1}}$, which corresponds to an uncertainty of ± 3 nm in the position of the rf node along the horizontal axis, assuming our typical radial secular frequencies of 5.2 MHz and 5.6 MHz.

We cannot use the correlation method to detect excess micromotion in the y-direction since the projection of the 397 nm cooling beam along that axis vanishes. In a different apparatus, our group has previously introduced a repumping beam incident along the vertical for this purpose [Har13], but adopting this approach would lead to additional complexity in our hardware setup. Instead, we exploit the fact that excess micromotion leads to the appearance of micromotion sidebands when coherent transitions between atomic states are driven [WOC+13b], as explained in section 5.2.3.2. Micromotion along an axis may be detected as long as the component of the driving field coupling the internal states exhibits a non-zero gradient along that axis. This means that we cannot use the Raman beams to estimate excess

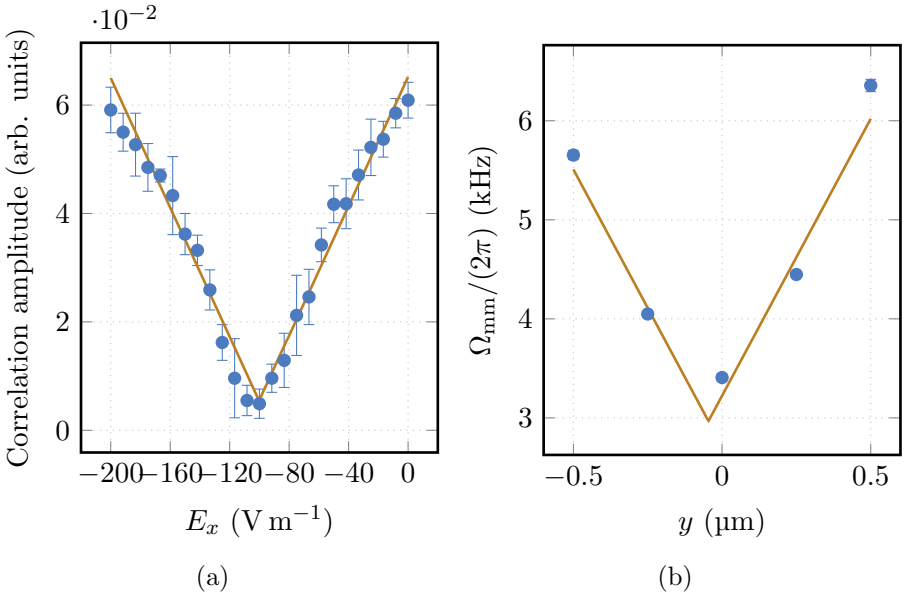


Figure 7.7: Compensation of micromotion in radial directions. a) The optimum compensation field in the x-direction is found by measuring the correlation of fluorescence at 397 nm with the rf frequency. b) The position of minimum excess micromotion in the y-direction, corresponding to the rf null, is determined by measuring the Rabi frequency for the micromotion sideband.

micromotion in the vertical direction since $k_{\mathrm{ram},y} = 0$, nor microwave transitions on a π-qubit in the ground level since $\partial_y B_\pi \approx 0$, as discussed in section 7.8. However, microwave transitions on a σ^+ or σ^- qubit are suitable because $\partial_y B_y \neq 0$ and therefore $\partial_y B_{\sigma^+}, \partial_y B_{\sigma^-} \neq 0$. We choose the qubit formed by $|4, +2\rangle$ and $|3, +1\rangle$ because its coherence time is relatively long. The method is implemented as follows. Initially, excess micromotion along the horizontal x-axis is minimised via fluorescence correlation. Only the compensation field E_x is varied. After this step the ion should be located in the yz-plane, but not necessarily on the rf null. We then displace the ion purely along the y-direction, at each position driving resonant Rabi flopping on the micromotion sideband as a function of pulse time and extracting the Rabi frequency by fitting a sinusoid. Since the principal axes of the dc potential are not aligned with the x- and y-axes and the radial secular frequencies are not degenerate, both E_x and E_y have to be changed during this step, taking into account the offset in E_x necessary to eliminate horizontal micromotion. A typical scan is plotted in fig. 7.7b. The minimum in Rabi frequency corresponds to optimal compensation voltages. We achieve a resolution of approximately ± 3 nm for the position of the

rf null on the vertical axis, comparable to the precision reached for the horizontal direction.

7.3 Validation of model for electric field of trap

There are several experiments that rely on the ability to displace the ion from the trap centre by a certain distance, most importantly the measurements of the spatial variation of the microwave magnetic field, which are presented in section 7.8. We move the ion radially by applying voltages to the dc electrodes that result in a non-zero electric field at the nominal trap centre[3]. This provides a constant force that offsets the atom from the rf null by an amount depending on the strength of the confinement along the principal axes of the harmonic potential in the pseudopotenial approximation. As mentioned in section 4.4.2, we calculate electric fields based on the analytic model provided in [Hou08]. We therefore deemed it necessary to check the validity of this model and ensure that displacements observed in reality match their target values.

We did so via two different methods. For a direct way, we made use of the EMCCD camera of our imaging system. The dimensions of the electrodes on the trap chip [Wol19] and the magnification of the imaging system are known, which means that we can infer the distance in the trap plane that one pixel in the camera image corresponds to. Dialling a target displacement into our control routine and measuring the number of pixels that the ion moves by therefore allows us to detect any mismatch in target and nominal values. This technique is of course only sensitive to position in the horizontal plane because the imaging lens is aligned perpendicular to the trap surface. We find that discrepancies in displacement are $< 3\,\%$.

The other method is not a measurement related to the displacement per se, but rather compares the values of secular frequencies expected from the trap model to those observed in practice for different mode angles. For the experiments in this section, we used only the ten dc electrodes in the central trapping zone, grouping them into four independent voltage sets. The axial frequency f_z and the electric field

[3]The required components E_x and E_y are added to the values found after micromotion compensation.

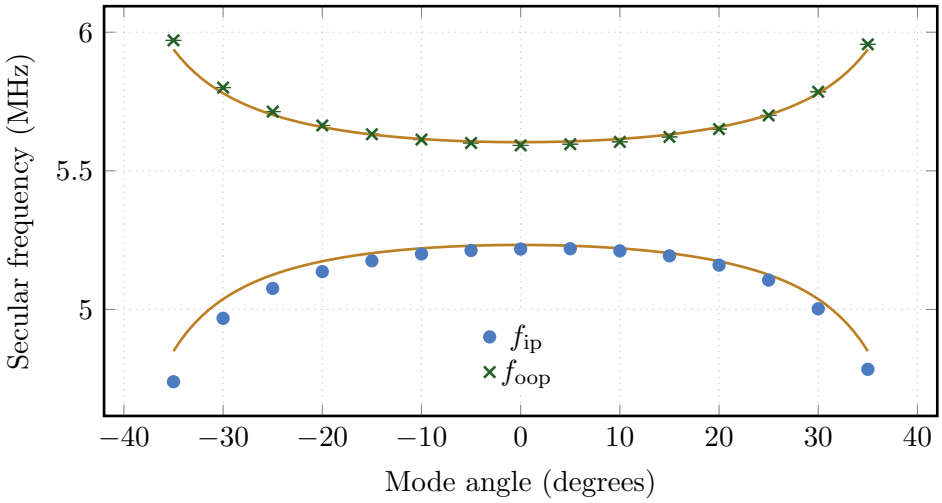


Figure 7.8: Secular frequencies of radial in-plane (f_{ip}) and out-of-plane (f_{oop}) motional modes as a function of mode angle for a single ion. The solid line is the theoretical prediction from the analytic model used for our trap.

components at the trap centre E_x, E_y are kept fixed, but θ is varied. Since there are four parameters and four unknown independent voltages, there is a unique voltage set satisfying the constraints. The curvatures A_{11} and A_{22} of the dc potential along the principal axes in the radial plane are not independent quantities, but rather are determined by whatever potential is needed to achieve the target parameters. Once the solution for the voltage set has been found, the curvatures can be calculated and combined with the Mathieu q parameter via $\nu = (\omega_{\text{rf}}/2)\sqrt{a + q^2/2}$ to obtain predictions for the secular frequencies of the radial modes. We then apply this voltage set to the dc electrodes and measure the secular frequencies observed in practice through sideband transitions using the Raman beams.

The results are shown in fig. 7.8. Lower frequencies correspond to the in-plane mode and higher frequencies to the out-of-plane mode. Micromotion compensation was carried out for $\theta = 15°$, but was not repeated for other mode angles. The solid line is the theoretical prediction in the pseudopotential approximation. Good agreement is observed, in particular for mode angles smaller than 30°.

7.4 Coherence times

Fast variations in the energies of internal atomic states due to fluctuations in the magnetic field providing the quantisation axis lead to decoherence, which shows itself as a decay in the amplitude of Rabi or Ramsey oscillations as a function of time [BP03]. For all experiments described in this thesis, the current flowing through the main coils was not actively stabilised, which means that any noise in the current provided by the Agilent 6671A power supply fully impacts on the stability of the magnetic field. To ensure that the decoherence resulting from these conditions would not have a significant detrimental effect on the experiments that we present in this work, we obtained rough estimates for the coherence times of the stretch and clock qubits.

We use the Ramsey method described in section 7.1.1 for this purpose. The relative phase $\phi_1 - \phi_2$ of the driving pulses is scanned for fixed Ramsey delay τ and the corresponding amplitude a extracted from fitting $P_{\downarrow\to\uparrow}$. Repeating the scan for different τ allows measuring the fringe contrast $2a(\tau)$ as a function of Ramsey delay time. In our trap, we find that the decay in contrast for the stretch qubit is described by a Gaussian of the form $\exp\left(-\tau^2/T_\mathrm{c}^2\right)$, where T_c denotes the coherence time. This indicates that dephasing for this qubit is dominated by noise with correlation time longer than the Ramsey delays used. We measure $T_\mathrm{c} \approx 50\,\mu\mathrm{s}$, from which we may estimate the rms magnetic field noise σ_B through [MTT19]

$$\sigma_B = \frac{\sqrt{2}}{2\pi\, T_\mathrm{c} \left|df/dB(B_0)\right|}\,, \tag{7.3}$$

where $\left|df/dB(B_0)\right| = 2.5\,\mathrm{kHz\,mG^{-1}}$ is the field sensitivity of the stretch qubit at $B_0 = 288\,\mathrm{G}$. We infer $\sigma_B \approx 1.8\,\mathrm{mG}$. This value is close to the rms field noise measured previously in a different lab of our group with a similar noise environment [MTT19]. It can be used to estimate the coherence times of other field-sensitive transitions through eq. (7.3) by inserting the relevant $\left|df/dB(B_0)\right|$. For the clock qubit, we experimentally observe exponential decay $\exp\left(-\tau/T_\mathrm{c}\right)$, whence we infer that relevant noise is correlated on timescales shorter than the Ramsey delays used for this qubit. We measure $T_\mathrm{c} \approx 500\,\mathrm{ms}$, highlighting the great advantage of field-

insensitive transitions with regards to internal dephasing. Taking into account the timescales of coherent operations on the various transitions used in this thesis, we may conclude that magnetic field noise should have negligible influence.

7.5 Transition frequency of clock qubit

We have carried out experiments to confirm the first-order insensitivity of the clock qubit to fluctuations in magnetic field around the predicted value of $B_0 = 28.8\,\mathrm{mT}$, using the following procedure: we start by adjusting the current running through the main coils to set the magnetic field to the desired strength at which we wish to probe the clock transition. For this purpose we use Rabi flopping on the stretch qubit in a similar way as for the field stabilisation routine described in section 7.2.4, but here we intentionally move the magnetic field away from B_0. We then perform a sequence of Ramsey scans on the clock qubit, in which we observe the transition probability $P_{\downarrow\rightarrow\uparrow}$ as a function of frequency of the applied microwave field for fixed Ramsey delay τ. The curves for $P_{\downarrow\rightarrow\uparrow}$ take the form shown schematically in the left plot of fig. 7.2. The resonance frequency of the qubit corresponds to the position of the central fringe. We start with short τ so as to be able to identify the central fringe unambiguously and subsequently increase τ in steps that are small enough that we can keep track of this fringe. The larger τ, the more accurately the position of the central fringe may be resolved. Once the last Ramsey scan, for which we use $\tau = 2\,\mathrm{ms}$, has been taken, we change the setpoint of the magnetic field and repeat the procedure. The resulting data is displayed in fig. 7.9. I have plotted $f - f_0$, where f is the measured transition frequency of the clock qubit and $f_0 = 3.123\,181\,794\,\mathrm{GHz}$ is the theoretical prediction at the field-independent point based on the Breit-Rabi formula. A parabola of the form $f - f_0 = (1/2)\, d^2f/dB^2\big|_{B_0}\,(B - B_0)^2 + b$ has been fitted to the data, from which $B_0 = 28.7782(1)\,\mathrm{mT}$, $d^2f/dB^2\big|_{B_0} = 253(2)\,\mathrm{kHz\,mT^{-2}}$ and $b = 144.0(7)\,\mathrm{Hz}$ are obtained. The parameter b represents a systematic offset between the measured transition frequency of the clock qubit at the critical field and the theoretical prediction. This offset will be discussed in the following paragraph. The estimates for B_0 and $d^2f/dB^2\big|_{B_0}$ are consistent with the theoretical values of

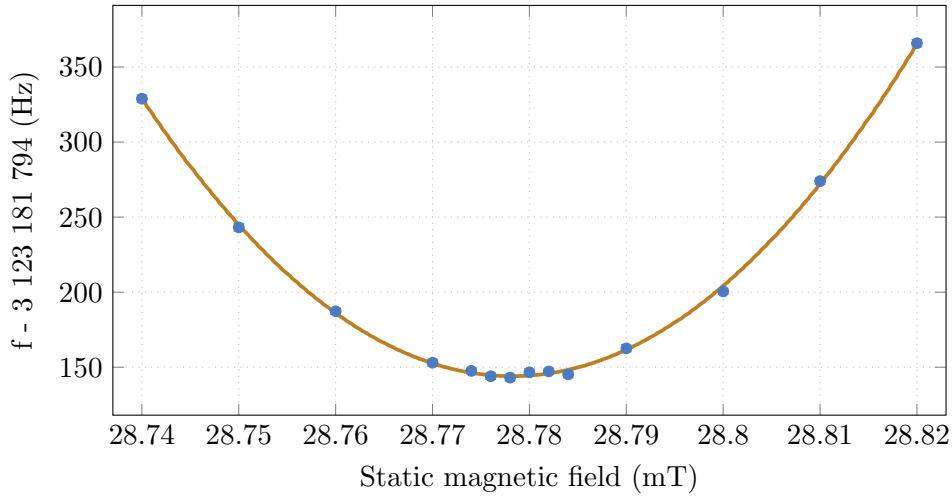


Figure 7.9: Transition frequency of qubit formed by states $|4,+1\rangle$ and $|3,+1\rangle$ in the $4\,S_{1/2}$ ground level as a function of static magnetic field.

28.778 28 mT and 251.4 kHz mT^{-2} calculated by means of the Breit-Rabi formula. Before accounting for systematic shifts, we thus measure a transition frequency of $f = 3.123\,181\,938\,0(7)$ GHz at the critical field strength.

While the purpose of this experiment was to confirm B_0 for the clock qubit, I find it necessary for completeness to briefly comment on the observed transition frequency. The reader is referred to ref. [Har13] for a thorough discussion of systematic effects in this kind of measurement. We estimate a quadratic Zeeman shift of approximately 30 mHz, while second-order Doppler shift and ac Stark shift are at most 1 mHz. These all lie significantly below the uncertainty in our measurement. More relevant is the systematic shift connected with the calibration of the rubidium reference used as part of the arrangement for the generation of microwaves. It was last compared to the global GPS reference about six years before the data presented here was taken. From observations made back then [Har13] and assuming that the rate of ageing over the last six years has remained the same, I expect a fractional error of roughly 9×10^{-10} by the time our experiments were conducted, such that the rubidium reference runs slightly faster than the GPS clock. Taking into account the uncertainty in ageing rate, I estimate a shift of $-3(2)$ Hz on the frequency of the clock qubit.

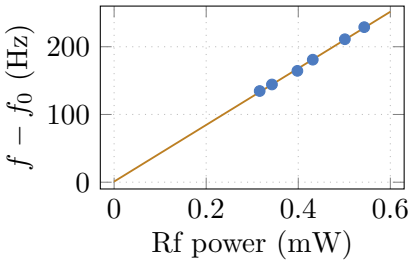


Figure 7.10: Measured transition frequency of clock qubit as a function of output power of rf source.

The largest systematic effect results from the ac Zeeman shift caused by the magnetic field generated by small currents flowing in the rf electrodes, as a consequence of the finite resistance of these electrodes. To estimate the magnitude of this shift, we have varied the output power of the DDS channel used to produce the rf voltage and measured the qubit frequency, with the static field set to the critical value B_0. The results are shown as an inset to fig. 7.9. The fitted line exhibits an offset of 1(4) Hz, indicating an ac Zeeman shift of 143(4) Hz at the rf power used for the earlier measurement. After adjusting for systematic shifts, we thus estimate a transition frequency of $f = 3.1231817980(7)(45)\,\mathrm{GHz}$, where the first number in parentheses denotes statistical uncertainty and the second systematic uncertainty.

7.6 Single-ion heating rates

One of the main sources of error for two-qubit gates in the Mølmer-Sørensen scheme is heating of the motional mode during the entangling operation. For the two-qubit gates which are to be implemented in our trap, the relevant mode is the two-ion rocking mode along the in-plane direction. Measurements of the corresponding heating rate will be presented in section 7.7, but here I first discuss the results obtained for the heating rate of a single ion. While the single-ion heating rate does not immediately translate to an absolute estimate of the heating rate of the two-ion mode, it is a very valuable diagnostic tool to monitor relative changes in heating rate as we add or rearrange hardware in our apparatus or operate the system at different temperatures. In general, the heating rates of single-ion and two-ion modes under the same experimental conditions are often directly proportional [BKR+15] and it follows that any improvements in single-ion heating rate should result in a reduced heating rate on the two-ion rocking mode and thus a lower gate error.

Motional heating refers to an increase in average occupation number $\bar{n}_m$ for a

given motional mode due to transitions between vibrational states that are caused by coupling of environmental electric field noise to the charge of the ion. A detailed review of heating mechanisms and experimental observations in ion traps has been provided in [BKR+15]. They derive a theoretical expression for the heating rate and show that for low $\bar{n}_m$ it is given by

$$\dot{\bar{n}}_m = \frac{e^2}{4\hbar M \nu_m} \left[c_{0,m}^2 S_\mathrm{e}\left(\nu_m\right) + c_{-2,m}^2 S_\mathrm{e}\left(\omega_\mathrm{rf} - \nu_m\right) + c_{2,m}^2 S_\mathrm{e}\left(\omega_\mathrm{rf} + \nu_m\right) \right] , \tag{7.4}$$

where $c_{2n,m}$ are the coefficients in the classical solution to the Mathieu equation (see chapter 4) and

$$S_\mathrm{e}(\omega) = 2 \int_{-\infty}^{\infty} \langle E_\mathrm{n}(t) E_\mathrm{n}(0) \rangle \, \mathrm{e}^{-\mathrm{i}\omega t} \, dt \tag{7.5}$$

is the single-sided spectral density of the electric field noise $E_\mathrm{n}(t)$. This shows that heating is caused by driving of secular motion and intrinsic micromotion by noisy environmental fields and it is therefore important to minimise noise at the corresponding frequencies.

There are several sources of heating in ion traps. Here I will only note the main contributions expected for our surface trap and measures taken to mitigate them. One important factor is what I will label "technical noise" for the purpose of this discussion. By this I mean all noisy electric fields resulting from equipment used in our experiments, except the trap chip itself (corresponding to sections IV B – D in ref. [BKR+15]). One such example is voltage noise caused by pick-up of electromagnetic interference by wires and electronic components of our apparatus. The dominant contribution in this case are voltages induced through fluctuating magnetic fields enclosed by loops in the wiring leading to the trap. Such loops are to some degree unavoidable in any experimental setup, but their area needs to be minimised. Great care has been taken in our apparatus to reduce this noise source as much as possible. Most cables used are shielded and we ensure that they are routed efficiently and in parallel, so as to avoid large loop areas. An attempt has been made to reference all electronic devices to a common ground. Where this is not directly possible, thick wires are used to minimise the voltage drop between different ground planes. Another example of technical noise are fluctuations in the output of power

supplies or output of the electronic devices generating the voltages applied to the electrodes. Since manufacturers usually characterise the performance properties of their components, the likely magnitude of this kind of noise may be estimated from their spec sheets and we mitigate it by ensuring that high-spec components are used as hardware for the trap. Thirdly, technical noise may result from stray fields that directly impinge on the ion, caused by radiation sources in the environment. This is especially relevant inside buildings containing a large number of electric devices such as our labs. We have not made specific efforts to eliminate this contribution in our apparatus, but instead rely on the fact that the ion is surrounded by metal surfaces such as the pillbox, vacuum chamber and optical table on most sides, which should provide a significant amount of shielding. Another relevant noise source is thermal noise in electronic components. This is unavoidable at finite temperatures, but it is important to note that what matters is the noise at the position of the ion, which is not in general the sum of the contributions from each individual component, but rather depends on the entire circuit. In particular, filters before the trap electrodes may be used to reduce noise in a certain frequency range. We have therefore integrated a set of low-pass filter PCBs for the DC electrodes into the pillbox within the vacuum chamber. This should of course also filter noise resulting from some of the other mechanisms mentioned above. Additionally, we expect thermal noise from components on the pillbox to diminish in cryogenic operation as the resistance of most metals decreases with temperature.

Apart from technical noise, the main contribution to motional heating results from microscopic noise in the trap chip itself. This effect, known as "anomalous heating", has been investigated in several experiments and different explanations proposed [BKR+15]. An important feature of this kind of noise is that it strongly increases as the distance d of the ion from the trap surface is reduced. Most theoretical models predict microscopic noise to decrease as the temperature is lowered, because the underlying mechanisms are thermally activated.

A large number of experimental measurements of heating rates for different trap geometries, secular frequencies and temperatures have been made to date by several groups. It is usually difficult to identify the main contribution to the heating rate

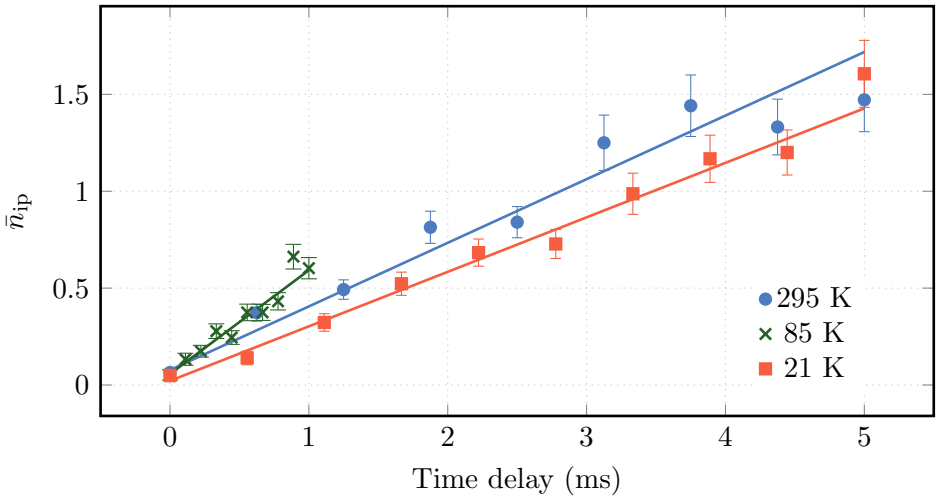


Figure 7.11: Heating rate of the in-plane mode of a single ion at different temperatures. From the linear fits we infer $\dot{\bar{n}}_{\mathrm{ip}} = 328(15)\,\mathrm{quanta\,s^{-1}}$ at room temperature, $\dot{\bar{n}}_{\mathrm{ip}} = 535(39)\,\mathrm{q\,s^{-1}}$ at 85 K and $\dot{\bar{n}}_{\mathrm{ip}} = 281(15)\,\mathrm{q\,s^{-1}}$ at 21 K.

for a given trap and the various heating mechanisms scale differently with experimental parameters. As highlighted in the review paper of [BKR+15], however, some general trends may be inferred. The exact dependence of $S_{\mathrm{e}}(\omega)$ on d depends on the dominant heating mechanism, but a scaling between $d^{-3.5}$ and $d^{-3.8}$ has been experimentally observed. This is likely due to anomalous heating. We would therefore expect the heating rate in our trap to be higher than that of the microwave trap previously used in our group [Sep16], if all other noise contributions were the same, since the ion height in the latter was almost double at 75 µm. Various scalings of $S_{\mathrm{e}}(\omega)$ with temperature have been observed, some of them vastly different, but it has been conjectured that on average the heating rate may be improved by 2 orders of magnitude by cooling a trap from room temperature to 6 K [BKR+15]. This is one of the reasons why our apparatus was designed for cryogenic operation.

We have taken measurements of the heating rate of the in-plane mode for a single ion in our trap at different temperatures. The ion is initially cooled close to the ground state via Raman sideband cooling and then left to evolve freely for a variable delay time. At each scan point the asymmetry between red and blue sidebands is measured and thus $\bar{n}_{\mathrm{ip}}$ as a function of time inferred. The heating rate $\dot{\bar{n}}_{\mathrm{ip}}$ is then extracted through a linear fit. The results are shown in fig. 7.11.

No clear trend in heating rate with temperature is observed, as we measure

$\dot{\bar{n}}_{\mathrm{ip}} = 328(15)\,\mathrm{quanta\,s^{-1}}(\mathrm{q\,s^{-1}})$ at room temperature, $535(39)\,\mathrm{q\,s^{-1}}$ at 85 K and $281(15)\,\mathrm{q\,s^{-1}}$ at 21 K. These rates correspond to noise spectral densities of $S_{\mathrm{e}}(\nu_{\mathrm{ip}}) = 1.26(6) \times 10^{-11}\,\mathrm{V^2\,m^{-2}\,Hz^{-1}}$ at room temperature, $2.1(1) \times 10^{-11}\,\mathrm{V^2\,m^{-2}\,Hz^{-1}}$ at 85 K and $1.08(6) \times 10^{-11}\,\mathrm{V^2\,m^{-2}\,Hz^{-1}}$ at 21 K, neglecting any contribution from micromotion. The voltages applied to the trap electrodes were kept the same for all scans shown in fig. 7.11. The secular frequency moved slightly as the trap cooled down due to a decrease in the resistances of the electrodes and slight changes in the dimensions of the trap, so one might argue that the frequency dependence of $S_{\mathrm{e}}(\omega)$ could play a role in the observed behaviour. However, when we changed dc voltages at fixed temperature, resulting in different values of the secular frequency, the heating rate did not change significantly. In particular, when the frequency at 80 K was adjusted to lie within 10 kHz of that used at room temperature, no decrease in heating rate compared to operation at room temperature was seen. It therefore seems likely that the limiting contribution to the heating rate is technical noise. Before moving to cryogenic operation, we had previously spent considerable time at room temperature changing the arrangement of hardware so as to minimise electric noise at the ion. During this process, we had observed heating rates up to $8000\,\mathrm{q\,s^{-1}}$, indicating that technical noise can have a large influence. We believe that the most important factors have been mitigated, as evident in the reduction of heating rate to $< 500\,\mathrm{q\,s^{-1}}$. In particular, we find no change in heating rate even when we completely disconnect the DACs supplying the dc voltages[4]. This indicates that remaining noise is probably dominated by fluctuations on the rf or mw electrodes or the ground plane. Even though it seems plausible that the heating rate is still dominated by technical noise, we have not made further efforts to improve it since we find that the heating rate of the two-ion rocking mode, as presented in the next section, is at this point low enough that we do not expect it to be the limiting factor for the fidelity of entangling gates in the Mølmer-Sørensen scheme.

[4]Charge leakage in our trap is slow, so that the potentials on the dc electrodes stay constant long enough for us to take a measurement of the heating rate via sideband thermometry.

7.7 Two-ion heating rates

A detailed discussion of heating rates for a string of ions may again be found in ref. [BKR+15]. The authors show that one may define a heating rate $\bar{n}_{m,p}$ for each normal mode p along coordinate axis m as

$$\dot{\bar{n}}_{m,p} = \frac{e^2}{4\hbar M \nu_{m,p}} S_{\mathrm{e}}(\nu_{m,p}) \ , \tag{7.6}$$

when effects due to micromotion are ignored. The relevant spectral noise density is given by

$$S_{\mathrm{e}}^{(m,p)}(\omega) = 2 \sum_{i,j} \int_{-\infty}^{\infty} \langle E_{\mathrm{n}}^{(i,m,p)}(t)\, E_{\mathrm{n}}^{(j,m,p)}(0) \rangle \, \mathrm{e}^{-\mathrm{i}\omega t} \, dt \ , \tag{7.7}$$

where $E_{\mathrm{n}}^{(i,m,p)}(t)$ is the projection of the noise fluctuations $\mathbf{E}_{\mathrm{n}}\big(\mathbf{x}^{(i)}, t\big)$ at the position of the i-th ion onto the normal mode labelled by m, p. The important point is that the heating rate of a mode depends on the correlation of the field noise at the positions of the different ions. For typical sources of field noise, the correlation length is significantly larger than the inter-ion spacing [BKR+15], so that the noise differs little from one ion to the next. Under this condition, one finds that the heating rates of the centre-of-mass modes of an ion string scale as $\dot{\bar{n}}_{m,\mathrm{com}} = N \dot{\bar{n}}_m$, where $\dot{\bar{n}}_m$ is the heating rate for the same mode of a single ion. For all other modes of the ion chain, $\dot{\bar{n}}_{m,p} \approx 0$. This highlights the fact that those normal modes in which the ions do not oscillate in lockstep can only be excited by a force with a non-zero differential component. In practice, the heating rates of these modes do not vanish completely, but are nevertheless much smaller than those of the centre-of-mass modes.

Measurements of heating rates typically observed in our trap for the radial in-plane modes of two ions in our trap, taken at a temperature of 85 K, are depicted in fig. 7.12. The method applied was the same as for a single ion: the two-ion crystal was cooled close to the ground state via Raman sideband cooling and the rise of $\bar{n}_{m,p}$ with time was inferred by monitoring the asymmetry of the corresponding motional sidebands. Linear fits yield $\dot{\bar{n}}_{\mathrm{ip,com}} = 380(31)\,\mathrm{q\,s^{-1}}$ and $\dot{\bar{n}}_{\mathrm{ip,rocking}} = 2.6(9)\,\mathrm{q\,s^{-1}}$ for these particular scans. I note that the small heating rate of the rocking mode allows us to reach lower temperatures after sideband cooling, as seen by comparing the

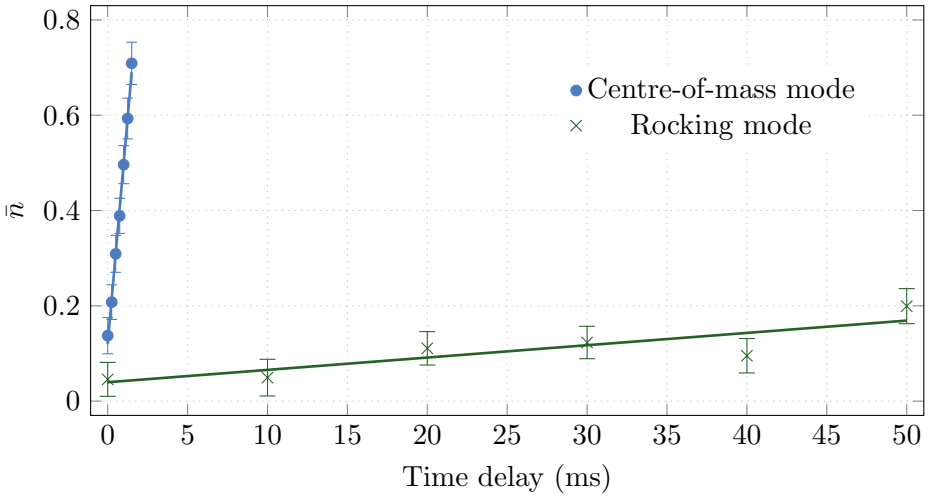


Figure 7.12: Heating rates of radial in-plane modes of two ions at a temperature of 85 K. We infer $\dot{\bar{n}}_{\mathrm{ip,com}} = 380(31)\,\mathrm{q\,s^{-1}}$ and $\dot{\bar{n}}_{\mathrm{ip,rocking}} = 2.6(9)\,\mathrm{q\,s^{-1}}$ from linear fits.

points at zero time delay. We observe slight variations in heating rates from day to day, but from repeated measurements we estimate average values of $\dot{\bar{n}}_{\mathrm{ip,com}} \leq 450\,\mathrm{q\,s^{-1}}$ and $\dot{\bar{n}}_{\mathrm{ip,rocking}} \leq 5\,\mathrm{q\,s^{-1}}$. Temperatures achieved through sideband cooling are typically $\bar{n}_{\mathrm{ip,com}} \leq 0.2$ and $\bar{n}_{\mathrm{ip,rocking}} \leq 0.1$. Since heating is a source of error for two-qubit MS gates, we choose to work with the rocking mode.

7.8 Microwave magnetic field

The design of the trap chip was presented in section 3.1.1, where I highlighted that one of its main features is a U-shaped microwave electrode. One end of this electrode is dc shorted to ground, while the other presents an open connection that capacitively couples to the input transmission line on the chip, such that the electrode forms a $\lambda/4$-resonator. In steady state, the microwave current along the electrode is therefore described by a standing wave, with a node at the open terminal and an anti-node at the short. The magnetic field at the trap centre then results from the superposition of the fields generated by the two sections of the microwave electrode at either side of the trap axis, return currents flowing in the ground plane and currents induced in other electrodes. Due to the symmetry of the microave electrode about the yz-plane of the trap coordinate system and taking into account the form of the magnetic field generated by a current-carrying wire, one might expect the total field around

the trap centre to be predominantly directed along the y-axis. With respect to the atom, this means that the π-component should be approximately zero in some vertical plane, while the gradient of this component should be large. These are desirable properties for two-qubit gates based on the Mølmer-Sørensen scheme. The B_π-field is thus passively nulled by the geometry of the microwave electrode.

7.8.1 Field model

Finding the exact spatial dependence of $\mathbf{B}(\mathbf{x}, t)$ requires solving Maxwell's equations, taking into account the electric properties of the materials comprising the trap chip. This was done using the software Ansys HFSS during the initial design stage of the chip to obtain quantitative estimates of the relevant parameters. However, a qualitative understanding of the factors affecting the depth and position of the nominal null in the B_π-component can be gained already with a simple model. Near the trap centre, the two sections of the microwave electrode appear as long straight conductors running in parallel. It therefore seems reasonable in a first approximation to model them as two infinite wires carrying oscillating currents, neglecting their finite cross-section and effects resulting from the bend far down the chip. This is illustrated in fig. 7.13.

The magnetic field of each conductor takes the form $\mathbf{B}_a(\mathbf{x}, t) = \mu_0 I_a(t)/(2\pi r_a)\, \mathbf{e}_{\phi,a}$, with $a \in \{1, 2\}$. The variable $I_a(t)$, denotes the current flowing in the conductor, r_a the radial distance from it and $\mathbf{e}_{\phi,a}$ the unit vector in the azimuthal direction. The currents flowing in the two wires are oriented opposite to each other due to the shape of the microwave electrode. To account for the standing-wave pattern along the electrode, I allow the amplitudes of the currents to be unequal, determined by the ratio k. The layout of the microwave electrode on the chip, from the location where it couples to the input feedline to the point where it is shorted to the ground plane, is asymmetric. This means that the two sections of the electrode adjacent to the ion on either side are much closer to the shorted end than the open terminal. Specifically, they lie at distances of 0.019λ and 0.056λ from the short [WLW+22]. One would therefore expect the discrepancy in amplitude between the currents flowing at these points to be small. Furthermore, I include the possibility of a phase

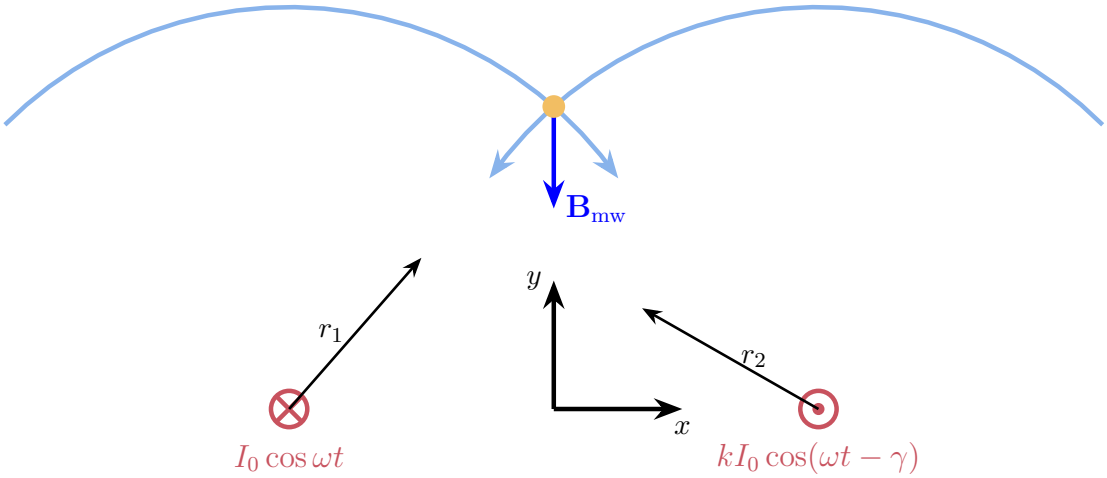


Figure 7.13: Configuration assumed to model microwave magnetic field in the radial plane. The two sections of the microwave electrode near the trap centre are modelled as straight wires carrying currents in opposite directions. Treating the electrode as a lossy transmission line, the currents flowing in the two sections are allowed to differ slightly in amplitude and phase. The ion (orange) indicates the position of the rf null half-way between the wires.

offset γ between the currents. For a lossless transmission line, no such offset exists, but for a lossy conductor the phase of the current varies slightly along the length of the line [Poz11]. I will thus write the currents in the two wires as $I_1(t) = I_0 \cos \omega t$ and $I_2(t) = kI_0 \cos(\omega t - \gamma)$. The Cartesian components of the total magnetic field in the trap coordinate system may be expressed as $B_i(\mathbf{x}, t) = B_{i,0}(\mathbf{x}) \cos[\omega t - \phi_i(\mathbf{x})]$, with $B_{i,0}(\mathbf{x}) \geq 0$. This form was also used in chapter 5.

Figure 7.14 contains the predictions of this model for $B_{x,0}$ and ϕ_x as a function of position along the x-axis at a height of 40 µm above the trap for different ratios and phase offsets of the currents. Since the quantisation axis provided by the main coils lies along the x-direction, $B_x(\mathbf{x}, t)$ is equal to the π-component $B_0(\mathbf{x}, t)$ in the spherical basis of the atomic coordinate system, which is the component driving transitions on the clock qubit. It is clear that the two parameters k and γ influence the field in different ways. Discrepancies in the magnitudes of the currents flowing through the wires lead to a shift in the position of the minimum of the π-component, while phase offsets affect the depth of the minimum. This can be understood in a straightforward way by considering the superposition of the individual fields generated by the conductors.

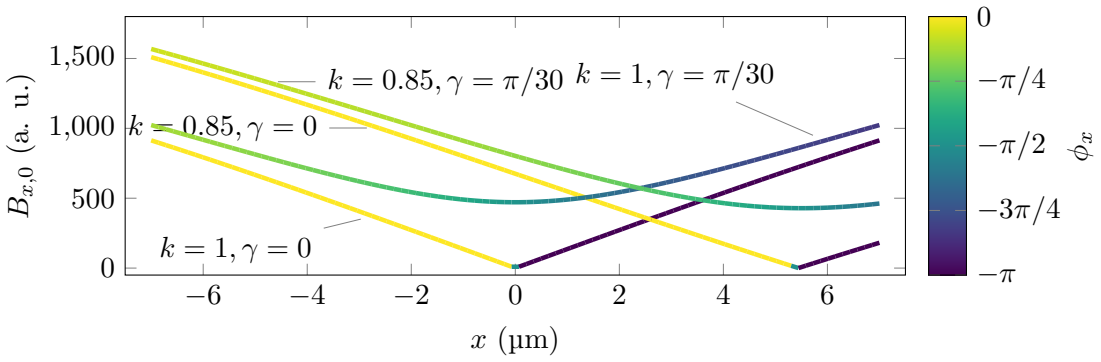


Figure 7.14: Amplitude and phase of $B_x(\mathbf{x}, t)$, corresponding to the π-component in our trap, as predicted by the model introduced in 7.13. A height of $y = 40\,\mu\text{m}$ has been assumed. Imbalances in the amplitudes of the currents cause the minimum in $B_{x,0}$ to shift away from the rf null, while phase differences reduce the depth of the minimum.

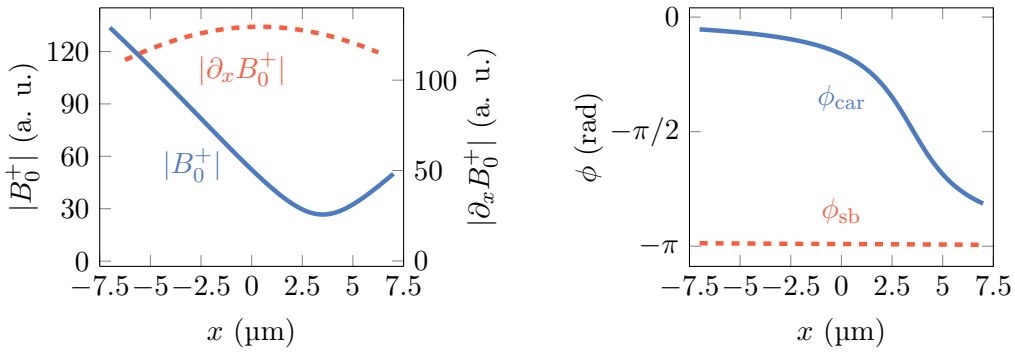


Figure 7.15: Magnitudes and phases of parameters relevant for carrier and sideband transitions, as predicted by the model introduced in fig. 7.13. The gradient $\left|\partial_x B_0^+(\mathbf{x})\right|$ does not vanish at the location of the minimum in field amplitude and the phases of carrier and sideband terms may in general be different.

Another important feature of the expected microwave field that may be deduced from the two-wire model is the relation between field amplitude and gradient as a function of position. In chapter 5, it was seen that the π-component may be written $B_0(\mathbf{x},t) = (1/2)\left[B_0^+(\mathbf{x})\exp(-\mathrm{i}\omega t) + \text{c. c.}\right]$ and found that for an ion trapped around some position $\mathbf{x}_0$ the Rabi frequency of the carrier is proportional to $\left|B_0^+(\mathbf{x}_0)\right|$, while that of a sideband is proportional to $\left|\partial_m B_0^+(\mathbf{x}_0)\right|$. One can use the analytical expressions for the magnetic field to calculate $B_0^+(\mathbf{x})$ and $\partial_x B_0^+(\mathbf{x})$ in our model. The magnitudes and phases of these complex quantities, where the latter are defined in accordance with eqs. (5.43) and (5.48) as $\phi_{\text{car}} = \arg\left[B_0^+(\mathbf{x})\right]$ and $\phi_{\text{sb}} = \arg\left[\partial_x B_0^+(\mathbf{x})\right]$, are plotted in fig. 7.15a and 7.15b, respectively. I have assumed a height of 40 µm above the trap surface, $k = 0.9$ and $\gamma = \pi/50$. The important point to note in fig. 7.15a is that even though $\left|B_0^+(\mathbf{x})\right|$ exhibits a minimum around which it is to first order independent of x, the gradient $\left|\partial_x B_0^+(\mathbf{x})\right|$ relevant for driving sidebands does not vanish at the position of the minimum. This highlights that $\partial_x\left|B_0^+(\mathbf{x})\right| \neq \left|\partial_x B_0^+(\mathbf{x})\right|$ and shows that it is possible to achieve low field amplitude, but large field gradient at the same position. Figure 7.15b demonstrates that the phases of carrier and sideband terms may in general be different.

While providing an intuitive picture, this simple model cannot be used for quantitative predictions regarding the gradient of the π-component, the field amplitude or the position of the minimum. The magnetic field observed in reality depends on the exact distribution of currents within the whole chip, including currents induced in dc and rf electrodes and return currents flowing in the ground plane. These are sensitive to several factors, such as the dimensions of the electrodes, material properties, which are themselves functions of temperature, and the frequency of the microwave current.

7.8.2 Measurements of field gradient

We measure the variation of the microwave magnetic field experimentally as follows. We displace the ion purely along the x-direction by applying appropriate voltages to the dc electrodes and at each position perform Rabi flopping on the carrier transition as a function of pulse time using the microwaves. We fit a sinusoid to the observed

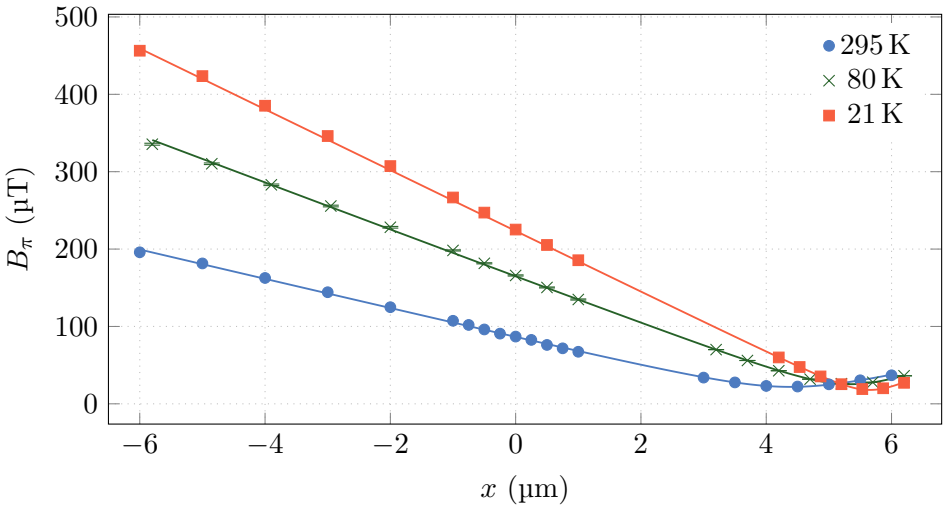


Figure 7.16: Measured variation of π-component of microwave magnetic field along the x-axis at different temperatures. The field strength has been estimated through carrier Rabi flopping on the clock qubit. Data have been normalised to 1 W of microwave input power. Fits are based on the function given in eq. 7.9.

oscillation in populations and extract the Rabi frequency, from which we infer the field strength through the relation $\left|B^+_{-q}(\mathbf{x})\right| = \hbar\Omega_{\text{car}}(\mathbf{x})/R_{\uparrow\downarrow,q}$. The matrix element $R_{\uparrow\downarrow,q}$ depends on the transition probed. The π-component is estimated using the $|4,+1\rangle \leftrightarrow |3,+1\rangle$ clock qubit. Additionally, we estimate the σ^-- component via the $|4,+2\rangle \leftrightarrow |3,+1\rangle$ qubit. Scans were repeated at different temperatures. At each temperature, we measured the microwave input power at the end of the coaxial cable that connects to the assembly of the vacuum chamber and normalised the inferred field strength to 1 W of input power.

The results for the π-component are contained in fig. 7.16. The position of the rf null $\mathbf{x}_0 = \mathbf{0}$ defines the origin of the trap coordinate system. The carrier Rabi frequency depends on the magnitude $B_\pi(\mathbf{x}) = \left|B^+_0(\mathbf{x})\right| = \left|B^-_0(\mathbf{x})\right|$. The field $B^+_0(\mathbf{x})$ is expanded around the rf null and, for displacements purely along the x-axis, it is found that $B^+_0(\mathbf{x}) \approx B^+_0(\mathbf{x}_0) + \partial_x B^+_0(\mathbf{x}_0)\, x$ to first order in x. The two terms may in general have different phases, so one writes

$$B^+_0(\mathbf{x}) = \left[\left|B^+_0(\mathbf{x}_0)\right| + \left|\partial_x B^+_0(\mathbf{x}_0)\right| x\, \mathrm{e}^{\mathrm{i}(\phi_{\text{sb,x}} - \phi_{\text{car}})}\right] \mathrm{e}^{\mathrm{i}\phi_{\text{car}}} \,. \tag{7.8}$$

The Rabi frequency Ω_{car} is only sensitive to the magnitude $\left|B^+_0(\mathbf{x})\right|$, which is found

Temperature (K)	$\partial_x B_\pi(\mathbf{x}_0)$ (T m^{-1})	$B_\pi(\mathbf{x}_0)$ (µT)	$x_{\min}$ (µm)	$B_\pi(x_{\min})$ (µT)
295	19.1(1)	86.6(3)	4.39(2)	21.9(3)
80	30.5(1)	164.9(4)	5.34(2)	25.4(4)
21	39.4(2)	223.4(9)	5.66(4)	17.9(9)

Table 7.1: Parameters characterising the spatial dependence of the π-component of the microwave magnetic field, as obtained from fits to the data in fig. 7.16. Values have been calculated for a normalised microwave input power of 1 W.

to be given by

$$\left|B_0^+(\mathbf{x})\right| = \sqrt{\left|B_0^+(\mathbf{x}_0)\right|^2 + \left|\partial_x B_0^+(\mathbf{x}_0)\right|^2 x^2 + 2\left|B_0^+(\mathbf{x}_0)\right|\left|\partial_x B_0^+(\mathbf{x}_0)\right| x\cos(\Delta\phi)} \tag{7.9}$$

with $\Delta\phi = \phi_{\mathrm{sb,x}} - \phi_{\mathrm{car}}$. This expression has been fitted to the data in fig. 7.16 to obtain the parameters $B_\pi(\mathbf{x}_0) = \left|B_0^+(\mathbf{x}_0)\right|$ and $\partial_x B_\pi(\mathbf{x}_0) = \left|\partial_x B_0^+(\mathbf{x}_0)\right|$.

There are several features worth noting in fig. 7.16. Firstly, there is a clear minimum in B_π along the horizontal direction. At the position of the rf null, we find $B_\pi = 223\,\mu\mathrm{T}$ for a temperature of 21 K and the field strength decreases by more than an order of magnitude towards the minimum. Consequently, there is a strong gradient in B_π, which exhibits a significant dependence on temperature. We observe a gradient of up to $\partial B_\pi/\partial x = 39.4(2)\,\mathrm{T\,m^{-1}}$ at 21 K for 1 W of microwave input power. Secondly, the null in B_π is not ideal and the field strength at the minimum slightly depends on temperature. Thirdly, the position of the minimum $x_{\min}$ is displaced from the rf null by several microns and shifts further away with lower temperatures. The relevant parameters are summarised in table 7.1. Using eq. (5.56), we may calculate the effective Lamb-Dicke parameter $\bar{\eta}$ corresponding to the measured field amplitude and gradient of the π-component. For a motional mode of frequency 5 MHz aligned with the x-axis and assuming $c_0 \approx 1$, we obtain $\bar{\eta} = 9\times10^{-4}$ on the rf null at a temperature of 21 K. At the position of the minimum, however, we find $\bar{\eta} = 2\times10^{-3}$.

We believe changes in amplitude and gradient of the π-component with temperature are mainly caused by the resistance of the gold comprising the electrodes. As the temperature decreases, it becomes possible to generate a larger current for given power dissipated. A smaller contribution comes from the shift in resonance

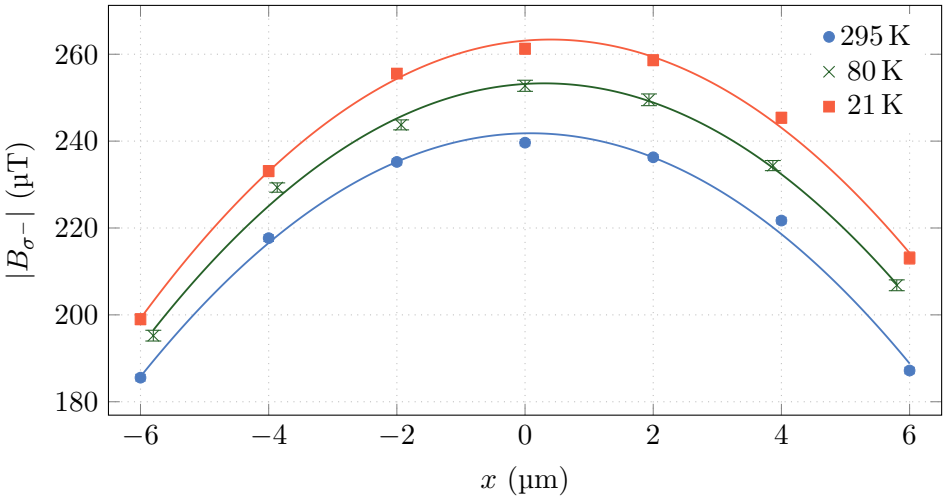


Figure 7.17: Measured variation of σ^--component of microwave magnetic field along the x-axis at different temperatures. The field strength has been estimated through carrier Rabi flopping on the qubit formed by the states $|4,+2\rangle$ and $|3,+1\rangle$. Data have been normalised to 1 W of microwave input power.

frequency of the microwave resonator as a function of temperature. Additionally, changes in electric properties of the gold and sapphire substrate lead to slight phase shifts in the distribution of currents on the trap chip, influencing the depth and location of the minimum.

Scans for the σ^--component are plotted in 7.17, where a parabola has been fitted to the data to guide the eye. As may be expected from the simple model introduced earlier, this component exhibits a maximum rather than a minimum, with only a weak dependence on temperature. However, the position of the maximum does not coincide with the location of the minimum of the π-component. Given the symmetry of the microwave electrode, we expect the σ^+-component to be similar in magnitude to the σ^--component.

It is important to note that the shape of the microwave electrode does not allow simultaneous nulling of all components of the magnetic field, only the π-component is strongly reduced. This bears on the implementation of Mølmer-Sørensen gates in our trap in two ways. Firstly, ac Zeeman shifts resulting from couplings via off-resonant σ-transitions will not be eliminated, but shifts caused by the carrier transition will be decreased if the ions are placed at the position of the minimum. Secondly, off-resonant excitation on the carrier driven by the two microwave tones

will be suppressed. Both effects have an influence on gate fidelity, as will be discussed further in section 8.5.

It is worth remarking on the validity of our method for measuring the field gradient. The quantity relevant for the spin-dependent Mølmer-Sørensen force is the field gradient at frequencies close to the two motional sidebands, given by $\omega_{\uparrow\downarrow} \pm \nu$, where ν is the secular frequency of the mode used for the entangling operation. In our trap, ν is approximately 5 MHz. However, we infer the gradient from experiments with the carrier transition of the clock qubit, which has a frequency of $\omega_{\uparrow\downarrow} = 3123\,\mathrm{MHz}$. It follows that our measurements are not quite taken at the target frequency, which raises the question whether the gradients at 3123 ± 5 MHz might be significantly different. This depends on the resonance curve of the microwave resonator. From the characterisation of this curve, presented in section 3.1.1.3, we may conclude that the variation in microwave power coupled into the chip over this frequency range is negligible and our estimate for the field strength should also hold at the sideband frequencies. This is further confirmed by the experiments concerned with the MS force on a single ion, discussed in section 8.3.2.

It should be noted that in general there is another method available to map the components of the microwave magnetic field as a function of position [WOC+13b]. Rather than driving resonant Rabi flopping, one measures ac Zeeman shifts on a set of suitable transitions by means of the Ramsey sequence described in 7.1.1.1 and subsequently uses least-squares fitting to estimate the field components that would give rise to the observed shifts. This method has the advantage that all components may be probed at the frequency of interest rather than requiring a different frequency for each respective transition. However, we could not make use of this technique at the time because the observed short coherence time of field-sensitive transitions caused a significant decay in contrast on timescales that were fast compared to the variation in signal resulting from ac Zeeman shifts.

7.8.2.1 Position of the field minimum

When the trap chip was being designed, numerical simulations were performed to estimate the magnetic field that would be generated by the microwave electrode.

These simulations, which included the effects of return currents and currents induced in other electrodes, predicted the minimum in π-component to be offset from the rf null by only a few hundreds of nanometres along the x-axis. We were therefore initially surprised to find the minimum at a distance of more than 4 µm from the rf null, in particular because a different chip from the same production run that been used in the previous version of the apparatus did not show this behaviour [Wol19]. In principle, the offset could be caused by incorrect dimensions of the trap electrodes resulting from errors during fabrication. However, the inaccuracies required to produce the observed displacement would have to be so large that they should be visible through our imaging system. We have checked the dimensions of electrodes on the camera and found that they match the target dimensions to within 0.7 µm, which means that fabrication errors are most likely not responsible.

A shift in position of the minimum of the π-component of the microwave magnetic field could also be caused by misalignment between the direction of the static magnetic field $\mathbf{B}_0$ and the x-axis. In this case, B_π (measured in the atomic coordinate system) would not be equal to B_x, but would also be a function of B_y and B_z. This means that even if the minimum in B_x occurred at the target position, the minimum in B_π would lie at a different point. Since $B_z = 0$ in our trap, one may infer that such a shift requires the static field to be rotated around the z-axis. However, given the way in which main coils and vacuum chamber are mounted on the optics table, we believe that the angle of rotation around the z-axis can only be very small. To check whether this effect could lead to the observed shift, we measured the position of the minimum as a function of current applied to the vertical trim coils. These trim coils add a y-component to $\mathbf{B}_0$, which results in a rotation of the static field around the z-axis and increases its magnitude. By measuring the transition frequency of the stretch qubit, the field strength $|\mathbf{B}_0|$ and hence the angle of rotation may be inferred for each current. We find that for angles as large as 3°, which we believe to be the upper limit on mechanical misalignment, the minimum moves by less than 200 nm. The shift observed in fig. 7.16 can therefore not be explained by a rotation of the static field.

Instead, we attribute the large offset to accidental resonant coupling between mi-

crowave and rf electrodes. As discussed in section 3.1.1.1, the rf PCB has undergone significant changes compared to the previous iteration. In particular, the area of the solder pads for the choke likely leads to a capacitance $C_{\mathrm{pad}} \approx 1.5\,\mathrm{pF}$, corresponding to an impedance of $\approx 30\,\Omega$ at microwave frequencies. Furthermore, the bare wire soldered across the crack, the capacitance of which is partially through air rather than only through the alumina of the PCB, is estimated to have an impedance of $\approx 200\,\Omega$. Both factors result in a strong impedance mismatch compared to the $50\,\Omega$ impedance of the trap chip and we expect a significant fraction of any microwave power coupled onto the rf electrodes to be reflected at this impedance interface. The resonance frequency of the cavity thus created depends on the dimensions of the rf electrodes and the location of the interface. Dr. Gely of our group has carried out simulations using the software COMSOL to investigate the influence of the boundary condition of the rf line on the microwave magnetic field [WLW+22]. It was found that for certain distances between impedance interface and trap chip the current induced in the rf electrode increased strongly, leading to a drastic change in position of the minimum. It therefore seems that the arrangement on this particular PCB happens to give rise to such a resonance for the frequency used.

Chapter 8

Spin-motion entanglement driven by microwaves

In this chapter I discuss how a spatially varying oscillating magnetic field can be used to generate entanglement between spin and motional degrees of freedom of trapped particles. I generalise the theory presented in chapter 5 to the case when multiple ions are confined in a linear Paul trap and show that the interaction Hamiltonian gives rise to a spin-dependent force which coherently drives the motional part of the wavefunction in phase space. We demonstrate this force in the Mølmer-Sørensen scheme for a single ion in our trap. Then I proceed to explain how spin-motion entanglement can be exploited to realise a two-qubit gate and present the results of an initial attempt at a Mølmer-Sørensen two-qubit gate in our apparatus. Calibration experiments were carried out by several members of our lab, but I conducted the experiments to acquire the data used for plots in this chapter. Those sections are followed by a discussion of simulations that I have carried out to determine which sources of gate error will likely need the most attention during future experiments.

8.1 Collective motion of a string of ions

If multiple ions are placed in a Paul trap, the equations of motion are no longer determined by the electric potential generated by the trap electrodes alone, but are also affected by the mutual Coulomb repulsion between ions. The general treatment

has to include the effects of the time-dependent rf trapping potential and allow for the possibility that the principal axes of the dc and rf potentials may not coincide. While such a description has been developed in ref. [LDR+12], I shall not find it necessary to use the full machinery provided there. Instead, I will make the pseudopotential approximation and thus neglect the effects of micromotion. This should be a valid assumption as long as the ions are cold enough that the amplitude of intrinsic micromotion is small and correct compensation fields are applied so that excess micromotion is eliminated. Since we work with a linear trap, the rf electric field along the axial direction may be assumed to vanish. It follows that if confinement in the radial directions is much stronger than in the axial direction, such that the particles line up along the trap axis in equilibrium, all ions may simultaneously be located on the rf null despite their electrostatic repulsion. This means that the requirement of zero excess micromotion may indeed be achieved.

I therefore consider a collection of N ions confined by a three-dimensional anisotropic ideal harmonic potential. The principal axes of the potential, which are given by the principal axes of the dc potential in our trap, will be labelled by the index m. As discussed in section 4.4.1, I identify x_1 with the radial in-plane coordinate, x_2 with the radial out-of-plane coordinate and x_3 with the axial coordinate. The corresponding (angular) natural frequencies of oscillation for a single ion are denoted by ν_m. I assume that the trapping potential in the radial plane is much stronger than along the trap axis, which translates to $\nu_1, \nu_2 \gg \nu_3$. Taking the centre of the harmonic potential to define the origin of the coordinate system, the classical Hamiltonian describing the motion of the centres of mass of the ions in the trap is given by

$$H_{\mathrm{mot}} = \sum_{i=1}^{N} \sum_{m=1}^{3} \left[\frac{1}{2M} \left(p_m^{(i)}\right)^2 + \frac{M\nu_m^2}{2} \left(x_m^{(i)}\right)^2 \right] + \sum_{i<j} \frac{e^2}{4\pi\epsilon_0 \left|\mathbf{x}^{(i)} - \mathbf{x}^{(j)}\right|} \,, \tag{8.1}$$

where $\mathbf{x}^{(i)}$ and $\mathbf{p}^{(i)}$ denote position and momentum of the i-th ion. The dynamics arising from this Hamiltonian have been discussed by several authors, see for example refs. [Jam98] and [MSJ03]. I will not go into details here, but only state relevant results to introduce notation I use in later sections. If the ions are hot, their motion

is influenced by the non-linear terms of the Coulomb force and is therefore highly irregular. Once their vibrational energy has been significantly reduced through laser cooling, however, the ions are expected to perform only small excursions from their equilibrium positions. The latter, which I denote $\bar{\mathbf{x}}^{(i)}$, correspond to the locations that the ions would adopt if they were completely stationary and are determined by the condition that the confining force from the harmonic potential and the repulsive force from the Coulomb potential balance. Under the strongly anisotropic conditions assumed here, the equilibrium positions lie along the trap axis. They may be calculated numerically for an arbitrary number of ions [Jam98]. The position of each ion may therefore be written as

$$\mathbf{x}^{(i)} = \bar{\mathbf{x}}^{(i)} + \boldsymbol{\rho}^{(i)} \ , \tag{8.2}$$

where $\boldsymbol{\rho}^{(i)}$ measures the displacement from its respective equilibrium position.

If the displacements are sufficiently small, it is valid to expand the Coulomb potential in a Taylor series in the variables $\rho_m^{(i)}$ around the equilibrium positions $\bar{x}_m^{(i)}$ and neglect terms of third and higher orders. This linearises the resulting equations of motion. The Hamiltonian is then quadratic in the displacements, but contains mixed terms $\rho_m^{(i)}\rho_n^{(j)}$. It is advantageous to diagonalise the Hamiltonian by introducing normal modes of motion [MSJ03]. The displacement of each ion may then be decomposed as

$$\rho_m^{(i)} = \sum_{p=1}^{N} b_i^{(m,p)} q^{(m,p)} \ . \tag{8.3}$$

The quantity $q^{(m,p)}$ is the normal-mode coordinate for the p-th normal mode along principal axis m, while $\mathbf{b}^{(m,p)}$ is the corresponding normal-mode vector. The latter are obtained as the eigenvectors of the coefficient matrices appearing in the Hamiltonian as a result of the quadratic approximation to the Coulomb potential [MSJ03]. It is found that the eigenvectors $\mathbf{b}^{(m,p)}$ are in fact the same for all axes and I will therefore only write $\mathbf{b}^{(p)}$ in the following. However, the eigenvalue corresponding to a given eigenvector will in general depend on the direction m considered. The eigenvectors are normalised in the sense that $\sum_{p=1}^{N} b_i^{(p)} b_j^{(p)} = \delta_{ij}$ and $\sum_{i=1}^{N} b_i^{(p)} b_i^{(q)} = \delta_{pq}$,

where δ_{ij} denotes the Kronecker delta. Each normal mode is characterised by an oscillation frequency $\nu_{m,p}$, which may be calculated once the eigenvalues of the coefficient matrices have been obtained.

The quantum-mechanical description builds on these considerations. The symbols $\rho_m^{(i)}$ and $q^{(m,p)}$ now represent operators, while $\bar{x}_m^{(i)}$ and $b_i^{(p)}$ remain constant numbers. When the normal-mode position operators are expressed in terms of the corresponding creation and annihilation operators $a_{m,p}^\dagger$ and $a_{m,p}$ as

$$q^{(m,p)} = q_0^{(m,p)} \left(a_{m,p}^\dagger + a_{m,p} \right) = \sqrt{\frac{\hbar}{2M\nu_{m,p}}} \left(a_{m,p}^\dagger + a_{m,p} \right) , \tag{8.4}$$

the quantum Hamiltonian describing the motion of the centres of mass of the ions may be written

$$H_{\text{mot}} = \sum_{m=1}^{3} \sum_{p=1}^{N} \hbar\nu_{m,p} \left(a_{m,p}^\dagger \, a_{m,p} + 1/2 \right) . \tag{8.5}$$

In the case of a single ion, there is only one mode of motion along each coordinate axis. The eigenvector reduces to the coefficient $b^{(1)} = 1$ and the oscillation frequency is given by ν_m.

For two ions, the eigenvectors $\mathbf{b}^{(p)}$ and oscillation frequencies $\nu_{m,p}$ may also be calculated analytically [Jam98]. The two eigenvectors are given by

$$\mathbf{b}^{(1)} = \frac{1}{\sqrt{2}} (1, 1) \tag{8.6}$$

$$\mathbf{b}^{(2)} = \frac{1}{\sqrt{2}} (1, -1) . \tag{8.7}$$

The first one corresponds to what we call the centre-of-mass (com) mode, in which the two particles oscillate in phase with each other. Its frequency $\nu_{m,\text{com}} = \nu_m$ is simply equal to the natural frequency of the harmonic oscillator along the respective axis. The other eigenvector describes out-of-phase oscillations of the two ions. For the axial direction in a linear trap, we refer to the corresponding mode as the breathing mode and find that its frequency is given by $\nu_{3,\text{breathing}} = \sqrt{3}\,\nu_3$. For the radial directions, we call it the rocking mode, with frequency $\nu_{r,\text{rocking}} = \sqrt{\nu_r^2 - \nu_3^2}$, $r \in \{1, 2\}$. Under typical operating conditions, our trap is characterised by fre-

quencies $\nu_1 = 2\pi \times 5.2\,\mathrm{MHz}$ in the radial in-plane direction and $\nu_3 = 2\pi \times 1.1\,\mathrm{MHz}$ along the trap axis. For a string containing two ions, we thus obtain frequencies of $\nu_{1,\mathrm{com}} = 2\pi \times 5.2\,\mathrm{MHz}$ and $\nu_{1,\mathrm{rocking}} = 2\pi \times 5.08\,\mathrm{MHz}$. These values are confirmed by experiments.

For reference, I also provide the equilibrium spacing of the two ions on the trap axis here. Using the expressions provided in ref. [Jam98], this distance is given by

$$\left|\bar{z}^{(1)} - \bar{z}^{(2)}\right| = 2\left(\frac{1}{2}\right)^{2/3}\left(\frac{e^2}{4\pi\epsilon_0 M\nu_3^2}\right)^{1/3} . \tag{8.8}$$

Inserting our trap parameters, one finds $\left|z^{(1)} - z^{(2)}\right| = 5.1\,\mu\mathrm{m}$.

8.2 Spin-dependent forces

The total Hamiltonian for a chain of ions also contains a contribution H_{itl} from the internal degrees of freedom. Generalising the notation introduced in chapter 5, we write the internal states of the i-th ion as $\{|u^{(i)}\rangle\}$ and thus

$$H_{\mathrm{itl}} = \sum_{i=1}^{N}\sum_{u}\hbar\omega_u\,|u^{(i)}\rangle\,\langle u^{(i)}| \ . \tag{8.9}$$

Application of a microwave magnetic field to the ions then gives rise to an interaction Hamiltonian

$$H_{\mathrm{int}}(t) = \sum_{i=1}^{N} -\boldsymbol{\mu}^{(i)}\cdot\mathbf{B}\big(\mathbf{x}^{(i)},t\big) \ , \tag{8.10}$$

where the strength of the interaction now depends on the magnetic field $\mathbf{B}\big(\mathbf{x}^{(i)},t\big)$ at the position of each individual ion. The contributions H_{mot}, H_{itl} and $H_{\mathrm{int}}(t)$ have all been defined in the Schrödinger picture. I now move to the interaction picture with respect to $H_0 = H_{\mathrm{mot}} + H_{\mathrm{itl}}$. Following the same steps as presented in section 5.2, one finds that each term $H_{\mathrm{int}}^{(i)}(t) = -\boldsymbol{\mu}^{(i)}\cdot\mathbf{B}\big(\mathbf{x}^{(i)},t\big)$ may be transformed separately

and becomes

$$\begin{aligned}\widetilde{H}_{\mathrm{int}}^{(i)}(t) = -\frac{1}{2}\Big(\frac{\mu_{\mathrm{e}}+\mu_{\mathrm{g}}}{2}\,\mathbb{I}^{(i)} + \frac{\mu_{\mathrm{e}}-\mu_{\mathrm{g}}}{2}\,\sigma_z^{(i)}\Big)\Bigg(B_0^+\big(\bar{\mathbf{x}}^{(i)}\big)\mathrm{e}^{-\mathrm{i}\omega t} \\ + \sum_m\sum_p \partial_m B_0^+\big(\bar{\mathbf{x}}^{(i)}\big)\, b_i^{(p)}\, q_0^{(m,p)}\big[\mathrm{e}^{\mathrm{i}\nu_{m,p}t}\,a_{m,p}^\dagger + \mathrm{e}^{-\mathrm{i}\nu_{m,p}t}\,a_{m,p}\big]\mathrm{e}^{-\mathrm{i}\omega t}\Bigg) \\ + \frac{1}{2}R_{\mathrm{eg},q}\,\sigma_+^{(i)}\Bigg(B_{-q}^+\big(\bar{\mathbf{x}}^{(i)}\big)\,\mathrm{e}^{\mathrm{i}(\bar{\omega}_{\mathrm{eg}}^{(i)}-\omega)t} \\ + \sum_m\sum_p \partial_m B_{-q}^+\big(\bar{\mathbf{x}}^{(i)}\big)\, b_i^{(p)}\, q_0^{(m,p)}\big[\mathrm{e}^{\mathrm{i}(\bar{\omega}_{\mathrm{eg}}^{(i)}+\nu_{m,p}-\omega)t}\,a_{m,p}^\dagger + \mathrm{e}^{\mathrm{i}(\bar{\omega}_{\mathrm{eg}}^{(i)}-\nu_{m,p}-\omega)t}\,a_{m,p}\big]\Bigg) \\ + \mathrm{H.c.}\,. \end{aligned} \tag{8.11}$$

I have defined the effective internal transition frequency for the i-th ion by $\bar{\omega}_{\mathrm{eg}}^{(i)} = \omega_{\mathrm{eg}} + \Delta_{\mathrm{eg}}^{ac,(i)}$, where $\Delta_{\mathrm{eg}}^{ac,(i)}$ denotes the relevant ac Zeeman shift. The amplitudes B_q^+ and gradients $\partial_m B_q^+$ may in general be different for each ion since they depend on the microwave magnetic field at the positions $\bar{\mathbf{x}}^{(i)}$. However, I will assume in the following that any such differences are negligible and thus take the parameters characterising the microwave field to be the same for all ions. This should hold to a very good approximation in our trap, considering that the equilibrium positions of the ions lie along the trap axis and the microwave magnetic field in the trapping region is essentially invariant with respect to translations along the axial direction. We will therefore take $B_q^+\big(\bar{\mathbf{x}}^{(i)}\big) = B_q^+(\mathbf{x}_0)$, where $\mathbf{x}_0$ is the centre of the harmonic trapping potential on the rf null. Under this assumption, the ac Zeeman shift also does not depend on the ion in question and therefore $\bar{\omega}_{\mathrm{eg}}^{(i)} = \bar{\omega}_{\mathrm{eg}}$.

I will omit the term involving the identity operator in the following as it only leads to a global rotation common to all ions. If one introduces the Rabi frequencies

$$\Omega_z = \frac{|\mu_{\mathrm{e}}-\mu_{\mathrm{g}}|}{2\hbar}\,\big|B_0^+(\mathbf{x}_0)\big| \tag{8.12}$$

$$\Omega_z^{(i,m,p)} = \frac{|\mu_{\mathrm{e}}-\mu_{\mathrm{g}}|}{2\hbar}\,\big|\partial_m B_0^+(\mathbf{x}_0)\big|\,\big|b_i^{(p)}\big|\,q_0^{(m,p)} \tag{8.13}$$

$$\Omega_q^{(i,m,p)} = \frac{|R_{\mathrm{eg},q}|}{\hbar}\,\big|\partial_m B_{-q}^+(\mathbf{x}_0)\big|\,\big|b_i^{(p)}\big|\,q_0^{(m,p)} \tag{8.14}$$

and phases

$$\phi_z = \arg B_0^+(\mathbf{x}_0) + \arg\left(\mu_\mathrm{e} - \mu_\mathrm{g}\right) \tag{8.15}$$

$$\phi_z^{(i,m,p)} = \arg \partial_m B_0^+(\mathbf{x}_0) + \arg\left(\mu_\mathrm{e} - \mu_\mathrm{g}\right) + \arg b_i^{(p)} \tag{8.16}$$

$$\phi_q^{(i,m,p)} = \arg \partial_m B_{-q}^+(\mathbf{x}_0) + \arg R_{\mathrm{eg},q} + \arg b_i^{(p)} \ , \tag{8.17}$$

the interaction Hamiltonian may be written more succinctly as

$$\begin{aligned}\widetilde{H}_\mathrm{int}^{(i)}(t) = \frac{\hbar}{2}\,\mathrm{e}^{-\mathrm{i}\omega t}\Bigg[&\Omega_z\,\mathrm{e}^{\mathrm{i}\phi_z}\,\sigma_z^{(i)} + \Omega_\mathrm{car}\,\mathrm{e}^{\mathrm{i}\phi_\mathrm{car}}\,\mathrm{e}^{\mathrm{i}\bar{\omega}_\mathrm{eg}t}\,\sigma_+^{(i)} \\ &+ \sum_{m,p}\Big(\Omega_z^{(i,m,p)}\,\mathrm{e}^{\mathrm{i}\phi_z^{(i,m,p)}}\,\sigma_z^{(i)} + \Omega_q^{(i,m,p)}\,\mathrm{e}^{\mathrm{i}\phi_q^{(i,m,p)}}\,\mathrm{e}^{\mathrm{i}\bar{\omega}_\mathrm{eg}t}\,\sigma_+^{(i)}\Big)\Big(\mathrm{e}^{\mathrm{i}\nu_{m,p}t}\,a_{m,p}^\dagger + \mathrm{e}^{-\mathrm{i}\nu_{m,p}t}\,a_{m,p}\Big)\Bigg] \\ &+ \mathrm{H.c.}\ .\end{aligned} \tag{8.18}$$

The Rabi frequency Ω_car and phase ϕ_car for the carrier term have been defined earlier in eq. (5.43). The expression above is analogous to eq. (1) in ref. [OWC+11], but here I allow the magnetic field to point in an arbitrary direction, containing components that possibly oscillate with different phases, and I explicitly include motional modes in all three dimensions.

The interpretation of the various contributions to the interaction Hamiltonian is similar to the case of a single trapped ion. The term involving Ω_z leads to a modulation of the energy of the qubit, caused by the component of the microwave field along the atomic quantisation axis. The carrier term drives internal spin-flips without affecting the motional state and is near-resonant when ω is close to the internal transition frequency $\bar{\omega}_\mathrm{eg}$. Both contributions result in single-qubit rotations on the Bloch spheres connected with the ions.

Conversely, the terms contained in the second line of eq. (8.18) represent couplings between the internal state of each qubit and the normal modes of motion of the ion string. Let us first focus on the contribution involving $\Omega_z^{(i,m,p)}$, which is near resonance when the magnetic field gradient oscillates with a frequency close to a motional frequency $\nu_{m,p}$. Making a rotating-wave approximation with respect to

$\pm(\omega + \nu_{m,p})$, the resonant term takes the form

$$\frac{\hbar}{2}\,\Omega_z^{(i,m,p)}\,\sigma_z^{(i)}\left[\mathrm{e}^{-\mathrm{i}(\omega-\nu_{m,p})t}\,\mathrm{e}^{\mathrm{i}\phi_z^{(i,m,p)}}\,a_{m,p}^{\dagger} + \mathrm{e}^{\mathrm{i}(\omega-\nu_{m,p})t}\,\mathrm{e}^{-\mathrm{i}\phi_z^{(i,m,p)}}\,a_{m,p}\right]. \tag{8.19}$$

The factor in brackets may be recognised as the interaction Hamiltonian for a driven harmonic oscillator [CN65]. Application of a spatially inhomogeneous field thus leads to spin-motion coupling which coherently excites the normal mode of motion that is being addressed. The important difference to the standard driven harmonic oscillator, however, lies in the fact that here the interaction also includes the spin operator $\sigma_z^{(i)}$, which means that the resulting force and the trajectory of the motional mode in phase space depend on the spin state of the respective ion. The interaction induced by the $\Omega_z^{(i,m,p)}$ term of the Hamiltonian is thus completely analogous to the classical case of a particle with magnetic dipole moment placed in an inhomogeneous magnetic field, which will feel a force that depends on the orientation of the dipole.

When time evolution under the total Hamiltonian $\widetilde{H}_{\mathrm{int}}(t) = \sum_i \widetilde{H}_{\mathrm{int}}^{(i)}(t)$ is considered (in the same manner as described below in section 8.4), it is found that the σ_z-dependent force provides a mechanism for the generation of multi-qubit entanglement. For two ions, this is usually referred to as a $\sigma_z \otimes \sigma_z$ gate. However, there are problems with this approach for microwave-driven gates in general and clock qubits in particular. For microwave electrodes with finite resistivity, application of a current for the generation of microwave fields will inevitably produce electric fields that will couple to the charge of the ion and cause heating. Since the magnetic field gradient is required to oscillate near the motional frequency in this gate scheme, the electric fields will also be close to resonance and the resulting heating will swamp the effects of the spin-dependent magnetic force [OLA+08]. For clock qubits, there is the additional problem that $\mu_{\mathrm{e}} \approx \mu_{\mathrm{g}}$ and thus the achievable Rabi frequency $\Omega_z^{(i,m,p)}$ is very small.

Instead, a spin-dependent force can also be implemented by utilising the contribution containing $\Omega_q^{(i,m,p)}$. Since a single microwave tone cannot be near resonance with $\bar{\omega}_{\mathrm{eg}} - \nu_{m,p}$ and $\bar{\omega}_{\mathrm{eg}} + \nu_{m,p}$ simultaneously, one finds that two microwave tones, symmetrically detuned from the motional sidebands, are required for the Hamilto-

nian to factor into a term acting on the spin and a term acting on the motional subspace. The corresponding interaction leads to a $\sigma_\phi \otimes \sigma_\phi$, or Mølmer-Sørensen, gate, which will be discussed in section 8.4. It is worth noting that the effective interaction Hamiltonians underlying the $\sigma_z \otimes \sigma_z$ or the $\sigma_\phi \otimes \sigma_\phi$ gates take the same form, but the difference lies in the basis of spin eigenstates in which they operate.

From now on, I focus on our clock qubit and thus the contribution characterised by $\Omega_q^{(i,m,p)}$. Therefore, let two microwave fields $\mathbf{B}_\mathrm{r}$ and $\mathbf{B}_\mathrm{b}$ be applied to the ion chain. I assume that $\mathbf{B}_\mathrm{r}$ oscillates with frequency $\omega_\mathrm{r} = \bar{\omega}_\mathrm{eg} - \nu_{m,p} - \epsilon_\mathrm{r}$ close to resonance with the red sideband of one motional mode[1] and $\mathbf{B}_\mathrm{b}$ with $\omega_\mathrm{b} = \bar{\omega}_\mathrm{eg} + \nu_{m,p} + \epsilon_\mathrm{b}$ near resonance with the blue sideband of the same mode. The resulting Rabi frequencies and phases are given by $\Omega_\mathrm{r}^{(i)} = \Omega_{q,\mathrm{r}}^{(i,m,p)}$, $\Omega_\mathrm{b}^{(i)} = \Omega_{q,\mathrm{b}}^{(i,m,p)}$ and $\phi_\mathrm{r}^{(i)} = \phi_{q,\mathrm{r}}^{(i,m,p)}$, $\phi_\mathrm{b}^{(i)} = \phi_{q,\mathrm{b}}^{(i,m,p)}$. I neglect the terms involving Ω_z and $\Omega_z^{(i,m,p)}$ because they are far off-resonant and their Rabi frequencies are very small for clock qubits. Furthermore, I will assume for now that the effects of off-resonant carrier excitation and coupling to spectator modes are negligible. Consequently, I discard all terms except those involving $\Omega_q^{(i,m,p)}$ of the motional mode that is being addressed. The interaction Hamiltonian $\widetilde{H}_\mathrm{int}^{(i)}(t)$ for each individual qubit then takes the form

$$\begin{aligned}\widetilde{H}_\mathrm{int}^{(i)}(t) = \frac{\hbar}{2}\Big[\sigma_+ \left(\Omega_\mathrm{r} \mathrm{e}^{\mathrm{i}\phi_\mathrm{r}} \mathrm{e}^{\mathrm{i}\epsilon_\mathrm{r} t}\, a_{m,p} + \Omega_\mathrm{b} \mathrm{e}^{\mathrm{i}\phi_\mathrm{b}} \mathrm{e}^{-\mathrm{i}\epsilon_\mathrm{b} t}\, a_{m,p}^\dagger\right) \\ + \sigma_- \left(\Omega_\mathrm{r} \mathrm{e}^{-\mathrm{i}\phi_\mathrm{r}} \mathrm{e}^{-\mathrm{i}\epsilon_\mathrm{r} t}\, a_{m,p}^\dagger + \Omega_\mathrm{b} \mathrm{e}^{-\mathrm{i}\phi_\mathrm{b}} \mathrm{e}^{\mathrm{i}\epsilon_\mathrm{b} t}\, a_{m,p}\right)\Big] . \end{aligned} \tag{8.20}$$

Next, I make the further assumption that the magnitudes of the gradients produced by the red and blue microwave tones and the detuning of each tone from its respective sideband are equal, so $\Omega_\mathrm{r}^{(i)} = \Omega_\mathrm{b}^{(i)} = \Omega^{(i)}$ and $\epsilon_\mathrm{r} = \epsilon_\mathrm{b} = \epsilon$. The interaction Hamiltonian for each qubit can then be written

$$\widetilde{H}_\mathrm{int}^{(i)}(t) = \frac{\hbar}{2}\,\Omega^{(i)}\,\sigma_\phi^{(i)} \left(\mathrm{e}^{\mathrm{i}\phi_\mathrm{m}} \mathrm{e}^{-\mathrm{i}\epsilon t}\, a_{m,p}^\dagger + \mathrm{e}^{-\mathrm{i}\phi_\mathrm{m}} \mathrm{e}^{\mathrm{i}\epsilon t}\, a_{m,p}\right) , \tag{8.21}$$

where I have defined a spin operator $\sigma_\phi^{(i)} = \sigma_+^{(i)} \exp(\mathrm{i}\phi_\mathrm{s}) + \sigma_-^{(i)} \exp(-\mathrm{i}\phi_\mathrm{s}) = \sigma_x^{(i)} \cos\phi_\mathrm{s} - \sigma_y^{(i)} \sin\phi_\mathrm{s}$, spin phase $\phi_\mathrm{s} = (\phi_\mathrm{b} + \phi_\mathrm{r})/2$ and motional phase $\phi_\mathrm{m} = (\phi_\mathrm{b} - \phi_\mathrm{r})/2$.

[1] Note that for the red sideband the definition of ϵ here is different from that used in section 5.2.3.

8.3 Mølmer-Sørensen force applied to a single ion

8.3.1 Theoretical description

I first consider the situation where a single ion is driven by the bichromatic field introduced in the previous section. In this case, the interaction Hamiltonian is derived from eq. (8.21) by dropping the superscript. For a single ion, the Rabi frequency entering $\widetilde{H}_{\rm int}(t)$ is defined asas $\Omega_{\rm MS} = \Omega$. The time evolution operator can be obtained analytically through the Magnus expansion and one finds

$$U(t;0) = \mathrm{e}^{\sigma_\phi[\alpha(t)a_m^\dagger - \alpha^*(t)a_m]}\,\mathrm{e}^{-\mathrm{i}\Phi(t)\sigma_\phi^2}\,, \tag{8.22}$$

where

$$\alpha(t) = \frac{\Omega_{\rm MS}}{2\epsilon}\,\mathrm{e}^{\mathrm{i}\phi_{\rm m}}\left(\mathrm{e}^{-\mathrm{i}\epsilon t} - 1\right) \tag{8.23}$$

$$\Phi(t) = \left(\frac{\Omega_{\rm MS}}{2}\right)^2 \int_0^t dt_1 \int_0^{t_1} dt_2 \sin[\epsilon(t_1 - t_2)] = \left(\frac{\Omega_{\rm MS}}{2\epsilon}\right)^2 (\epsilon t - \sin\epsilon t)\,. \tag{8.24}$$

The spin operator σ_ϕ has eigenvectors $|{\uparrow_\phi}\rangle$ and $|{\downarrow_\phi}\rangle$, with eigenvalues $+1$ and -1, respectively. I will denote the set of these eigenvectors as $\{|s\rangle\}$ and the set of corresponding eigenvalues as $\{\lambda_s\}$. Since $\sigma_\phi^2 = \mathbb{I}$, the second factor in $U(t)$ just results in a global phase independent of spin state. By expanding the operator exponential, using the decomposition $\sigma_\phi = \sum_s \lambda_s |s\rangle\langle s|$ and taking into account that the λ_s are real, one finds that $U(t)$ may be written

$$U(t) = \mathrm{e}^{-\mathrm{i}\Phi(t)} \sum_s D_m[\lambda_s \alpha(t)]\;|s\rangle\langle s|\,, \tag{8.25}$$

where $D(\alpha) = \exp\left(\alpha a^\dagger - \alpha^* a\right)$ denotes the displacement operator for a harmonic oscillator. This expression makes it obvious that the time-evolution operator describes a time-dependent displacement of the normal mode addressed, depending on the spin state that the ion occupies. While the force is active, the normal mode traces out a path in the corresponding phase space, determined by the parameter $\alpha(t)$. In the case of a sinusoidal force with constant amplitude considered here, the trajectory is circular. During the evolution, internal and motional states will

in general be entangled. At certain times, however, corresponding to the condition $\alpha(t) = 0$, the loop in phase space closes and the normal mode returns to its initial state, at which instant spin and motion become disentangled again. It is important to note that the times at which this occurs are determined only by the detuning ϵ and do not depend on the driving strength. Since the phase factor $\exp[-\mathrm{i}\Phi(t)]$ does not depend on σ_ϕ for a single ion, the particle will at those times also be found in its initial spin state.

8.3.2 Observation of the Mølmer-Sørensen force on a single ion

Rather than moving straight to two ions, we decided to first investigate MS dynamics for a single ion in our trap. The reason for this decision is the fact that the calibration steps involved in the single- and two-ion cases are very similar, but handling only one ion in the trap is much easier. Most importantly, the lifetime of a single ion in our trap at room temperature is of the order of tens of minutes, while the average two-ion lifetime was measured to be approximately four minutes. It is therefore advantageous to develop and test control code for experiments concerned with the MS force using a single ion at room temperature before cooling the system to cryogenic temperatures and working with two ions.

Entanglement of the internal spin and external centre-of-mass degrees of freedom according to the MS scheme, caused by a force operating in the σ_ϕ basis, has been demonstrated before for a single trapped ion manipulated by lasers [HBD+05] or microwaves in combination with a static magnetic field gradient [LWR+15]. We implement the method in our apparatus using the clock qubit, comprised of the states $|\uparrow\rangle = |3, +1\rangle$ and $|\downarrow\rangle = |4, +1\rangle$, and drive the in-plane radial mode. The ion is cooled to $\bar{n}_{\mathrm{ip}} < 2$ via Doppler cooling on the standard dark resonance and initialised in state $|\downarrow\rangle$. A pulse containing two microwave tones of frequencies $\omega_{\mathrm{r}} = \omega_{\uparrow\downarrow} + \Delta^{\mathrm{ac}}_{\uparrow\downarrow} - \nu_{\mathrm{ip}} - \epsilon$ and $\omega_{\mathrm{b}} = \omega_{\uparrow\downarrow} + \Delta^{\mathrm{ac}}_{\uparrow\downarrow} + \nu_{\mathrm{ip}} + \epsilon$ is then applied, where $\Delta^{\mathrm{ac}}_{\uparrow\downarrow}$ is the differential ac Zeeman shift on the qubit in the presence of both tones and ϵ is the symmetric detuning of each tone from the respective sideband. I will denote the duration of the pulse by T.

The base sideband Rabi frequency of each tone is found from eq. (8.14) as

$$\Omega_a = \frac{|R_{\uparrow\downarrow}|}{\hbar}\,|\partial_1 B_{0,a}(\mathbf{x}_0)|\,\sqrt{\frac{\hbar}{2M\nu_{\mathrm{ip}}}}\,, \tag{8.26}$$

with $a \in \{\mathrm{r}, \mathrm{b}\}$. The quantity $R_{\uparrow\downarrow}$ represents the matrix element between the states $|4,+1\rangle$ and $|3,+1\rangle$, while ∂_1 denotes the partial derivative along the x_1-axis of the motional coordinate system. I have assumed the pseudopotential approximation and used the fact that the spherical component $B_0(\mathbf{x},t)$ is real, so $|\partial_1 B_{0,a}(\mathbf{x}_0)| = \left|\partial_1 B^+_{0,a}(\mathbf{x}_0)\right| = \left|\partial_1 B^-_{0,a}(\mathbf{x}_0)\right|$ is unambiguous. The quantity $\left|\partial_1 B_{0,a}(\mathbf{x}_0)\right|$ may be calculated from a measurement of the gradient $|\partial_x B_0|$ at the microwave power used, which we carried out separately on the day that the data presented further down were taken. Using the method described in section 7.8.2, we estimated[2] $\left|\partial_x B^+_0(\mathbf{x}_0)\right| = 13.3\,\mathrm{T\,m^{-1}}$. Taking into account the mode angle $\theta = 15^\circ$ that the in-plane direction forms with the x-axis, we predicted a base sideband Rabi frequency of $\Omega_a = 2\pi \times 822\,\mathrm{Hz}$. In general, Ω_a might be slightly different for each tone since the gradient $\partial_1 B_{0,a}(\mathbf{x}_0)$ depends on the microwave power at frequency ω_a contained in the tone. The aim is therefore to ensure that the Rabi frequencies of both tones are equal.

Application of the bichromatic field results in driving of the harmonic oscillator corresponding to the in-plane mode, as described by the time-evolution operator derived in section 8.3. Without loss of generality, we set the phases of the two sideband fields to $\phi_\mathrm{r} = 0$ and $\phi_\mathrm{b} = 0$, which results in a σ_x-dependent force. Expressing the energy eigenstate that the ion initially occupies in the basis of eigenstates of σ_x, one may write $|\psi(0)\rangle = |\downarrow\rangle\,|n_{\mathrm{ip}}\rangle = \left(|\uparrow_x\rangle - |\downarrow_x\rangle\right)|n\rangle\,/\sqrt{2}$. I have omitted the states corresponding to the other motional modes. Application of the MS force for duration T then leads to a wave function $|\psi(T)\rangle = \left[|\uparrow_x\rangle\,|\alpha(T),n\rangle - |\downarrow_x\rangle\,|-\alpha(T),n\rangle\right]/\sqrt{2}$, where $|\alpha,n\rangle = D(\alpha)\,|n\rangle$ denotes a displaced number state. Converting back to the measurement basis, one finds

$$|\psi(T)\rangle = \frac{1}{2}\,|\uparrow\rangle\left[|\alpha(T),n\rangle - |-\alpha(T),n\rangle\right] + \frac{1}{2}\,|\downarrow\rangle\left[|\alpha(T),n\rangle + |-\alpha(T),n\rangle\right]. \tag{8.27}$$

[2]The trap was operated at room temperature during these experiments.

We then read out the qubit states to determine the probability of finding the ion in state $|\uparrow\rangle$. The theoretical prediction may be obtained by summing eq. (8.27) over all possible initial and final motional states, so that

$$P_{\downarrow\rightarrow\uparrow} = \sum_{m,n} P(n) \Big| \langle m | \langle \uparrow | \psi(T) \rangle \Big|^2 = \frac{1}{4} \sum_{m,n} P(n) \Big| \langle m | \alpha(T), n \rangle - \langle m | -\alpha(T), n \rangle \Big|^2 , \tag{8.28}$$

where $P(n)$ is the probability that the ion initially occupies the number state $|n\rangle$. If heating of the motion during the pulse time T is significant, it will modify the observed transition probability. The general expression for an ion initially described by a thermal distribution with average occupation number $\bar{n}$ and affected by a non-negligible heating rate $\dot{\bar{n}}$ has been derived in [HBD+05]. It takes the form

$$P_{\downarrow\rightarrow\uparrow}(T) = \frac{1}{2} \Big(1 - \exp\Big[-\dot{\bar{n}} |4\alpha_0|^2 T - (\bar{n} + 1/2) |2\alpha(T)|^2 \Big] \Big) , \tag{8.29}$$

with $\alpha_0 = \Omega/(2\epsilon)$.

Formula 8.29 is valid under the conditions that the base Rabi frequencies of the two tones are equal and that they are symmetrically detuned from their respective sideband transitions. To realise these requirements in practice, we perform a few calibration steps before probing the MS force on the ion. We start by balancing the powers in the two microwave tones. To this end, we separately use each microwave tone to drive carrier Rabi flopping as a function of pulse time on the clock qubit. We monitor the π-times and adjust the amplitude of one relative to the other until the π-times match. The power coupled into the trap at the frequencies $\omega \pm (\nu_{\mathrm{ip}} + \epsilon)$ might be slightly different, but taking into account the width of the microwave resonator we expect the resulting fractional difference in Ω_a to be $< 1\,\%$.

Next we determine the secular frequency of the in-plane mode by exciting the motion through a tickling pulse and monitoring the height of the red sideband. This is followed by a measurement of the ac Zeeman shift observed when both microwave tones are applied simultaneously. We apply the spin-echo method described in section 7.1.1.1 to the carrier transition of the clock qubit for this purpose. The frequencies of the two tones during the ac shift pulse in the second half of the Ramsey

sequence are detuned sufficiently from the sidebands so as not to cause significant changes in populations of the states.

After these calibration steps, the MS force on a single ion may be probed. We vary the symmetric detuning ϵ while measuring the transition probability $P_{\downarrow\to\uparrow}(T)$. If calibration was completely accurate, a symmetric curve centred on $\epsilon = 0$ should be observed. In practice, however, some parameters will still deviate slightly from their ideal values at this point. The effects caused by imperfections may be modelled by going back to the general Hamiltonian given in eq. (8.20) and numerically simulating the resulting time evolution. Based on such simulations, we find that mismatches in Ω_r and Ω_b result in an asymmetric profile for the transition probability. Using an incorrect value for $\Delta^{\mathrm{ac}}_{\uparrow\downarrow}$ causes the detunings ϵ_r, ϵ_b to be unequal, which also gives rise to asymmetries. A wrong estimate for ν_ip does not affect the relative difference between detunings, but changes the true ϵ compared to its nominal value. This causes the curve to be offset from $\epsilon = 0$.

We find that the main inaccuracy comes from the initial estimate for the ac Zeeman shift. We therefore use the value obtained during the calibration routine as a starting point and empirically optimise it by probing MS dynamics. We perform detuning scans and change the parameter $\Delta^{\mathrm{ac}}_{\uparrow\downarrow}$ in the control code for the experiment until the symmetry of the population curve is maximised by eye.

Figure 8.1 shows a plot of the transition probability $P_{\downarrow\to\uparrow}(\epsilon)$ obtained when the optimal value for $\Delta^{\mathrm{ac}}_{\uparrow\downarrow}$ is used. This particular scan was taken a few months after the other experiments presented in this chapter and used the improved setup for generation of microwaves, described in section 3.5.5.2. The pulse duration of the bichromatic driving field was $T = 1\,\mathrm{ms}$. We have fitted a function based on eq. (8.29), but extended to include a possible offset ϵ_0 for the centre of the curve and a non-zero pedestal in transition probability. The heating rate, which had been measured separately that day as $\dot{\bar{n}}_\mathrm{ip} = 360\,\mathrm{quanta\,s^{-1}}$ was kept fixed during fitting. Other parameters were allowed to float, resulting in estimates $\Omega_a = 2\pi \times 810(20)\,\mathrm{Hz}$, $\bar{n}_\mathrm{ip} = 0.20(5)$ and $\epsilon_0 = 2\pi \times 1.578(5)\,\mathrm{kHz}$. The value of Ω_a obtained from the fit is consistent with the prediction based on our gradient measurement, which confirms the validity of the method used to infer the field gradient.

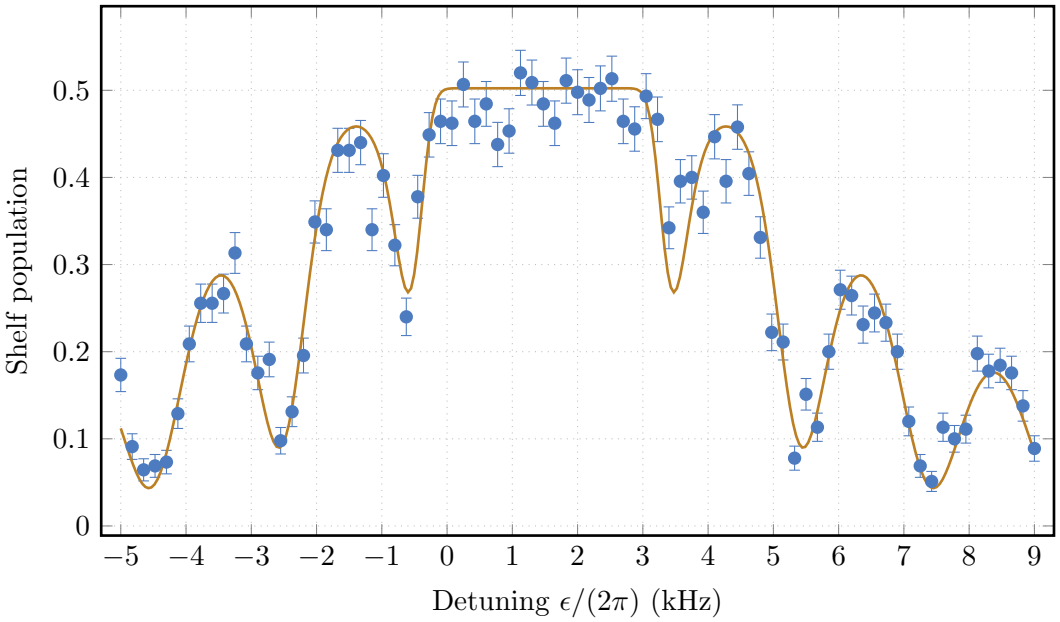


Figure 8.1: Spin-motion entanglement for a single ion using the Mølmer-Sørensen scheme. The spin-dependent force is driven on the radial in-plane mode by two microwave tones, symmetrically detuned by ϵ from the motional sidebands.

We believe that the detuning offset ϵ_0 is not caused by inaccuracies in the calibration procedure since the method used to measure the secular frequency should not suffer from systematic errors. Instead, it is caused by a real change in secular frequency during the bichromatic driving pulse. A similar shift has been observed in other experiments before [WOC+13b]. It was suggested that it results from a small, but non-vanishing electric potential on the microwave electrode, which leads to a modification of the pseudopotential felt by the ion.

8.4 Mølmer-Sørensen force applied to two ions

8.4.1 Theoretical description

I now consider the case of two ions. With the approximations introduced at the end of section 8.2, one finds that the total Hamiltonian for the two-qubit system in the Mølmer-Sørensen scheme can be written

$$\widetilde{H}_{\mathrm{MS}}(t) = \frac{\hbar}{2}\,\Omega_{\mathrm{MS}}\,S_{\phi}\left(\mathrm{e}^{\mathrm{i}\phi_{\mathrm{m}}}\,\mathrm{e}^{-\mathrm{i}\epsilon t}\,a_{m,p}^{\dagger} + \mathrm{e}^{-\mathrm{i}\phi_{\mathrm{m}}}\,\mathrm{e}^{\mathrm{i}\epsilon t}\,a_{m,p}\right). \tag{8.30}$$

I have defined the Rabi frequency $\Omega_{\rm MS}$ and collective spin operator S_ϕ for two ions as

$$\Omega_{\rm MS} = \frac{|R_{{\rm eg},q}|}{\hbar} \left|\partial_m B^+_{-q}(\mathbf{x}_0)\right| \left|b_i^{(p)}\right| q_0^{(m,p)} \tag{8.31}$$

$$S_\phi = \sum_{i=1}^{2} \operatorname{sgn} b_i^{(p)}\, \sigma_\phi^{(i)} \ . \tag{8.32}$$

Expressions for $\sigma_\phi^{(i)}$, $\phi_{\rm m}$ and $\phi_{\rm s}$ were given in section 8.2. It should be noted that for two ions $\Omega_{\rm MS} = \Omega_q^{(i,m,p)}$. The interaction Hamiltonian $\widetilde{H}_{\rm MS}(t)$ above is of the same form as the one found earlier for a single ion, but now involves a spin operator acting on both ions and a normal mode describing collective motion. The time evolution expected to result from this Hamiltonian is therefore similar: a spin-dependent force excites the motion of the string of ions and entangles internal and external degrees of freedom. The time-evolution operator may again be calculated analytically via the Magnus expansion and one finds

$$U_{\rm MS}(t;0) = \mathrm{e}^{S_\phi[\alpha(t)\, a^\dagger_{m,p} - \alpha^*(t)\, a_{m,p}]}\, \mathrm{e}^{-\mathrm{i}\Phi(t) S_\phi^2} \ . \tag{8.33}$$

The coefficients $\alpha(t)$ and $\Phi(t)$ are given by eqs. (8.23) and (8.24), but now $\Omega_{\rm MS}$ is set by expression (8.31).

In the following, I will denote the eigenstates of the individual spin operators $\sigma_\phi^{(i)}$ by $|+\rangle_i = |\uparrow_\phi\rangle_i$ and $|-\rangle_i = |\downarrow_\phi\rangle_i$. The set $\{|s\rangle\}$ of eigenstates of the collective spin operator S_ϕ for the composite two-qubit system is then given by $\{|{+}{+}\rangle, |{+}{-}\rangle, |{-}{+}\rangle, |{-}{-}\rangle\}$, where the first entry identifies the spin state of the first particle. To each eigenstate corresponds an eigenvalue λ_s. I proceed in the same way as in section 8.3 and, by decomposing the spin operator as $S_\phi = \sum_s \lambda_s |s\rangle\langle s|$, one finds that $U_{\rm MS}(t)$ may be written

$$U_{\rm MS}(t) = \sum_s D_{m,p}[\lambda_s \alpha(t)]\ \mathrm{e}^{-\mathrm{i}\lambda_s^2 \Phi(t)}\, |s\rangle\langle s| \ . \tag{8.34}$$

The time-evolution operator thus leads to a time-dependent displacement of the normal mode labelled by m and p, depending on the spin states which the ions

occupy. For $\epsilon \neq 0$, the trajectory describing the centre-of-mass motion traces out a circle in phase space, with radius $r = |\lambda_s|\Omega_{\mathrm{MS}}/\epsilon$. Whenever $\alpha(t) = 0$, the normal mode returns to its initial state, such that spin and motion become disentangled. However, the total wavefunction for the two-qubit system will have acquired a spin-dependent geometric phase $-\lambda_s^2\Phi(t)$, equal to the area enclosed by the trajectory. The phase arises from the second factor contained in $U_{\mathrm{MS}}(t)$. Here lies the crucial difference between the behaviour of a single- and a two-qubit system, because $S_\phi^2 \neq \mathbb{I}$ for the latter and thus leads to different phase factors for different spin eigenstates. This is the mechanism underlying two-qubit entangling gates.

I now specialise to the in-plane rocking mode as this is the mode that we work with in our implementation of the MS scheme. The collective spin operator in this case becomes $S_\phi = \sigma_{\phi_{\mathrm{s}}}^{(1)} - \sigma_{\phi_{\mathrm{s}}}^{(2)}$ and hence $S_\phi^2 = 2\left(\mathbb{I} - \sigma_{\phi_{\mathrm{s}}}^{(1)} \otimes \sigma_{\phi_{\mathrm{s}}}^{(2)}\right)$, which highlights why it is called a $\sigma_\phi \otimes \sigma_\phi$ gate. The eigenvalues of S_ϕ for $|+-\rangle$ and $|-+\rangle$ are $\lambda_2 = +2$ and $\lambda_3 = -2$, respectively, while the eigenvalues for other eigenstates are zero. The latter therefore do not undergo a displacement in phase space and consequently do not accumulate a geometric phase.

The evolution of the former is illustrated in fig. 8.2. Both states acquire the same geometric phase as they traverse their loops in motional phase space. In order to implement an ideal two-qubit gate in the computational basis formed by the eigenstates $\{|\uparrow\rangle_i, |\downarrow\rangle_i\}$ of the operators $\sigma_z^{(i)}$, it is necessary that spin and motion are separable at the end of the gate operation and thus that the loop closes. When this condition is fulfilled, the exact kind of gate obtained depends on the area enclosed by the path in phase space. A maximally entangling gate is achieved if the total accumulated phase $-\lambda^2\Phi = -4\Phi$ is equal to $\pm\pi/2$. These demands result in constraints on the duration and detuning to be used for the gate drive. By considering expressions (8.23) and (8.24) for $\alpha(t)$ and $\Phi(t)$, one may infer that the ideal parameters for a maximally entangling MS gate are given by

$$t_{\mathrm{gate}} = \frac{2\pi K}{|\epsilon_{\mathrm{gate}}|} \tag{8.35}$$

$$\epsilon_{\mathrm{gate}} = \mp 2\Omega_{\mathrm{MS}}\sqrt{K}\,, \tag{8.36}$$

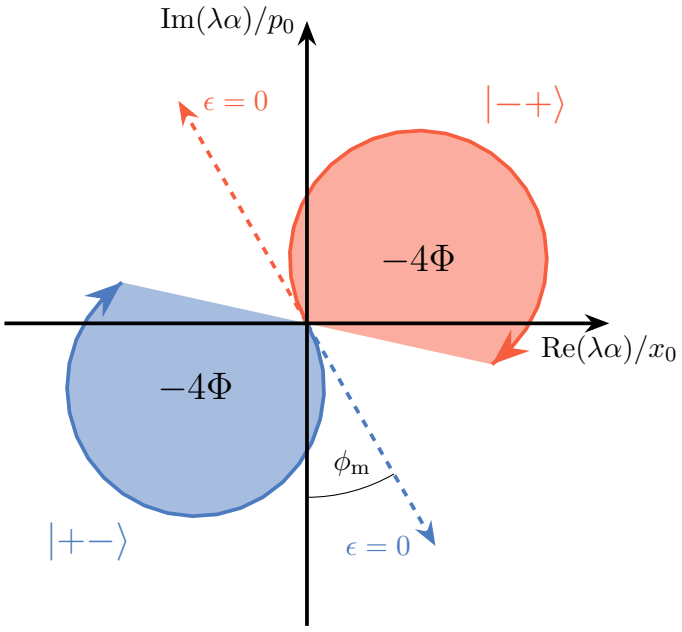


Figure 8.2: Evolution of two-qubit system in phase space under the action of the Mølmer-Sørensen Hamiltonian. It is assumed that the rocking mode of two ions is driven and that $\epsilon \geq 0$. The coefficients α and Φ are given by eqs. 8.23 and 8.24. The trajectory of each eigenstate of the collective spin operator $S_\phi = \sigma^{(1)}_{\phi_\mathrm{s}} - \sigma^{(2)}_{\phi_\mathrm{s}}$ is determined by its eigenvalue λ. The states $|{+}{+}\rangle$ and $|{-}{-}\rangle$ have eigenvalue $\lambda = 0$, which means they are not displaced and do not acquire geometric phase. Conversely, the states $|{+}{-}\rangle$ and $|{-}{+}\rangle$ are characterised by $\lambda = \pm 2$ and consequently trace out paths in opposite directions. The geometric phase accumulated is given by $-\lambda^2\Phi$ and depends on the area enclosed by the path. Whenever a state returns to the origin, spin and motion become disentangled, but the wavefunction is multiplied by a phase factor.

where $K \in \{1, 2, \ldots\}$ denotes the number of loops traversed during the gate. Splitting the accumulation of phase over a number of smaller loops rather than one big loop is advantageous to suppress certain kinds of errors, as discussed in section 8.5. Taking into account the expression for ϵ_{gate} just obtained, one finds that the gate duration may also be written $t_{\text{gate}} = (\pi/\Omega_{\text{MS}})\sqrt{K}$. It follows that if one would like to increase the number of loops from K_1 to K_2 while keeping the gate time constant, the Rabi frequency has to be increased according to $\Omega_{\text{MS},2}/\Omega_{\text{MS},1} = \sqrt{K_2/K_1}$. The required microwave power therefore scales as K_2/K_1.

For the ideal gate, the time evolution leads to the mapping

$$|{+}{+}\rangle \mapsto |{+}{+}\rangle \tag{8.37}$$

$$|{+}{-}\rangle \mapsto \pm\mathrm{i}\,|{+}{-}\rangle \tag{8.38}$$

$$|{-}{+}\rangle \mapsto \pm\mathrm{i}\,|{-}{+}\rangle \tag{8.39}$$

$$|{-}{-}\rangle \mapsto |{-}{-}\rangle \tag{8.40}$$

in the basis in which the spin-dependent force operates. Taking into account that

$$|\pm\rangle_i = \frac{1}{\sqrt{2}}\left(|\uparrow\rangle_i \pm \mathrm{e}^{-\mathrm{i}\phi_{\text{s}}}\,|\downarrow\rangle_i\right)\,, \tag{8.41}$$

the mapping induced by the MS gate in the computational basis is found to be given by

$$|{\uparrow}{\uparrow}\rangle \mapsto \frac{1}{\sqrt{2}}\,\mathrm{e}^{\pm\mathrm{i}\pi/4}\left(|{\uparrow}{\uparrow}\rangle \mp \mathrm{i}\,\mathrm{e}^{-\mathrm{i}2\phi_{\text{s}}}\,|{\downarrow}{\downarrow}\rangle\right) \tag{8.42}$$

$$|{\uparrow}{\downarrow}\rangle \mapsto \frac{1}{\sqrt{2}}\,\mathrm{e}^{\pm\mathrm{i}\pi/4}\left(|{\uparrow}{\downarrow}\rangle \mp \mathrm{i}\,|{\downarrow}{\uparrow}\rangle\right) \tag{8.43}$$

$$|{\downarrow}{\uparrow}\rangle \mapsto \frac{1}{\sqrt{2}}\,\mathrm{e}^{\mp\mathrm{i}\pi/4}\left(|{\uparrow}{\downarrow}\rangle \pm \mathrm{i}\,|{\downarrow}{\uparrow}\rangle\right) \tag{8.44}$$

$$|{\downarrow}{\downarrow}\rangle \mapsto \frac{1}{\sqrt{2}}\,\mathrm{e}^{\mp\mathrm{i}\pi/4}\left(\mathrm{e}^{\mathrm{i}2\phi_{\text{s}}}\,|{\uparrow}{\uparrow}\rangle \pm \mathrm{i}\,|{\downarrow}{\downarrow}\rangle\right)\,. \tag{8.45}$$

The upper sign applies for $-4\Phi = \pi/2$ and the lower sign for $-4\Phi = -\pi/2$.

8.4.1.1 Measuring gate fidelity

The time evolution induced on a string of ions during the course of a gate operation in a physical apparatus will not quite be described by the ideal operator U_{MS} given in eq. (8.33). One reason for this lies in the fact that several contributions to the general Hamiltonian were neglected in order to arrive at $\widetilde{H}_{\mathrm{MS}}$ earlier. The other reason is that various noise processes not considered in the treatment so far may result in non-unitary behaviour, which makes it necessary to describe the system by means of a density matrix. To assess the performance of a gate operation, one therefore requires a measure of how closely the gate realised in practice approximates the ideal gate that one is trying to implement.

A complete method to characterise gate performance is offered by quantum process tomography [PCZ97]. Once the superoperator corresponding to the experimental process has been determined, it is possible to predict its action on an arbitrary input state. It should be noted that quantum process tomography relies on the ability to prepare a complete set of basis states for the Hilbert space (for example, the computational basis), which requires addressing of individual ions to perform single-qubit rotations on their Bloch spheres. Furthermore, one needs to be able to measure the population of each basis state and thus discriminate between $|{\uparrow\downarrow}\rangle$ and $|{\downarrow\uparrow}\rangle$ during readout. It should be possible to achieve both requirements in our trap in the future.

Another method is provided by randomised benchmarking [KLR+08]. While it does not allow reconstruction of the complete superoperator, it makes it possible to estimate the average error per gate for different input states, which is usually the most relevant metric in practice.

For the initial attempts at a two-qubit gate in our apparatus, as presented in section 8.4.2, the two characterisation methods mentioned above were not necessary. Instead, we demonstrated two-qubit entanglement by preparing one particular input state and comparing the observed output to the target state that would result from an ideal MS gate. While this does not allow us to verify the complete mapping given in eq. (8.42), it enables us to check correct operation of our apparatus. We describe

the output by means of a density operator ρ that acts on the spin subspace and the ideal target state by the pure spion state $|\psi_{\text{ideal}}\rangle$. The performance of the gate operation is measured by the fidelity $\mathcal{F}$, defined as

$$\mathcal{F} = \langle\psi_{\text{ideal}}|\rho|\psi_{\text{ideal}}\rangle \ . \tag{8.46}$$

We use $|\downarrow\downarrow\rangle$ as the input state and choose $\epsilon_{\text{gate}} > 0$, which means that $-4\Phi = -\pi/2$ in the ideal case. The target state may be obtained from eq. (8.42) and is given by

$$\begin{aligned}\mathcal{F} &= \frac{1}{2}\Big[\rho_{\uparrow\uparrow,\uparrow\uparrow} + \rho_{\downarrow\downarrow,\downarrow\downarrow} - 2\,\mathrm{Re}\big(\mathrm{i}\,\mathrm{e}^{-\mathrm{i}2\phi_{\mathrm{s}}}\,\rho_{\uparrow\uparrow,\downarrow\downarrow}\big)\Big] \\ &= \frac{\rho_{\uparrow\uparrow,\uparrow\uparrow} + \rho_{\downarrow\downarrow,\downarrow\downarrow}}{2} - \big|\rho_{\uparrow\uparrow,\downarrow\downarrow}\big|\sin\big[2\phi_{\mathrm{s}} - \arg(\rho_{\uparrow\uparrow,\downarrow\downarrow})\big] \ . \end{aligned} \tag{8.47}$$

I have denoted the components of the density matrix in the computational two-qubit basis by $\rho_{i,j} = \langle i|\rho|j\rangle$. For an ideal MS gate, one finds $\rho_{\uparrow\uparrow,\uparrow\uparrow} = \rho_{\downarrow\downarrow,\downarrow\downarrow} = 1/2$ and $\big|\rho_{\uparrow\uparrow,\downarrow\downarrow}\big| = 1/2$, $\arg(\rho_{\uparrow\uparrow,\downarrow\downarrow}) = 2\phi_{\mathrm{s}} + \pi/2$ after the gate pulse, so that both terms in the above expression give a contribution of $1/2$.

The diagonal elements $\rho_{\uparrow\uparrow,\uparrow\uparrow}$ and $\rho_{\downarrow\downarrow,\downarrow\downarrow}$ are just the populations of the states $|\uparrow\uparrow\rangle$ and $|\downarrow\downarrow\rangle$. They can be determined straightforwardly by reading out the two-qubit register directly after the gate pulse. The coherence between $|\uparrow\uparrow\rangle$ and $|\downarrow\downarrow\rangle$, however, is not directly observable since state-dependent fluorescence detection only projects onto the atomic states $|\uparrow\rangle$ and $|\downarrow\rangle$. In order to infer the off-diagonal element $\rho_{\uparrow\uparrow,\downarrow\downarrow}$, it is therefore necessary to map coherences onto populations before readout. This can be achieved by appending an analysis pulse after the gate operation [SKK+00]. This analysis pulse takes the form of a resonant Rabi $\pi/2$-pulse with phase ϕ_{a} that is globally applied to both ions, resulting in single-qubit rotations on the respective Bloch spheres around an axis determined by ϕ_{a}. We subsequently measure the populations $P_{\uparrow\uparrow}$, $P_{\uparrow\downarrow} + P_{\downarrow\uparrow}$, $P_{\downarrow\downarrow}$ and construct the parity Π, defined as

$$\Pi = P_{\uparrow\uparrow} + P_{\downarrow\downarrow} - \big(P_{\uparrow\downarrow} + P_{\downarrow\uparrow}\big) \tag{8.48}$$

$$= 2\,\mathrm{Re}\big(\rho_{\uparrow\downarrow,\downarrow\uparrow}\big) - 2\big|\rho_{\uparrow\uparrow,\downarrow\downarrow}\big|\cos\big[2\phi_{\mathrm{a}} + \arg(\rho_{\uparrow\uparrow,\downarrow\downarrow})\big] \ . \tag{8.49}$$

As the phase of the analysis pulse is scanned, the parity signal thus exhibits char-

acteristic oscillations with $2\phi_a$. Fitting a function $a\cos(2\phi_a + \kappa) + b$, with $a > 0$, enables us to infer $\left|\rho_{\uparrow\uparrow,\downarrow\downarrow}\right| = a/2$ and $\arg(\rho_{\uparrow\uparrow,\downarrow\downarrow}) = \kappa + \pi$ from the contrast and phase offset of the observed variation.

8.4.2 Implementation of a Mølmer-Sørensen gate with two ions

Having demonstrated the spin-dependent force for a single ion, we proceeded with an initial attempt at a two-qubit gate. When the data presented in this section were taken, our apparatus was still missing several important features. In particular, neither the absolute nor the relative power in the microwave tones was actively stabilised. As a consequence, the offset in microwave frequency required to compensate the ac Zeeman shift drifted by several hundreds of Hertz over tens of minutes. Furthermore, the components generating the rf trapping field were not temperature-stabilised, which meant that the secular frequencies exhibited similar changes. Additionally, the trap was not operated at cryogenic temperatures yet. Since such conditions prevented a high-fidelity gate at the time, the aim was instead to show in general that our surface trap is suitable for entangling operations.

We choose the in-plane rocking mode as the bus to mediate entanglement because its heating rate is significantly lower than that of the centre-of-mass mode. Our apparatus was only capable of generating two microwave tones at the time, which meant that variations of the MS scheme requiring more than two frequencies were not an option. We therefore adhere to the original proposal and use two microwave tones, with frequencies $\omega_r = \omega_{\uparrow\downarrow} + \Delta^{ac}_{\uparrow\downarrow} - \nu_{ip,rocking} - \epsilon_r$ and $\omega_b = \omega_{\uparrow\downarrow} + \Delta^{ac}_{\uparrow\downarrow} + \nu_{ip,rocking} + \epsilon_b$. Before investigation of gate dynamics, a measurement of the field gradient is performed, the result of which enables us to predict the gate Rabi frequency Ω_{MS}. We use a microwave power of 1 W per tone. A suite of calibration routines is also executed to balance the microwave powers in the two frequency components, obtain an estimate for the ac Zeeman shift and measure the secular frequency of the rocking mode. These are essentially the same experiments as described earlier in the case of a single ion. We choose to use one loop for the initial gate implementation. Taking into account our estimate of Ω_{MS}, we therefore set the duration of the bichromatic pulse to 635 µs.

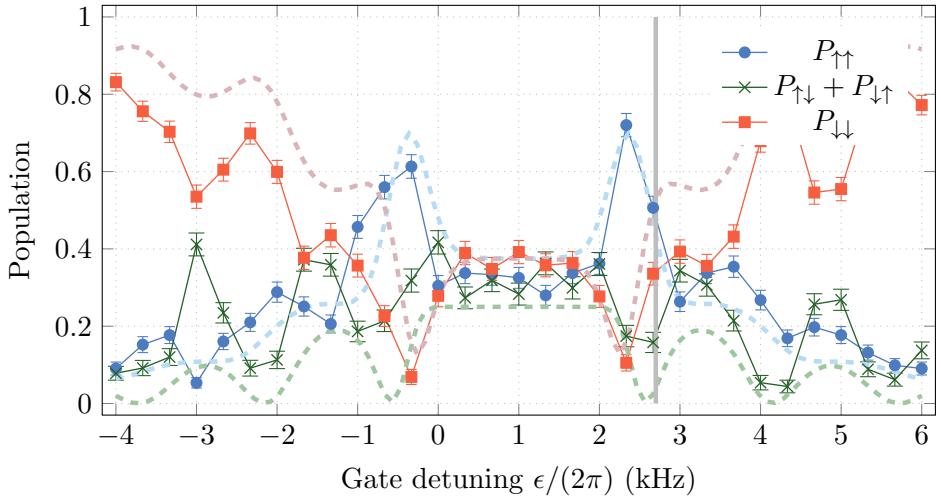


Figure 8.3: Populations of qubit states as a function of symmetric detuning ϵ of gate pulse. The pulse duration was fixed at 635 µs, which was the value assumed to be optimal for a one-loop gate, given the estimate of field gradient obtained during calibration. This estimate was later found to be slightly incorrect, see main text. The offset of ≈ 1 kHz in the pattern results from a change in secular frequency when the microwave magnetic field is applied. Solid lines serve as a guide for the eye, while dashed lines are the results of simulations for evolution under the ideal gate Hamiltonian assuming an updated estimate of field gradient, but unchanged pulse duration of 635 µs. The vertical line at 2.7 kHz indicates the detuning at which parity scans were subsequently carried out.

The two-qubit system is prepared in state $|{\downarrow\downarrow}\rangle = |4,+1\rangle \otimes |4,+1\rangle$ by optical pumping and subsequent microwave transfer pulses. We enforce $\epsilon_\mathrm{r} = \epsilon_\mathrm{b} = \epsilon$ in the control code of the experiment and start by scanning ϵ while observing through our usual readout method the probabilities that both ions fluoresce, either ion fluoresces or both ions are shelved. These probabilities are used to infer the populations $P_{\uparrow\uparrow}$, $P_{\uparrow\downarrow} + P_{\downarrow\uparrow}$ and $P_{\downarrow\downarrow}$ after the gate pulse. If the resulting curves are not symmetric about a certain detuning, we adjust our estimate of the ac Zeeman shift and conduct another detuning scan. We continue this procedure until the symmetry is optimised by eye. Figure 8.3 contains a plot of observed populations after compensation of the ac Zeeman shift has nominally been optimised. Each data point represents the average of 300 repetitions of the experimental sequence. Solid lines are guides for the eye.

Similar to what was observed for a single ion, we find that the pattern is not centred on $\epsilon = 0$. The offset is estimated from the plot to be approximately 1 kHz.

The gate dynamics are far from ideal, for several reasons. Firstly, we realised during analysis of the data that the estimate of the field gradient had been slightly incorrect. We believe the true gradient applied during gate pulses was higher and the optimal gate time would have been 609 µs. I have performed numerical simulations assuming the updated estimate of the gradient, but the pulse duration of 635 µs used in practice. The populations predicted by these simulations are drawn as dashed lines in fig. 8.3. Secondly, we expect significant drifts in $\Delta^{\mathrm{ac}}_{\uparrow\downarrow}$ and $\nu_{\mathrm{ip,rocking}}$ to have occurred within and between scan points, which means that the true ϵ_{r} and ϵ_{b} present during pulses are not given by the nominal ϵ in the control code. Thirdly, it is likely that off-resonant driving of the carrier transition has a non-negligible impact since $\Omega_{\mathrm{car}} \approx 2\pi \times 1.2\,\mathrm{MHz}$ on the rf null at room temperature for the microwave power used, while the microwave tones are only detuned by $\nu_{\mathrm{ip,rocking}} \approx 5\,\mathrm{MHz}$.

Nevertheless, we proceeded to see what fidelity could be obtained under these circumstances. If a system evolves under the ideal Hamiltonian $\widetilde{H}_{\mathrm{MS}}$ for a time equal to the optimal duration t_{gate}, then the curves of $P_{\uparrow\uparrow}$ and $P_{\downarrow\downarrow}$ intersect at 1/2 when the detuning reaches its optimal value ϵ_{gate} and $P_{\uparrow\downarrow} + P_{\downarrow\uparrow}$ should drop to zero at this detuning. This is visible for the dashed lines in fig. 8.3 around 2.6 kHz and −0.6 kHz. We therefore choose to operate at the point where the observed $P_{\uparrow\downarrow} + P_{\downarrow\uparrow}$ reaches its minimum, estimated as $\epsilon = 2\pi \times 2.7\,\mathrm{kHz}$. This position is marked by a line in fig. 8.3. The relevant populations at $\epsilon = 2\pi \times 2.7\,\mathrm{kHz}$ are measured to be $P_{\uparrow\uparrow} = 0.48(3)$ and $P_{\downarrow\downarrow} = 0.34(3)$. If we assume a one-loop MS gate for which the optimal gate time is 635 µs and take into account the observed shift of 1 kHz in secular frequency, the optimal detuning is predicted to be $2\pi \times 2.6\,\mathrm{kHz}$. This is reasonably close to the value we estimate from the plot.

Using a detuning of $\epsilon = 2\pi \times 2.7\,\mathrm{kHz}$, we then added an analysis $\pi/2$-pulse after the gate drive and measured the parity as a function of the phase ϕ_{a} of the analysis pulse. The results are given in fig. 8.4. A function of the form $a\cos(2\phi_{\mathrm{a}} + \kappa) + b$ has been fitted to the data, from which $\left|\rho_{\uparrow\uparrow,\downarrow\downarrow}\right| = 0.363(5)$ and $\arg(\rho_{\uparrow\uparrow,\downarrow\downarrow}) = 0.066(6)\pi\,\mathrm{rad}$ are calculated. Combining this with the estimates for $P_{\uparrow\uparrow}$ and $P_{\downarrow\downarrow}$, we infer a fidelity of $\mathcal{F} = 0.77(2)$.

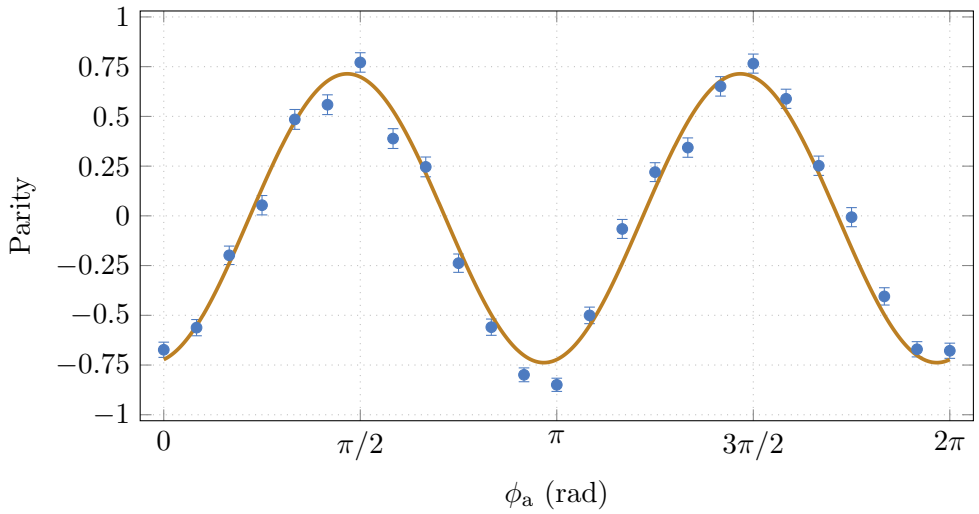


Figure 8.4: Observed parity as a function of phase ϕ_a of $\pi/2$-analysis pulse. The gate pulse had a duration of 635 µs and a detuning of 2.7 kHz. The latter was chosen after inspecting the populations plotted in fig. 8.3. A fit to a sinusoid indicates $\left|\rho_{\uparrow\uparrow,\downarrow\downarrow}\right| = 0.363(5)$.

8.5 Simulations of projected gate fidelity

In chapter 7, I presented measurements of characteristic parameters of our surface trap that will affect the fidelity and speed of two-qubit gates which may be achieved in future experiments. These include the amplitude of the π-component of the microwave field, its gradient along the principal axis of the two-ion in-plane rocking mode and the heating rate of this mode. Armed with estimates of these parameters, I now investigate the impact of various sources of error on the expected gate fidelity. The results of such an analysis provide guidance as to which areas will need particular attention as work on a high-fidelity two-qubit gate progresses.

Our starting point is the ideal implementation of a Mølmer-Sørensen gate, based on the Hamiltonian $\widetilde{H}_{\text{gate}}$ given in eq. (8.30) and the relations (8.35) and (8.36). I then allow deviations from this ideal situation and calculate the resulting reduction in fidelity, if necessary by numerical solution of the master equation

$$\frac{d\rho}{dt} = -\frac{\mathrm{i}}{\hbar}[H,\rho] + \mathcal{L}\rho\,, \tag{8.50}$$

where $H(t)$ is the full Hamiltonian for the system in the presence of gate imperfections. To estimate the relative importance of different sources of infidelity, I only

consider one error mechanism at a time.

In the following subsections, I have assumed that our trap is operated at a temperature around 20 K and an input power of 5 W per microwave tone is used. The relevant trap parameters are then obtained by scaling the values presented in section 7.8.2 appropriately. We expect a field gradient of $\partial_x B_\pi = 88\,\mathrm{T\,m^{-1}}$, giving rise to a gate Rabi frequency of[3] $\Omega_0 = 2\pi \times 4\,\mathrm{kHz}$, assuming $\nu_{\mathrm{ip,rocking}} = 2\pi \times 5\,\mathrm{MHz}$ and $\theta = 15°$. The optimal detuning and duration of a gate pulse utilising one loop in phase space are consequently found as $\epsilon_{\mathrm{gate}} = 2\pi \times 8\,\mathrm{kHz}$ and $t_{\mathrm{gate}} = 122\,\mu\mathrm{s}$. Unless indicated otherwise, only the in-plane rocking mode was included for simulations. For simulations based on the master equation, its Hilbert space was truncated to 30 Fock states, which I found to be sufficient for the accuracy desired. The temperature of the mode at the start of the gate pulse was taken to be $\bar{n}_{\mathrm{ip,rocking}} = 0.2$, which I believe to be a rather conservative assumption. Whenever I make a reference to gate parameters hereafter, these are the values I mean.

8.5.1 Fluctuations in microwave power

Although care is taken to keep the microwave power in each sideband tone as stable as possible, fluctuations cannot be eliminated completely in practice. This means that Ω_{r} and Ω_{b} may change slightly over time, which has three effects: variations that are common to both tones cause fluctuations in Ω, while differential variations lead to an imbalance between the Rabi frequencies of the two tones. Furthermore, both kinds of fluctuations give rise to changes in the ac Zeeman shift induced on the ions. In general, these three sources of error will all be present simultaneously. However, to estimate their relative importance, I analyse them independently in the following subsections. In principle, there may be variations in microwave power that are fast compared to the duration of a gate pulse. Their influence on the dynamics could be modelled by allowing the parameter of interest in the master equation to be time-dependent. Given that the typical duration of a gate pulse will be $< 1\,\mathrm{ms}$ in future experiments, however, one may expect changes in microwave power on this timescale to be small and therefore I will assume that the relevant parameter

[3] I drop the explicit subscript in this section.

is approximately constant during the gate operation. Nevertheless, there may be fluctuations between individual shots of the experimental sequence that we repeat to build up the necessary statistics. These shot-to-shot fluctuations will therefore affect the observed average gate fidelity.

8.5.1.1 Incorrect geometric phase

I assume in this section that the Rabi frequencies of the two microwave tones are always balanced, but fluctuate around a mean value $\bar{\Omega} = \Omega_0$. This means that any noise in microwave power is common to both tones. I choose ϵ_{gate} and t_{gate} to be set to the values that result in an ideal gate for $\bar{\Omega}$. As the power fluctuates, the Rabi frequency changes to $\Omega = \bar{\Omega} + \delta\Omega = \bar{\Omega}\,(1 + r_\Omega)$, where $r_\Omega = \delta\Omega/\bar{\Omega}$ is the relative size of the fluctuation. Since I ignore the impact of the resulting changes in ac Zeeman shift in this section, the gate error is caused exclusively by acquiring incorrect geometric phase. Under these conditions, the fidelity of an individual gate pulse may be shown to be given by

$$\mathcal{F} = \frac{1}{2} + \frac{1}{2}\sin\left[2\pi K\left(\frac{\Omega}{\epsilon_{\text{gate}}}\right)^2\right] = \frac{1}{2} + \frac{1}{2}\sin\left[\frac{\pi}{2}\,(1 + r_\Omega)^2\right]. \tag{8.51}$$

It follows that, regardless of $\bar{\Omega}$, the gate error only depends on the relative magnitude of fluctuations. I model the variations in Ω by assuming that from shot to shot $\delta\Omega$ behaves as a random variable with standard deviation $\delta\Omega_{\text{rms}}$. The average gate fidelity may then be calculated by averaging eq. (8.51) over the underlying probability distribution and is only a function of $\delta\Omega_{\text{rms}}/\bar{\Omega}$. If slow drifts have been removed via active stabilisation of the microwave power, it seems reasonable to take $\delta\Omega$ to be normally distributed. I have performed a Monte Carlo simulation for this purpose, the results of which are shown in fig. 8.5. Each data point represents an average over 10^5 samples drawn from a normal distribution with standard deviation $\delta\Omega_{\text{rms}}$. For $\delta\Omega_{\text{rms}} \approx 5 \times 10^{-4}$, which is the size of fluctuations we expect in our trap with active stabilisation, an error of $\epsilon \approx 6 \times 10^{-7}$ is found, which is negligible compared to other error mechanisms.

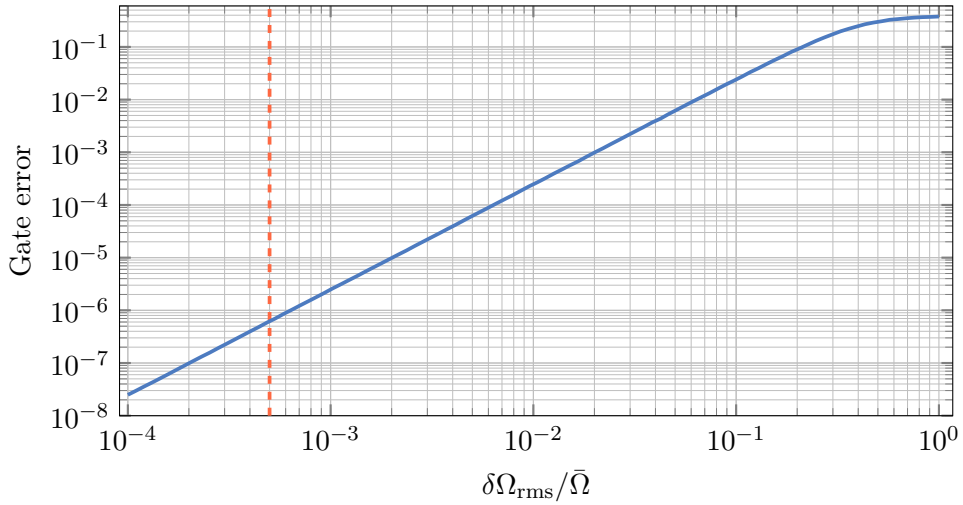


Figure 8.5: Gate error caused by fluctuations in Rabi frequency. It is assumed that the only consequence of variations in microwave power are changes in gate Rabi frequency $\Omega = \bar{\Omega} + \delta\Omega$ and thus errors are caused purely by accumulating the wrong geometric phase. Each data point results from averaging eq. (8.51) over 10^5 samples drawn from a normal distribution with standard deviation $\delta\Omega_{\mathrm{rms}}$. Errors are independent of the number of loops used. The dashed red line indicates the conditions under which we expect our trap to operate.

8.5.1.2 Imbalance in Rabi frequencies of microwave tones

Fluctuations in power that are not common to both microwave tones will cause Ω_{r} and Ω_{b} to become unequal. Under the assumption that any changes in power are purely differential, the Rabi frequencies of the tones will move in opposite directions around an average $\bar{\Omega} = \Omega_0$. The influence of this effect on the gate dynamics may be estimated by going back to the general Hamiltonian 8.20 and numerically integrating the master equation, keeping t_{gate} and ϵ_{gate} fixed at the values calculated to be optimal for $\bar{\Omega}$. I have not run such simulations directly, but instead suppose that the gate error is determined only by the relative fluctuations $(\Omega_{\mathrm{r}} - \Omega_{\mathrm{b}})/\bar{\Omega}$. The results presented in [Sep16] then also hold for our trap and, taking $(\Omega_{\mathrm{r}} - \Omega_{\mathrm{b}})/\bar{\Omega} \approx 10^{-3}$, I predict an error contribution of $\epsilon \approx 5 \times 10^{-7}$.

8.5.1.3 Fluctuations in ac Zeeman shift

The amplitudes of the magnetic fields generated by the two tones at the positions of the ions result in ac Zeeman shifts on the qubit states that have to be taken into account when setting the frequencies of the tones. In the absence of fluctuations

in microwave power, the shift is stable and may in theory be determined precisely during calibration of the gate sequence. I will assume that such an ideal calibration has been performed. Errors then only arise from variations in microwave power between gate pulses because they lead to fluctuations in ac Zeeman shift. I write the differential ac Zeeman shift on the qubit states as $\Delta^{\mathrm{ac}}_{\uparrow\downarrow} = \bar{\Delta}^{\mathrm{ac}} + \Delta^{\mathrm{ac,err}}$, where $\bar{\Delta}^{\mathrm{ac}}$ denotes the average shift measured during calibration. I start by assuming that ϵ_{gate} and t_{gate} have been calculated for the ideal gate and the frequencies of the microwave tones accordingly been set to $\omega_{\mathrm{r}} = \omega_{\uparrow\downarrow} + \bar{\Delta}^{\mathrm{ac}} - \nu - \epsilon_{\mathrm{gate}}$ and $\omega_{\mathrm{b}} = \omega_{\uparrow\downarrow} + \bar{\Delta}^{\mathrm{ac}} + \nu + \epsilon_{\mathrm{gate}}$. In the presence of $\Delta^{\mathrm{ac,err}}$, the detunings of the tones from their respective sidebands are no longer equal, but rather $\epsilon_{\mathrm{r}} = \epsilon_{\mathrm{gate}} + \Delta^{\mathrm{ac,err}}$ and $\epsilon_{\mathrm{b}} = \epsilon_{\mathrm{gate}} - \Delta^{\mathrm{ac,err}}$. One may expect the resulting gate error to depend on the relative size of $\Delta^{\mathrm{ac,err}}$ compared to the ideal ϵ_{gate}.

Fluctations in ac Zeeman shift can be modelled by adding a contribution[4]

$$\widetilde{H}_{\mathrm{ac}} = \frac{\hbar}{2}\Delta^{\mathrm{ac,err}} \sum_i \sigma_z^{(i)} \tag{8.52}$$

to the Hamiltonian. Since $\sigma_z^{(i)}$ does not commute with $\sigma_\phi^{(i)}$, this perturbation does not commute with the gate operation and one can therefore not just add single- or two-qubit pulses to compensate for its effect. I again assume that the microwave power and thus $\Delta^{\mathrm{ac,err}}$ is a normally distributed random variable, with standard deviation $\Delta^{\mathrm{ac,err}}_{\mathrm{rms}}$. In principle, the average gate fidelity as a function of $\Delta^{\mathrm{ac,err}}_{\mathrm{rms}}$ could be estimated by generating a large number of samples drawn from the corresponding normal distribution, numerically solving the master equation with $H = \widetilde{H}_{\mathrm{MS}}(t) + \widetilde{H}_{\mathrm{ac}}$ for each and subsequently calculating the mean of the fidelities. However, this is computationally intensive and I therefore choose a slightly different method for an approximate estimate. I assume that $\int \mathcal{F}(\Delta^{\mathrm{ac,err}})\, P(\Delta^{\mathrm{ac,err}})\, d\Delta^{\mathrm{ac,err}} \approx \mathcal{F}\,(\Delta^{\mathrm{ac,err}}_{\mathrm{rms}})$, so the fidelity averaged over a normal distribution characterised by standard deviation $\Delta^{\mathrm{ac,err}}_{\mathrm{rms}}$ is approximately equal to the fidelity calculated for the value $\Delta^{\mathrm{ac,err}}_{\mathrm{rms}}$. I thus obtain estimates for the gate error by solving the master equation once for each $\Delta^{\mathrm{ac,err}}_{\mathrm{rms}}$. The outcome of such simulations is contained in fig. 8.6, in which I plot the

[4]Note that $\widetilde{H}_{\mathrm{ac}}$ is defined in the same rotating frame as $\widetilde{H}_{\mathrm{MS}}(t)$.

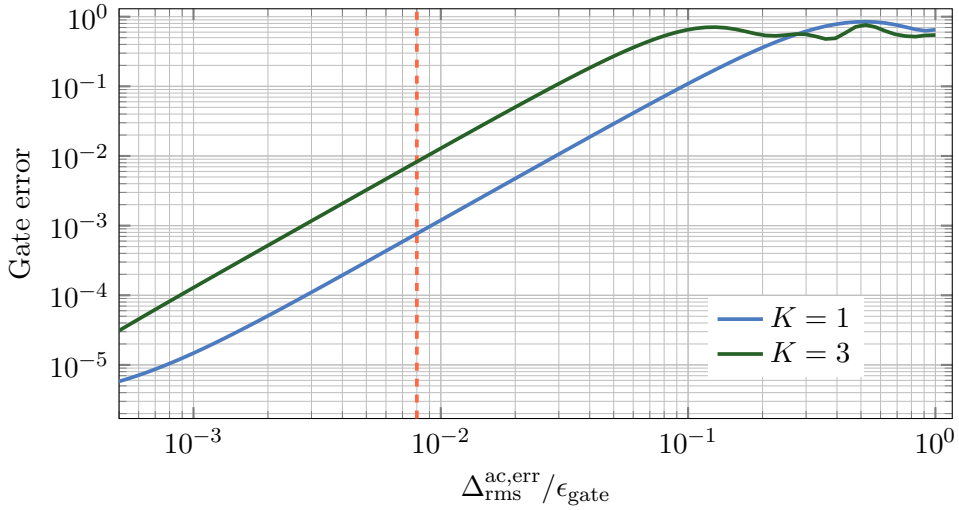


Figure 8.6: Gate error resulting from fluctuations in ac Zeeman shift. Here it is assumed that changes in microwave power only give rise to variations in ac Zeeman shift. The parameters Ω, ϵ_{gate} and t_{gate} are kept fixed during simulations. The dashed red line indicates the conditions under which we expect our trap to operate.

gate error as a function of $\Delta_{\mathrm{rms}}^{\mathrm{ac,err}}/\epsilon_{\mathrm{gate}}$. It is found that the results do not change if a different Rabi frequency Ω_0 is assumed and t_{gate}, ϵ_{gate} are adjusted appropriately, which indicates that the gate error resulting from fluctuations in ac Zeeman shift indeed depends only on $\Delta_{\mathrm{rms}}^{\mathrm{ac,err}}/\epsilon_{\mathrm{gate}}$ and K.

As evident from eq. (5.68), the ac Zeeman shift is a function of the square of the amplitude of the microwave field and thus proportional to microwave power. It follows that $\Delta_{\mathrm{rms}}^{\mathrm{ac,err}}/\bar{\Delta}^{\mathrm{ac}} = \delta P_{\mathrm{mw,rms}}/\bar{P}_{\mathrm{mw}} = r_{\mathrm{mw,rms}}$ and therefore $\Delta_{\mathrm{rms}}^{\mathrm{ac,err}}/\epsilon_{\mathrm{gate}} = r_{\mathrm{mw,rms}}\,\bar{\Delta}^{\mathrm{ac}}/\epsilon_{\mathrm{gate}}$. For fixed relative microwave stability $r_{\mathrm{mw,rms}}$, an increase in microwave power leads to a larger error from fluctuations in ac Zeeman shift since $\Delta_{\mathrm{rms}}^{\mathrm{ac,err}}/\epsilon_{\mathrm{gate}}$ scales as $r_{\mathrm{mw,rms}}\sqrt{\bar{P}_{\mathrm{mw}}}$. One thus conclude that not only the relative stability matters, but also the overall shift $\bar{\Delta}^{\mathrm{ac}}$ induced on the qubit states. This is the reason why a strong field gradient, but weak field amplitude is desirable for the Mølmer-Sørensen scheme. At the position of the rf null, we observe a typical ac Zeeman shift of $\bar{\Delta}^{\mathrm{ac}} \approx 2\pi \times 12\,\mathrm{kHz}$ when 1 W of input power in each microwave tone is used at a temperature around 20 K. This shift is predominantly caused by the σ^+ and σ^--components of the microwave magnetic field and therefore does not decrease even when the ion is located at the position of the minimum in π-component. Assuming a relative microwave stability of $r_{\mathrm{mw,rms}} \approx 10^{-3}$, the expected $\Delta_{\mathrm{rms}}^{\mathrm{ac,err}}$ is

of order $2\pi \times 60\,\mathrm{Hz}$ for a power of 5 W in each tone. With the optimal detuning $\epsilon_{\mathrm{gate}} = 2\pi \times 8\,\mathrm{kHz}$ for a single loop with our standard trap parameters, I therefore expect an error of $\epsilon \approx 8 \times 10^{-4}$.

8.5.2 Variations in motional frequency

Instabilities in the secular frequency ν of the motional mode used to entangle the qubits, expected to result mainly from variations in the amplitude of the rf voltage, may lead to gate errors. I will distinguish between different timescales over which changes may occur. Slow drifts over minutes may be eliminated by measuring the secular frequency regularly and either updating gate parameters based on the new estimate of ν or feeding back via control electronics to keep ν at the desired setpoint. Remaining fluctuations may thus occur in the interval between runs of the calibration routine, which is of the order of a few minutes. These include variations that are fast compared to the duration of a gate pulse, corresponding to noise at frequencies of approximately 10 kHz and higher. They cause rapid fluctuations in the energies of states with different occupation numbers, which leads to decoherence between motional states. I discuss the influence of this effect on gate fidelity separately in section 8.5.8. Here I concentrate on changes in ν that are slow with respect to the duration of a gate pulse, but fast in comparison to the interval between calibration runs.

The starting point for our analysis is the general analytic expression for the fidelity obtained when the Rabi frequency Ω, duration t and symmetric detuning ϵ for the bichromatic pulse are chosen arbitrarily and therefore do not necessarily satisfy relations (8.35) and (8.36). It is found that in this case

$$\mathcal{F} = \frac{1}{8}\Big(3 + \mathrm{e}^{-16|\alpha(t)|^2(\bar{n}+1/2)} + 4\,\mathrm{e}^{-4|\alpha(t)|^2(\bar{n}+1/2)}\sin[4\Phi(t)]\Big)\,, \tag{8.53}$$

where $\alpha(t)$ and $\Phi(t)$ are given by eqs. (8.23) and (8.24), respectively. I now assume that the gate Rabi frequency Ω_0 is fixed and the optimal detuning ϵ_{gate} and duration t_{gate} have been calculated. The frequencies of the microwave tones have correspondingly been set to $\omega_{\mathrm{r}} = \bar{\omega}_{\uparrow\downarrow} - \nu - \epsilon_{\mathrm{gate}}$ and $\omega_{\mathrm{b}} = \bar{\omega}_{\uparrow\downarrow} + \nu + \epsilon_{\mathrm{gate}}$, where ν

is the value of the mode frequency obtained during calibration. If ν subsequently changes to $\nu + \delta\nu$, the detunings ϵ_{r} and ϵ_{b} will no longer be optimal, but will still be symmetric. If one writes the true detuning as $\epsilon = \epsilon_{\mathrm{gate}} - \delta\nu = \epsilon_{\mathrm{gate}}\,(1 - r_\nu)$, with $r_\nu = \delta\nu/\epsilon_{\mathrm{gate}}$, then the fidelity of an individual pulse may be obtained from expression (8.53). One finds that under these circumstances

$$\left|\alpha(t_{\mathrm{gate}})\right|^2 = \frac{1 - r_\nu}{4K}\sin^2\left[\pi K\,(1 - r_\nu)\right] \tag{8.54}$$

$$4\Phi\left(t_{\mathrm{gate}}\right) = \frac{1}{4K\,(1 - r_\nu)^2}\Big(2\pi K\,(1 - r_\nu) - \sin^2\left[2\pi K\,(1 - r_\nu)\right]\Big)\,. \tag{8.55}$$

Hence it follows that the fidelity depends on $\bar{n}$, K and the relative size of fluctuations r_ν, but not the value of Ω assumed. The gate error decreases with smaller $\bar{n}$ and K.

It remains to introduce a model for the variation of $\delta\nu$ with time. In general, there may be a linear drift in addition to faster changes that appear as random fluctuations from shot to shot of gate pulses. Our calibration routine measures ν via the method discussed in section 7.2.5.3, based on tickling and subsequent probing of the red sideband. One run of this routine takes tens of seconds, which means that it is not straightforward to monitor variations in the motional frequency on the millisecond-timescale. In principle, fluctuations in ν during the routine should result in broadening of the resonance, but the width of the curve is also affected by the strength of the tickling force. The width is therefore only a useful indication if the former contribution dominates. We have not investigated this experimentally in detail so far and therefore I choose a different way to gauge the size of $\delta\nu$. Using the data presented in fig. 7.6, I calculate the mean magnitudes of the changes in ν between consecutive runs of the calibration routine and assume that this provides an upper bound on the rms fluctuations from one gate pulse to the next during the interval between calibration routines. A mean of $\approx 70\,\mathrm{Hz}$ is found.

I take $\delta\nu$ to be normally distributed, with standard deviation $\delta\nu_{\mathrm{rms}}$, and conduct Monte Carlo simulations to estimate the average gate fidelity expected. The results are plotted in fig. 8.7. Each data point corresponds to an average over 10^5 samples. With $\delta\nu_{\mathrm{rms}} = 2\pi \times 70\,\mathrm{Hz}$ and $\epsilon_{\mathrm{gate}} = 2\pi \times 8\,\mathrm{kHz}$, I expect a gate error of $\epsilon \approx 8 \times 10^{-4}$ for a single-loop gate. Note that this translates to a fractional stability of $\delta\nu/\nu =$

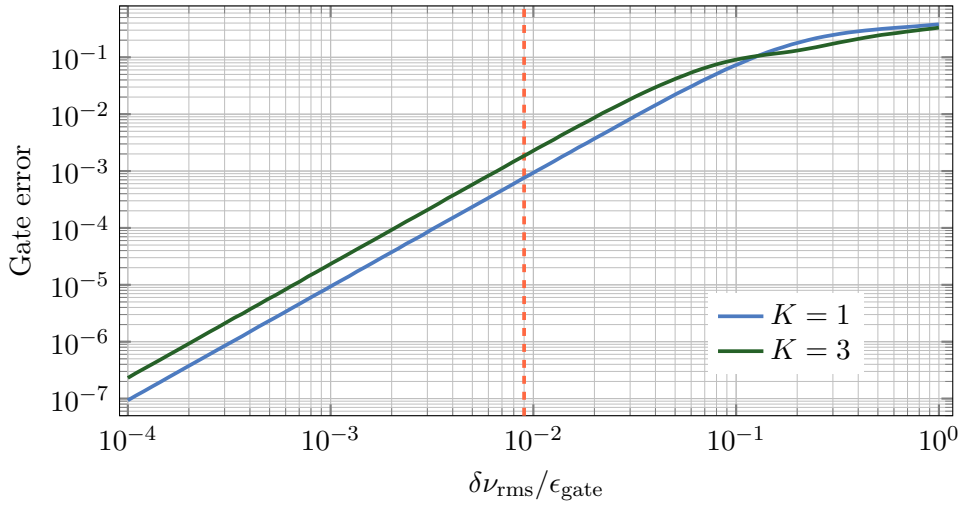


Figure 8.7: Gate error resulting from variations in motional frequency. The parameters Ω, ϵ_{gate} and t_{gate} are kept fixed during simulations. Each data point represents an average over 10^5 samples drawn from a normal distribution with standard deviation $\delta\nu_{\mathrm{rms}}$. The dashed red line indicates the conditions under which we expect our trap to operate.

1.4×10^{-5} for the motional frequency.

8.5.3 Off-resonant excitation on the carrier

During derivation of the ideal gate Hamiltonian $\widetilde{H}_{\mathrm{MS}}$, the effect of the carrier term was neglected on the basis that the microwave tones are near resonance with the motional sidebands. If this contribution is included, one finds that the single-qubit spin flips induced by carrier transitions may lead to reductions in gate fidelity. The microwave tones are detuned from the carrier by $\pm(\nu + \epsilon)$, so the impact of the carrier term may be expected to increase with larger $\Omega_{\mathrm{car}}/\nu$. Since Ω_{car} is in our case proportional to the amplitude of the π-component at the position of the ion, this provides a reason for field nulling.

The contribution from carrier excitation can be found by going back to the general Hamiltonian (8.18). Assuming $\Omega_{\mathrm{car,r}} = \Omega_{\mathrm{car,b}} = \Omega_{\mathrm{car}}$ and $\epsilon_{\mathrm{r}} = \epsilon_{\mathrm{b}} = \epsilon$, it takes the form

$$\widetilde{H}^{(i)}_{\mathrm{car}}(t) = \frac{\hbar}{2}\,\Omega_{\mathrm{car}} \Big(\sigma_x^{(i)} \left[\cos(\delta t - \phi_{\mathrm{car,b}}) + \cos(\delta t + \phi_{\mathrm{car,r}})\right] + \sigma_y^{(i)} \left[\sin(\delta t - \phi_{\mathrm{car,b}}) - \sin(\delta t + \phi_{\mathrm{car,r}})\right] \Big) \tag{8.56}$$

for each ion, where $\delta = \omega - \bar{\omega}_{\downarrow\uparrow}$ as before denotes the detuning from the effective internal transition frequency. Without loss of generality, suppose that the gate is driven in the σ_x basis, which translates to $\phi_\mathrm{s} = 0$ and therefore $\phi_\mathrm{r} = -\phi_\mathrm{b}$. For the carrier term to commute with the gate operation therefore requires $\sin(\delta t - \phi_\mathrm{car,b}) - \sin(\delta t + \phi_\mathrm{car,r}) = 0$ for all t, which can only be satisfied if $\phi_\mathrm{car,r} = -\phi_\mathrm{car,b}$. Taking into account the possibility of a fixed phase difference between carrier and gradient terms, such that $\phi_\mathrm{car,b} = \phi_\mathrm{b} + \Delta\phi$ and $\phi_\mathrm{car,r} = \phi_\mathrm{r} + \Delta\phi$, one finds that the carrier term only commutes with the gate if $\Delta\phi = 0$ or $\Delta\phi = \pi$. In this case, the total time-evolution operator for $\widetilde{H}_\mathrm{gate} + \widetilde{H}_\mathrm{car}$ factors into a part describing the ideal two-qubit gate and a part describing undesired single-qubit rotations for each ion, which lead to fast modulations of the two-qubit gate fidelity [SSB19]. In principle, the strength of the microwaves may be adjusted such that the evolution induced by the carrier reduces to the identity operator at the end of the gate. However, this approach is not robust to fluctuations in microwave power and requires precise pulse timing. Alternatively, the effect of the carrier may be cancelled through controllable single-qubit gates that are applied after the bichromatic field. If $\Delta\phi \notin \{0, \pi\}$, then the carrier term will cause gate errors that cannot be compensated easily and the exact dynamics have to be found by numerically solving the master equation.

I have not yet carried out a detailed investigation of the effects of the carrier term on two-qubit gate fidelity because $\Delta\phi$ is not currently known for our trap. However, to gauge the general relevance of this term, I will for the moment assume that $\widetilde{H}_\mathrm{car}$ and $\widetilde{H}_\mathrm{gate}$ commute, in which case an analytical expression for the gate fidelity may be found [SSB19] as $\mathcal{F} = \cos^4\left[\Omega_\mathrm{car}\sin(\delta t)/(2\delta)\right]$. For our trap parameters, one finds $\Omega_\mathrm{car} = 2\pi \times 7\,\mathrm{MHz}$ on the rf null and $\Omega_\mathrm{car} = 2\pi \times 0.6\,\mathrm{MHz}$ at the position of the minimum in B_π, both of which are not negligible compared to $\nu = 2\pi \times 5\,\mathrm{MHz}$. Without protective measures, the carrier term is therefore expected to have a strong impact on gate dynamics.

8.5.4 Off-resonant driving of spectator modes

When moving from eq. (8.18) to eq. (8.20), the effect of the bichromatic driving field on all motional modes except the one used for the gate operation was ignored.

I will now consider the effects that result when the evolution of spectator modes, which will in general be excited weakly, is taken into account. I will assume that the magnetic field strengths of the red and blue components of the bichromatic driving field are equal and that their frequencies are symmetrically detuned from the motional frequency ν_{gate} of the mode which mediates the gate operation. This means that the detuning ϵ_{s} for a given spectator mode with motional frequency ν_{s} is also symmetric and given by $\epsilon_{\mathrm{s}} = \nu_{\mathrm{gate}} - \nu_{\mathrm{s}} + \epsilon_{\mathrm{gate}}$. The relevant term in the interaction Hamiltonian becomes

$$\frac{\hbar}{2}\,\Omega_{\mathrm{s}}\,S_{\phi,\mathrm{s}}\left(\mathrm{e}^{\mathrm{i}\phi_{\mathrm{m}}}\,\mathrm{e}^{-\mathrm{i}\epsilon_{\mathrm{s}}t}\,a_{\mathrm{s}}^{\dagger} + \mathrm{e}^{-\mathrm{i}\phi_{\mathrm{m}}}\,\mathrm{e}^{\mathrm{i}\epsilon_{\mathrm{s}}t}\,a_{\mathrm{s}}\right). \tag{8.57}$$

The Rabi frequency Ω_{s} is determined by eq. (8.14) and an expression analogous to eq. (8.31). Importantly, Ω_{s} is proportional to the magnitude of the gradient $\partial_{x_{\mathrm{s}}} B_{-q}^{+}(\mathbf{x}_0)$ of the microwave field along the direction of the spectator mode. The collective spin operator $S_{\phi,\mathrm{s}}$ is defined analogous to eq. (8.32) and thus depends on the normal-mode vector $\mathbf{b}_{\mathrm{s}}$ and the single-ion spin operator $\sigma_{\phi,\mathrm{s}}$. The latter is a function of the phase of $\partial_{x_{\mathrm{s}}} B_{-q}^{+}(\mathbf{x}_0)$, which may in general be different from the phase of the gradient $\partial_{x_{\mathrm{gate}}} B_{-q}^{+}(\mathbf{x}_0)$ of the microwave field along the direction of the gate mode. If the spectator mode considered is the remaining mode along the same spatial axis as the gate mode, then $\Omega_{\mathrm{s}} = \Omega_{\mathrm{gate}}$ and $\sigma_{\phi,\mathrm{s}} = \sigma_{\phi,\mathrm{gate}}$, while the spin operators $S_{\phi,\mathrm{s}}$ and $S_{\phi,\mathrm{gate}}$ differ only in the sign of one of the coefficients $b_i^{(p)}$. In this case, $S_{\phi,\mathrm{s}}$ and $S_{\phi,\mathrm{gate}}$ commute. Therefore, the total time-evolution operator for the two-ion system factors into two contributions, one describing the influence of the spin-dependent force on the gate mode and the other describing the influence on the spectator mode, leading to $U(t) = U_{\mathrm{gate}}(t)U_{\mathrm{s}}(t)$. Hence, the two modes evolve independently, such that each individual time-evolution operator $U_m(t)$ is given by an expression which takes the same form as eq. (8.33), but differs in the operators and parameters $\alpha(t)$, $\Phi(t)$ involved. Assuming that duration and detuning of the microwave pulse have been adjusted to the optimal values t_{gate} and ϵ_{gate} for a maximally entangling gate, then $U_{\mathrm{gate}}(t_{\mathrm{gate}}) = \exp\bigl(\pm\mathrm{i}\pi S_{\phi,\mathrm{gate}}^2/8\bigr)$. The contribution $U_{\mathrm{s}}(t)$ thus represents a deviation from the ideal gate Hamiltonian and causes a gate error. The resulting

fidelity may be calculated as $\mathcal{F} = \sum_{n_\mathrm{s},n_\mathrm{s}'} P\left(n_\mathrm{s}\right) \left|\langle n_\mathrm{s}'|\langle\phi(0)|U_\mathrm{s}(t_\mathrm{gate})|\phi(0)\rangle|n_\mathrm{s}\rangle\right|^2$, where n_s denotes the occupation number of the spectator mode. Assuming $|\phi(0)\rangle = |\downarrow\downarrow\rangle$, one finds

$$\mathcal{F} = \frac{1}{8}\Big(3 + \mathrm{e}^{-16|\alpha_\mathrm{s}(t_\mathrm{gate})|^2(\bar{n}_\mathrm{s}+1/2)} + 4\,\mathrm{e}^{-4|\alpha_\mathrm{s}(t_\mathrm{gate})|^2(\bar{n}_\mathrm{s}+1/2)}\cos[4\Phi_\mathrm{s}(t_\mathrm{gate})]\Big)\,. \quad (8.58)$$

Off-resonant excitation of the spectator mode degrades fidelity through residual spin-motion entanglement and accumulation of excess geometric phase. In order to eliminate these error mechanisms, two conditions would have to be met: the loop in phase space of the spectator mode needs to close and the additional geometric phase $4\Phi_\mathrm{s}(t_\mathrm{gate})$ has to be zero or equal a multiple of 2π. The former requirement translates to $\epsilon_\mathrm{s} t_\mathrm{gate} = 2\pi K_\mathrm{s}$, where K_s denotes the integer number of loops traversed. The parameters t_gate and ϵ_gate are fixed properties of the gate mode, which means that ϵ_s can only be adjusted by varying the frequency splitting $\nu_\mathrm{gate} - \nu_\mathrm{s}$ between gate and spectator modes. This may be achieved by changing the strength of the axial confinement slightly. The other requirement cannot be satisfied in practice. By using eq. (8.24) and imposing conditions (8.35) and (8.36) on the gate mode, one may verify that the phase accumulated through evolution of the spectator mode is given by $4\Phi_\mathrm{s}\left(t_\mathrm{gate}\right) = \pi\Omega_\mathrm{s}^2\epsilon_\mathrm{gate}/\left(2\Omega_\mathrm{gate}^2\epsilon_\mathrm{s}\right)$. Since the gate is driven on the mode that features strongest spin-motion coupling and the mode splitting is typically much larger than the gate detuning, one may infer that $\Omega_\mathrm{gate} \geq \Omega_\mathrm{s}$ and $\epsilon_\mathrm{s} \gg \epsilon_\mathrm{gate}$. This means that $4\Phi_\mathrm{s}\left(t_\mathrm{gate}\right) \ll 1$ and the excess phase under these conditions is therefore never a multiple of 2π. To minimise gate error, it is instead necessary to reduce $\Phi_\mathrm{s}\left(t_\mathrm{gate}\right)$ by increasing the difference in frequency between gate and spectator modes.

Let me now apply this analysis to the surface trap used for this work. The two-qubit gate is driven on the radial in-plane rocking mode, while the in-plane centre-of-mass mode represents the spectator mode that is closest in frequency. The out-of-plane modes lie further away and exhibit a much lower Rabi frequency because of the weak microwave gradient along the out-of-plane direction. The error will therefore be dominated by the in-plane centre-of-mass mode, with $\Omega_\mathrm{s} = \Omega_\mathrm{gate} = \Omega_0$.

For each of the following error estimates, I assume that the in-plane centre-of-mass mode has only been Doppler-cooled to $\bar{n}_\mathrm{s} \approx 2$ and its frequency has been adjusted by slightly changing the axial frequency so as to close the loop in its motional phase space at the end of the gate. The gate error then arises purely from the excess geometric phase acquired. It may be suppressed by increasing the frequency splitting between rocking and centre-of-mass modes, which can be achieved by raising the axial frequency. However, this comes at the expense of increasing the error from cross-coupling between modes, as will be discussed in the following section.

For a one-loop gate and an axial frequency of approximately $\nu_z = 2\pi \times 1.1\,\mathrm{MHz}$, corresponding to a mode splitting of $\nu_\mathrm{gate} - \nu_\mathrm{s} = -2\pi \times 123\,\mathrm{kHz}$, an error of $\epsilon \approx 3 \times 10^{-3}$ is found. If the axial frequency is raised to around $\nu_z = 2\pi \times 2\,\mathrm{MHz}$, resulting in a mode splitting of 392 kHz, the error is reduced to $\epsilon \approx 3 \times 10^{-4}$. In both cases, the error approximately doubles if two loops are used for the gate.

8.5.5 Cross-coupling of motional modes

In section 8.1 it was assumed that terms higher than second order in the coordinates for the confining potential and the inter-ionic Coulomb potential could be discarded. As a result, the motion was described by means of decoupled harmonic oscillators, one for each normal mode (see eq. (8.5)). In reality, higher-order terms influence the motion slightly, which may cause gate errors. Both potentials may in general deviate from the quadratic model, but I will assume that the anharmonicity of the confining potential is much smaller than that of the Coulomb potential and will therefore focus on the latter. Since the electrostatic interaction only depends on the relative displacement between ions, not their absolute position in the trap, the Coulomb potential may be expressed purely in terms of the coordinates of those normal modes for which the ions do not all oscillate in phase. In the case of two ions, these are the radial rocking and axial breathing modes. As an important consequence, one may conclude that the Coulomb interaction does not couple the centre-of-mass modes to any other modes and therefore does not lead to errors for gates carried out on a centre-of-mass mode.

For a linear Paul trap with much stronger confinement in the radial plane

than along the trap axis, the additional contributions to the motional Hamiltonian [MSJ03] take the form

$$V^{(3)} = \frac{3M\nu_z^2}{z_0}\left[(q_1^2+q_2^2)q_3 - \frac{2}{3}q_3^3\right] \tag{8.59}$$

$$V^{(4)} = \frac{3M\nu_z^2}{z_0}\left[\frac{1}{4}\left(q_1^2+q_2^2\right)^2 + \frac{2}{3}q_3^4 - 2\left(q_1^2+q_2^2\right)q_3^2\right] . \tag{8.60}$$

Here, I use q_m as short-hand for the normal-mode coordinates $q^{(m,2)}$ of the out-of-phase normal modes along the different spatial axes, while ν_z as before denotes the frequency of the axial centre-of-mass mode and z_0 the equilibrium position of each ion along the trap axis. The radial rocking modes thus couple to the axial breathing mode (to third and fourth order) and also to each other (to fourth order), with a coupling strength that depends on the confinement in the axial direction and varies as $\nu_z^{5/3}$.

As a result of the cross-coupling, the harmonic oscillator eigenstates $|\mathbf{n}\rangle$ are no longer true eigenstates of the modified motional Hamiltonian $H'_{\mathrm{mot}} = H_{\mathrm{mot}} + V^{(3)} + V^{(4)}$, where H_{mot} was given in eq. 8.5. The anharmonicity of the Coulomb potential then mainly causes a shift in the energy levels, which may be interpreted as a change in mode frequencies. The energy corrections may be written $\Delta E = \hbar\chi n_i n_j$, where n_i and n_j represent the occupation numbers of two coupled modes [NRJ09]. This means that the frequency of one mode depends on the occupation number of the other modes. The coefficient for coupling between a radial rocking mode of frequency ν_{r} and the axial breathing mode is found to be

$$\chi_{\mathrm{r-b}} = -\sqrt{3}\nu_z\left[1 + \frac{3\nu_z^2}{2\left(4\nu_{\mathrm{r}}^2 - 3\nu_z^2\right)}\right]\frac{\nu_z}{\nu_{\mathrm{r}}}\left(\frac{2\hbar\nu_z}{\alpha^2 Mc^2}\right)^{1/3} , \tag{8.61}$$

where α denotes the fine-structure constant and c the speed of light. For coupling between the two radial rocking modes, one obtains

$$\chi_{\mathrm{r-r}} = \frac{3}{4}\nu_z\frac{\nu_z^2}{\nu_{\mathrm{r},1}\nu_{\mathrm{r},2}}\left(\frac{2\hbar\nu_z}{\alpha^2 Mc^2}\right)^{1/3} . \tag{8.62}$$

With regards to the Mølmer-Sørensen scheme, cross-coupling causes gate errors

since the exact detuning of the bichromatic field from the gate mode becomes dependent on the occupation numbers of spectator modes during the gate operation, which are random variables. The effective detuning $\delta\nu$ induced by a single spectator mode [Bal14] is given by $\delta\nu = \chi n_\mathrm{s}$. To estimate the resulting gate error, I will assume that n_s follows a thermal distribution with average occupation number $\bar{n}_\mathrm{s}$. The mean shift in mode frequency is accounted for during calibration, but fluctuations of n_s around its mean cannot be compensated. I will take the variance as a measure of the size of these fluctuations, which is given by $\mathrm{Var}(n) = \bar{n}\,(\bar{n}+1)$ for a thermal distribution. The gate error may be calculated in the same way as in section 8.5.2. For small $\delta\nu$, one may find first-order approximations [Bal14] for eqs. (8.53), (8.54) and (8.55), such that the error may be written

$$\epsilon \simeq \frac{2\bar{n}_\mathrm{gate}+1}{8K}\,\bar{n}_\mathrm{s}\,(\bar{n}_\mathrm{s}+1)\,(\chi t_\mathrm{gate})^2 \ . \tag{8.63}$$

It is worth noting that the error is independent of the number of loops since t_gate is proportional to $\sqrt{K}$.

This expression may now be used to estimate the gate error expected in our trap. Assuming radial modes characterised by $\nu_\mathrm{ip,rocking} = 2\pi \times 5\,\mathrm{MHz}$, $\bar{n}_\mathrm{ip,rocking} = 0.1$ and $\nu_\mathrm{oop,rocking} = 2\pi \times 5.5\,\mathrm{MHz}$, $\bar{n}_\mathrm{oop,rocking} = 35$, errors of $\epsilon_\mathrm{r-b} \approx 7\times10^{-4}$ and $\epsilon_\mathrm{r-r} \approx 4\times10^{-5}$ are found for axial parameters $\nu_z = 2\pi \times 1.1\,\mathrm{MHz}$ and $\bar{n}_\mathrm{z,breathing} = 12$. If the axial frequency is increased, such that $\nu_z = 2\pi \times 2\,\mathrm{MHz}$ and $\bar{n}_\mathrm{z,breathing} = 6$, then the errors grow to $\epsilon_\mathrm{r-b} \approx 3\times10^{-3}$ and $\epsilon_\mathrm{r-r} \approx 2\times10^{-3}$.

8.5.6 Off-resonant excitation of internal spectator states

I have so far ignored the influence of other internal atomic states. These were removed via adiabatic elimination in chapter 5, based on the assumption that they receive negligible population when a driving field near-resonant with the target transition is applied. I take the ratio $(\Omega_{ij}/\delta_{ij})^2$ as a measure of the population transferred from the qubit subspace to off-resonant spectator states. Here, Ω_{ij} is the Rabi frequency of a relevant transition and δ_{ij} is the detuning of the microwave fields from the resonance frequency of that transition. For the clock qubit, off-resonant exci-

tation may occur on σ-transitions, which means that Ω_{ij} is determined by the σ^+- and σ^--components of the microwave magnetic field. We find typical Rabi frequencies of 6 MHz and detunings of 100 MHz for our standard trap parameters, which yields $(\Omega_{ij}/\delta_{ij})^2 \approx 4 \times 10^{-3}$. This is only a small fraction of total population and highlights the advantage of operating at higher static magnetic field, where energy splittings between atomic states are larger. As long as any population excited to spectator states returns to the qubit subspace at the end of the gate pulse, which may be achieved through pulse shaping [Roo08; BKR+08], I expect a negligible error contribution.

8.5.7 Heating rate

Heating of the motion during the gate pulse causes errors since loops in phase space may not close even when ϵ_{gate} and t_{gate} are set to the optimal values. Heating may be included in the dynamics [TMK+00] through the master equation

$$\frac{d\rho}{dt} = -\frac{\mathrm{i}}{\hbar}[\widetilde{H}, \rho] + \frac{1}{2}\dot{\bar{n}}\left(2a^\dagger \rho a + 2a\rho a^\dagger - aa^\dagger\rho - a^\dagger a\rho - \rho a^\dagger a - \rho a a^\dagger\right) . \tag{8.64}$$

The simulated fidelity as a function of heating rate is shown in fig. 8.8, obtained via numerical solution of the master equation assuming standard trap parameters. Assuming a heating rate of $\dot{\bar{n}} \approx 5\,\text{quanta}\,\text{s}^{-1}$ for the in-plane rocking mode of two ions, I expect an error contribution of $\epsilon \approx 3 \times 10^{-4}$ for a single loop.

8.5.8 Motional dephasing

Interaction with the environment may cause off-diagonal elements in the motional part of the density matrix to decay. This effect contributes a gate error because disentangling spin and motion relies on the action of the displacement operator, which also depends on off-diagonal elements. Decoherence may be caused by electric field noise, in which case the timescale of the decoherence rate is set by the heating rate [TMK+00]. It may additionally also result from fluctuations in the motional frequency that are fast compared to the duration of a gate pulse. These variations do not change the energy of the system, but cause dephasing between motional

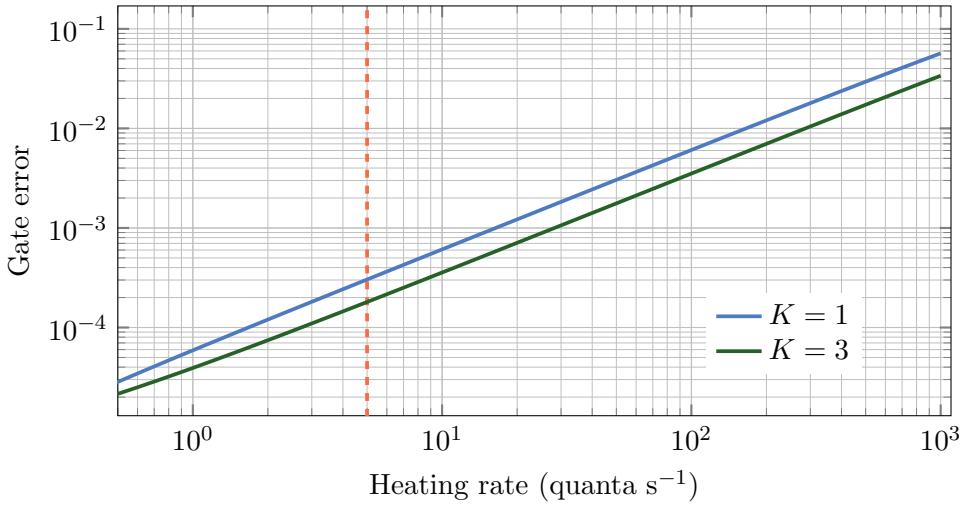


Figure 8.8: Gate error caused by heating of the motional mode used to mediate entanglement. Gate duration and detuning were set to the optimal values for our standard trap parameters. The dashed red line indicates the conditions under which we expect our trap to operate.

states. Following ref. [TMK+00], I model the resulting dynamics through the master equation

$$\frac{d\rho}{dt} = -\frac{\mathrm{i}}{\hbar}[\widetilde{H}, \rho] + \tau_{\mathrm{mot}}^{-1}\left[2a^\dagger a \rho a^\dagger a - (a^\dagger a)^2\rho - \rho(a^\dagger a)^2\right] . \tag{8.65}$$

The motional coherence time τ_{mot} is defined such that off-diagonal elements of the motional part of the density matrix in the Fock state basis decay as $\rho_{ij}(t) = \exp[-(i-j)^2 t/\tau_{\mathrm{mot}}]\,\rho_{ij}(0)$.

The results of numerical simulations assuming our trap parameters are shown in fig. 8.9. Duration and detuning of the gate pulse were set to their optimal values. We have not been able to measure the motional coherence time in our trap yet, but an upper bound is set by the observed heating rate. As an order-of-magnitude estimate, I will take $\tau_{\mathrm{mot}} \approx \dot{\bar{n}}^{-1} = 200\,\mathrm{ms}$. One can also rely on observations made in other experiments as a guideline. In ref. [Sri20], for example, the authors estimate a coherence time of 100 ms to 200 ms in a surface trap of similar dimensions. I would therefore expect an error contribution of $\epsilon \leq 10^{-3}$ in our trap.

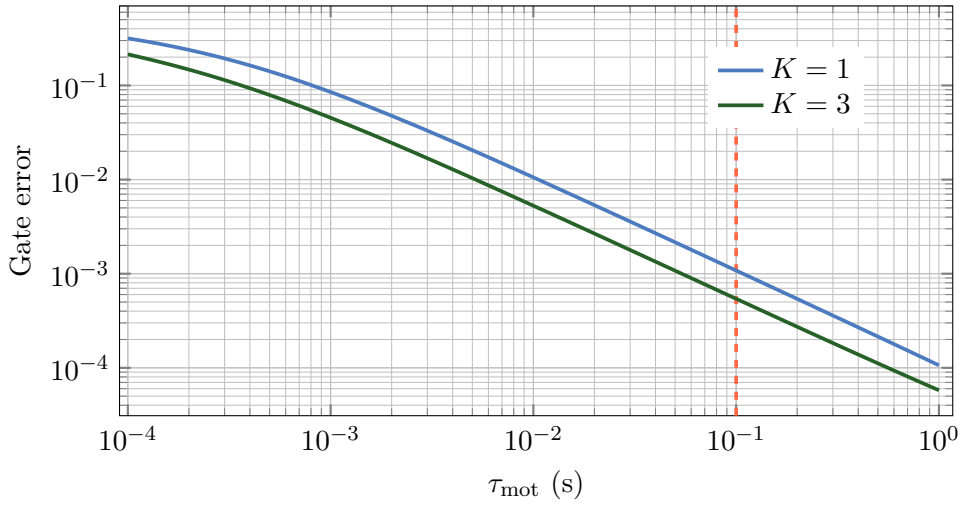


Figure 8.9: Gate error resulting from dephasing between motional states. Gate duration and detuning were set to the optimal values for our standard trap parameters. The dashed red line indicates the conditions under which we expect our trap to operate.

8.5.9 Suppression of gate errors

From the analysis presented in the preceding subsections, I anticipate a total gate error on the order of $\epsilon \approx 7 \times 10^{-3}$ for a basic one-loop Mølmer-Sørensen gate in our trap, excluding the effects of the carrier term. It seems likely that fluctuations in secular frequency, variations in ac Zeeman shift, off-resonant excitation of the spectator mode, cross-coupling between modes and motional dephasing will cause the most important contributions to gate error.

Fortunately, since the original proposal for a phase gate by Mølmer and Sørensen, significant efforts have been made to come up with variations of the basic gate mechanism that offer protection against different sources of error. A detailed discussion of such schemes is beyond the scope of this work, but I point out a number of approaches that might be relevant for future work in our trap. As already evident from the simulations presented earlier, increasing the number of loops reduces the gate errors from motional heating and dephasing. This reduction may, however, be offset by errors from other sources that increase with gate time. It is more efficient to instead consider more complex configurations of driving pulses. They result in more involved trajectories in phase space that cause the qubits to end up closer to the origin at the end of the gate for a given level of noise. Walsh modulation or, more

generally, phase and amplitude modulation of the gate pulse, may reduce the infidelity from symmetric detuning errors (caused by fluctations in motional frequency) [HCD12]. Another important method is provided by the use of more than two tones in the driving field. Depending on the exact implementation, such multi-tone gates can lower infidelities arising from fluctuations in motional frequency, heating and dephasing of the motion, pulse timing errors and also off-resonant excitation on the carrier [WWC18; SSM+18]. Since these approaches mitigate the detrimental effects of detuning fluctuations, they also reduce gate errors from motional cross-coupling. Dynamical decoupling schemes may be used to protect against errors caused by fluctuating ac Zeeman shifts [HSA+16; MRS+17]. Perhaps surprisingly, it is possible to make use of a non-vanishing carrier term to enable decoupling without the use of additional microwave tones [SSB19]. Additionally, pulse shaping provides a way to strongly reduce errors resulting from excitation to internal spectator states and off-resonant driving of the carrier [Roo08; WBD19; SSB19].

The exact amount of error suppression achieved depends on the specific schemes used, the accuracy with which experimental parameters can be controlled and the interplay between different error mechanisms. For the particular source of error addressed, improvements by more than an order of magnitude may in theory be obtained for some schemes. If one therefore tentatively assumes that the overall gate infidelity may be reduced by an order of magnitude through use of suitable methods for error mitigation, then an error of a few 10^{-4} may possibly be reached in future experiments in our trap. Since an infidelity of 10^{-4} is often quoted as a stringent threshold for the feasibility of quantum error correction, this would represent a significant step in this direction.

Chapter 9

Conclusions

We have demonstrated use of a new hyperfine qubit for trapped-ion quantum logic, formed by the states $|4,+1\rangle$ and $|3,+1\rangle$ in the ground level of $^{43}Ca^{+}$ at a static magnetic field of 28.8 mT. The corresponding transition frequency is confirmed to be to first order independent of fluctuations in the quantisation field. Despite the complex atomic structure of this isotope in the intermediate-field regime, we have succeeded in cooling a single ion to temperatures close to the Doppler limit expected for a two-state system by exploiting the strong variation of fluorescence in the vicinity of a dark resonance. We achieve an average occupation number of $\bar{n}_{\mathrm{ip}} \approx 1.3$ for the radial in-plane mode of a single ion, corresponding to a temperature of 0.5 mK. For the radial in-plane rocking mode of two ions, which is the mode used for two-qubit gates, we measure $\bar{n}_{\mathrm{ip,rocking}} \approx 2$, with secular frequencies around 5 MHz. Through resolved-sideband cooling with a laser-driven Raman transition, we are able to reduce the vibrational energies further to $\bar{n}_{\mathrm{ip}} \approx 0.1$ and $\bar{n}_{\mathrm{ip,rocking}} \approx 0.08$, respectively. These low average occupation numbers should strongly reduce the impact of certain errors during two-qubit operations that rely on transient excitation of the collective motion.

The qubit states may be coupled directly by a microwave magnetic field to drive single- and two-qubit gates, both of which we have implemented in a surface trap suitable for operation at cryogenic temperatures. The trap chip features a novel design that achieves a strong gradient, but low amplitude in the π-component of the microwave field by integrating a single U-shaped microwave electrode. These

properties are desirable for two-qubit entangling operations based on the Mølmer-Sørensen scheme chosen for this work. We have characterised key parameters of the trap at different operating temperatures, in particular heating rates, ion lifetimes and the spatial dependence of the microwave magnetic field. In measurements with a single ion, we observe no clear trend in heating rate with temperature, inferring a typical noise spectral density on the order of $S_{\mathrm{e}}(\nu) = 1 \times 10^{-11}\,\mathrm{V^2\,m^{-2}\,Hz^{-1}}$ at $\nu = 2\pi \times 5.2\,\mathrm{MHz}$. For the heating rate of the in-plane rocking mode of two ions, which is the parameter that is more directly relevant to the anticipated performance of two-qubit gates, we find $\dot{\bar{n}}_{\mathrm{ip,rocking}} = 3(2)\,\mathrm{quanta\,s^{-1}}$ at a temperature around 20 K. One of the main benefits of cryogenic operation lies in the vastly reduced background pressure, which in our trap increases the average lifetime of a two-ion crystal from approximately four minutes at room temperature to one hour at 20 K.

We have determined the spatial variation of the π-component of the microwave magnetic field along the horizontal axis by means of Rabi flopping on the carrier transition and find that the field amplitude is a strong function of position, reaching a minimum at a distance of 4.4 µm to 5.7 µm from the rf null, slightly dependent on temperature. The observed location of the minimum deviates significantly from the target position expected from the trap design, which we believe to be caused by accidental resonances of currents induced in the rf electrodes. Nevertheless, the trap generates a strong field gradient, measured as $39\,\mathrm{T\,m^{-1}}$ at a temperature of 20 K for a microwave input power of 1 W.

Building on the results of characterisation experiments, we have created a spin-dependent force according to the Mølmer-Sørensen scheme via two microwave tones oscillating near the qubit frequency and used it to entangle internal and centre-of-mass degrees of freedom of a single ion. Furthermore, we have applied the same force to two ions for an initial implementation of a $\sigma_\phi \otimes \sigma_\phi$ gate, obtaining a fidelity of $\mathcal{F} = 0.77(2)$. This represents only the beginning of two-qubit gate experiments in our trap and we expect the fidelity to increase significantly once a number of hardware improvements have been made. I have therefore performed simulations of gate errors predicted for operating conditions that we believe to be within reach of our apparatus. Based on this analysis, I speculate that by employing more complex

pulse sequences in future experiments errors in the low 10^{-4} range may be possible.

9.1 Comparison with other experiments

Given that work on two-qubit experiments in our trap has only just started, it is not very informative to compare the fidelity achieved in our initial attempt to the state of the art in laser-free quantum logic. As far as raw numbers are concerned, the introductory chapter may be consulted. I do note, however, that our fidelity is similar to that obtained in the original demonstration of two-qubit entanglement via a spin-dependent force generated by microwaves [OWC+11].

Since a large part of this work is concerned with the characterisation of our cryogenic surface trap, it is probably more useful to relate two key parameters of our trap chip, the heating rate and microwave magnetic field, to results obtained in other experiments. Regarding heating rates, we can make a comparison between the spectral density of field noise measured in our trap and fig. 8 of ref. [BKR+15]. The plot presented there primarily used data for a motional frequency of 1 MHz. Assuming $1/f$ scaling for the frequency dependence of noise, we estimate $S_\mathrm{e} \approx 5 \times 10^{-11}\,\mathrm{V^2\,m^{-2}\,Hz^{-1}}$ at $\nu = 2\pi \times 1\,\mathrm{MHz}$ in our trap. Taking into account our ion height of $d = 40\,\mu\mathrm{m}$, we conclude that electric field noise in our trap is approximately equal to the average observed for traps of similar size. One big difference, however, is the behaviour as a function of operating temperature. We observe no clear scaling of noise density with temperature, which likely indicates that the heating rate in our trap is currently not dominated by anomalous heating or thermal noise on the trap electrodes, but rather technical noise caused by other parts of the apparatus. We have already invested significant effort in eliminating technical noise and at this point there is no obvious candidate for its source.

As far as the microwave magnetic field is concerned, it is worth comparing the field gradient achieved in our trap to other experiments that used a gradient oscillating near the qubit frequency. I have compiled relevant data in table 9.1. Where possible, I have normalised parameters to 1 W of input power to the trap. From the data provided it is clear that, accounting for ion height, the surface trap described

Ion height (µm)	Frequency (GHz)	Gradient ($\mathrm{T\,m^{-1}}$)	Reference
30	1.7	35*	[OWC+11]
70	1.1	8	[ZHM+19; Hah19]
35	1.1	40	[Hah19]
75	3.2	4	[Sep16]
40	3.1	39	this work

Table 9.1: Field gradients observed in experiments using a gradient oscillating near the qubit frequency for two-qubit entangling operations. Where possible, values have been normalised to 1 W of input power to the trap. For ref. [OWC+11], the input power was not provided in the publication, the quoted gradient is therefore the bare value without scaling. The multi-layer trap of ref. [Hah19] exhibited a strong field gradient, but as far as we can tell from published information, no two-qubit gate has been demonstrated in that apparatus.

in this work offers the highest near-qubit-frequency gradient observed so far in any single-layer trap. I point out in particular that the gradient obtained in our trap is an order of magnitude larger than the gradient measured in the previous generation of microwave trap used in our group [Sep16]. This underscores the advantage of reduced ion height, modified trap geometry and operation at cryogenic temperatures. We therefore expect to be able to drive two-qubit gate operations with significantly higher speed and believe that a gate duration of a few hundreds of microseconds should be possible.

9.2 Outlook

The near-term goal lies in achieving high-fidelity two-qubit entangling operations in our trap, using pulse durations on the order of a few hundred microseconds. This would put microwave-driven gates closer to the speeds obtained with traditional laser-driven gates. Ultimately, the gate speed will be limited by the microwave power that may be applied without breaking the trap. In experiments with a trap chip that had previously been used in our apparatus, we found that at a temperature of 80 K no damage occurred up to a total microwave input power of 16 W, which was the maximum that could be generated at the time. If I assume that more power may safely be dissipated at lower temperatures, it might be possible to use a power of up to 10 W in each microwave tone at 20 K, which would enable the trap to produce field gradients of more than $100\,\mathrm{T\,m^{-1}}$. This would lead to a further improvement in gate speed. In order to achieve errors below 10^{-3}, it will be necessary to use more complex gate schemes. This will likely mean trading gate speed for fidelity, but increases in gate duration for many methods of error mitigation are predicted to be modest. We are therefore confident that microwave-driven gates will continue on their path towards fault-tolerant quantum computing in ion traps.

Bibliography

[ABG+94] F. Arbes, M. Benzing, T. Gudjons et al. "Precise determination of the ground state hyperfine structure splitting of ^{43}Ca II". *Zeitschrift für Physik D Atoms, Molecules and Clusters* 31 (1994), pp. 27–30.

[AIV77] E. Arimondo, M. Inguscio and P. Violino. "Experimental determinations of the hyperfine structure in the alkali atoms". *Reviews of Modern Physics* 49 (1977), p. 31.

[ANK+15] N. Akerman, N. Navon, S. Kotler et al. "Universal gate-set for trapped-ion qubits using a narrow linewidth diode laser". *New Journal of Physics* 17 (2015), p. 113060.

[Arm71] L. Armstrong. *Theory of the Hyperfine Structure of Free Atoms*. New York: Wiley-Interscience, 1971.

[Bal14] C. J. Ballance. "High-fidelity quantum logic in Ca^+". PhD thesis. University of Oxford, 2014.

[BB02] D. J. Berkeland and M. G. Boshier. "Destabilization of dark states and optical spectroscopy in Zeeman-degenerate atomic systems". *Physical Review A* 65 (2002), p. 033413.

[BBC+95] A. Barenco, C. H. Bennett, R. Cleve et al. "Elementary gates for quantum computation". *Physical Review A* 52 (1995), p. 3457.

[BDD+02] M. J. Bremner, C. M. Dawson, J. L. Dodd et al. "Practical Scheme for Quantum Computation with Any Two-Qubit Entangling Gate". *Physical Review Letters* 89 (2002), p. 247902.

[BGN+18] T. G. Ballance, J. F. Goodwin, B. Nichol et al. "A short response time atomic source for trapped ion experiments". *Review of Scientific Instruments* 89 (2018), p. 053102.

[BHL+16] C. J. Ballance, T. P. Harty, N. M. Linke et al. "High-Fidelity Quantum Logic Gates Using Trapped-Ion Hyperfine Qubits". *Physical Review Letters* 117 (2016), p. 060504.

[BKR+07] J. Benhelm, G. Kirchmair, U. Rapol et al. "Measurement of the hyperfine structure of the $S_{1/2} - D_{5/2}$ transition in $^{43}Ca^+$". *Physical Review A* 75 (2007), p. 032506.

[BKR+08] J. Benhelm, G. Kirchmair, C. Roos et al. "Towards fault-tolerant quantum computing with trapped ions". *Nature Physics* 4 (2008), pp. 463–466.

[BKR+15] M. Brownnutt, M. Kumph, P. Rabl et al. "Ion-trap measurements of electric-field noise near surfaces". *Reviews of Modern Physics* 87 (2015), p. 1419.

[BMB+98] D. J. Berkeland, J. D. Miller, J. C. Bergquist et al. “Minimization of ion micromotion in a Paul trap”. *Journal of Applied Physics* 83 (1998), p. 5025.

[BP03] S. Brouard and J. Plata. “Internal-state dephasing of trapped ions”. *Physical Review A* 68 (2003), p. 012311.

[BSM+17] A. Bermudez, P. Schindler, T. Monz et al. “Micromotion-enabled improvement of quantum logic gates with trapped ions”. *New Journal of Physics* 19 (2017), p. 113038.

[Bur10] A. Burrell. “High fidelity readout of trapped ion qubits”. PhD thesis. University of Oxford, 2010.

[BXN+17] A. Bermudez, X. Xu, R. Nigmatullin et al. “Assessing the Progress of Trapped-Ion Processors Towards Fault-Tolerant Quantum Computation”. *Physical Review X* 7 (2017), p. 041061.

[CBK+09] M. Chwalla, J. Benhelm, K. Kim et al. “Absolute Frequency Measurement of the $^{40}Ca^{+}$ $4s\,^2S_{1/2}-3d\,^2D_{5/2}$ Clock Transition”. *Physical Review Letters* 102 (2009), p. 023002.

[CBZ+92] J. I. Cirac, R. Blatt, P. Zoller et al. “Laser cooling of trapped ions in a standing wave”. *Physical Review A* 46 (1992), p. 2668.

[CG69] K. E. Cahill and R. J. Glauber. “Ordered Expansions in Boson Amplitude Operators”. *Physical Review* 177 (1969), p. 1857.

[Chi06] C. Chicone. *Ordinary Differential Equations with Applications*. New York: Springer, 2006.

[CLS17] D. P. L. Aude Craik, N. M. Linke and M. A. Sepiol. “High-fidelity spatial and polarization addressing of $^{43}Ca^{+}$ qubits using near-field microwave control”. *Physical Review A* 95 (2017), p. 022337.

[CN65] P. Carruthers and M. M. Nieto. “Coherent States and the Forced Quantum Oscillator”. *American Journal of Physics* 33 (1965), p. 537.

[CTS+21] C. R. Clark, H. N. Tinkey, B. C. Sawyer et al. “High-Fidelity Bell-State Preparation with $^{40}Ca^{+}$ Optical Qubits”. *Physical Review Letters* 127 (2021), p. 130505.

[CZ95] J. I. Cirac and P. Zoller. “Quantum Computations with Cold Trapped Ions”. *Physical Review Letters* 74 (1995), p. 4091.

[Deh68] H. G. Dehmelt. “Radiofrequency Spectroscopy of Stored Ions I: Storage”. *Advances in Atomic and Molecular Physics* 3 (1968), pp. 53–72.

[DHK+83] R. W. P. Drever, J. L. Hall, F. V. Kowalski et al. “Laser phase and frequency stabilization using an optical resonator”. *Applied Physics B* 31 (1983), pp. 97–105.

[DiV00] D. P. DiVincenzo. “The Physical Implementation of Quantum Computation”. *Fortschritte der Physik* 48 (2000), pp. 771–783.

[DMD+13] M. W. Doherty, N. B. Manson, P. Delaney et al. “The nitrogen-vacancy colour centre in diamond”. *Physics Reports* 528 (1 2013), pp. 1–46.

[EMS+03] J. Eschner, G. Morigi, F. Schmidt-Kaler et al. "Laser cooling of trapped ions". *Journal of the Optical Society of America B* 20 (5 2003), pp. 1003–1015.

[Fey82] R. Feynman. "Quantum simulation". *International Journal of Theoretical Physics* 21 (6 1982), p. 467.

[FMM+12] A. G. Fowler, M. Mariantoni, J. M. Martinis et al. "Surface codes: towards practical large-scale quantum computation". *Physical Review A* 86 (2012), p. 032324.

[GAN14] I. M. Georgescu, S. Ashhab and F. Nori. "Quantum simulation". *Reviews of Modern Physics* 86 (2014), p. 153.

[GCS17] J. M. Gambetta, J. M. Chow and M. Steffen. "Building logical qubits in a superconducting quantum computing system". *npj Quantum Information* 3 (2017), p. 2.

[Gho95] P. K. Ghosh. *Ion traps*. Oxford: Clarendon Press, 1995.

[GKZ+08] R. Gerritsma, G. Kirchmair, F. Zähringer et al. "Precision measurement of the branching fractions of the $4p\,^2\mathrm{P}_{3/2}$ decay of Ca II". *European Physical Journal D* 50 (2008), pp. 13–19.

[Gla92] R. J. Glauber. "Laser Manipulation of Atoms and Ions". Ed. by E. Arimondo, W. D. Phillips and F. Strumia. 1992, p. 643.

[Gro22] Oxford Ion Trap Group. 2022. URL: `https://github.com/OxfordIonTrapGroup/Squareatron-5000`.

[GTL+16] J. P. Gaebler, T. R. Tan, Y. Lin et al. "High-Fidelity Universal Gate Set for $^9\mathrm{Be}^+$ Ion Qubits". *Physical Review Letters* 117 (2016), p. 060505.

[HAB+14] T. P. Harty, D. T. C. Allcock, C. J. Ballance et al. "High-Fidelity Preparation, Gates, Memory, and Readout of a Trapped-Ion Quantum Bit". *Physical Review Letters* 113 (2014), p. 220501.

[Hah19] H. Hahn. "Two-qubit microwave quantum logic gate with $^9\mathrm{Be}^+$ ion in scalable surface-electrode ion traps". PhD thesis. Leibniz University Hannover, 2019.

[Har13] T. P. Harty. "High-fidelity microwave-driven quantum logic in intermediate-field $^{43}\mathrm{Ca}^+$". PhD thesis. University of Oxford, 2013.

[HBD+05] P. C. Haljan, K.-A. Brickman, L. Deslauriers et al. "Spin-Dependent Forces on Trapped Ions for Phase-Stable Quantum Gates and Entangled States of Spin and Motion". *Physical Review Letters* 94 (2005), p. 153602.

[HCD12] D. Hayes, S. M. Clark and S. Debnath. "Coherent Error Suppression in Multiqubit Entangling Gates". *Physical Review Letters* 109 (2012), p. 020503.

[HGR03] H. Häffner, S. Gulde and M. Riebe. "Precision Measurement and Compensation of Optical Stark Shifts for an Ion-Trap Quantum Processor". *Physical Review Letters* 90 (2003), p. 143602.

[Hom06] J. Home. "Entanglement trapped ions". PhD thesis. University of Oxford, 2006.

[Hou08] M. G. House. “Analytic model for electrostatic fields in surface-electrode ion traps”. *Physical Review A* 78 (2008), p. 033402.

[HRK15] M. Hettrich, T. Ruster and H. Kaufmann. “Measurement of Dipole Matrix Elements with a Single Trapped Ion”. *Physical Review Letters* 115 (2015), p. 143003.

[HSA+16] T. P. Harty, M. A. Sepiol, D. T. C. Allcock et al. “High-Fidelity Trapped-Ion Quantum Logic Using Near-Field Microwaves”. *Physical Review Letters* 117 (2016), p. 140501.

[HZB+19] H. Hahn, G. Zarantonello, A. Bautista-Salvador et al. “Multilayer ion trap with three-dimensional microwave circuitry for scalable quantum logic applications”. *Applied Physics B* 125 (2019), p. 154.

[Jam98] D.F.V. James. “Quantum dynamics of cold trapped ions, with application to quantum computation”. *Applied Physics B* 66 (1998), pp. 181–190.

[Jan15] H. Janacek. “Optical Bloch equations for simulating trapped-ion qubits”. PhD thesis. University of Oxford, 2015.

[JBT+09] M. Johanning, A. Braun, N. Timoney et al. “Individual Addressing of Trapped Ions and Coupling of Motional and Spin States Using rf Radiation”. *Physical Review Letters* 102 (2009), p. 073004.

[JY93] J. Javanainen and S. M. Yoo. “Semiclassical laser-cooling theory for a trapped multistate ion”. *Physical Review A* 48 (1993), p. 3776.

[KAN+14] S. Kotler, N. Akerman, N. Navon et al. “Measurement of the magnetic interaction between two bound electrons of two separate ions”. *Nature* 510 (2014), pp. 376–380.

[KLR+08] E. Knill, D. Leibfried, R. Reichle et al. “Randomized benchmarking of quantum gates”. *Physical Review A* 77 (2008), p. 012307.

[KMW02] D. Kielpinski, C. Monroe and D. J. Wineland. “Architecture for a large-scale ion-trap quantum computer”. *Nature* 417 (2002), pp. 709–711.

[Kni05] E. Knill. “Quantum computing with realistically noisy devices”. *Nature* 434 (2005), pp. 39–44.

[KPB+15] J. Keller, H. L. Partner, T. Burgermeister et al. “Precise determination of micromotion for trapped-ion optical clocks”. *Journal of Applied Physics* 118 (2015), p. 104501.

[KPS12] A. Khromova, Ch. Piltz and B. Scharfenberger. “Designer Spin Pseudomolecule Implemented with Trapped Ions in a Magnetic Gradient”. *Physical Review Letters* 108 (2012), p. 220502.

[Kra20] A. Kramida. “Isotope shifts in neutral and singly-ionized calcium”. *Atomic Data and Nuclear Data Tables* 133-134 (2020), p. 101322.

[LBM+03] D. Leibfried, R. Blatt, C. Monroe et al. “Quantum dynamics of single trapped ions”. *Reviews of Modern Physics* 75 (2003), p. 281.

[LDR+12] H. Landa, M. Drewsen, B. Reznik et al. “Classical and quantum modes of coupled Mathieu equations”. *Journal of Physics A* 45 (2012), p. 455305.

[LGR04] V. Letchumanan, P. Gill and E. Riis. “Optical Ramsey spectroscopy of a single trapped $^{88}Sr^{+}$ ion”. *Physical Review A* 70 (2004), p. 033419.

[LJL+10] T. D. Ladd, F. Jelezko, F. Laflamme et al. “Quantum computers”. *Nature* 464 (2010), pp. 45–53.

[LRH+04] D. M. Lucas, A. Ramos, J. P. Home et al. “Isotope-selective photoionization for calcium ion trapping”. *Physical Review A* 69 (2004), p. 012711.

[LWR+15] K. Lake, S. Weidt, J. Randall et al. “Generation of spin-motion entanglement in a trapped ion using long-wavelength radiation”. *Physical Review A* 91 (2015), p. 012319.

[Mag54] W. Magnus. “On the exponential solution of differential equations for a linear operator”. *Communications on Pure and Applied Mathematics* 7 (1954), pp. 649–673.

[MBM+16] K. K. Mehta, C. D. Bruzewicz, R. McConnell et al. “Integrated optical addressing of an ion qubit”. *Nature Nanotechnology* 11 (2016), pp. 1066–1070.

[MMK+95] C. Monroe, D. M. Meekhof, B. E. King et al. “Demonstration of a Fundamental Quantum Logic Gate”. *Physical Review Letters* 75 (1995), p. 4714.

[MRR+14] C. Monroe, R. Raussendorf, A. Ruthven et al. “Large-scale modular quantum-computer architecture with atomic memory and photonic interconnects”. *Physical Review A* 89 (2014), p. 022317.

[MRS+17] T. Manovitz, A. Rotem, R. Shaniv et al. “Fast Dynamical Decoupling of the Mølmer-Sørensen Entangling Gate”. *Physical Review Letters* 119 (2017), p. 220505.

[MS99] K. Mølmer and A. Sørensen. “Multiparticle Entanglement of Hot Trapped Ions”. *Physical Review Letters* 82 (1999), p. 1835.

[MSJ03] C. Marquet, F. Schmidt-Kaler and D. F. V. James. “Phonon-phonon interactions due to non-linear effects in a linear ion trap”. *Applied Physics B* 199-208 (2003).

[MSS+20] Z. Meir, M. Sinhal, M. Safronova et al. “Combining experiments and relativistic theory for establishing accurate radiative quantities in atoms: The lifetime of the $^2P_{3/2}$ state in $^{40}Ca^{+}$”. *Physical Review A* 101 (2020), p. 012509.

[MTT19] B. Merkel, K. Thirumalai and J. E. Tarlton. “Magnetic field stabilization system for atomic physics experiments”. *Review of Scientific Instruments* 90 (2019), p. 044702.

[MW01] F. Mintert and C. Wunderlich. “Ion-Trap Quantum Logic Using Long-Wavelength Radiation”. *Physical Review Letters* 87 (2001), p. 257904.

[NBI+98] W. Nörtershäuser, K. Blaum, K. Icker et al. “Isotope shifts and hyperfine structure in the $3d\,^2D_J \rightarrow 4p\,^2P_J$ transitions in calcium II”. *The European Physical Journal D* 2 (1998), pp. 33–39.

[NRJ09] X. R. Nie, C. F. Roos and D. F. V. James. “Theory of cross phase modulation for the vibrational modes of trapped ions”. *Physics Letters A* 373 (4 2009), pp. 422–425.

[NSD86] W. Nagourney, J. Sandberg and H. Dehmelt. “Shelved optical electron amplifier: Observation of quantum jumps”. *Physical Review Letters* 56 (1986), p. 2797.

[OIB+07] R. Ozeri, W. M. Itano, R. B. Blakestad et al. “Errors in trapped-ion quantum gates due to spontaneous photon scattering”. *Physical Review A* 75 (2007), p. 042329.

[OLA+08] C. Ospelkaus, C. E. Langer, J. M. Amini et al. “Trapped-Ion Quantum Logic Gates Based on Oscillating Magnetic Fields”. *Physical Review Letters* 101 (2008), p. 090502.

[OWC+11] C. Ospelkaus, U. Warring, Y. Colombe et al. “Microwave quantum logic gates for trapped ions”. *Nature* 476 (2011), pp. 181–184.

[PCZ97] J. F. Poyatos, J. I. Cirac and P. Zoller. “Complete Characterization of a Quantum Process: The Two-Bit Quantum Gate”. *Physical Review Letters* 78 (1997), p. 390.

[PFA+21] E. Pelucchi, G. Fagas, I. Aharonovich et al. “The potential and global outlook of integrated photonics for quantum technologies”. *Nature Reviews Physics* (2021).

[PM21] S. Pezzagna and J. Meijer). “Quantum computer based on color centers in diamond”. *Applied Physics Reviews* 8 (2021), p. 011308.

[Poz11] D. M. Pozar. *Microwave engineering*. Wiley Global Education, 2011.

[Pre98] J. Preskill. “Reliable quantum computers”. *Proceedings of the Royal Society A* 454 (1969 1998).

[PSV+14] C. Piltz, T. Sriarunothai, A. F. Varon et al. “A trapped-ion-based quantum byte with 10^{-5} next-neighbour cross-talk”. *Nature Communications* 5 (2014), p. 4679.

[Ram50] N. F. Ramsey. “A Molecular Beam Resonance Method with Separated Oscillating Fields”. *Physical Review* 78 (1950), p. 695.

[RLB96] D. Reiß, A. Lindner and R. Blatt. “Cooling of trapped multilevel ions: A numerical analysis”. *Physical Review A* 54 (1996), p. 5133.

[Roo08] C. Roos. “Ion trap quantum gates with amplitude-modulated laser beams”. *New Journal of Physics* 10 (2008), p. 013002.

[RPK+13] M. Ramm, T. Pruttivarasin, M. Kokish et al. “Precision Measurement Method for Branching Fractions of Excited $P_{1/2}$ States Applied to $^{40}Ca^{+}$”. *Physical Review Letters* 111 (2013), p. 023004.

[Saf16] M. Saffman. “Quantum computing with atomic qubits and Rydberg interactions: progress and challenges”. *Journal of Physics B: Atomic, Molecular and Optical Physics* 49 (2016), p. 202001.

[SBK+21] R. Srinivas, S. C. Burd, H. M. Knaack et al. “High-fidelity laser-free universal control of trapped ion qubits”. *Nature* 597 (2021), pp. 209–213.

[SBS+19] R. Srinivas, S. C. Burd, R. T. Sutherland et al. “Trapped-Ion Spin-Motion Coupling with Microwaves and a Near-Motional Oscillating Magnetic Field Gradient”. *Physical Review Letters* 122 (2019), p. 163201.

[SD02] P. Staanum and M. Drewsen. “Trapped-ion quantum logic utilizing position-dependent ac Stark shifts”. *Physical Review A* (2002), 040302(R).

[Sep16] M. Sepiol. “A high-fidelity microwave driven two-qubit quantum logic gate in $^{43}Ca^{+}$”. PhD thesis. University of Oxford, 2016.

[SHG+16] H. Shao, Y. Huang, H. Guan et al. “Precision measurement of the $3d^2D_{3/2}$-state lifetime in a single trapped $^{40}Ca^{+}$”. *Physical Review A* 94 (2016), p. 042507.

[SHG+17] H. Shao, Y. Huang, H. Guan et al. “Precise determination of the quadrupole transition matrix element of $^{40}Ca^{+}$ via branching-fraction and lifetime measurements”. *Physical Review A* 95 (2017), p. 053415.

[Sho90] B. Shore. *The Theory of Coherent Atomic Excitation, Volume 1, Simple Atoms and Fields*. New York: Wiley-Interscience, 1990.

[Sho95] P. W. Shor. “Scheme for reducing decoherence in quantum computer memory”. *Physical Review A* 52 (1995), R2493(R).

[SHR+03] F. Schmidt-Kaler, H. Häffner, M. Riebe et al. “Realization of the Cirac-Zoller controlled-NOT quantum gate”. *Nature* 422 (2003), pp. 408–411.

[Sin22] Sinara. 2022. URL: `https://github.com/sinara-hw`.

[SKK+00] C. A. Sackett, D. Kielpinski, B. E. King et al. “Experimental entanglement of four particles”. *Nature* 404 (2000), pp. 256–259.

[SM00] A. Sørensen and K. Mølmer. “Entanglement and quantum computation with ions in thermal motion”. *Physical Review A* 62 (2000), p. 022311.

[SO12] F. A. Shaikh and A. Ozakin. “Stability analysis of ion motion in asymmetric planar ion traps”. *Journal of Applied Physics* 112 (2012), p. 074904.

[SP19] S. Slussarenko and G. J. Pryde. “Photonic quantum information processing: A concise review”. *Applied Physics Reviews* 6 (2019), p. 041303.

[Sri20] R. Srinivas. “Laser-free trapped-ion quantum logic with a radiofrequency magnetic field gradient”. PhD thesis. University of Colorado, Boulder, 2020.

[SSB19] R. T. Sutherland, R. Srinivas and S. C. Burd. “Versatile laser-free trapped-ion entangling gates”. *New Journal of Physics* 21 (2019), p. 033033.

[SSM+18] Y. Shapira, R. Shaniv, T. Manovitz et al. “Robust Entanglement Gates for Trapped-Ion Qubits”. *Physical Review Letters* 121 (2018), p. 180502.

[Ste19] L. J. Stephenson. “Entanglement between nodes of a quantum network”. PhD thesis. University of Oxford, 2019.

[Ste85] S. Stenholm. “Dynamics of trapped particle cooling in the Lamb-Dicke limit”. *Journal of the Optical Society of America B* 2 (11 1985), pp. 1743–1750.

[Ste86] S. Stenholm. "The semiclassical theory of laser cooling". *Reviews of Modern Physics* 58 (1986), p. 699.

[Ste96] A. Steane. "Multiple-particle interference and quantum error correction". *Proceedings of the Royal Society A* 452 (1996), p. 1954.

[SVN+91] R. E. Silverans, L. Vermeeren, R. Neugart et al. "Hyperfine structure constants of the CaII states $4s^2S_{1/2}$ and $4p^2P_{1/2,3/2}$ and the nuclear quadrupole moment of ^{43}Ca". *Zeitschrift für Physik D Atoms, Molecules and Clusters* 18 (1991), pp. 351–356.

[SWM10] M. Saffman, T. G. Walker and K. Mølmer. "Quantum information with Rydberg atoms". *Reviews of Modern Physics* 82 (2010), p. 2313.

[Szw09] D. Szwer. "High fidelity readout and protection of a $^{43}Ca^+$ ion". PhD thesis. University of Oxford, 2009.

[TBJ+11] N. Timoney, I. Baumgart, M. Johanning et al. "Quantum gates and memory using microwave-dressed states". *Nature* 476 (2011), pp. 185–188.

[TMK+00] Q. A. Turchette, C. J. Myatt, B. E. King et al. "Decoherence and decay of motional quantum states of a trapped atom coupled to engineered reservoirs". *Physical Review A* 62 (2000), p. 053807.

[TPR+03] G. Tommaseo, T. Pfeil, G. Revalde et al. "The g_J-factor in the ground state of Ca^+". *The European Physical Journal D - Atomic, Molecular, Optical and Plasma Physics* 25 (2003), pp. 113–121.

[TWK+98] Q. A. Turchette, C. S. Wood, B. E. King et al. "Deterministic Entanglement of Two Trapped Ions". *Physical Review Letters* 81 (1998), p. 3631.

[WBD19] K. Wright, K. M. Beck and S. Debnath. "Benchmarking an 11-qubit quantum computer". *Nature Communications* 10 (2019), p. 5464.

[Web22] M. Weber. "to be published". PhD thesis. University of Oxford, 2022.

[Wen17] G. Wendin. "Quantum information processing with superconducting circuits: a review". *Reports on Progress in Physics* 80 (2017), p. 106001.

[WHZ17] M. Wahnschaffe, H. Hahn and G. Zarantonello. "Single-ion microwave near-field quantum sensor". *Applied Physics Letters* 110 (2017), p. 034103.

[WLG+09] S. X. Wang, J. Labaziewicz, Y. Ge et al. "Individual addressing of ions using magnetic field gradients in a surface-electrode ion trap". *Applied Physics Letters* 94 (9 2009), p. 094103.

[WLQ+21] P. Wang, C.-Y. Luan, M. Qiao et al. "Single ion qubit with estimated coherence time exceeding one hour". *Nature Communications* 12 (2021), p. 233.

[WLW+22] M. A. Weber, C. M. Löschnauer, J. Wolf et al. "Cryogenic ion trap system for high-fidelity near-field microwave-driven quantum logic". *arXiv:2207.11364 preprint* (2022).

[WMI+98] D. J. Wineland, C. Monroe, W. M. Itano et al. "Experimental Issues in Coherent Quantum-State Manipulation of Trapped Atomic Ions". *Journal of Research of the National Institute of Standards and Technology* 103 (1998), p. 259.

[WOC+13a] U. Warring, C. Ospelkaus, Y. Colombe et al. “Individual-Ion Addressing with Microwave Field Gradients”. *Physical Review Letters* 110 (2013), p. 173002.

[WOC+13b] U. Warring, C. Ospelkaus, Y. Colombe et al. “Techniques for microwave near-field quantum control of trapped ions”. *Physical Review A* 87 (2013), p. 013437.

[Wol19] J. Wolf. “Cryogenic, near-field quantum logic chips with passive field nulling in $^{43}Ca^{+}$”. PhD thesis. University of Oxford, 2019.

[Woo80] G. K. Woodgate. *Elementary atomic structure*. Oxford: Clarendon Press, 1980.

[WRW+16] S. Weidt, J. Randall, S. C. Webster et al. “Trapped-Ion Quantum Logic with Global Radiation Fields”. *Physical Review Letters* 117 (2016), p. 220501.

[WUZ+17] Y. Wang, M. Um, J. Zhang et al. “Single-qubit quantum memory exceeding ten-minute coherence time”. *Nature Photonics* 11 (2017), pp. 646–650.

[WWC18] A. E. Webb, S. C. Webster and S. Collingbourne. “Resilient Entangling Gates for Trapped Ions”. *Physical Review Letters* 121 (2018), p. 180501.

[ZCA11] T. Zanon-Willette, E. de Clercq and E. Arimondo. “Ultrahigh-resolution spectroscopy with atomic or molecular dark resonances: Exact steady-state line shapes and asymptotic profiles in the adiabatic pulsed regime”. *Physical Review A* 84 (2011), p. 062502.

[ZHM+19] G. Zarantonello, H. Hahn, J. Morgner et al. “Robust and Resource-Efficient Microwave Near-Field Entangling $^{9}Be^{+}$ Gate”. *Physical Review Letters* 123 (2019), p. 260503.

Appendix A

Atomic structure of Ca^+ ions

The ground-state configuration of Ca^+ ions in the central-field approximation is $1s^2 2s^2 2p^6 3s^2 3p^6 4s$. This represents a single valence electron outside full inner subshells, the same arrangement as in neutral alkali atoms. Due to the spherical symmetry of closed shells, the residual electrostatic interaction is negligible. Therefore, configuration mixing is insignificant and the configurations obtained in the central-field approximation for the ground level and the first few excited levels are an excellent approximation to the true atomic energy eigenstates. The fine-structure levels are designated in order of increasing energy as $4s\,^2S_{1/2}$, $3d\,^2D_{3/2}$, $3d\,^2D_{5/2}$, $4p\,^2P_{1/2}$ and $4p\,^2P_{3/2}$. We will omit the superscript indicating the total spin hereafter since it may only take the value $S = 1/2$ for a single electron in an unfilled shell. Resonance frequencies of transitions between these levels for the isotope $^{40}Ca^+$ are presented in table A.1. In $^{43}Ca^+$, the hyperfine interaction leads to splittings between energy eigenstates within each fine-structure level. However, the centre of mass of each level, which is the energy that each energy eigenstate in that level would have in the absence of the hyperfine interaction, is not changed and one may calculate nominal transition frequencies between the centres of mass of the fine-structure levels. These are slightly different for each calcium species due to isotope shifts. Values for the resonance frequencies in $^{43}Ca^+$ are provided in table A.2.

Further atomic properties are listed in table A.3.

Transition	Frequency (kHz)	Branching fraction
$4\,^2S_{1/2} \leftrightarrow 4\,^2P_{3/2}$	761 905 012 599(82)	0.9347(3) [GKZ+08]
$4\,^2S_{1/2} \leftrightarrow 4\,^2P_{1/2}$	755 222 765 771(65)	0.93565(7) [RPK+13]
$4\,^2S_{1/2} \leftrightarrow 4\,^2D_{5/2}$	411 042 129 776.4017(11)	—
$4\,^2S_{1/2} \leftrightarrow 4\,^2D_{3/2}$	409 222 530 754.868(8)	—
$3\,^2D_{3/2} \leftrightarrow 4\,^2P_{3/2}$	352 682 481 844(82)	0.00661(4) [GKZ+08]
$3\,^2D_{5/2} \leftrightarrow 4\,^2P_{3/2}$	350 862 882 823(82)	0.0587(2) [RPK+13]
$3\,^2D_{3/2} \leftrightarrow 4\,^2P_{1/2}$	346 000 235 016(65)	0.06435(7) [RPK+13]

Table A.1: Transition frequencies and branching fractions in $^{40}Ca^+$. All frequency values have been taken from ref. [Kra20].

Transition	Frequency (kHz)
$4\,^2\mathrm{S}_{1/2} \leftrightarrow 4\,^2\mathrm{P}_{3/2}$	761 905 691 400(90)
$4\,^2\mathrm{S}_{1/2} \leftrightarrow 4\,^2\mathrm{P}_{1/2}$	755 223 443 810(70)
$4\,^2\mathrm{S}_{1/2} \leftrightarrow 4\,^2\mathrm{D}_{5/2}$	411 046 264 488.1(4)
$4\,^2\mathrm{S}_{1/2} \leftrightarrow 4\,^2\mathrm{D}_{3/2}$	409 226 671 030(50)
$3\,^2\mathrm{D}_{3/2} \leftrightarrow 4\,^2\mathrm{P}_{3/2}$	352 679 020 370(100)
$3\,^2\mathrm{D}_{5/2} \leftrightarrow 4\,^2\mathrm{P}_{3/2}$	350 859 426 910(90)
$3\,^2\mathrm{D}_{3/2} \leftrightarrow 4\,^2\mathrm{P}_{1/2}$	345 996 772 780(70)

Table A.2: Frequencies corresponding to energy differences between centres of mass of fine-structure levels in $^{43}\mathrm{Ca}^+$. All frequency values have been taken from ref. [Kra20].

Level	Property	Symbol	Value
$4\,^2\mathrm{S}_{1/2}$	Electronic g-factor	g_J	2.00225664(9) [TPR+03]
$3\,^2\mathrm{D}_{3/2}$	Lifetime	τ	1.195(8) s [SHG+16]
$3\,^2\mathrm{D}_{5/2}$	Lifetime	τ	1.1649(44) s [SHG+17]
	Electronic g-factor	g_J	1.2003340(3) [CBK+09]
$4\,^2\mathrm{P}_{1/2}$	Lifetime	τ	6.904(26) ns [HRK15]
$4\,^2\mathrm{P}_{3/2}$	Lifetime	τ	6.639(42) ns [MSS+20]

Table A.3: Properties of fine-structure levels of $^{40}\mathrm{Ca}^+$.

A.1 Hyperfine interaction

If the nucleus of an atom carries internal angular momentum, it may support higher-order electromagnetic multipole moments in addition to its overall electric charge. These multipole moments interact with the electromagnetic field generated by the surrounding electrons, which gives rise to additional contributions to the total Hamiltonian describing the atomic system. This applies, for example, to $^{43}\mathrm{Ca}^+$, for which the nuclear angular momentum quantum number takes the value $I = 7/2$. The lowest-order contribution is given by the magnetic-dipole hyperfine Hamiltonian

$$H_{\mathrm{hfs,M1}} = 2\frac{g_I \mu_\mathrm{B} \mu_\mathrm{N}}{r^3}\frac{\mu_0}{4\pi}\mathbf{I}\cdot\left(\frac{\mathbf{l}}{r^3} - \left[\frac{\mathbf{s}}{r^3} - \frac{(\mathbf{s}\cdot\mathbf{r})\mathbf{r}}{r^5}\right] + \frac{8\pi}{3}\delta(\mathbf{r})\,\mathbf{s}\right) . \tag{A.1}$$

Derivations of this Hamiltonian can be found in refs. [Arm71; AIV77; Woo80]. We use a convention whereby a general angular momentum operator takes the form $\hbar\mathbf{j}$, with $\mathbf{j}$ dimensionless. In the equation above, $\mathbf{l}$ and $\mathbf{s}$ refer to orbital and spin angular momenta of the valence electron, while $\mathbf{I}$ refers to the total angular momentum of the nucleus. The quantities $\mu_\mathrm{B} = e\hbar/(2m_e)$ and $\mu_\mathrm{N} = e\hbar/(2m_p)$ are the Bohr and nuclear magnetons, where m_e and m_p represent the mass of the electron or proton, respectively. For a single valence electron outside closed shells, the total electronic orbital and spin angular momenta result only from this electron and therefore $\mathbf{L} = \mathbf{l}$, $\mathbf{S} = \mathbf{s}$.

The action of a general angular momentum operator $\mathbf{j}$ on its eigenstates $\{|\gamma jm\rangle\}$, where the label γ denotes any other quantum numbers required to fully specify the

state of the system, is defined by

$$\mathbf{j}^2 \,|\gamma jm\rangle = j(j+1)\,|\gamma jm\rangle \tag{A.1a}$$

$$j_z \,|\gamma jm\rangle = m\,|\gamma jm\rangle\,. \tag{A.1b}$$

We will also make use of the ladder operators $j_\pm = j_x \pm \mathrm{i} j_y$, which transform eigenstates as

$$j_\pm \,|\gamma jm\rangle = \sqrt{j(j+1) - m(m\pm 1)}\,|\gamma jm \pm 1\rangle\ . \tag{A.2}$$

The changes in energy eigenvalues caused by $H_{\mathrm{hfs,M1}}$ are much smaller than the spacings between fine-structure levels. It is therefore possible to calculate the energy corrections and energy eigenstates using degenerate perturbation theory. To first order, they are given by the eigenvalues and eigenvectors of the matrix representing $H_{\mathrm{hfs,M1}}$ within each subspace corresponding to a fine-structure level. Each subspace is spanned by the states $|\gamma LSIm_I Jm_J\rangle$, which means that, within each level, one has to calculate the matrix elements $\langle Im_I Jm_J|H_{\mathrm{hfs,M1}}|Im'_I Jm'_J\rangle$ and diagonalise the resulting matrix. From expression (A.1) it follows that this involves matrix elements of L_i, S_i and r_i between states $|Jm_J\rangle$. These are all vector operators with respect to the total electronic angular momentum $\mathbf{J}$. It follows that one may use the projection theorem for vector operators, which is a special case of the Wigner-Eckart theorem and expresses the relation

$$\langle \gamma jm|V_q|\gamma' jm'\rangle = \frac{\langle \gamma jm|(\mathbf{V}\cdot\mathbf{J})J_q|\gamma' jm'\rangle}{j(j+1)}\ , \tag{A.3}$$

where V_q are the spherical components of a general vector operator $\mathbf{V}$ with respect to $\mathbf{J}$. Since the Cartesian components V_i can be written as a linear combination of the spherical components V_q, the same relation also holds for the former. By making use of the projection theorem it may be shown [Woo80] that as far as the calculation of matrix elements within the subspace corresponding to a fine-structure level characterised by J is concerned, the magnetic-dipole hyperfine interaction can effectively be written in the form

$$H_{\mathrm{hfs,M1}} = A_{\mathrm{hfs}}\,\mathbf{I}\cdot\mathbf{J}\ . \tag{A.4}$$

The magnetic-dipole hyperfine constant A_{hfs} depends on the fine-structure level in question.

For a nucleus with $I \geq 1$ and electrons in states with $J \geq 1$, an additional interaction occurs between the nuclear electric quadrupole moment and the gradient of the electric field produced by the electrons at the position of the nucleus. One finds that, for the purpose of calculating matrix elements between states within a given fine-structure level, the corresponding electric-quadrupole Hamiltonian can be written [AIV77]

$$H_{\mathrm{hfs,E2}} = B_{\mathrm{hfs}}\,\frac{6(\mathbf{I}\cdot\mathbf{J})^2 + 3(\mathbf{I}\cdot\mathbf{J}) - I(I+1)J(J+1)}{4I(2I-1)J(2J-1)}\ . \tag{A.5}$$

For $I \geq 3/2$ and $J > 3/2$, which applies to the $3\,\mathrm{D}_{5/2}$ states in $^{43}\mathrm{Ca}^+$, the atomic Hamiltonian in principle also contains a magnetic-octupole contribution. However, the effect of this term on the energies of atomic states is very small and has not yet been measured experimentally in calcium. It may be neglected for our purposes.

Level	Hyperfine constant	Value
$4\,^2\mathrm{S}_{1/2}$	A_{hfs}	$h \times -806.402\,071\,60(8)\,\mathrm{MHz}$ [ABG+94]
$3\,^2\mathrm{D}_{3/2}$	A_{hfs}	$h \times -47.3(2)\,\mathrm{MHz}$ [NBI+98]
	B_{hfs}	$h \times -3.7(19)\,\mathrm{MHz}$ [NBI+98]
$3\,^2\mathrm{D}_{5/2}$	A_{hfs}	$h \times -3.8931(2)\,\mathrm{MHz}$ [BKR+07]
	B_{hfs}	$h \times -4.241(4)\,\mathrm{MHz}$ [BKR+07]
$4\,^2\mathrm{P}_{1/2}$	A_{hfs}	$h \times -145.4(1)\,\mathrm{MHz}$ [NBI+98]
$4\,^2\mathrm{P}_{3/2}$	A_{hfs}	$h \times -31.0(2)\,\mathrm{MHz}$ [NBI+98]
	B_{hfs}	$h \times -6.7(14)\,\mathrm{MHz}$ [SVN+91]

Table A.4: Hyperfine constants for fine-structure levels in $^{43}\mathrm{Ca}^+$.

We have compiled values of the hyperfine constants for the relevant levels in $^{43}\mathrm{Ca}^+$ in table A.4.

The total angular momentum of the atom is given by $\mathbf{F} = \mathbf{I} + \mathbf{J}$ and there exist simultaneous eigenstates $|\gamma LSIJFm_F\rangle$ of the operators $\mathbf{F}^2$ and F_z, labelled by quantum numbers F and m_F, respectively. In the following, I will drop the explicit label on the latter and write m for the quantum number corresponding to F_z, the projection of the total angular momentum on the z-axis. The hyperfine Hamiltonian $H_{\mathrm{hfs}} = H_{\mathrm{hfs,M1}} + H_{\mathrm{hfs,E2}}$ is diagonal in the $\{|F, m\rangle\}$ basis. If the hyperfine interaction is the only perturbation to be considered, these states are therefore to first order the energy eigenstates of the atom. The energy corrections relative to the centre of mass of each fine-structure level are obtained as [AIV77]

$$E_{\mathrm{hfs}} = \frac{A_{\mathrm{hfs}}}{2} K + B_{\mathrm{hfs}} \,, \tag{A.6}$$

where $K = F(F+1) - I(I+1) - J(J+1)$. For fine-structure levels with $J = 1/2$, such as the ground level of an alkali-like atom, this simplifies to

$$E_{\mathrm{hfs}} = \frac{A_{\mathrm{hfs}}}{2} \left[F(F+1) - I(I+1) - \frac{3}{4} \right] \,. \tag{A.7}$$

It follows that for $A_{\mathrm{hfs}} > 0$, states with larger F will lie higher in energy. When $J = 1/2$, there are only two possible values $F = I \pm 1/2$. The energy difference between these hyperfine sublevels is found to be

$$\Delta E_{\mathrm{hfs}} = E_{\mathrm{hfs}}(F = I + 1/2) - E_{\mathrm{hfs}}(F = I - 1/2) = A_{\mathrm{hfs}}\,(I + 1/2) \,. \tag{A.8}$$

A.2 Interaction with an external static magnetic field

If the atom is placed in an external magnetic field, there arises an additional contribution to the total atomic Hamiltonian from the interaction between the atomic magnetic dipole moment with the applied field, as expressed by the Zeeman Hamiltonian

$$H_{\mathrm{Zeeman}} = -\left(\boldsymbol{\mu}_e + \boldsymbol{\mu}_I\right) \cdot \mathbf{B} \,, \tag{A.9}$$

where $\boldsymbol{\mu}_e$ represents the magnetic dipole moment of the valence electron, $\boldsymbol{\mu}_I$ the magnetic dipole moment of the nucleus and $\mathbf{B} = B\hat{\mathbf{z}}$ the static external magnetic field. We have omitted the diamagnetic term since its effect is negligible for the magnetic field strengths used in our experiments. The magnetic dipole moments are related to the respective angular momenta through

$$\boldsymbol{\mu}_e = -g_l \mu_\mathrm{B} \mathbf{l} - g_s \mu_\mathrm{B} \mathbf{s}, \tag{A.9a}$$

$$\boldsymbol{\mu}_I = g_I \mu_\mathrm{N} \mathbf{I}\,, \tag{A.9b}$$

in terms of the electronic and nuclear g-factors. For a single valence electron, one may identify $\mathbf{L} = \mathbf{l}$ and $\mathbf{S} = \mathbf{s}$ as before.

For atomic species with $I > 0$, perturbations to the fine structure are caused by both hyperfine and Zeeman interactions. The total perturbation is described by the Hamiltonian[1]

$$H_1 = A_\mathrm{hfs}\, \mathbf{I} \cdot \mathbf{J} + \left(g_J \mu_\mathrm{B} J_z - g_I \mu_\mathrm{N} I_z\right) B\,. \tag{A.10}$$

The energy corrections E_1 relative to the centre-of-mass of each fine-structure level may be obtained by diagonalising H_1 within the subspace connected with each level. Since H_1 in eq. (A.10) is directly expressed in terms of components of $\mathbf{I}$ and $\mathbf{J}$, a suitable basis for this purpose is again provided by the states $|\gamma L S I m_I J m_J\rangle$. As explained in the main text, the magnetic quantum number $m = m_I + m_J$ is conserved. This means that an eigenstate $|E_{1,i}, m_i\rangle$ of H_1 is therefore in general a superposition of all basis states $|I m_I J m_J\rangle$ which are characterised by this value m_i.

For levels with $J \geq 1$, it is usually most convenient to find the eigenvalues and eigenstates numerically. For $J = 1/2$, however, a relatively simple analytical expression may be obtained. In this case, there are at most two states with the same value of m within each fine-structure level. If the basis vectors $|I m_I J m_J\rangle$ are arranged such that vectors with the same m are adjacent, the matrix representation of H_1 is block-diagonal, where each block is given by at most a 2×2 matrix. In order to diagonalise H_1, it is therefore only necessary to diagonalise each block separately, which can easily be done by hand. Denoting the basis vectors for a given value of m as

$$|+\rangle = |m_I = m + 1/2, m_J = -1/2\rangle\,, \tag{A.10a}$$

$$|-\rangle = |m_I = m - 1/2, m_J = +1/2\rangle\ , \tag{A.10b}$$

and using $\mathbf{I} \cdot \mathbf{J} = I_z J_z + (I_+ J_- + I_- J_+)/2$, the matrix elements for each block can be written

$$\langle \pm | H_1 | \pm \rangle = -\frac{A_\mathrm{hfs}}{4} - m g_I \mu_\mathrm{N} B \mp \frac{1}{2}\left[m A_\mathrm{hfs} + \left(g_J \mu_\mathrm{B} + g_I \mu_\mathrm{N}\right) B\right], \tag{A.10c}$$

$$\langle \pm | H_1 | \mp \rangle = \frac{A_\mathrm{hfs}}{2}\sqrt{(I + 1/2)^2 - m^2}\,. \tag{A.10d}$$

Diagonalisation of the corresponding 2×2 matrix leads to the Breit-Rabi formula [Woo80] for the eigenvalues

$$E_1 = -\frac{\Delta E_\mathrm{hfs}}{2(2I+1)} - m g_I \mu_\mathrm{N} B \pm \frac{\Delta E_\mathrm{hfs}}{2}\sqrt{1 + \frac{4m}{2I+1}x + x^2}\,, \tag{A.11}$$

[1] We neglect the electric-quadrupole interaction in this section.

where ΔE_{hfs} is the hyperfine splitting given in eq. (A.8) and

$$x = \frac{(g_J \mu_{\mathrm{B}} + g_I \mu_{\mathrm{N}})\, B}{\Delta E_{\mathrm{hfs}}} \,. \tag{A.12}$$

The dimensionless parameter x measures the strength of the Zeeman interaction relative to the hyperfine splitting. For the extremal values $m = \pm(I + 1/2)$, the formula above is replaced by

$$E_1 = -\frac{\Delta E_{\mathrm{hfs}}}{2(2I+1)} \mp (I + 1/2)\, \mu_{\mathrm{N}} B + \frac{\Delta E_{\mathrm{hfs}}}{2}(1 \pm x) \,. \tag{A.13}$$

As regards the eigenvectors, there are at most two of them for each value of m. We will denote the one higher in energy as $|m, \mathrm{u}\rangle$ (up) and the one lower in energy as $|m, \mathrm{d}\rangle$ (down). They can be expanded in terms of the respective basis vectors for each block as

$$|m, \mathrm{u}\rangle = \alpha_{\mathrm{u}}^{(m)} \, |m_I = m + 1/2, m_J = -1/2\rangle + \beta_{\mathrm{u}}^{(m)} \, |m_I = m - 1/2, m_J = +1/2\rangle, \tag{A.13a}$$

$$|m, \mathrm{d}\rangle = \alpha_{\mathrm{d}}^{(m)} \, |m_I = m + 1/2, m_J = -1/2\rangle + \beta_{\mathrm{d}}^{(m)} \, |m_I = m - 1/2, m_J = +1/2\rangle \tag{A.13b}$$

The matrix representation of H_1 in the $\{|+\rangle, |-\rangle\}$ basis is real, which means that there exists a real eigenvector for each eigenvalue. We always choose this eigenvector for the states $|m, \mathrm{u}\rangle$ or $|m, \mathrm{u}\rangle$. The coefficients $\alpha^{(m)}$ and $\beta^{(m)}$ are therefore real and one finds

$$\alpha^{(m)} = \frac{\pm k(x) - m - (I + 1/2)x}{\sqrt{[\pm k(x) - m - (I + 1/2)x]^2 + (I + 1/2)^2 - m^2}}, \tag{A.13c}$$

$$\beta^{(m)} = \frac{\sqrt{(I + 1/2)^2 - m^2}}{\sqrt{[\pm k(x) - m - (I + 1/2)x]^2 + (I + 1/2)^2 - m^2}} \,, \tag{A.13d}$$

with $k(x) = \sqrt{(I + 1/2)\,[2mx + (I + 1/2)(1 + x^2)]}$. In the expressions above, the plus sign is to be taken for the eigenvector corresponding to the eigenvalue E_1 obtained through the plus sign in the Breit-Rabi formula (A.11), while the minus sign is to be taken for the eigenvector corresponding to the eigenvalue obtained through the minus sign. The sign of ΔE_{hfs} then determines which coefficients should be assigned to $|m, \mathrm{u}\rangle$ and which to $|m, \mathrm{d}\rangle$.

The transition frequencies for transitions within a fine-structure level for which $J = 1/2$ are easily obtained from the Breit-Rabi formula. If the transition involves a state $|m_i, u\rangle$ from the higher-energy sublevel and a state $|m_j, d\rangle$ from the lower-energy sublevel, the energy difference is given by

$$E_{\mathrm{u}}(m_i) - E_{\mathrm{d}}(m_j) = -(m_i - m_j) g_I \mu_{\mathrm{N}} B + \frac{|\Delta E_{\mathrm{hfs}}|}{2} \left(\sqrt{1 + \frac{4m_i}{2I+1} x + x^2} + \sqrt{1 + \frac{4m_j}{2I+1} x + x^2} \right) \tag{A.14}$$

Figures A.1 to A.5 show plots of the energy eigenvalues E_1 as a function of the external magnetic field for the different fine-structure levels in $^{43}\mathrm{Ca}^+$. In the $4\,\mathrm{S}_{1/2}$ ground level, the hyperfine splitting is much larger than the Zeeman term for the field strengths considered here. As a result, the energy eigenstates are close enough to the hyperfine states that it makes sense to label each of the former in terms of

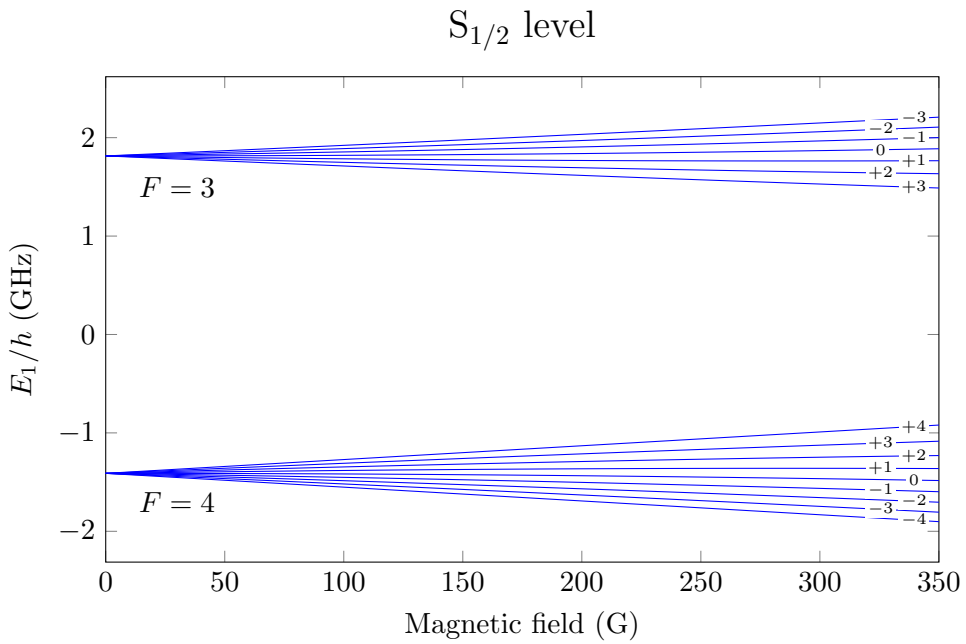


Figure A.1: Energies of states in $4\,S_{1/2}$ ground level as a function of external magnetic field.

the state $|F, m\rangle$ that it would reduce to if the magnetic field was slowly ramped down to zero. For $|m| \neq 4$, the higher-energy states $|m, \mathrm{u}\rangle$ may then be identified as deriving from the $F = 3$ sublevel, while the lower-energy states $|m, \mathrm{d}\rangle$ arise from the $F = 4$ sublevel. A similar situation is encountered in the $4\,P_{1/2}$ level, although the hyperfine splitting here is smaller and consequently states with different F mix more strongly as the field increases. For the $3\,D_{3/2}$ and $4\,P_{3/2}$ levels, the mixing becomes so significant that neither the states $|F, m\rangle$ nor the states $|m_I, m_J\rangle$ provide adequate approximations to the true energy eigenstates for field strengths above a few tens of Gauss. In the case of the $3\,D_{5/2}$ level, the hyperfine splitting is so small that the high-field regime is reached already around 100 G. In this regime, the nuclear and electronic angular momenta can be considered decoupled and the energy eigenstates are closely approximated by the states $|m_I, m_J\rangle$.

The nonlinear dependence of the energies E_1 with respect to the external magnetic field gives rise to the possibility that the transition frequency for certain transitions may to first order become independent of the applied field. This requires that $df/dB = 0$ at some critical field strength B_0. The point B_0, if it exists for a given transition, may be found by calculating the derivative and numerically finding its root. For transitions within a fine-structure level with $J = 1/2$ between states in higher- and lower-energy sublevels, the derivative may be calculated analytically from eq. (A.14).

A.3 The ground level of $^{43}Ca^+$

The constant A_{hfs} for the $4\,S_{1/2}$ ground level is negative, which means that hyperfine states with $F = 4$ lie lower in energy than states with $F = 3$. In the presence of an external magnetic field, the energy eigenstates $|m_i, \mathrm{d}\rangle = |F = 4, m_i\rangle$ are therefore derived from states in the $F = 4$ sublevel, while the eigenstates $|m_i, \mathrm{u}\rangle = |F = 3, m_i\rangle$

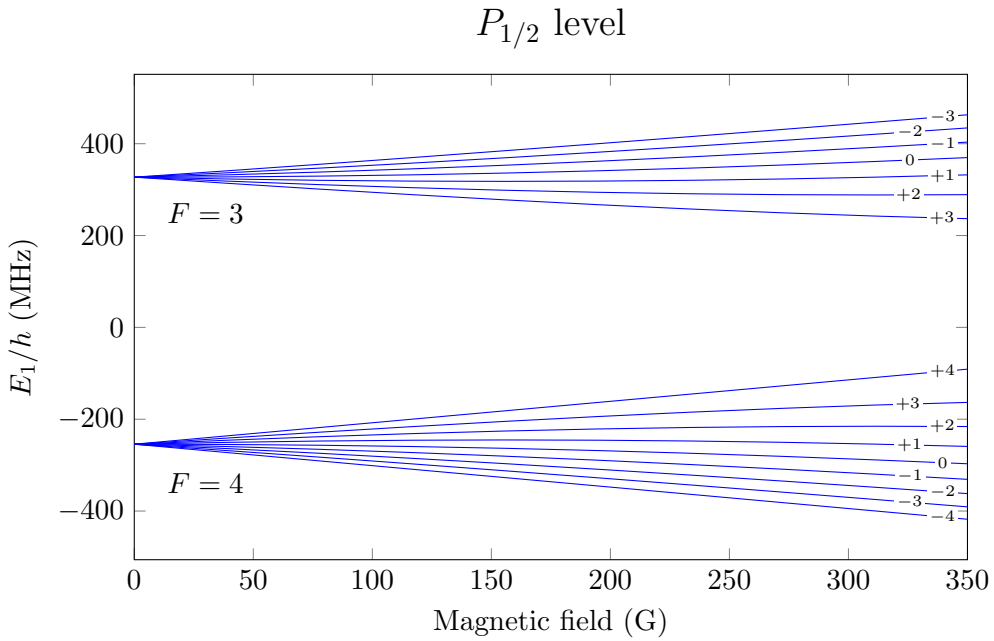


Figure A.2: Energies of states in $4\,\mathrm{P}_{1/2}$ level as a function of external magnetic field.

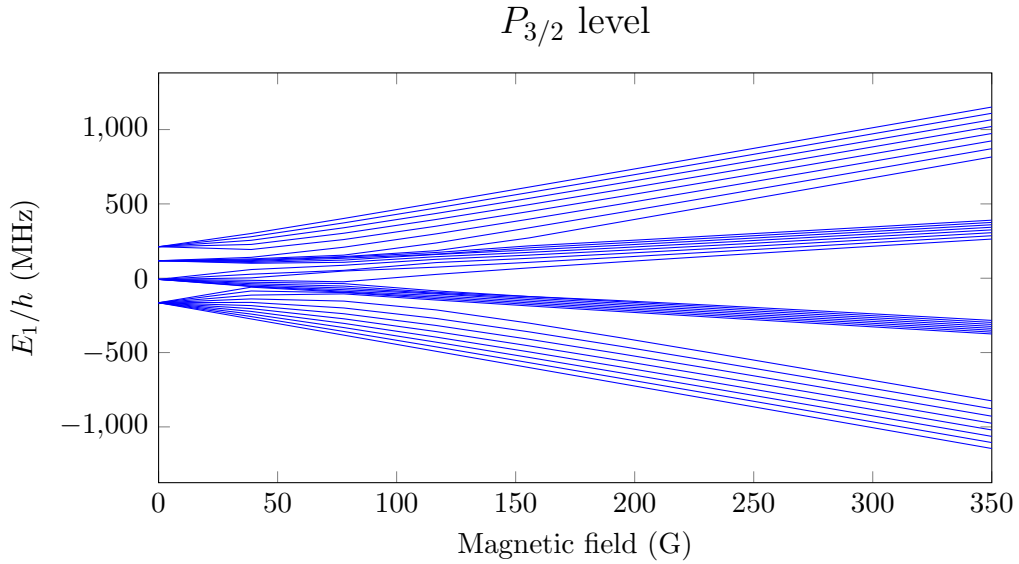


Figure A.3: Energies of states in $4\,\mathrm{P}_{3/2}$ level as a function of external magnetic field.

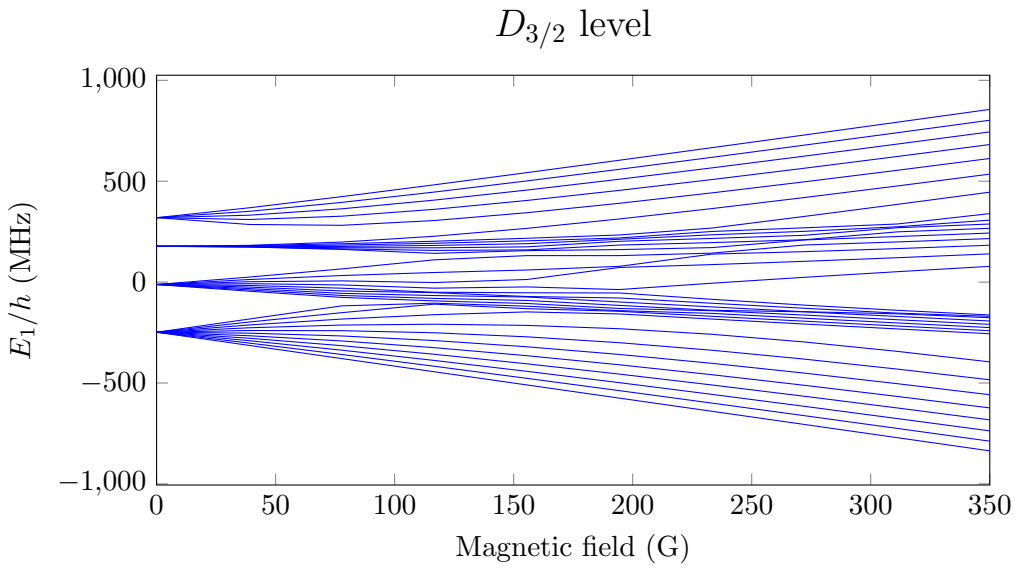


Figure A.4: Energies of states in $3\,\mathrm{D}_{3/2}$ level as a function of external magnetic field.

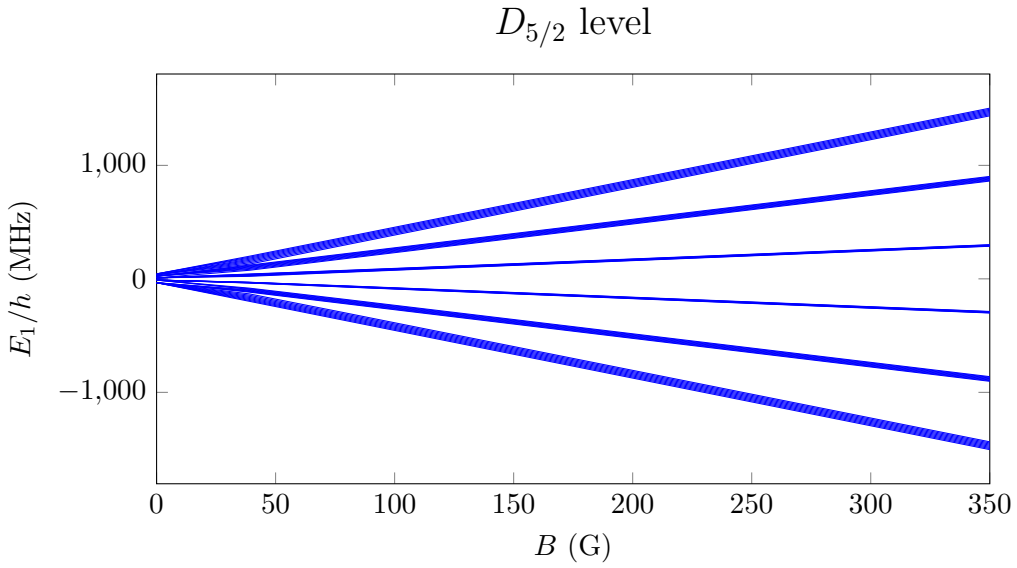


Figure A.5: Energies of states in $3\,\mathrm{D}_{5/2}$ level as a function of external magnetic field.

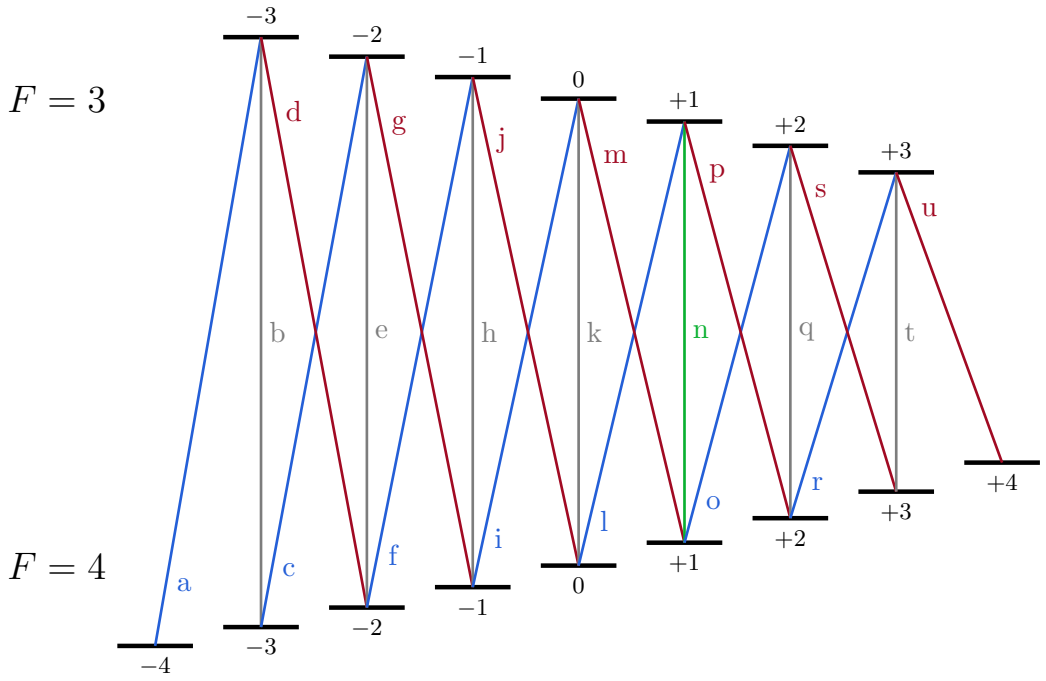


Figure A.6: Structure of the $4\,S_{1/2}$ ground level of $^{43}Ca^{+}$ in a static magnetic field of 287.7828 G. Each state is designated by its magnetic quantum number m. The transition between the states $|4,+1\rangle$ and $|3,+1\rangle$, which form the qubit used for quantum computation in our experiments, is highlighted in green. Transitions between states deriving from different hyperfine sublevels have been labelled for use with table A.7. Colours indicate the different types of transition σ^- (red), π (grey) and σ^+ (blue). The separation between hyperfine levels is not to scale.

come from states in the $F = 3$ sublevel. We will denote a general energy eigenstate in the ground level as $|E_i\rangle = |m_i, \chi_i\rangle$, where $\chi_i \in \{\mathrm{F3}, \mathrm{F4}\}$ signifies whether $|E_i\rangle$ is the higher- or lower-energy eigenstate for given m_i.

Figure A.6 shows the energy structure of the ground level for a $^{43}Ca^{+}$ ion in a static magnetic field of 287.7828 G, as obtained from the Breit-Rabi formula. At this field strength, the transition between the states $|4,+1\rangle$ and $|3,+1\rangle$ is to first order insensitive to fluctuations in the field, as discussed in the following subsection. The expansion coefficients $\alpha^{(m)}$ and $\beta^{(m)}$ for the energy eigenstates at this field, calculated using eq. (A.14), can be found in table A.5. Since all states are characterised by $L = 0$ and thus have the same parity, transitions between them cannot proceed via the electric-dipole interaction, but may instead be driven by a time-varying external magnetic field through the magnetic-dipole interaction. Transitions may occur both between states from different hyperfine sublevels and between states within the same hyperfine sublevel, but we only drive the former kind with microwaves in our experiments. The corresponding transition frequencies can be calculated by means of eq. (A.14). We have listed them in table A.7 further down, identified by the labels defined in fig. A.6. Expression (A.14) for the transition frequency between states from different hyperfine levels consists of two terms. The first one is anti-symmetric under the exchange $m_i \mapsto m_j$, while the second term is symmetric. Hence, the two transitions $|F = 4, m_i\rangle \leftrightarrow |F = 3, m_j\rangle$ and $|F = 4, m_j\rangle \leftrightarrow |F = 3, m_i\rangle$ differ in frequency only by $-2(m_i - m_j)g_I\mu_N B/h$, which amounts to approximately 165 kHz at a field

m_d	$\alpha_\mathrm{d}^{(m)}$	$\beta_\mathrm{d}^{(m)}$
-4	1	0
-3	0.957616	0.288047
-2	0.909575	0.415540
-1	0.854058	0.520177
0	0.788205	0.615412
+1	0.707107	0.707107
+2	0.601103	0.799171
+3	0.445521	0.895272
+4	0	1

(a)

m_u	$\alpha_\mathrm{u}^{(m)}$	$\beta_\mathrm{u}^{(m)}$
-3	0.288047	0.288047
-2	0.415540	-0.957616
-1	0.415540	-0.909575
0	0.520177	-0.854058
+1	0.707107	-0.707107
+2	0.799171	-0.601103
+3	0.895272	-0.445521

(b)

Table A.5: Expansion coefficients for energy eigenstates in ground level of $^{43}\mathrm{Ca}^+$ with respect to $|I, m_I, J, m_J\rangle$ basis, as defined in eq. (A.14), at a field of 287.7828 G.

Label	Transition	Critical field B_0 (G)
k	$\|4,0\rangle \leftrightarrow \|3,0\rangle$	0.0
l	$\|4,0\rangle \leftrightarrow \|3,1\rangle$	146.094202
m	$\|4,1\rangle \leftrightarrow \|3,0\rangle$	146.331413
n	$\|4,1\rangle \leftrightarrow \|3,1\rangle$	287.782750
o	$\|4,1\rangle \leftrightarrow \|3,2\rangle$	439.582300
p	$\|4,2\rangle \leftrightarrow \|3,1\rangle$	439.803531
q	$\|4,2\rangle \leftrightarrow \|3,2\rangle$	575.565499
r	$\|4,2\rangle \leftrightarrow \|3,2\rangle$	738.637762
s	$\|4,3\rangle \leftrightarrow \|3,2\rangle$	738.831447
t	$\|4,3\rangle \leftrightarrow \|3,3\rangle$	863.348249

Table A.6: Critical field strengths required for transitions within the ground level of $^{43}\mathrm{Ca}^+$ to become field-insensitive.

strength of 288 G. It follows that these σ^+- and σ^--transitions form near-degenerate pairs, which has to be taken into account when performing readout transfer pulses for π-qubits.

A.3.1 Field-insensitive transitions

We have plotted the derivative df/dB for transitions between states from different hyperfine sublevels within the ground level in figure A.7. All transitions except those involving states with $|m| = 4$ feature a critical point B_0 at which the derivative vanishes. Those transitions that are nearly degenerate in frequency, for reasons discussed above, also have almost the same derivatives, only distinguished by the slight offset $2g_I\mu_\mathrm{N}$. The corresponding curves therefore appear plotted on top of each other. Since the Hamiltonian H_1 is invariant under the transformation $z \mapsto -z$, the state $|F, m\rangle$ has the same energy for $B > 0$ as the state $|F, -m\rangle$ for $B < 0$. This is reflected in the symmetry of the graphs in fig. A.7. The field strengths B_0 at which the various transitions become to first order field-independent, obtained by numerical solution of $df/dB = 0$, are compiled in table A.6.

At the point where a transition becomes field-insensitive, the magnitude of the

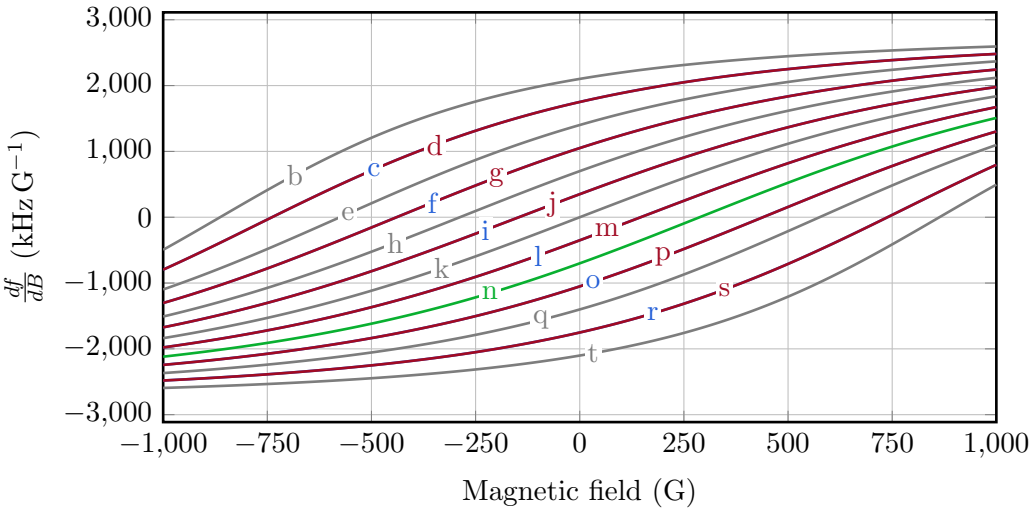


Figure A.7: Sensitivity of transition frequency to changes in magnetic field for transitions in ground level of ^{43}Ca+. Labels are defined in fig. A.6. For certain pairs of σ-transitions, the derivative of the transition frequency with respect to the field strength is almost degenerate, which explains the overlapping curves.

expansion coefficients of the two states involved in the transition is nearly equal, as noted in [HBD+05]. This may be explained by considering the variation of the energy eigenvalue with magnetic field as a function of those coefficients. Letting $|E_i(B)\rangle$ denote a state that is an energy eigenstate at a given magnetic field B, one finds

$$\begin{aligned}\frac{dE_i(B)}{dB} &= \frac{d}{dB}\langle E_i(B)|H_1(B)|E_i(B)\rangle = \langle E_i(B)|dH_1/dB|E_i(B)\rangle + \frac{d}{dB}\left[\langle E_i(B)|E_i(B)\rangle\right] = \\ &= \langle E_i(B)|\left(g_J\mu_\mathrm{B}J_z - g_I\mu_\mathrm{N}I_z\right)|E_i(B)\rangle \ , \end{aligned} \tag{A.15}$$

where I have used the fact that energy eigenstates at all field strengths are normalised, so $d\left[\langle E_i(B)|E_i(B)\rangle\right]/dB = 0$. Using eq. (A.14), eq. (A.15) and the relation $\beta^2 = 1-\alpha^2$, the energy difference for a transition between states $|E_i\rangle$ and $|E_j\rangle$ is found to depend on magnetic field as

$$\frac{d(E_i-E_j)}{dB} = g_J\mu_\mathrm{B}\left[\left(\alpha_{\chi_j}^{(m_j)}\right)^2 - \left(\alpha_{\chi_i}^{(m_i)}\right)^2\right] + g_I\mu_\mathrm{N}\left[\left(\alpha_{\chi_j}^{(m_j)}\right)^2 - \left(\alpha_{\chi_i}^{(m_i)}\right)^2 + m_j - m_i\right] \ . \tag{A.16}$$

The requirement $d(E_i-E_j)/dB = 0$ then leads to

$$\left(\alpha_{\chi_i}^{(m_i)}\right)^2 = \left(\alpha_{\chi_j}^{(m_j)}\right)^2 + \frac{g_I\mu_\mathrm{N}}{g_J\mu_\mathrm{B}+g_I\mu_\mathrm{N}}\left(m_j-m_i\right) \ . \tag{A.17}$$

Since $g_I\mu_\mathrm{N} \ll g_J\mu_\mathrm{B}$, the term involving $m_j - m_i$ above can be neglected and therefore $|\alpha_{\chi_i}^{(m_i)}| \approx |\alpha_{\chi_j}^{(m_j)}|$ and $|\beta_{\chi_i}^{(m_i)}| \approx |\beta_{\chi_j}^{(m_j)}|$ at a field-insensitive point.

A.3.2 Magnetic-dipole transition matrix elements

The interaction Hamiltonian for the magnetic-dipole interaction takes the form

$$H_\mathrm{M2} = -\boldsymbol{\mu}\cdot\mathbf{B}_\mathrm{mw}(t) \ , \tag{A.18}$$

where $\mathbf{B}_{\mathrm{mw}}(t)$ represents a time-varying magnetic field and

$$\boldsymbol{\mu} = -g_J \mu_{\mathrm{B}} \mathbf{J} + g_I \mu_{\mathrm{N}} \mathbf{I} \tag{A.19}$$

is the total magnetic dipole moment of the atom. In the spherical basis with respect to the atomic coordinate system, the interaction Hamiltonian becomes

$$H_{\mathrm{M2}} = \sum_q (-1)^q \, \mu_q B_{-q} \, , \tag{A.20}$$

which means that modelling the dynamics of the system requires calculation of matrix elements of the form $\langle E_i | \mu_q | E_j \rangle$, where $|E_i\rangle$ are the eigenstates of the total internal atomic Hamiltonian H_{itl}. Using eq. (A.19), the spherical components μ_q can be expressed in terms of the ladder and z-projection operators for the electronic and nuclear angular momenta as

$$\mu_{+1} = \frac{1}{\sqrt{2}} \left(g_J \mu_{\mathrm{B}} J_+ - g_I \mu_{\mathrm{N}} I_+ \right) , \tag{A.20a}$$

$$\mu_0 = -g_J \mu_{\mathrm{B}} J_z + g_I \mu_{\mathrm{N}} I_z , \tag{A.20b}$$

$$\mu_{-1} = -\frac{1}{\sqrt{2}} \left(g_J \mu_{\mathrm{B}} J_- - g_I \mu_{\mathrm{N}} I_- \right) \, . \tag{A.20c}$$

We will focus on the case of the ground level of $^{43}\mathrm{Ca}^+$, for which the energy eigenstates $|E_i\rangle$ are given by the states $|m_i, \chi_i\rangle$, as introduced in the previous section. Depending on the value of q, three different types of transition may be distinguished.

For $q = +1$, the magnetic-dipole transition matrix element $\langle m_i, \chi_i | \mu_{+1} | m_j, \chi_j \rangle$ is non-zero only if $m_i = m_j + 1$. With $E_i > E_j$, this constitutes a σ^+-transition. Taking into account that $I = 7/2$ for $^{43}\mathrm{Ca}^+$, one finds

$$\begin{aligned} \langle m_i, \chi_i | \mu_{+1} | m_j, \chi_j \rangle = {} & \frac{g_J \mu_{\mathrm{B}}}{\sqrt{2}} \, \beta_{\chi_i}^{(m_i)} \alpha_{\chi_j}^{(m_j)} \\ & - \frac{g_I \mu_{\mathrm{N}}}{\sqrt{2}} \left[\alpha_{\chi_i}^{(m_i)} \alpha_{\chi_j}^{(m_j)} \sqrt{15 - 2m_j - m_j^2} + \beta_{\chi_i}^{(m_i)} \beta_{\chi_j}^{(m_j)} \sqrt{16 - m_j^2} \right] \, . \end{aligned} \tag{A.21}$$

For $q = 0$, the matrix element $\langle m_i, \chi_i | \mu_0 | m_j, \chi_j \rangle$ is non-zero only if $m_i = m_j$. We call this a π-transition. The matrix element is given by

$$\begin{aligned} \langle m_i, \chi_i | \mu_0 | m_j, \chi_j \rangle = {} & \frac{g_J \mu_{\mathrm{B}}}{2} \left[\alpha_{\chi_i}^{(m_i)} \alpha_{\chi_j}^{(m_j)} - \beta_{\chi_i}^{(m_i)} \beta_{\chi_j}^{(m_j)} \right] \\ & + \frac{g_I \mu_{\mathrm{N}}}{2} \left[\alpha_{\chi_i}^{(m_i)} \alpha_{\chi_j}^{(m_j)} \, (2m + 1) + \beta_{\chi_i}^{(m_i)} \beta_{\chi_j}^{(m_j)} \, (2m - 1) \right] \, . \end{aligned} \tag{A.22}$$

For $q = -1$, the matrix element $\langle m_i, \chi_i | \mu_{-1} | m_j, \chi_j \rangle$ is non-zero only if $m_i = m_j - 1$. With $E_i > E_j$, I refer to this as a σ^--transition and find

$$\begin{aligned} \langle m_i, \chi_i | \mu_{-1} | m_j, \chi_j \rangle = {} & -\frac{g_J \mu_{\mathrm{B}}}{\sqrt{2}} \, \alpha_{\chi_i}^{(m_i)} \beta_{\chi_j}^{(m_j)} \\ & + \frac{g_I \mu_{\mathrm{N}}}{\sqrt{2}} \left[\alpha_{\chi_i}^{(m_i)} \alpha_{\chi_j}^{(m_j)} \sqrt{16 - m_j^2} + \beta_{\chi_i}^{(m_i)} \beta_{\chi_j}^{(m_j)} \sqrt{15 + 2m_j - m_j^2} \right] \, . \end{aligned} \tag{A.23}$$

Rather than using these matrix elements of the magnetic-dipole operator directly, I find it more convenient for the theoretical treatment in the main text to define

Label	m_{F4}	m_{F3}	Frequency (GHz)	df/dB (MHz G^{-1}) [d^2f/dB^2 (kHz G^{-2})]	Transition strength R (μ_B)
a	-4	-3	3.949771863	2.569912	1.355692
b	-3	-3	3.867368475	2.337130	-0.552243
c	-3	-2	3.781465951	2.086061	1.233104
d	-2	-3	3.781301059	2.085488	-0.169444
e	-2	-2	3.695398534	1.834419	0.756705
f	-2	-1	3.605294282	1.560347	-1.099756
g	-1	-2	3.605129390	1.559774	0.305995
h	-1	-1	3.515025138	1.285701	-0.889435
i	-1	0	3.420035474	0.982944	0.953011
j	0	-1	3.419870582	0.982371	0.453176
k	0	0	3.324880918	0.679614	-0.971138
l	0	+1	3.224113802	0.340094	0.789034
m	+1	0	3.223948910	0.339521	0.616028
n	+1	+1	3.123181794	0 [2.514]	-1.001026
o	+1	+2	3.015435352	-0.388298	0.601736
p	+2	+1	3.015270460	-0.388871	-0.799970
q	+2	+2	2.907524018	-0.777169	-0.961755
r	+2	+3	2.791111006	-1.233169	-0.379132
s	+3	+2	2.790946114	-1.233742	-1.012843
t	+3	+3	2.674533102	-1.689743	-0.798542
u	+4	+3	2.546781212	-2.246218	-1.267363

Table A.7: Transition frequencies and matrix elements for magnetic-dipole transitions between states of different hyperfine sublevels in $^{43}Ca^+$ at a static magnetic field of 287.7828 G.

variables $R_{ij,q}$ given by

$$R_{ij,q} = (-1)^{q+1} \langle m_i, \chi_i | \mu_q | m_j, \chi_j \rangle \ . \tag{A.24}$$

Their values at a static magnetic field of 287.7828 G for transitions between different hyperfine sublevels within the ground level are contained in table A.7.

Appendix B

Solutions to Mathieu equation

We will here discuss solutions to the equation of motion for a particle in the form

$$\frac{d^2\mathbf{x}(t)}{dt^2} + \frac{\omega_{\mathrm{rf}}^2}{4}\left(A - 2Q\cos\omega_{\mathrm{rf}}t\right)\mathbf{x}(t) = \frac{\omega_{\mathrm{rf}}^2}{4}\,\mathbf{s}(t)\ . \tag{B.1}$$

Such an equation may, for example, describe an ion in a Paul trap. After the substitution $\tau = \omega_{\mathrm{rf}}t/2$, one obtains the three-dimensional inhomogeneous coupled Mathieu equation

$$\frac{d^2\mathbf{x}(\tau)}{d\tau^2} + \left(A - 2Q\cos 2\tau\right)\mathbf{x}(\tau) = \mathbf{s}(\tau)\ . \tag{B.2}$$

The inhomogeneous term $\mathbf{s}(\tau) = (s_1(\tau), s_2(\tau), s_3(\tau))^T$ is a time-dependent 3×1 column vector, while A and Q are time-independent 3×3 matrices. Through the standard introduction of a new 6×1 vector $\mathbf{g}(\tau) = (\mathbf{x}(\tau), d\mathbf{x}(\tau)/d\tau)^T$, this can be transformed into a first-order system of differential equations of the form

$$\frac{d\mathbf{g}(\tau)}{d\tau} = K(\tau)\mathbf{g}(\tau) + \mathbf{b}(\tau)\ , \tag{B.3}$$

with the 6×6 matrix $K(\tau)$ and 6×1 vector $\mathbf{b}(\tau)$ defined as

$$K(\tau) = \begin{pmatrix} 0 & \mathbb{I}_3 \\ -(A - 2Q\cos 2\tau) & 0 \end{pmatrix}, \quad \mathbf{b}(\tau) = \begin{pmatrix} 0 \\ \mathbf{s}(\tau) \end{pmatrix}\ , \tag{B.4}$$

where $\mathbb{I}_3$ is the 3×3 identity matrix. For the Mathieu equation, $K(\tau)$ is periodic with period π.

Before treating the inhomogeneous case, it will be useful to focus on the corresponding homogeneous equation for which $\mathbf{s}(\tau) = \mathbf{0}$. One thus has

$$\frac{d\mathbf{g}(\tau)}{d\tau} = K(\tau)\mathbf{g}(\tau)\ . \tag{B.5}$$

It is a fundamental result in the theory of differential equations that a homogeneous system of n first-order coupled linear differential equations has n linearly independent solutions. These form a basis for the space of all solutions. If one denotes the individual solutions as $\boldsymbol{\phi}_i(\tau)$, $i \in 1, \ldots, n$, the general solution to the homogeneous equation can therefore be expressed as $\mathbf{g}(\tau) = \sum_i c_i\boldsymbol{\phi}_i(\tau)$ for some unique constants c_i. The basis solutions are usually collected into a matrix $\Phi(\tau)$, called the fundamental matrix solution, such that the $\boldsymbol{\phi}_i(\tau)$ form the columns of $\Phi(\tau)$ and thus $\Phi(\tau) = (\boldsymbol{\phi}_1 \ldots \boldsymbol{\phi}_n)$. It follows that the fundamental matrix solution satisfies

the matrix differential equation

$$\frac{d}{d\tau}\Phi(\tau) = K(\tau)\Phi(\tau) \; . \tag{B.6}$$

At this point I make use of the fact that for the Mathieu equation the resulting first-order system of eq. (B.5) has periodic coefficients in the form of $K(\tau)$. This means that it may be treated through Floquet theory. A thorough discussion is outside the scope of this appendix and the reader is instead referred to the vast literature that exists on this subject, see for example ref. [Chi06]. We skip straight away to the central result that if the motion of the particle is bounded ($|\mathbf{x}(\tau)| < \infty$ as $\tau \to \pm\infty$), as required for trapping, each basis solution can be expressed in the form

$$\boldsymbol{\phi}_i(\tau) = \mathrm{e}^{\mathrm{i}\beta_i\tau}\,\mathbf{p}(\tau) \tag{B.7}$$

for some real number β_i. Here, $\mathbf{p}(\tau)$ is a vector of periodic functions with the same period as $K(\tau)$. Whether a complete set of real β_i exists (and thus whether the motion is stable in all directions) depends on the values of the elements of A and Q. One finds that only certain regions in the corresponding parameter space lead to bounded motion along all axes and it is therefore crucial that these parameters are chosen correctly in order to trap a particle. In the one-dimensional case, for which the parameter matrices reduce to simple numbers a and q, this results in the standard Mathieu stability diagrams.

Once a set of solutions $\boldsymbol{\phi}_i(\tau)$ and thus a fundamental matrix $\Phi(\tau)$ for the homogeneous equation (B.5) has been found, the solution of the inhomogenous equation can be constructed through the method of variation of constants. In particular, the solution $\tilde{\mathbf{g}}(\tau)$ to the inhomogeneous equation that satisfies the initial condition $\tilde{\mathbf{g}}(\tau = 0) = \mathbf{g}_0$ is given by

$$\tilde{\mathbf{g}}(\tau) = \Phi(\tau)\left[\int_0^\tau \Phi^{-1}(\sigma)\,\mathbf{b}(\sigma)\,d\sigma + \Phi^{-1}(0)\,\mathbf{g}_0\right] \; , \tag{B.8}$$

where $\Phi^{-1}(\tau)$ is the matrix inverse of $\Phi(\tau)$. If one denotes the indefinite integral as $\mathbf{r}(\tau) = \int \Phi^{-1}(\tau)\mathbf{b}(\tau)\,d\tau$, then another solution may be found by requiring the initial condition to be $\mathbf{g}_0 = \Phi(0)\mathbf{r}(0)$. This solution then takes the simple form

$$\tilde{\mathbf{g}}(\tau) = \Phi(\tau)\int \Phi^{-1}(\tau)\mathbf{b}(\tau)\,d\tau \; . \tag{B.9}$$

We will now apply the techniques presented above to obtain explicit solutions to the inhomogeneous Mathieu equation, for the two cases where the motion along different spatial axes is decoupled or coupled.

B.1 Homogeneous case

If A and Q can be simultaneously diagonalised, a suitable set of axes may be found along which the equations of motion decouple. Considering for now the homogeneous case, one obtains a set of three independent Mathieu equations, each of the form

$$\frac{d^2x_i}{d\tau^2} + (a_i - 2q_i\cos 2\tau)\;x_i = 0, \tag{B.10}$$

with $i \in \{1, 2, 3\}$. We will drop the subscript i denoting the different principal axes in the following for ease of notation, but it should be borne in mind that a separate equation like (B.10), with different a_i and q_i in general, holds along each direction. Each such equation may be treated independently as a one-dimensional case.

The corresponding first-order system results from the substitution $\mathbf{g} = (x, dx/dt)^T$. It follows that there are two linearly independent solutions $\boldsymbol{\phi}_1(\tau)$ and $\boldsymbol{\phi}_2(\tau)$, which I write

$$\boldsymbol{\phi}_i(\tau) = \begin{pmatrix} u_i(\tau) \\ du_i(\tau)/d\tau \end{pmatrix} = \mathrm{e}^{\mathrm{i}\beta_i t} \begin{pmatrix} p_i(\tau) \\ dp_i(\tau)/d\tau \end{pmatrix} . \tag{B.11}$$

We have made use of the general result of eq. (B.7). It may be shown that the pair of characteristic exponents is related via $\beta_2 = -\beta_1$. Since the $p_i(\tau)$ are π-periodic, they may be expanded in Fourier series and one finds that the solutions take the form

$$u_1(\tau) = \mathrm{e}^{\mathrm{i}\beta\tau} \sum_{n\in\mathbb{Z}} c_{2n}\, \mathrm{e}^{\mathrm{i}2n\tau} \tag{B.12}$$

$$u_2(\tau) = \mathrm{e}^{-\mathrm{i}\beta\tau} \sum_{n\in\mathbb{Z}} c_{2n}\, \mathrm{e}^{-\mathrm{i}2n\tau} . \tag{B.13}$$

The quantity β is a function of the Mathieu parameters a and q. The set of time-independent coefficients c_{2n} is the same in both solutions and may be chosen to be real. Explicit values for the c_{2n} may be obtained by inserting the expression from eq. (B.12) into the Mathieu equation (B.10) and collecting terms for each exponential. This leads to the three-term recursion relation

$$c_{2n-2} + \frac{(\beta + 2n)^2 - a}{q}\, c_{2n} + c_{2n+2} = 0 . \tag{B.14}$$

After introducing the ratios $s_{2n} = c_{2n}/c_{2n-2}$, this can be written

$$\frac{1}{s_{2n}} + s_{2n+2} = d_{2n} \qquad \text{with } d_{2n} = \frac{a - (\beta + 2n)^2}{q} . \tag{B.15}$$

Using backward recursion, s_{2n+2} is replaced by the corresponding expression involving s_{2n+4} and this process continued for increasing $2n$. This leads to the continued fraction

$$s_{2n} = \cfrac{1}{d_{2n} - \cfrac{1}{d_{2n+2} - \cfrac{1}{d_{2n+4} - \ldots}}} . \tag{B.16}$$

Similarly, forward recursion gives

$$s_{2n} = d_{2n-2} - \cfrac{1}{d_{2n-4} - \cfrac{1}{d_{2n-6} - \ldots}} . \tag{B.17}$$

It may be shown that these continued fractions converge [Chi06]. For given a, q and β, the continued fractions provide a means to calculate the ratios s_{2n}. After setting one of the coefficients, usually c_0, to some arbitrary value, all other coefficients c_{2n} may be obtained. In fact, the continued fractions can also be used to obtain

an implicit equation that determines β. Consistency in the value obtained for s_{2n} through backward and forward recursion requires that the two expressions above are equal, which leads to

$$d_{2n} = \frac{1}{d_{2n-2} - \dfrac{1}{s_{2n-2}}} + \frac{1}{d_{2n+2} - s_{2n+4}} \,. \tag{B.18}$$

For fixed a and q, this is an equation for β through the various d_{2n}.

In terms of the original variable t, the solutions are expressed as

$$u_1(t) = e^{\mathrm{i}\nu t} \sum_{n\in\mathbb{Z}} c_{2n}\, \mathrm{e}^{\mathrm{i}n\omega_{\mathrm{rf}}t} \tag{B.19}$$

$$u_2(t) = e^{-\mathrm{i}\nu t} \sum_{n\in\mathbb{Z}} c_{2n}\, \mathrm{e}^{-\mathrm{i}n\omega_{\mathrm{rf}}t} \,, \tag{B.20}$$

where the angular frequency ν, called the secular frequency, is given by $\nu = \beta\omega_{\mathrm{rf}}/2$.

The general solution to the Mathieu equation can be expressed by means of the complex basis solutions of eq. (B.12). However, since $x(t)$ is real, it is slightly more convenient to first construct real linearly independent solutions through the combinations $[u_1(t) + u_2(t)]/2$ and $[u_1(t) - u_2(t)]/(2\mathrm{i})$, so that the general solution can be written $x(t) = k_1 \sum_n c_{2n} \cos(\nu + n\omega_{\mathrm{rf}})t + k_2 \sum_n c_{2n} \sin(\nu + n\omega_{\mathrm{rf}})t$ for some constants k_1, k_2 determined by initial conditions. In particular, for a particle starting at $t = 0$ at position x_0 with velocity $\dot{x}_0$, one finds that the solution $x(t)$ to the homogeneous Mathieu equation is given by

$$x(t) = \sigma \sum_{n\in\mathbb{Z}} c_{2n} \cos\left[(\nu + n\omega_{\mathrm{rf}})\, t + \phi\right] \tag{B.21}$$

with

$$\sigma = \sqrt{\left(\frac{x_0}{\sum_n c_{2n}}\right)^2 + \left[\frac{\dot{x}_0}{\sum_n c_{2n}(\beta + 2n)}\right]^2} \tag{B.22}$$

$$\phi = \arctan\left[-\frac{\dot{x}_0}{\sum_n c_{2n}(\beta + 2n)} \Big/ \frac{x_0}{\sum_n c_{2n}}\right] \tag{B.23}$$

B.1.1 Lowest-order approximation

The values of the coefficients c_{2n} may in practice be determined by truncating the continued fractions presented in the previous section at increasing $|n|$ until the desired precision has been achieved. This would usually be done numerically. The same principle applies to the implicit equation for β, which may be solved numerically while retaining a growing number of terms in the denominators. If this procedure is followed to calculate the exact value of β to high precision, one finds that if $|a|, q^2 \ll 1$, then $\beta \ll 1$ and the $|s_{2n}|$ drop rapidly with increasing $|n|$. Under these conditions, it is possible to obtain approximate values for β and s_{2n} by using the result $\beta \ll 1$ directly in the continued fractions.

From the expression in (B.15), it is seen that $d_{2n} \gg 1$ even for small $|n|$ when $|a|, q^2, \beta \ll 1$. Using eq. (B.18) for d_0, an approximation to lowest order in $|a|$, q^2

may therefore be obtained by truncating after $n = \pm 1$, which results in

$$d_0 \simeq \frac{1}{d_2} + \frac{1}{d_{-2}} \, . \tag{B.24}$$

Discarding terms with $|n| > 1$ amounts to setting $s_4 \simeq 0$ and $1/s_{-2} \simeq 0$, which means that $c_4 \simeq 0$ and $c_{-4} \simeq 0$. Inserting the explicit expression for d_{2n} into eq. (B.24) gives

$$\frac{a - \beta^2}{q} \simeq \frac{q}{a - (\beta + 2)^2} + \frac{q}{a - (\beta - 2)^2} \, . \tag{B.25}$$

We now invoke $|a|, \beta \ll 1$ so that $a - (\beta \pm 2)^2 \simeq -4$, which leads to the approximation

$$\beta \simeq \sqrt{a + \frac{q^2}{2}} \, . \tag{B.26}$$

The relations between relevant coefficients are found accordingly through $s_2 \simeq 1/d_2 \simeq -q/4$ and $1/s_0 \simeq 1/d_{-2} \simeq -q/4$. When these are substituted in the general solution (B.21), the approximate motion is found to be

$$x(t) = r \cos\left(\nu t + \phi\right) \left(1 - \frac{q}{2} \cos \omega_{\mathrm{rf}} t\right) \tag{B.27}$$

with

$$r = \frac{\sqrt{x_0^2 + \left(\dot{x}_0/\beta\right)^2}}{1 - q/2} \tag{B.28}$$

$$\phi = \arctan\left(\frac{-\dot{x}_0/\beta}{x_0}\right) \, . \tag{B.29}$$

B.2 Inhomogeneous case

We will assume that the inhomogeneous term in the decoupled Mathieu equation does not depend on time, which means that the rescaled equation of motion takes the form

$$\frac{d^2 x(\tau)}{d\tau^2} + \left(a - 2q \cos \omega_{\mathrm{rf}} \tau\right) \, x(\tau) = s, \tag{B.30}$$

for constant s. A set of linearly independent solutions to the corresponding homogeneous equation was discussed in the previous section and one may therefore write down a fundamental matrix solution as

$$\Phi(\tau) = \begin{pmatrix} u_1(\tau) & u_2(\tau) \\ du_1(\tau)/d\tau & du_2(\tau)/d\tau \end{pmatrix} \, . \tag{B.31}$$

To find a solution to the inhomogeneous equation, one applies the general method offered by eq. (B.9). As $\Phi(\tau)$ is a 2×2 matrix, a tractable analytic expression for the inverse is available in the one-dimensional case that I am considering here. One finds that the first component of $\tilde{\mathbf{g}}(\tau)$ is given by

$$\tilde{u}(\tau) = -u_1(\tau) \int \frac{u_2(\tau) \, s}{\det \Phi(\tau)} \, d\tau + u_2(\tau) \int \frac{u_1(\tau) \, s}{\det \Phi(\tau)} \, d\tau \, . \tag{B.32}$$

It may be shown that the Wronskian $\det \Phi(\tau)$ is in fact constant in the case of the Mathieu equation and therefore $\det \Phi(\tau) = \det \Phi(0)$. We now make use of the expressions for $u_1(\tau)$ and $u_2(\tau)$ in eqs. (B.12). This allows us to find

$$\det \Phi(0) = u_1(0)\, du_2/d\tau(0) - du_1/d\tau(0)\, u_2(0) = -2\mathrm{i} \sum_{m,n\in\mathbb{Z}} c_{2m} c_{2n} (\beta + 2n) \quad \text{(B.33)}$$

and explicitly compute the required integrals. We obtain

$$\tilde{u}(\tau) = \frac{s}{\det \Phi(0)} \left[-u_1(\tau) \int \sum_n c_{2n}\, \mathrm{e}^{-\mathrm{i}(\beta+2n)\tau}\, d\tau + u_2(\tau) \int \sum_n c_{2n}\, \mathrm{e}^{\mathrm{i}(\beta+2n)\tau}\, d\tau \right] \quad \text{(B.34)}$$

$$= \frac{s}{\det \Phi(0)} \left[-\sum_m c_{2m}\, \mathrm{e}^{\mathrm{i}(\beta+2m)\tau} \sum_n c_{2n} \frac{\mathrm{e}^{-\mathrm{i}(\beta+2n)\tau}}{-\mathrm{i}(\beta+2n)} \right. \quad \text{(B.35)}$$

$$\left. + \sum_m c_{2m}\, \mathrm{e}^{-\mathrm{i}(\beta+2m)\tau} \sum_n c_{2n} \frac{\mathrm{e}^{\mathrm{i}(\beta+2n)\tau}}{\mathrm{i}(\beta+2n)} \right] \quad \text{(B.36)}$$

$$= -\mathrm{i} \frac{s}{\det \Phi(0)} \left[\sum_m \sum_n \frac{c_{2m} c_{2n}}{\beta+2n}\, \mathrm{e}^{\mathrm{i}2(m-n)\tau} + \sum_m \sum_n \frac{c_{2m} c_{2n}}{\beta+2n}\, \mathrm{e}^{-\mathrm{i}2(m-n)\tau} \right] \quad \text{(B.37)}$$

$$= -2\mathrm{i} \frac{s}{\det \Phi(0)} \sum_m \sum_n \frac{c_{2m} c_{2n}}{\beta+2n} \cos\left[2(m-n)\tau\right] \quad \text{(B.38)}$$

We point out that this particular solution to the inhomogeneous equation in terms of the variable τ is periodic with period π. We will therefore denote it $\tilde{u}_\mathrm{p}(\tau)$. Reverting to the original variable t, this means that $\tilde{u}_\mathrm{p}(t)$ has period $T = 2\pi/\omega_\mathrm{rf}$. Inserting the expression for $\det \Phi(0)$ then gives

$$\tilde{u}(t) = \tilde{u}_\mathrm{p}(t) = \frac{s}{\sum\limits_{m,n\in\mathbb{Z}} c_{2m} c_{2n} (\beta+2n)} \left(\sum_{m,n\in\mathbb{Z}} \frac{c_{2m} c_{2n}}{\beta+2n} \cos\left[(m-n)\omega_\mathrm{rf} t\right] \right) . \quad \text{(B.39)}$$

To satisfy arbitrary initial conditions, it is necessary to add to $\tilde{u}_\mathrm{p}(t)$ the general solution of the homogeneous equation. The general solution to the inhomogeneous equation is thus written $\tilde{x}(t) = \tilde{u}_\mathrm{p}(t) + k_1 \sum_n c_{2n} \cos(\nu + n\omega_\mathrm{rf})t + k_2 \sum_n c_{2n} \sin(\nu + n\omega_\mathrm{rf})t$, where the constants k_1, k_2 depend on initial conditions. For a particle starting at $t = 0$ at position x_0 with velocity $\dot{x}_0$, the solution $\tilde{x}(t)$ to the inhomogeneous Mathieu equation is found to be

$$\tilde{x}(t) = \tilde{u}_\mathrm{p}(t) + \tilde{\sigma} \sum_{n\in\mathbb{Z}} c_{2n} \cos\left[(\nu + n\omega_\mathrm{rf})\, t + \tilde{\phi} \right] \quad \text{(B.40)}$$

with

$$\tilde{\sigma} = \sqrt{ \left[\frac{x_0 - \tilde{u}_\mathrm{p}(0)}{\sum_n c_{2n}} \right]^2 + \left[\frac{\dot{x}_0 - \dot{\tilde{u}}_\mathrm{p}(0)}{\sum_n c_{2n}(\beta+2n)} \right]^2 } \quad \text{(B.41)}$$

$$\tilde{\phi} = \arctan\left[-\frac{\dot{x}_0 - \dot{\tilde{u}}_\mathrm{p}(0)}{\sum_n c_{2n}(\beta+2n)} \Big/ \frac{x_0 - \tilde{u}_\mathrm{p}(0)}{\sum_n c_{2n}} \right] . \quad \text{(B.42)}$$

B.2.1 Lowest-order approximation

Similar to the homogeneous case, it is possible to obtain a lowest-order approximation for $\tilde{x}(t)$ when $|a|$, $q^2 \ll 1$. In this case, one takes $c_{\pm 2} \simeq -(q/4)\, c_0$ and $c_{\pm 2n} \simeq 0$ for $|n| > 1$. One obtains

$$\sum_m \sum_n c_{2m} c_{2n} (\beta + 2n) \simeq c_0^2 \beta \left(1 - q + \frac{q^2}{4}\right) \simeq c_0^2 \beta (1 - q) \tag{B.43}$$

to first order in q. The particular solution $\tilde{u}_\mathrm{p}(t)$ then becomes

$$\tilde{u}_\mathrm{p}(t) \approx \frac{s}{\beta(1-q)} \left[\frac{q^2}{16(\beta-2)} + \frac{1}{\beta} + \frac{q^2}{16(\beta+2)} \right. \tag{B.44}$$

$$- \frac{q}{4} \left(\frac{2}{\beta} + \frac{1}{\beta-2} + \frac{1}{\beta+2} \right) \cos \omega_\mathrm{rf} t \tag{B.45}$$

$$\left. + \frac{q^2}{16} \left(\frac{1}{\beta-2} + \frac{1}{\beta+2} \right) \cos 2\omega_\mathrm{rf} t \right] . \tag{B.46}$$

Neglecting the term proportional to q^2 and making use of the approximation $\beta \pm 2 \simeq \pm 2$ that was introduced in the earlier section on the homogeneous case, one finds

$$\tilde{u}_\mathrm{p}(t) \approx \frac{s}{\beta^2(1-q)} \left(1 - \frac{q}{2} \cos \omega_\mathrm{rf} t\right) . \tag{B.47}$$

The lowest-order approximation to the general solution $\tilde{x}(t)$ can then be constructed through eq. (B.40) as

$$\tilde{x}(t) \approx \frac{s}{\beta^2(1-q)} - \frac{s}{\beta^2(1-q)} \frac{q}{2} \cos \omega_\mathrm{rf} t - r_0 \frac{q}{2} \cos(\nu t + \tilde{\phi}) \cos \omega_\mathrm{rf} t + r_0 \cos(\nu t + \tilde{\phi}) . \tag{B.48}$$

with $r_0 = \tilde{\sigma} c_0$. By defining $r_1 = s/[\beta^2(1-q)]$, this can also be written as

$$\tilde{x}(t) \approx \left[r_0 \cos(\nu t + \tilde{\phi}) + r_1 \right] \left(1 - \frac{q}{2} \cos \omega_\mathrm{rf} t\right) . \tag{B.49}$$

Appendix C

Dynamics of multi-state quantum systems

A situation that is often encountered in quantum mechanics is the coupling of eigenstates of a time-independent Hamiltonian H_0 through a time-dependent interaction Hamiltonian $H_{\mathrm{int}}(t)$. An important example is the interaction of an atom with an electromagnetic plane wave, which forms the basis for the qubit gates described in this work. A brief summary of the key results that have been used throughout the thesis is provided in this appendix.

Assuming that relaxation processes such as spontaneous emission or decoherence, which would require a formulation in terms of the density matrix, are absent or can be neglected, the time evolution of the state vector $|\psi(t)\rangle$ in the Schrödinger picture is completely described by the time-dependent Schrödinger equation (TDSE)

$$\mathrm{i}\hbar\frac{d\,|\psi(t)\rangle}{dt} = H(t)\,|\psi(t)\rangle \ . \tag{C.1}$$

Here, $H(t)$ is the total Hamiltonian operator of the system in the Schrödinger picture. If the state vector at some initial time $t = t_0$ is prescribed as $|\psi(t_0)\rangle$.

The unique solution $|\psi(t)\rangle$ that satisfies $|\psi(t = t_0)\rangle = |\psi(t_0)\rangle$ is obtained by the action of a unitary operator $U(t; t_0)$, known as the time-evolution operator, through

$$|\psi(t)\rangle = U(t; t_0)\,|\psi(t_0)\rangle \ . \tag{C.2}$$

It follows directly from the Schrödinger equation that the time-evolution operator itself satisfies the operator differential equation

$$\mathrm{i}\hbar\frac{dU(t; t_0))}{dt} = H(t)U(t; t_0), \qquad U(t = t_0; t_0) = \mathbb{I}\,, \tag{C.3}$$

where $\mathbb{I}$ denotes the identity operator. Once $U(t; t_0)$ has been found, the whole problem of calculating the evolution of a quantum system after it has been prepared in some arbitrary initial state reduces to applying this operator to $|\psi(t_0)\rangle$. The difficulty, of course, lies in finding $U(t; t_0)$.

If $H(t) = H_0$ is time-independent, the solution is relatively straightforward. By using the definition of the operator exponential, it may be verified that

$$U(t; t_0) = \mathrm{e}^{-\mathrm{i}H_0(t-t_0)/\hbar} \tag{C.4}$$

solves (C.3).

In general, however, the Hamiltonian may be time-dependent and may not commute with itself at different times. In this case, it may not be possible to find a closed-form expression for the time-evolution operator. A formal solution may be obtained by considering the integral equation corresponding to (C.3), given by

$$U(t;t_0) = \mathbb{I} - \frac{\mathrm{i}}{\hbar}\int_{t_0}^{t} H(s)U(s;t_0)\,ds\ . \tag{C.5}$$

Through recursive substitution for U inside the integral, this becomes

$$U(t;t_0) = \mathbb{I} + \left(-\frac{\mathrm{i}}{\hbar}\right)\int_{t_0}^{t} H(t_1)\,dt_1 + \left(-\frac{\mathrm{i}}{\hbar}\right)^2 \int_{t_0}^{t}\int_{t_0}^{t} H(t_1)H(t_2)\,dt_1 dt_2 + \ldots \tag{C.6}$$

$$= \mathcal{T}\mathrm{e}^{-\frac{\mathrm{i}}{\hbar}\int_{t_0}^{t} H(s)\,ds}\ , \tag{C.7}$$

where $\mathcal{T}$ denotes the time-ordering operator . If higher-order nested integrals may be neglected, the series contained in the exponential may be truncated, which results in a perturbative approximate solution for $U(t;t_0)$. If this assumption cannot be made, the formal series solution is only of limited practical use.

By introducing a set of basis vectors $\{|i\rangle\}$ for the Hilbert space of the system, the state vector can be expanded as

$$|\psi(t)\rangle = \sum_{i=1}^{n} c_i(t)\,|i\rangle\ , \tag{C.8}$$

where n is the dimension of the Hilbert space. The TDSE can then be mapped to a set of n coupled linear first-order differential equations

$$i\hbar\frac{dc_i(t)}{dt} = \sum_{j=1}^{n} H_{ij}(t)\,c_j(t) \tag{C.9}$$

for the expansion coefficients $c_i(t) = \langle i|\psi(t)\rangle$, which evolve through the matrix representation of the Hamiltonian in the chosen basis, with elements $H_{ij}(t) = \langle i|H(t)|j\rangle$. Usually one is interested in the state of the system $|\psi(t)\rangle$ at some time t, given that it started out in state $|\psi(t_0)\rangle$ at time $t = t_0$. With this initial condition, the evolution of the quantum state can be formulated as a first-order linear initial value problem (IVP) for the vector of components $\mathbf{c} = (c_1, \ldots, c_n)^T$:

$$\mathrm{i}\hbar\frac{d\mathbf{c}}{dt} = H(t)\,\mathbf{c}(t), \qquad \mathbf{c}(t = t_0) = \mathbf{c}_0\ . \tag{C.10}$$

C.1 Rotating frames

When conducting experiments, we measure expectation values of observables $\langle A^{(\mathrm{S})}(t)\rangle = {}^{(\mathrm{S})}\langle\psi(t)|A^{(\mathrm{S})}(t)|\psi(t)\rangle^{(\mathrm{S})}$ and probabilities $|\langle a_i|\psi(t)\rangle^{(\mathrm{S})}|^2$, where $A^{(\mathrm{S})}(t)$ is the corresponding operator in the Schrödinger picture and $\{|a_i\rangle\}$ are its eigenvectors. I will explicitly use superscripts in this section to make it evident which picture I am referring to. The operators $x^{(\mathrm{S})}$ and $p^{(\mathrm{S})}$ representing the dynamical variables in the Schrödinger picture are time-independent. A general operator $A^{(\mathrm{S})}(t)$ is a function of $x^{(\mathrm{S})}$ and $p^{(\mathrm{S})}$, but may nevertheless be time-dependent because the coefficients

multiplying the latter two operators may be functions of time.

Calculating the relevant expectation values and probabilities requires knowledge of $|\psi(t)\rangle^{(\mathrm{S})}$, which means that the Schrödinger equation (C.1) determined by $H^{(\mathrm{S})}(t)$ has to be solved. Rather than trying to do this directly in the Schrödinger picture, it is often advantageous to apply a unitary transformation to $|\psi(t)\rangle^{(\mathrm{S})}$ and instead consider the evolution equation for the transformed state vector. This is especially useful if the transformation results in an evolution equation that is simpler to solve (for example, because it involves only time-independent operators).

Let $R(t)$ be a time-dependent unitary operator[1]. This implies by definition that $R^\dagger(t)R(t) = \mathbb{I}$ for all t. Application of $R(t)$ to $|\psi(t)\rangle^{(\mathrm{S})}$ results in the transformed vector

$$|\widetilde{\psi}(t)\rangle = R(t)\,|\psi(t)\rangle^{(\mathrm{S})} \ . \tag{C.11}$$

Inserting the inverse relation $|\psi(t)\rangle^{(\mathrm{S})} = R^\dagger(t)\,|\widetilde{\psi}(t)\rangle$ into the Schrödinger-picture equation (C.1), it is found that for $|\psi(t)\rangle^{(\mathrm{S})}$ to be a solution, the transformed state vector has to satisfy

$$\mathrm{i}\hbar\frac{d\,|\widetilde{\psi}(t)\rangle}{dt} = \widetilde{H}(t)\,|\widetilde{\psi}(t)\rangle\,, \qquad |\widetilde{\psi}(t_0)\rangle = R(t_0)\,|\psi(t_0)\rangle^{(\mathrm{S})} \ , \tag{C.12}$$

where

$$\widetilde{H}(t) = R(t)H^{(\mathrm{S})}(t)R^\dagger(t) + \mathrm{i}\hbar\frac{dR(t)}{dt}R^\dagger(t)\ . \tag{C.13}$$

In deriving $\widetilde{H}(t)$, I have used the relation $d/dt(R^\dagger R) = dR^\dagger/dt\,R + R^\dagger\,dR/dt = 0$ since $R^\dagger R = \mathbb{I}$ is a constant operator. I will refer to the evolution equation (C.12) for the transformed vector as the Schrödinger equation in a rotating frame, in analogy with the classical picture of rotating coordinate axes. The operator $\widetilde{H}(t)$ can thus be considered the Hamiltonian in the rotating frame. The evolution equation may be solved to obtain the time-evolution operator $\widetilde{U}(t;t_0)$ in that frame and hence find

$$|\psi(t)\rangle^{(\mathrm{S})} = R^\dagger(t)\widetilde{U}(t;t_0)\,|\widetilde{\psi}(t_0)\rangle = R^\dagger(t)\widetilde{U}(t;t_0)R(t_0)\,|\psi(t_0)\rangle^{(\mathrm{S})} \ . \tag{C.14}$$

One may thus conclude that $U^{(\mathrm{S})}(t;t_0) = R^\dagger(t)\widetilde{U}(t;t_0)R(t_0)$.

The procedure described above consists in finding $\widetilde{H}(t)$, solving the Schrödinger equation in the rotating frame, transforming back to the lab frame and then calculating necessary quantities using $A^{(\mathrm{S})}(t)$. It is also possible, however, to find desired expectation values directly in the rotating frame, since

$${}^{(\mathrm{S})}\langle\psi(t)|A^{(\mathrm{S})}(t)|\psi(t)\rangle^{(\mathrm{S})} = \langle\widetilde{\psi}(t)|R(t)A^{(\mathrm{S})}(t)R^\dagger(t)|\widetilde{\psi}(t)\rangle = \langle\widetilde{\psi}(t)|\widetilde{A}(t)|\widetilde{\psi}(t)\rangle \tag{C.15}$$

with

$$\widetilde{A}(t) = R(t)A^{(\mathrm{S})}(t)R^\dagger(t)\ . \tag{C.16}$$

The operator $\widetilde{A}(t)$ may be considered the operator corresponding to the respective observable in the rotating frame. Making use of eq. (C.16), one finds that it obeys

[1] I reserve the symbol U for the time-evolution operator.

the evolution equation

$$\frac{d\widetilde{A}(t)}{dt} = \frac{dR}{dt}A^{(\mathrm{S})}R^\dagger + R\frac{dA^{(\mathrm{S})}}{dt}R^\dagger + RA^{(\mathrm{S})}\frac{dR^\dagger}{dt} \tag{C.17}$$

$$= \widetilde{A}R\frac{dR^\dagger}{dt} - R\frac{dR^\dagger}{dt}\widetilde{A} + R\frac{\partial A^{(\mathrm{S})}}{\partial t}R^\dagger \tag{C.18}$$

$$= \left[\widetilde{A}(t), R(t)\frac{dR^\dagger(t)}{dt}\right] + \widetilde{\frac{\partial A^{(\mathrm{S})}(t)}{\partial t}} \; . \tag{C.19}$$

For reasons that will become clear in the next section, I now define $\widetilde{H}_{\mathrm{op}}(t) = \mathrm{i}\hbar R(t)\, dR^\dagger(t)/dt$ and write

$$\frac{d\widetilde{A}(t)}{dt} = -\frac{\mathrm{i}}{\hbar}\left[\widetilde{A}(t), \widetilde{H}_{\mathrm{op}}(t)\right] + \widetilde{\frac{\partial A^{(\mathrm{S})}(t)}{\partial t}} \; . \tag{C.20}$$

One thus finds that the time dependence of $\widetilde{A}(t)$ is determined by the operator $\widetilde{H}_{\mathrm{op}}(t)$, which plays the role of a Hamiltonian for the operator in the rotating frame.

As an important example of the application of rotating frames, let us consider a transformation of the form

$$R(t) = \sum_i \exp\left[\mathrm{i}\,\phi_i(t)\right]|i\rangle\langle i| \; , \tag{C.21}$$

where $\phi_i(t)$ are arbitrary phase functions. The matrix representation of this operator in the $\{|i\rangle\}$ basis is diagonal and thus effectively multiplies each basis vector by a time-dependent phase factor. In the rotating frame, this leads to the Hamiltonian

$$\widetilde{H}(t) = \left[\sum_i \mathrm{e}^{\mathrm{i}\phi_i(t)}|i\rangle\langle i|\right]H^{(\mathrm{S})}(t)\left[\sum_j \mathrm{e}^{\mathrm{i}\phi_j(t)}|j\rangle\langle i|\right] \tag{C.22}$$

$$+ \mathrm{i}\hbar\left[\sum_i \mathrm{e}^{\mathrm{i}\phi_i(t)}\mathrm{i}\frac{d\phi_i(t)}{dt}|i\rangle\langle i|\right]\left[\sum_j \mathrm{e}^{\mathrm{i}\phi_j(t)}|j\rangle\langle i|\right] \tag{C.23}$$

$$= \sum_i \left[\langle i|H^{(\mathrm{S})}(t)|i\rangle - \hbar\frac{d\phi_i(t)}{dt}\right]|i\rangle\langle i| + \sum_{i\neq j}\mathrm{e}^{\mathrm{i}[\phi_i(t)-\phi_j(t)]}\,\langle i|H^{(\mathrm{S})}(t)|j\rangle\,|i\rangle\langle j| \; . \tag{C.24}$$

The transformation leads to a shift in the diagonal elements, while the off-diagonal elements acquire additional phase factors. If the phase functions are chosen as $\phi_i(t) = r_i t$ for constant r_i, the Hamiltonian in the rotating frame is given by the expression

$$\widetilde{H}(t) = \sum_i \left[\langle i|H^{(\mathrm{S})}(t)|i\rangle - \hbar r_i\right]|i\rangle\langle i| + \sum_{i\neq j}\mathrm{e}^{\mathrm{i}(r_i-r_j)t}\,\langle i|H^{(\mathrm{S})}(t)|j\rangle\,|i\rangle\langle j| \; . \tag{C.25}$$

This is particularly useful if the elements $\langle i|H^{(\mathrm{S})}|i\rangle$ are time-independent, as the transformation to the rotating frame then allows removal of constant additive offsets, such as ac shifts, from the diagonal elements. Alternatively, if the off-diagonal elements $\langle i|H^{(\mathrm{S})}(t)|j\rangle$ themselves contain oscillating exponentials, it may be possible to cancel some of these factors by judicious choice of the variables r_i. This may result in a Hamiltonian $\widetilde{H}(t)$ that has either simpler time dependence or is even time-independent. In the latter case, the time evolution operator is easily found. I make use of this technique throughout.

C.1.1 Heisenberg picture

This picture is defined by the choice $R(t) = (U^{(\mathrm{S})}(t;t_0))^\dagger$, where $U^{(\mathrm{S})}(t;t_0)$ denotes the time-evolution operator in the Schrödinger picture. Following the steps outlined above, one finds that

$$\mathrm{i}\hbar\frac{d\,|\psi(t)\rangle^{(\mathrm{H})}}{dt} = 0 \tag{C.26}$$

and therefore

$$|\psi(t)\rangle^{(\mathrm{H})} = |\psi(t_0)\rangle^{(\mathrm{S})} \ . \tag{C.27}$$

The state vector in the Heisenberg picture is constant and all time dependence is contained in the operators. The latter are determined via eq. (C.16) as $A^{(\mathrm{H})}(t) = U^\dagger(t;t_0)A^{(\mathrm{S})}(t)U(t;t_0)$. Furthermore, $dR^\dagger(t)/dt = -(\mathrm{i}/\hbar)\,U^{(\mathrm{S})}(t;t_0)H^{(\mathrm{S})}(t)$ for this particular choice of $R(t)$ and the Heisenberg evolution equation for operators is thus given by

$$\frac{dA^{(\mathrm{H})}(t)}{dt} = -\frac{\mathrm{i}}{\hbar}\left[A^{(\mathrm{H})}(t), H^{(\mathrm{H})}(t)\right] + U^\dagger(t;t_0)\frac{\partial A^{(\mathrm{S})}(t)}{\partial t}U(t;t_0)\ , \tag{C.28}$$

where $H^{(\mathrm{H})}(t) = \widetilde{H}_{\mathrm{op}}(t) = U^\dagger(t;t_0)H^{(\mathrm{S})}(t)U(t;t_0)$. In this picture, $\widetilde{H}_{\mathrm{op}}(t)$ is just the transformed Hamiltonian operator, which explains why I initially referred to this operator as a kind of Hamiltonian earlier.

C.1.2 Interaction picture

A different rotating frame may be useful if the Hamiltonian in the Schrödinger picture can be split into two terms, one of which leads to an evolution that can be solved explicitly. I will take $H^{(\mathrm{S})}(t) = H_1^{(\mathrm{S})}(t) + H_2^{(\mathrm{S})}(t)$ and assume that the time evolution operator $U_1^{(\mathrm{S})}(t;t_0)$, which satisfies

$$\mathrm{i}\hbar\frac{dU_1^{(\mathrm{S})}(t;t_0)}{dt} = H_1^{(\mathrm{S})}(t)U_1^{(\mathrm{S})}(t;t_0), \qquad U_1^{(\mathrm{S})}(t_0;t_0) = \mathbb{I} \tag{C.29}$$

has been found. The interaction picture is then defined by the transformation $R(t) = \left(U_1^{(\mathrm{S})}(t;t_0)\right)^\dagger$. Using the general procedure described above, one finds that

$$\mathrm{i}\hbar\frac{d\,|\psi(t)\rangle^{(\mathrm{I})}}{dt} = H_2^{(\mathrm{I})}(t)\ , \tag{C.30}$$

where $H_2^{(\mathrm{I})}(t) = \left(U_1^{(\mathrm{S})}(t;t_0)\right)^\dagger H_2^{(\mathrm{S})}(t)U_1^{(\mathrm{S})}(t;t_0)$. The time evolution of the state vector in the interaction picture with respect to $H_1^{(\mathrm{S})}(t)$ is thus determined only by the contribution arising from the other part $H_2^{(\mathrm{S})}(t)$ of the Hamiltonian, transformed into the rotating frame.

C.2 Magnus expansion

As remarked earlier, the solution $|\psi(t)\rangle$ to the time-dependent Schrödinger equation (C.1) for arbitrary initial state $|\psi(t_0)\rangle$ can be calculated straightforwardly once the time-evolution operator $U(t;t_0)$ has been found. The operator $U(t;t_0)$ is the solution

to the initial value problem given in eq. (C.3), which I reproduce here in the form

$$\frac{dU(t;t_0)}{dt} = G(t)U(t;t_0), \qquad U(t_0;t_0) = \mathbb{I}\,, \tag{C.31}$$

with $G(t) = (-\mathrm{i}/\hbar)H(t)$. When $G(t)$ does not commute with itself at different times, a closed-form solution to this problem is in general very difficult to find. Nevertheless, it may be possible to find series expansions for $U(t;t_0)$ that provide increasingly accurate approximations to the true time-evolution operator the more terms of the series are retained. One such example, the time-ordered exponential, was introduced earlier. A different kind of expansion was suggested by Magnus in a highly impactful paper [Mag54]. In analogy with the time-independent case, he suggested looking for a solution of the form

$$U(t;t_0) = \exp\Omega(t;t_0), \qquad \Omega(t_0;t_0) = \mathbb{O}\,. \tag{C.32}$$

He went on to prove that such a solution can be found and the operator $\Omega(t;t_0)$ written as the series

$$\Omega(t;t_0) = \sum_{n=1}^{\infty} \Omega_n(t;t_0)\,, \tag{C.33}$$

where $\Omega_n(t;t_0)$ may be expressed by means of nested commutators involving $G(t)$ at different times. The first few terms are given by

$$\Omega_1(t;t_0) = \int_{t_0}^{t} dt_1 G(t_1) \tag{C.34}$$

$$\Omega_2(t;t_0) = \frac{1}{2}\int_{t_0}^{t} dt_1 \int_{t_0}^{t_1} dt_2\,[G(t_1), G(t_2)] \tag{C.35}$$

$$\Omega_3(t;t_0) = \frac{1}{6}\int_{t_0}^{t} dt_1 \int_{t_0}^{t_1} dt_2 \int_{t_0}^{t_2} dt_3\,[G(t_1),[G(t_2),G(t_3)]] + [[G(t_1),G(t_2)]\,,G(t_3)] \tag{C.36}$$

The advantage of the Magnus expansion compared to the time-ordered exponential lies in the fact that $\exp\Omega(t;t_0)$ is unitary regardless of the term at which $\Omega(t;t_0)$ is truncated.

C.3 Adiabatic elimination of intermediate states

The time-dependent Schrödinger equation (C.9) results in a system of coupled first-order differential equations for the expansion coefficients $c_i(t)$ in some basis $\{|i\rangle\}$ of the Hilbert space of the system. If an exact description of the evolution of the system for arbitrary initial conditions is desired, these equations must be solved for all coefficients. If the dimension of the Hilbert space is large or the form of the Hamiltonian complicated, this can be a difficult task, even when numerical integration is used. However, it is found in some situations that attention may be restricted to a subset of states of the complete Hilbert space, while the remaining states may effectively be eliminated from the description. This considerably simplifies the treatment.

One such case is an interaction Hamiltonian with sinusoidal time-dependence. Let $H_0(t)$ denote some base Hamiltonian for the system in the Schrödinger picture and assume that the corresponding time-evolution operator $U_0(t)$ has been found.

An additional interaction is then introduced, of the form

$$H_{\mathrm{int}}(t) = V(t) = \frac{1}{2}\sum_a V^{a,+}\mathrm{e}^{-\mathrm{i}\omega_a t} + V^{a,-}\mathrm{e}^{\mathrm{i}\omega_a t} \;, \tag{C.37}$$

where $a \in \{1,\ldots,n\}$ labels the different frequency components of the perturbation and $V^{a,+}$ are time-independent operators that may in general be non-Hermitian. However, one requires $V^{a,-} = (V^{a,+})^\dagger$ to ensure that $H_{\mathrm{int}}(t)$ is Hermitian. Such a Hamiltonian arises, for example, from the interaction of an atom with a superposition of electromagnetic fields.

I now transform to the interaction picture with respect to $H_0(t)$, in which the interaction Hamiltonian is given by

$$V^{(\mathrm{I})}(t) = U_0^\dagger(t)V(t)U_0(t) \;. \tag{C.38}$$

Then one partitions the Hilbert space into a set of relevant states, labelled by p, and a set of irrelevant states, labelled by q [Sho90]. The former are those states that one is interested in and for which one wants to find the explicit time dependence. They include all states that are populated at the initial time t_0. The irrelevant states are those that should be eliminated from the dynamics, usually states that are presumed to receive negligible population during the evolution, such that $|c_q(t)| \ll 1$ at all times. A priori it is not necessarily obvious which states may be considered irrelevant, but it should become evident during the elimination procedure which conditions have to be satisfied for a state to fall in this category.

I now assume that the base Hamiltonian H_0 is time-independent, so that one may write

$$H_0 = \sum_i \hbar\omega_i |i\rangle\langle i| \tag{C.39}$$

and find the time-evolution operator $U_0(t)$ analytically as

$$U_0(t) = \mathrm{e}^{-\mathrm{i}\sum_i \omega_i t|i\rangle\langle i|} \;. \tag{C.40}$$

Hence one obtains

$$V^{(\mathrm{I})}(t) = \frac{1}{2}\sum_{i,j}\sum_a \left[\langle i|V^{a,+}|j\rangle\,\mathrm{e}^{\mathrm{i}(\omega_{ij}-\omega_a)t} + \langle i|V^{a,-}|j\rangle\,\mathrm{e}^{\mathrm{i}(\omega_{ij}+\omega_a)t}\right]|i\rangle\langle j| \;, \tag{C.41}$$

where $\omega_{ij} = \omega_i - \omega_j$. In the interaction picture, the wave function is expanded in terms of its components in the relevant and irrelevant subspaces as $|\psi(t)\rangle^{(\mathrm{I})} = \sum_p C_p(t)\,|p\rangle + \sum_q C_q(t)\,|q\rangle$ and evolves according to

$$\mathrm{i}\hbar\frac{dC_p(t)}{dt} = \frac{\hbar}{2}\sum_{a,\pm}\left[\sum_{p'}\Omega^{a,\pm}_{pp'}\mathrm{e}^{\mathrm{i}(\omega_{pp'}\mp\omega_a)t}\,C_{p'}(t) + \sum_q \Omega^{a,\pm}_{pq}\mathrm{e}^{\mathrm{i}(\omega_{pq}\mp\omega_a)t}\,C_q(t)\right] \tag{C.41a}$$

$$\mathrm{i}\hbar\frac{dC_q(t)}{dt} = \frac{\hbar}{2}\sum_{a,\pm}\sum_p \Omega^{a,\pm}_{qp}\mathrm{e}^{\mathrm{i}(\omega_{qp}\mp\omega_a)t}\,C_p(t) \;, \tag{C.41b}$$

where I have defined the Rabi frequencies

$$\Omega_{ij}^{a,+} = \frac{\langle i|V^{a,+}|j\rangle}{\hbar} \tag{C.42}$$

$$\Omega_{ij}^{a,-} = \frac{\langle i|V^{a,-}|j\rangle}{\hbar} = \left(\Omega_{ji}^{a,+}\right)^* . \tag{C.43}$$

In writing the differential equation for $C_q(t)$, I have neglected the coupling to other irrelevant states q'. This is based on the assumption that at the initial time t_0 all population resides in the relevant subspace and the states $|q\rangle$ are off resonance, so that at all later times $C_q(t) \ll 1$ and the effects of transitions within the irrelevant subspace are of order $|C_q|^2$. A formal integration of (C.41b) results in

$$C_q(t) = -\frac{\mathrm{i}}{2}\sum_{a,\pm}\sum_{p}\int_0^t \Omega_{qp}^{a,\pm}\mathrm{e}^{\mathrm{i}(\omega_{qp}\mp\omega_a)t'}\,C_p(t')\,dt' \tag{C.44}$$

for initial condition $C_q(0) = 0$. Integrating by parts and discarding the boundary and remaining integral terms leads to the approximate solution

$$C_q(t) = -\frac{1}{2}\sum_{a,\pm}\sum_{p}\frac{\Omega_{qp}^{a,\pm}}{\omega_{qp}\mp\omega_a}\,\mathrm{e}^{\mathrm{i}(\omega_{qp}\mp\omega_a)t}\,C_p(t)\ . \tag{C.45}$$

Adiabatic elimination then consists in substituting this approximate solution in (C.42), resulting in a differential equation involving only states in the relevant subspace:

$$\mathrm{i}\hbar\frac{dC_p(t)}{dt} = \hbar\sum_{p'}\left[\frac{1}{2}\sum_{a,\pm}\Omega_{pp'}^{a,\pm}\mathrm{e}^{\mathrm{i}(\omega_{pp'}\mp\omega_a)t} - \frac{1}{4}\sum_{a,\pm}\sum_{b,\pm}\sum_{q}\frac{\Omega_{pq}^{a,\pm}\Omega_{qp'}^{b,\pm}}{\omega_{qp}\mp\omega_b}\mathrm{e}^{\mathrm{i}(\omega_{pp'}\mp\omega_a\mp\omega_b)t}\right]C_{p'}(t)\ . \tag{C.46}$$

This shows that - within the approximations leading up to this equation - the evolution in the subspace of relevant states is determined by an effective Hamiltonian that is the sum of a term representing direct couplings and a term containing the indirect effects of off-resonant states. The latter has matrix elements given by

$$H_{pp'}^{\mathrm{offres}} = -\frac{\hbar}{4}\sum_{a,\pm}\sum_{b,\pm}\sum_{q}\frac{\Omega_{pq}^{a,\pm}\,\Omega_{qp'}^{b,\pm}}{\omega_{qp}\mp\omega_b}\mathrm{e}^{\mathrm{i}(\omega_{pp'}\mp\omega_a\mp\omega_b)t} \tag{C.47}$$

Most of the exponentials will be oscillating fast and can be neglected in the rotating-wave approximation. However, if the perturbation frequencies satisfy a resonance condition such that $\omega_{pp'} - (\omega_a - \omega_b) \approx 0$, two-photon transitions occur that lead to population oscillations on slow timescales. This is, for example, the mechanism underlying Raman transitions.

A notable feature resulting from off-resonant coupling is a time-independent contribution to the diagonal elements

$$\hbar\Delta_p^{\mathrm{ac}} = H_{pp}^{\mathrm{offres}} = -\frac{\hbar}{4}\sum_{a}\sum_{q}\frac{\left|\Omega_{qp}^{a,+}\right|^2}{\omega_{qp}-\omega_a} + \frac{\left|\Omega_{pq}^{a,+}\right|^2}{\omega_{qp}+\omega_a} \tag{C.48}$$

These apparent energy shifts induced on the relevant states are called ac Stark shifts for electric-dipole and ac Zeeman shifts for magnetic-dipole interactions.

C.3.1 Ac Zeeman shifts

I will now apply the formalism introduced above to derive explicit expressions for the ac Zeeman shifts appearing when an ion in our trap interacts with a magnetic field via the magnetic-dipole interaction. As discussed in section 5.2, the interaction Hamiltonian takes the form

$$H_{\rm int}(t) = \sum_q (-1)^{q+1} \mu_q B_{-q}, \tag{C.49}$$

which, using eq. (5.19) may be written

$$H_{\rm int}(t) = \frac{1}{2}\left(\left[\sum_q (-1)^{q+1} \mu_q B^+_{-q}(\mathbf{x})\right] {\rm e}^{-{\rm i}\omega t} + \left[\sum_q (-1)^{q+1} \mu_q B^-_{-q}(\mathbf{x})\right] {\rm e}^{{\rm i}\omega t} \right), \tag{C.50}$$

where to first order in x_m

$$B^\rho_{-q}(\mathbf{x}) = B^\rho_{-q}(\mathbf{x}_0) + \sum_m \partial_m B^\rho_{-q}(\mathbf{x}_0)\, x_{m,0} \left(a^\dagger_m + a_m\right). \tag{C.51}$$

The Hamiltonian is therefore of the form given in eq. (C.37), with $V^+ = \sum_q (-1)^{q+1} \mu_q B^+_{-q}(\mathbf{x})$.

I will use the pseudopotential approximation for the trapping potential and hence describe the atomic system as characterised by internal states $\{|s\rangle\}$ and moving in a three-dimensional pure harmonic oscillator potential with number states $\{|vecn\rangle\}$, where the vector $\mathbf{n} = (n_1, n_2, n_3)$ represents the motional part. The base Hamiltonian H_0 for this case is time-independent and may be expressed as

$$H_0 = \sum_s \hbar\omega_s |s\rangle\langle s| + \sum_m \hbar\nu_m \left(n_m + 1/2\right) |n_m\rangle\langle n_m| . \tag{C.52}$$

A basis $\{|i\rangle\}$ for the total Hilbert space is therefore given by the eigenstates $|i\rangle = |s_i\rangle\,|\mathbf{n}_i\rangle$ of H_0, with energy $\hbar\omega_i = \hbar\omega_{s,i} + \sum_m \hbar\nu_m \left(n_{m,i} + 1/2\right)$. The Rabi frequencies for the interaction, as given by (C.42), are found to be

$$\Omega^+_{ij} = \sum_q (-1)^{q+1} \langle s_i|\mu_q|s_j\rangle \left[\langle \mathbf{n}_i|B^+_{-q}(\mathbf{x}_0)|\mathbf{n}_j\rangle + \sum_m \partial_m B^+_{-q}(\mathbf{x}_0)\, x_{m,0}\, \langle \mathbf{n}_i|\left(a^\dagger_m + a_m\right)|\mathbf{n}_j\rangle \right] \tag{C.53}$$

Given a state $|s_i\rangle\,|n_{1,i}\rangle\,|n_{2,i}\rangle\,|n_{3,i}\rangle$, it will couple to another internal state $|s_j\rangle$ and the motional states connected with the latter via the carrier, the three red sideband and the three blue sideband terms (one for each mode). One can therefore reduce the sum over all irrelevant states specified by the composite label q in eq. (C.48) to a sum over all eliminated internal states $|s_k\rangle$ and the seven motional contributions connected with each of them. The first term of the sum in eq. (C.48) becomes

$$\sum_k R^2_{q,ki} \frac{\left|B^+_{-q}(\mathbf{x}_0)\right|^2}{\omega_{s,ki} - \omega} + \sum_k \sum_m R^2_{q,ki} \left|\partial_m B^+_{-q}(\mathbf{x}_0)\right|^2 x^2_{m,0} \left(\frac{n_{m,i}}{\omega_{s,ki} - \nu_m - \omega} + \frac{n_{m,i}+1}{\omega_{s,ki} + \nu_m - \omega} \right), \tag{C.54}$$

where $R_{ki,q} = (-1)^{q+1} \langle s_k|\mu_q|s_i\rangle$ is the matrix element for the unique spherical component $q = m_k - m_i$ that couples the two internal states in question. The quantity $\omega_{s,ki} = \omega_{s,k} - \omega_{s,i}$ represents the difference in frequency between the two internal states. The second term in eq. (C.48) takes the same form, but involves the quan-

tities $R_{-q,ik}$, $B_q^+(\mathbf{x}_0)$ and $\partial_m B_q^+(\mathbf{x}_0)$. Using the relations $R_{-q,ik} = (-1)^q R_{q,ki}$ and $B_q^+(\mathbf{x}_0) = (-1)^q \big(B_{-q}^-(\mathbf{x}_0)\big)^*$, one obtains the following expression for the ac Zeeman shift induced on state $|s_i\rangle\,|\mathbf{n}_i\rangle$

$$\begin{aligned}\Delta_i^{\mathrm{ac}} = -\frac{1}{4}\Bigg(&\sum_k R_{q,ki}^2\left[\frac{\left|B_{-q}^+(\mathbf{x}_0)\right|^2}{\omega_{s,ki}-\omega} + \frac{\left|B_{-q}^-(\mathbf{x}_0)\right|^2}{\omega_{s,ki}+\omega}\right] \\ &+ \sum_k\sum_m R_{q,ki}^2\, x_{m,0}^2\, n_{m,i}\left[\frac{\left|\partial_m B_{-q}^+(\mathbf{x}_0)\right|^2}{\omega_{s,ki}-\nu_m-\omega} + \frac{\left|\partial_m B_{-q}^-(\mathbf{x}_0)\right|^2}{\omega_{s,ki}-\nu_m+\omega}\right] \\ &+ \sum_k\sum_m R_{q,ki}^2\, x_{m,0}^2\,(n_{m,i}+1)\left[\frac{\left|\partial_m B_{-q}^+(\mathbf{x}_0)\right|^2}{\omega_{s,ki}+\nu_m-\omega} + \frac{\left|\partial_m B_{-q}^-(\mathbf{x}_0)\right|^2}{\omega_{s,ki}+\nu_m+\omega}\right]\Bigg)\end{aligned} \tag{C.55}$$

where the index k runs over all eliminated internal states and m over the three motional modes. Carrier couplings are usually much larger than sideband couplings, so one may neglect the contributions from the second and third lines above, resulting in the approximate shift

$$\Delta_i^{\mathrm{ac}} = -\frac{1}{4}\sum_k R_{q,ki}^2\left[\frac{\left|B_{-q}^+(\mathbf{x}_0)\right|^2}{\omega_{s,ki}-\omega} + \frac{\left|B_{-q}^-(\mathbf{x}_0)\right|^2}{\omega_{s,ki}+\omega}\right]. \tag{C.56}$$

C.4 Rabi Hamiltonian

In this section, I consider the time evolution of a two-state system under the influence of an interaction Hamiltonian that varies sinusoidally with time. The description will be similar to that of section C.3, except here I assume that the Hilbert space of the system is only two-dimensional. A basis for the space is formed by states $|\downarrow\rangle$ and $|\uparrow\rangle$, the latter lying higher in energy. I take the total Hamiltonian $H(t) = H_0 + H_{\mathrm{int}}(t)$ in the Schrödinger picture to consist of a time-independent term H_0 and a time-dependent interaction Hamiltonian of the form

$$H_{\mathrm{int}}(t) = \frac{1}{2}\Big(V\,\mathrm{e}^{-\mathrm{i}\omega t}\,\mathrm{e}^{\mathrm{i}\phi} + V^\dagger\,\mathrm{e}^{\mathrm{i}\omega t}\,\mathrm{e}^{-\mathrm{i}\phi}\Big). \tag{C.57}$$

The operator V is time-independent and may be non-Hermitian, while the variable ω denotes the frequency of the driving term. Transforming to the interaction picture with respect to H_0, one finds

$$\begin{aligned}H_{\mathrm{int}}^{(\mathrm{I})}(t) = \frac{1}{2}&\left[\langle\uparrow|V|\downarrow\rangle\,\mathrm{e}^{-\mathrm{i}\left(\omega-\omega_{\uparrow\downarrow}\right)t}\,\mathrm{e}^{\mathrm{i}\phi} + \langle\uparrow|V^\dagger|\downarrow\rangle\,\mathrm{e}^{\mathrm{i}\left(\omega+\omega_{\uparrow\downarrow}\right)t}\,\mathrm{e}^{-\mathrm{i}\phi}\right] \\ &+ \frac{1}{2}\left[\langle\downarrow|V|\uparrow\rangle\,\mathrm{e}^{-\mathrm{i}\left(\omega+\omega_{\uparrow\downarrow}\right)t}\mathrm{e}^{\mathrm{i}\phi} + \langle\downarrow|V^\dagger|\uparrow\rangle\,\mathrm{e}^{\mathrm{i}\left(\omega-\omega_{\uparrow\downarrow}\right)t}\mathrm{e}^{-\mathrm{i}\phi}\right],\end{aligned} \tag{C.58}$$

where I have defined $\omega_{\uparrow\downarrow} = (E_\uparrow - E_\downarrow)/\hbar$. The Hamiltonian above arises, for example, from the interaction of the electric dipole moment of an ideal two-state system with an electric field varying as $\mathbf{E}(\mathbf{x},t) = \mathbf{E}_0\cos(\mathbf{k}\cdot\mathbf{x} - \omega t + \phi)$. More generally, the Hamiltonian for an effective two-state system resulting from adiabatic elimination of states in a Hilbert space of larger dimension also takes the same form. In the latter case, however, the frequency $\omega_{\uparrow\downarrow}$ has to be replaced by $\bar{\omega}_{\uparrow\downarrow} = \omega_{\uparrow\downarrow} + \Delta_{\uparrow\downarrow}^{\mathrm{ac}}$ to account for the differential ac shift $\Delta_{\uparrow\downarrow}^{\mathrm{ac}} = \Delta_\uparrow^{\mathrm{ac}} - \Delta_\downarrow^{\mathrm{ac}}$ derived in the previous section.

Under the assumption $\omega \approx \omega_{\uparrow\downarrow}$, such that the driving term is close to resonance

with the transition, two timescales can be identified: there occur fast oscillations at frequencies $\pm(\omega+\omega_{\uparrow\downarrow})$, along with relatively slow oscillations at frequencies $\pm(\omega-\omega_{\uparrow\downarrow})$. If the coupling strength $\langle\uparrow|V^{\dagger}|\downarrow\rangle$ relevant for fast oscillations is sufficiently small, the rapidly varying terms in the Hamiltonian will only result in low-amplitude modulation of the expansion coefficients of the state vector, superposed on the larger-amplitude oscillation caused by slowly varying terms. Over the timescales that one is interested in, the former will average out and the corresponding terms in the Hamiltonian may thus be ignored. This is the familiar rotating-wave approximation. With this approximation, the Hamiltonian becomes

$$H_{\mathrm{int}}^{(\mathrm{I})}(t)=\frac{\hbar}{2}\,\Omega\left(\mathrm{e}^{-\mathrm{i}\epsilon t}\,\mathrm{e}^{\mathrm{i}\kappa}\,\sigma_{+}+\mathrm{e}^{\mathrm{i}\epsilon t}\,\mathrm{e}^{-\mathrm{i}\kappa}\,\sigma_{-}\right)\,, \tag{C.59}$$

where the detuning $\epsilon=\omega-\omega_{\uparrow\downarrow}$ has been introduced. When the more general case of a transition within an effective two-state system, such as a sideband transition between two atomic states $|\downarrow\rangle|\mathbf{n}\rangle\leftrightarrow|\uparrow\rangle|\mathbf{n}'\rangle$, is considered, the detuning ϵ relevant for the particular transition has to be used (see section 5.2.3). The matrix element $\langle\uparrow|V|\downarrow\rangle$ may be complex in general, so I have defined the Rabi frequency $\Omega=\left|\langle\uparrow|V|\downarrow\rangle\right|$ and moved a possible complex phase into the variable $\kappa=\phi+\arg\bigl(\langle\uparrow|V|\downarrow\rangle\bigr)$.

Even though the counter-rotating term has been removed, the interaction Hamiltonian is still time-dependent. I now move to a different rotating frame through the transformation $R(t)=\exp(\mathrm{i}\epsilon t\sigma_z/2)$. In that frame, the Hamiltonian takes the final time-independent form

$$H_{\mathrm{rabi}}=-\frac{\hbar\epsilon}{2}\sigma_z+\frac{\hbar\Omega}{2}\left(\mathrm{e}^{\mathrm{i}\kappa}\,\sigma_{+}+\mathrm{e}^{-\mathrm{i}\kappa}\,\sigma_{-}\right)\,. \tag{C.60}$$

In the basis

$$|\uparrow\rangle=\begin{pmatrix}1\\0\end{pmatrix},\quad|\downarrow\rangle=\begin{pmatrix}0\\1\end{pmatrix}\,, \tag{C.61}$$

the matrix representation of this Hamiltonian is given by

$$H_{\mathrm{rabi}}=\hbar\begin{pmatrix}-\frac{\epsilon}{2} & \frac{\Omega}{2}\,\mathrm{e}^{\mathrm{i}\kappa}\\ \frac{\Omega}{2}\,\mathrm{e}^{-\mathrm{i}\kappa} & \frac{\epsilon}{2}\end{pmatrix}\,. \tag{C.62}$$

One finds that H_{rabi} can be expressed in terms of the Pauli matrices as

$$H_{\mathrm{rabi}}=\frac{\hbar}{2}\left(\Omega\cos\kappa\,\sigma_x-\Omega\sin\kappa\,\sigma_y-\epsilon\,\sigma_z\right)=\frac{\hbar}{2}\widetilde{\Omega}\,\mathbf{n}\cdot\boldsymbol{\sigma}\,, \tag{C.63}$$

where $\mathbf{n}=(\Omega\cos\kappa,-\Omega\sin\kappa,-\epsilon)/\widetilde{\Omega}$ is a unit vector, $\boldsymbol{\sigma}=(\sigma_x,\sigma_y,\sigma_z)$ is the vector of Pauli matrices and I have introduced the generalised Rabi frequency $\widetilde{\Omega}=\sqrt{\Omega^2+\epsilon^2}$.

Since this Hamiltonian is time-independent, the general solution (C.4) for the time evolution operator is applicable. Assuming that a driving pulse is applied from time t_0 to t, one obtains $U_{\mathrm{rabi}}(t;t_0)=\exp(-\mathrm{i}\theta\mathbf{n}\cdot\boldsymbol{\sigma})$, with $\theta=\widetilde{\Omega}\,(t-t_0)\,/2$. Using the identity $\exp(-\mathrm{i}\theta\mathbf{n}\cdot\boldsymbol{\sigma})=\cos\theta\,\mathbb{I}-\mathrm{i}\sin\theta\,\mathbf{n}\cdot\boldsymbol{\sigma}$, the representation of the time-evolution operator in the basis $\{|\uparrow\rangle\,,|\downarrow\rangle\}$ is given by

$$U_{\mathrm{rabi}}(t;t_0)=\begin{pmatrix}\cos\theta+\mathrm{i}\frac{\epsilon}{\widetilde{\Omega}}\sin\theta & -\mathrm{i}\frac{\Omega}{\widetilde{\Omega}}\mathrm{e}^{\mathrm{i}\kappa}\sin\theta\\ -\mathrm{i}\frac{\Omega}{\widetilde{\Omega}}\mathrm{e}^{-\mathrm{i}\kappa}\sin\theta & \cos\theta-\mathrm{i}\frac{\epsilon}{\widetilde{\Omega}}\sin\theta\end{pmatrix}\,. \tag{C.64}$$

In order to find the state vector in the original Schrödinger picture, one would now

have to apply the inverses of the transformations used earlier to define the rotating frame. However, if one is only interested in the populations of the two states, this is not necessary because transformations of the form (C.21) only add phase factors to each basis vector, which do not change the magnitudes of the expansion coefficients.